Development of a desktop device for automated laser ablation in liquids

Dissertation

to obtain the academic degree of
Doctor of Natural Sciences
– Dr. rer. nat. –

by

Sarah Dittrich

born in Cologne

Faculty of Chemistry
Institute for Technical Chemistry I
University of Duisburg-Essen
Essen, 2021

DOI: 10.17185/duepublico/74559
URN: urn:nbn:de:hbz:465-20220721-122253-7

The present thesis was conducted from September 2017 to December 2020 in the group of Priv.-Doz. Dr. Bilal Gökce at the Institute for Technical Chemistry I (headed by Prof. Dr.-Ing. Stephan Barcikowski) at the University of Duisburg-Essen.

Referees: Prof. habil. Dr.-Ing. Stephan Barcikowski
University of Duisburg-Essen, Essen

Prof. Dr. Heinz Huber
University of Applied Sciences, Munich

Chairman: Prof. Dr. Michael Giese
University of Duisburg-Essen, Essen

Date of Disputation: 29 June 2021

Non quia difficilia sunt non audemus, sed quia non audemus difficilia sunt.

Nicht weil es schwer ist, wagen wir es nicht, sondern weil wir es nicht wagen, ist es schwer.

Lucius Annaeus Seneca,
Epistulae morales ad
Lucilium, XVII/XVIII, CIV, 26

Table of contents

Abbreviations and Dimensionless Numbers

Bo ..... Bodenstein number
CB ..... cavitation bubble
EDX ..... energy-dispersive X-ray spectroscopy
EEPROMs ..... Electrically Erasable Programmable Read-Only Memories
Fo ..... Fourier number
LAL ..... laser ablation in liquids, laser ablation in liquid
LED ..... light-emitting diode
LFL ..... laser fragmentation in liquids
LIPSS ..... laser-induced periodic surface structures
LML ..... laser melting in liquids
MDS ..... material data sheets
MOPA ..... master oscillator power amplifier system
NPs ..... nanoparticles
ns ..... nanosecond
PA12 ..... polyamide 12
PBs ..... persistent bubbles
PHA ..... preliminary hazard analysis
PID ..... piping and instrumentation diagram
PMMA ..... poly(methyl methacrylate)
ps ..... picosecond
PVP ..... polyvinylpyrrolidone
Re ..... Reynolds numbers
SEM ..... scanning electron microscopy
SERS ..... surface-enhanced Raman scattering
SPR ..... surface plasmon resonance
TEM ..... transmission electron microscopy
TPU ..... thermoplastic polyurethane
YIG ..... yttrium-iron garnet

Symbol & Indices

Symbols

α	absorption coefficient
β	mass transfer coefficient
γ	electron heat diffusion length
δ	penetration depth, boundary layer thickness
ε	shielding factor
ζ	zeta potential
η	dynamic viscosity
λ	wavelength
ρ	density
σ	surface tension
τ	pulse duration
A	absorption
c	heat capacity
c, d	constants
D	thermal diffusivity
d	diameter
E	energy
F	fluence
f	focal length
f_R	repetition rate
I	intensity
k	number of photons required for ionization, constant
l	reaction rate constant
M	molar mass
m	mass
n	order of reaction, refractive index
P	laser power
p	pressure
Q	heat
R	ideal gas constant, Pearson correlation coefficient, reflectivity
S	surface
T	temperature
t	time
v	flow velocity
V	volume
w	mass fraction, beam waist
z	distance, e.g., between the target surface and the lens

Subscription

0	Initial, incident
$1, 2, \ldots$	consecutive numbering
10	smaller than 10 nm
20	smaller than 20 nm
50	cutoff at 50 %
90	cutoff at 90 %
∞	infinite, without disturbance or limitation
A	air
amb	ambient
B	bubble, Boltzmann
eff	effective
ep	electron-phonon
G	glass
L	laser
l	layer
m	molar
max	maximal
in	inlet
N	number
opt	optimal
P	pulse
R	Rayleigh
$single$	single, regarding one
$spec$	specific
th	threshold
$total$	total, overall
v	vapor
w	water

Superscription

$'$	after focusing
$\bar{}$	mean
$\dot{}$	first derivative with respect to the time

Abstract

Laser Ablation in Liquids (LAL) has been evolved since the 1990s as a promising technique for producing pure colloids. LAL is a scalable method for producing nanoparticles (NPs), which show high catalytic activity, are easily functionalized, and, when supported onto polymer and metal powders, enhance the 3D printing powders' properties. However, in-depth knowledge of the process and suitable equipment are essential to ensure a highly reproducible process. Moreover, the process is only economically feasible if high productivities and a high automatization degree are achieved due to substantial investment and labor costs. A desktop-sized device enabling the automated production of NPs can be the solution to these challenges. A compact laser is required to ensure the compact device design. However, these lasers are limited in their power and, consequently, limit NP productivity. An intermediate pulse duration could provide an increased ablation efficiency and, thus, enhance the NP productivity. Therefore, in this work, the influence of pulse duration on the ablation efficiency is examined. Additionally, the process parameters are optimized, a safety analysis is performed, and future perspectives are analyzed to maximize the device's productivity.

At first, a suitable laser system for the device is identified by comparing different laser systems' ablation efficiencies. An intermediate laser pulse duration of about several hundred ps to ~2 ns is determined as a system leading to the highest efficiency. Shadowgraph imaging and pump-probe microscopy revealed that that for pulse durations >5 ns, more energy is absorbed by a laser-induced vapor layer leading to an energy loss for the ablation. The vapor layer expansion starts approximately 2 ns after the laser pulse impact allowing higher efficiencies for short pulse durations.

Second, the process parameters for a device for automated LAL are optimized. Here, the relation between productivity and particle size is demonstrated and explained by in-process fragmentation. Due to a low-power laser chosen for the device, the parameters, as the focal distance and liquid flow rate, are adjusted, focusing on high productivity. It is found that the focal distance, liquid flow rate, and laser energy can be combined to the volume-specific energy dose, which determined the NP size.

Third, the safety of the device is evaluated. Therefore, different sensors are implemented and evaluated. The future perspectives and possibilities of the device are considered. The current capacities are sufficient to provide enough colloid for laboratory-scaled testing of functionalized materials as catalysts, bio-inks, and 3d printing powder. The efficiency of the device could be increased by beam splitting.

Overall, this work shows that a high LAL efficiency is found for a pulse duration of about several hundred ps to ~2 ns. This finding enabled the development and construction of a compact and automated LAL device.

1. Introduction

Although nanoparticles (NPs) are often related to modern science, even in Ancient Rome, these particles were used. One famous example from the 4th century AD is the Lycurgus Cup made of silver (Ag) and gold (Au) NPs dispersed in a glass matrix [1]. These embedded NPs lead to a dichroism where the cup seems red when illuminated from the back and purple-green from the front view. Although this cup was found in the 19th century only in the 1960s, its underlying high-tech principle was understood due to the invention, improvement, and spread of transmission electron microscopy (TEM) [2]. The cup produced more than 2000 years ago is an early example of a nanocomposite. Nowadays, Au, Ag, and Pt are the most commonly mentioned colloids in publications considering NP applications (see Fig. 1).

Fig. 1: Word cloud of materials referred to in literature investigating applications of NPs. The size of a word reflects the frequency of mentions. All individual alloys, as AgAu or PtPd, are summarized under the term "alloy". The string "nanoparticle, application" is searched in the Scopus database (status April 2020).

Nowadays, examples of nanocomposites are antibacterial food packaging [3] or catheter, and tympanostomy tubes [4], where Ag NPs are embedded in polymers. In these applications, the release of Ag^+ ions leads to an antibacterial effect [5]. However, the therapeutic window for Ag NPs is very narrow [6] so that often alloy NPs, such as AgCu [7], are used, which slows the release rate of Ag^+. Next to the inhibition of bacterial growth, polymers can also be nano-functionalized to improve the biocompatibility of implants or artificial organs by increasing the cell adhesion, as shown for Au and Pt NP [8]. It should also be mentioned that for the nano-functionalization, already very low NP mass loads with about 0.1 wt.% [8], can be sufficient for the desired effect.

While the Au NPs in the Lycurgus Cup might be included due to unwanted or even wanted contamination [2], they are the most frequently analyzed NPs these days and most often mentioned in the literature elucidating possible applications (Fig. 1). Contrary to the Ag particles, not the ion release is crucial, but the specific Au NP surface. Since Au is a weak acid, S-H-bonds can be split under hydrogen release. Thus, molecules attached to the thiol group are bound to the Au NPs [9]. This attachment of biomolecules is also called bioconjugation. Also, the Au colloid appears red due to the surface plasmon resonance (SPR). With bioconjugation, specific drug delivery systems [10, 11], and lateral flow assays for point of case diagnostics [12] can be designed. Another kind of biological sensor can be fabricated with photonic crystals doped with Au NPs to vary dielectric properties [13]. Next to biological application, Au NPs are also used for the oxidation of methane [14], glucose [15], and reduction of 4-nitrophenols [16].

However, generally, the most common material for catalysis is platinum (Pt). In the literature, Pt is discussed as a catalyst for water splitting [17, 18], exhaust gas treatment [19], and methanol oxidation [20]. As already mentioned for the nanocomposites, the catalytic performance can be improved by using alloy NPs. For example, PtAu catalysts showed 5 times higher conversion rates than pure Pt catalysts [21]. Another advantage of alloy catalysts is the improved long time stability, as achieved with PtPd catalysts for automotive exhaust treatment [22, 23].

The NPs are further classified by their synthesis route. One common way is by reducing metal salts, as described by Turkevich [24] and advanced by Frens [25, 26] for Au NP. In this case, chloroauric acid is reduced and simultaneously stabilized by citric acid. For many applications of NPs, however, purity is crucial so that residual educts and side products need to be eliminated in post-processing steps [27]. Another synthesis route, established in the 1990s by Fojtik and Hegelein [28], is the NP production by pulsed laser ablation in liquid (LAL) [29–31]. This procedure provides a wide range of target-liquid-variations: as target material e.g. the ablation of (noble) metals [28, 32], semiconductors [33–36], ceramics [37, 38], alloys (AuAg [39], AuFe [40], PtPb [41], AgCu [42]) or doped materials [43–45] in water [46], organic solvents like acetone [47], ethanol [33], toluene [48], alkanes [49, 50], oils [51], lubricants [52, 53], and even nail polish [54] is reported. The purity of these laser-generated NPs enables new applications. It was shown that laser-generated NPs are a good reference material in nanotoxicology studies due to their controlled surface chemistry [55]. Thus, it was demonstrated that residuals of chemically prepared NPs, as citrate or cetrimonium bromide, harm cell viability [56]. Also, for surface-enhanced Raman scattering (SERS), laser-generated Au [57] and Ag [58, 59] NPs enhance SERS signal, when employed as the active surface, due to lack of impurities compared to chemically produced particles. Also, in catalysis, laser-generated Au NPs showed lower CO conversion temperature than chemically synthesized NPs [27].

Compared to the chemical synthesis of NPs, LAL provides a green and sustainable method for NP production according to the twelve green chemistry principles [60]. For example, the educt for a LAL process is a pure metal target, whereas precursor salts are required for the chemical reduction [24]. These salts, e.g., chloroauric acid [61] for the production of Au NPs, are more hazardous than the pure metal. Chloroauric acid can lead to chemical burns and is water contaminating [62]. Moreover, chloroauric acid is produced on an industrial scale by solving elemental Au in aqua regia and subsequent evaporation of the solvent. Agua regia needs to be handled with great precaution and toxic nitrogen dioxide is produced during the solvation of Au [63] so that LAL compromises the "less hazardous chemical synthesis". According to the "prevention" principle, pure colloids without residuals and side products from the precursor are produced via LAL [64].

Scientists working on the different applications of NPs either need to purchase NPs or synthesize them themselves. In both cases, it can be chosen between laser-generated and chemically produced colloids. Jendrzej et al. compared the economic feasibility of both process routes for the production of Au NPs [65]. They showed that for productivities higher than 550 mg/h, LAL is the more cost-efficient NP production method. This high break-even productivity is caused by the substantial investment cost for LAL and additional labor costs. They also demonstrated that, on average, 55 % of the total expenses result from labor costs [65]. However, the economic feasibility of LAL is dependent on NP productivity. Trenque et al. demonstrated that although the laser-generated CeO_2 NPs showed higher catalytic activity than the other samples, they are the most expensive tested sample due to their low productivity [66]. With 0.25 g/day, laser-generated particles show a productivity of less than 2 % of the other tested NPs so that due to the increased work time necessary for the production, the costs rise to more than 980 €/g [66].

Both examples ([65, 66]) show that the labor costs drastically influence colloid price so that an automated synthesis, where almost no labor is needed, can decrease the production costs for laser-generated NPs. Compared to the chemical synthesis, the automated LAL NP synthesis has the advantage that untrained users can produce colloids and no chemical laboratory is required. Moreover, colloids are metastable systems so that, in the case that colloids are purchased, the colloid quality might have altered. With an automated LAL NP synthesis, the on-demand production of colloids is possible. Also, if sufficiently high amounts of colloids are required, the automated production might be economically more feasible than colloid purchase.

In conclusion, laser-generated colloids exhibit several advantages compared to chemically synthesized ones. Although numerous different material-liquid combinations are treated in the literature, most applications focus on Au, Ag, and Pt NPs produced in water. Economic investigations showed that labor costs mainly determine the colloid price. This thesis will

present a desktop device that enables a simple, on-demand, and cost-efficient production of laser-generated NPs demonstrated by Ag, Au, and Pt NPs in water.

2. Fundamentals of laser ablation in liquids

Pulsed laser ablation in liquids (LAL) is a top-down method for NP generation comprising a simple setup. A target material with the desired NP composition is put in a liquid containing vessel. By focusing a pulsed laser beam through the liquid onto the target surface, NPs are removed from the target material and suspended in the liquid. Thereby, it is necessary to deeply understand both the laser beam's interaction with the liquid layer (section 2.1) and the target material (section 2.2) to control the process. Despite this simple setup, there are plenty of adjustable parameters influencing the NP properties (section 2.3) and productivity (section 2.4). In that sense, the technique's productivity and scalability are crucial to its employment in industrial applications (section 2.5).

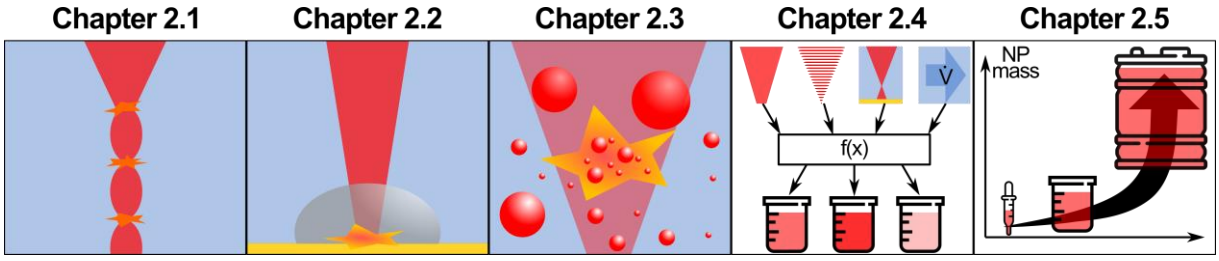

Fig. 2: Overview of the fundamentals of LAL. First, the laser-liquid interactions (section 2.1) and the laser-target interactions are (section 2.2) discussed. In the following, the influence of the laser parameters on the NP properties (section 2.3) and the NP productivity (section 2.4) are considered. Finally, the scalability of LAL is addressed (section 2.5).

2.1. Laser-liquid interaction

For LAL, a laser beam is focused on a target immersed in liquid as described in [67] for discontinuous and in [68] for continuous setups. Therefore, contrary to ablation in air, the laser beam interaction with the liquid environment needs to be considered. This interaction leads to a loss of laser energy reaching the target surface and should be kept as low as possible. In general, linear and non-linear laser-liquid interactions occur.

The laser beam as a light wave consists of an electric and magnetic field, where the former excites the electrons in a surrounding media. Consequently, the electrons start to swing along with the wave. Thereby, a temporal dipole is induced, and the medium is electrically polarized. For low light intensities, i.e., low wave amplitudes, the electric field strength and polarization are linearly connected. For this linear regime, a part, proportionally to the incident laser beam intensity, is absorbed by the liquid and reflected at the interfaces. These linear effects and their resulting energy losses are inevitable for LAL but easy to calculate.

For high laser intensities, higher-order electric field strength and polarization gain impact. The threshold intensities for the transition from linear to non-linear is material dependent and described by its non-linear refractive index. For water at 1064 nm (n_0 = 1.32 and $n_2 = 4.1 \cdot 10^{-16}$ cm^2/W), a critical peak power for non-linear optical effects of 3.0 MW can be calculated [69]. Due to the high intensity required to initialize these effects, they are only observed for fs and short ps laser pulses and are negligible for ns LAL. For the different laser systems used in [70], a ns laser reaches a peak power (Eq. 2) of 0.07 MW, far below the critical power. On the other side, the ps laser systems exceed the power threshold by a factor of ten (30 MW). Thus, non-linear effects are expected for the latter case.

$$P_{crit} = \frac{\pi \cdot 0.37 \cdot \lambda^2}{8 \cdot n_0 \cdot n_2} \quad \text{Eq. 1}$$

$$P_{peak} = \frac{E_P}{\tau_P} = \frac{\bar{P}}{\tau_P \cdot f_R} \quad \text{Eq. 2}$$

In the non-linear regime, the optical Kerr effect leads to a change in the refractive index, which causes effects like filamentation, optical breakdown, and formation of a supercontinuum, and leads to additional energy losses. Filamentation occurs due to a spatial-dependent change of the medium's refractive index caused by the intensity gradient of the beam profile. During self-focusing of the beam, the medium's refractive index increases with the beam intensity, leading to focusing of the electromagnetic wave as with a lens. The focusing, plasma formation, and defocusing of the laser beam due to the generated plasma changes the laser beam's spatial energy distribution [71–73]. LAL's drawbacks are spatial change, energy losses of up to 55 % [74], and change of the wavelength spectrum of

the laser (supercontinuum). Also, the self-focusing of the laser beams leads to a shift in the focal plane position so that the spot of maximal productivity is found before the geometrical focal plane [75, 76].

The optical breakdown describes the free electron plasma generation. It occurs when free electrons of the medium are accelerated so that they collide with other atoms and molecules, leading to the formation of secondary free carriers, which starts an avalanche. Depending on the process parameters, like laser pulse duration, intensity, or material, avalanche ionization or multiphoton absorption are the dominant mechanisms inducing optical breakdown. Thus, a high density of free carriers is built up, a plasma forms, the absorption coefficient increases drastically, and the medium becomes conductive. The intensity required for optical breakdown depends on the pulse duration and, contrary to filamentation, optical breakdown also occurs for ns laser pulses (Fig. 3) [77, 78]. Vogel et al. found it to be $\propto {\tau_L}^{-0.8}$ [78]. The threshold remains constant as long as the pulse duration exceeds the cascade's rise time of several hundred ps [78]. For shorter pulse durations, the energy must be increased to start the avalanche during the laser pulse.

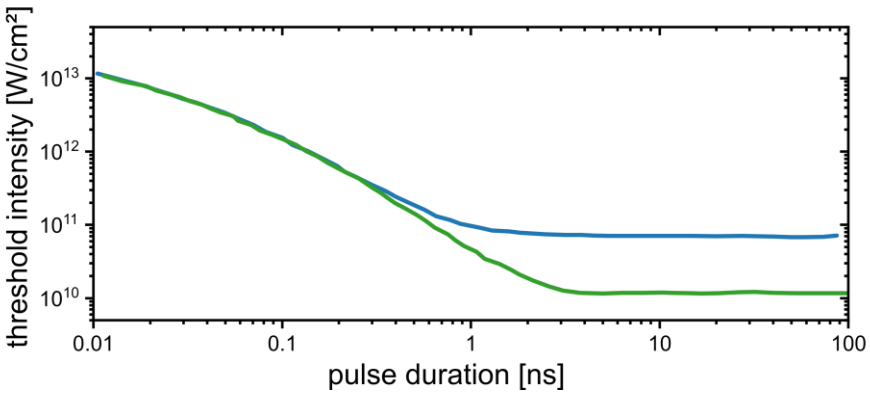

Fig. 3: Dependency of the optical breakdown threshold intensity on the laser pulse duration in water at 1064 nm in pure water (blue line) and water with impurities (green line) for a laser spot size of 5 µm [78].

Fig. 3 also shows that impurities in the liquid can lead to a 6 times lower optical breakdown threshold in the case of 1 ns pulse duration [78] because electrons from the impurities are already present, easing the generation of the breakdown. The threshold intensities for non-linear effects are reported to be lower when NPs or impurities are present in the liquid [79–81] (Fig. 3). For 1 ns laser ablation fluences of <15 J/cm² are reported [82], resulting in $<10^{10}$ W/cm². For this intensity during ns LAL, a breakdown is not expected, even if impurities are present in the liquid. When discussing the kind of impurity, it was found that for plasmonic NP, the non-linear effects at ps irradiation were stronger the closer the plasmon frequency was to the laser wavelength (and thus the higher the NP absorption) [83]. The non-linear effects at different NP sizes for copper (Cu) NP under fs irradiation have been

discussed [84]. The authors found that for larger NP, saturable absorption is mainly found due to a high amount of occupied densities of state. In contrast, for smaller particles, free carrier absorption and two-photon absorption is observed. Also, studies quantifying the non-linear effects of colloidal solutions are performed for colloids (Au [85–88], Ag [89], Pt [90]). In general, an enhancement of the non-linear refractive index is observed with increasing NP concentration so that, according to Eq. 1, the critical power is lowered.

Lastly, for LAL, the linear effects of the laser beam-NPs or –microbubble interaction must be considered. As is shown by Kalus et al., Ag, Au, and Pt, with concentrations between 40 – 60 mg/L, shield about 20 % of the energy of a 10 ns laser [91]. A consecutive study revealed that this effect is NP concentration-dependent, and for 100 mg/L, about 40 % of the laser energy is shielded by Au NPs [92]. Additionally, up to 30 % of the incoming laser energy is shielded by microbubbles in water, which appears to be independent of the laser fluence [93].

In summary, for LAL, three different mechanisms can lead to energy shielding: shielding effects caused by the water layer, NPs, and microbubbles. The energy loss caused by non-linear effects can be reduced by applying longer ps and ns laser pulses. The reduction of energy losses during LAL provides a promising way to increase the ablation efficiency.

2.2. Laser-solids interaction

After the laser beam propagates through the liquid, the interaction with the target material starts. Here, essential factors for the ablation of metals, as the laser pulse duration and the number of free charge carriers in the target, must be considered [31]. Two scenarios can be differentiated depending on the pulse duration compared to the material electron-phonon coupling time, in the range of ps for metals. The different sequences of the physical steps during the ablation with ultrashort, much shorter than electron-phonon coupling time, and short pulse, larger than the electron-phonon coupling durations, are sketched in Fig. 4 and will be discussed in the following.

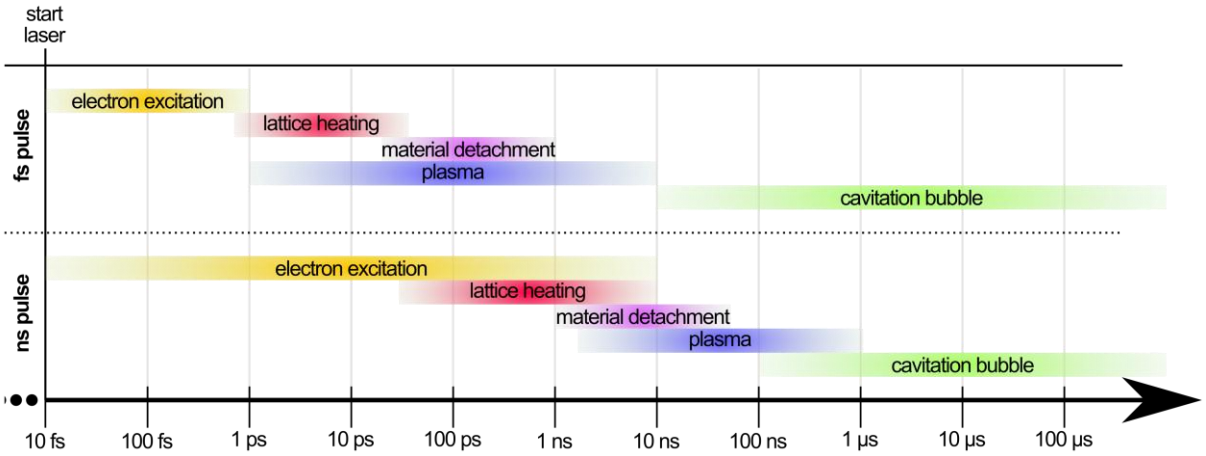

Fig. 4: Timeline of the mechanism for LAL for a fs laser pulse (top section) and a ns laser pulse (bottom section), the figure is adapted from [31]

When analyzing the laser-matter interaction, firstly, the laser radiation hits the target surface and is partially reflected and partially absorbed. It has been mentioned in the literature that these properties are not constant under irradiation. It is reported that, for example, the reflectivity strongly decreases as soon as the plasma formation is initiated [94–97]. The absorption of laser energy is limited by the metal's optical penetration depth, being in the range of tens of nm [98, 99]. For metals, the ballistic motion of excited electrons can increase the penetration depth by a factor of about 10 [100, 101]. Due to the electron-lattice collision, the energy of the electrons is transferred to the lattice system. However, due to a substantial mass difference between the electron and lattice atoms, only small amounts of kinetic energy is transferred per collision, resulting in a comparable long equilibration time of a few ps. This equilibration time is called electron-phonon coupling time [102, 103]. For laser pulse durations smaller than the electron-phonon coupling time, the ablation process is less affected by the laser pulse duration [104–106]. However, for ns pulse durations, the laser continues to emit when consecutive processes have started, leading laser beam shielding by an opalescent critical water layer or the ablation plume [107]. Fig. 5 explains the difference in

the resulting target surface temperature for different pulse durations. Ultrafast fs laser pulses lead to isochore heating ($A_1 \rightarrow A_2$) and high internal pressure released by rapid expansion ($A_2 \rightarrow A_3$). On the contrary, for ns laser pulses, the material heating occurs slowly so that the built-up pressure is released during the heating by expansion ($D_1 \rightarrow D_2$). For laser pulses in between, a middle path is followed ($B_1 \rightarrow B_2$).

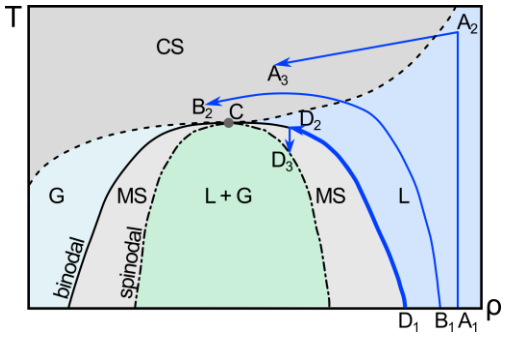

Fig. 5: Different energy absorption mechanisms for fs (A), ps (B), and ns (D) laser irradiation (C: critical point, L: liquid, G: gas, MS: meta-stable, CS: supercritical) adapted from [108].

As a consequence of the energy absorption, the material starts to melt. Now it is differentiated between homogeneous, heterogeneous, and non-thermal melting. The former occurs at very high laser energy densities and leads to melting of an entire area within ps [109]. Heterogeneous melting occurs at a slower time scale of up to 100 ps, when less energy is deposited in the material [110]. Usually, surface layers undergo homogeneous melting, whereas heterogeneous melting is found in deeper material layers. Non-thermal melting is observed in the case of the ablation of semiconductors and dielectrics. Here, hot electrons lead to a movement of lattice ions [111, 112].

Due to the temperature change, material physiology undergoes a change determined by the liquid's confinement. A detailed description of the difference between the material's response to laser irradiation under air and water can be found in [95]. A larger internal pressure within the material is built up for a target surrounded by water since the liquid layer is strongly overheated [113]. By simulations [114] and experimentally, two regimes, depending on the incident laser fluence, were identified. For lower fluences, which are slightly above the material ablation threshold, the regime is called spallation. The internal pressure is released by pressure waves into the liquid and deeper material layers by expanding voids [114]. In the case of explosive boiling or phase explosion regime at fluences far above the threshold fluence, a hot dense layer forms at the target-liquid interface, which is confined by the liquid [114]. For both fluence regimes, a supercritical water layer between the molten material and bulk water is found [113].

A plasma is ignited during the previously explained material detachment and evolves from the target surface into the surrounding liquid. It should be mentioned that for longer pulse

durations, the plasma state gains additional energy from the irradiating laser beam (see Fig. 4), which results in a longer plasma lifetime and a brighter plasma emission for increasing ns laser ablation [115, 116]. The plasma lifetime usually lies in the time range of some nanoseconds for fs (<10 ns for fs pulses at ~1 J/cm² [117, 118]) and several microseconds for ps and ns irradiation (5 µs for 500 ps, 14 J/cm² [119]; >1 µs for 20 ns, 1.2 kJ/cm² [120]). During the expansion, a plasma state is sustained inside the plume. Due to energy transfer from the plume into the liquid to process is cooling, and finally, the plasma state cannot be maintained anymore. Due to the pressure and temperature increase, which easily exceeds 10 MPa and 1000 K [121], in the surrounding liquid, the supercritical state is reached at the plume-water interface, which allows the plasma plume, due to lower surface tension and density, to expand into the liquid. Due to the opalescence of the critical water layer, parts of the laser beam are scattered and do not reach the target. Starinsky et al. showed that shielding by the critical opalescence only shields the first 300 ps of the laser beam of 9 ns [107]. Afterward, a critical electron density in the plasma is reached, which the laser beam cannot penetrate anymore, so that the ablation efficiency is decreased [115]. However, less data for pulse durations of 500 ps to 2 ns is available in the literature.

During plasma cooling, the energy is dissipated, a vapor layer is formed, and a hemispherical shock wave is observed, expanding with approximately 1500 m/s in water for a pulse duration of 10 ns [122] and 1000 m/s for 150 fs [123]. The faster shock wave expansion for ns pulses can be explained by the higher plasma energy, which is transformed into mechanical energy [124]. The shock wave also propagates into the target material. Due to the shock wave reflectance, sound waves propagate parallel to the target about 1 µs after the primary shock wave is observed [122]. The lifetime of the cavitation bubble (CB) can be divided into expansion, shrinking, collapse, and, for sufficient high energies, rebound [122]. The expansion of the cavitation bubble can be distinguished from the collapsing step by a necking of the contact angle between liquid, bubble, and target surface. It was found that the extent of this angle is determined by the liquid's viscosity [125]. Already during the expansion of the bubble, persistent microbubbles are present in the surrounding fluid [122, 126]. These are attributed to pre-existing NPs in the liquid for ns laser ablation [122], and NPs emerged from the CB for ps pulses [127]. After expansion, the cavitation bubble reaches its maximal size, determined by the laser fluence and pulse length. In general, the cavitation bubble volume scales linearly with the laser fluence [126]. However, for fluences lower than 50 J/cm² and a pulse duration of 7 ns, Reich et al. observed smaller CBs than expected for a linear trend [128]. Regarding the CB volume's pulse duration-dependency, larger bubbles are formed with longer laser pulse durations. For example, at about 2 J/cm² and 25 ps, CB of $30 \cdot 10^{-3}$ mm³ are observed [126], and they decrease to $0.5 \cdot 10^{-3}$ mm³, for 50 fs pulses [129]. For ns pulse durations, the CB volume exceeds several mm³ (7 ns pulse duration, 150 J/cm², 24 mm³ [128], 10 ns, 18 J/cm², 14 mm³ 36 J/cm², 34 mm³ [130] 10 ns, 50 – 100 mJ, 14 –

34 mm^3 [122]). As mentioned previously, this can be attributed to the higher plasma energies and resulting mechanical energy for ns pulse durations. Finally, the collapse of the CB occurs after several hundreds of microseconds [122, 131]. As for plasma plume evolution studies, insights into the complete CB dynamics and parameter dependencies for an intermediate pulse duration of 500 ps to 2 ns are missing.

The seeds for the NP formation evolve during the plume formation. The rapid temperature quenching due to the surrounding liquid and rapid expansion from thousands of Kelvin leads to particle formation. For laser ablation, initial cooling rates of 10^{12} K/s for fs [114] and 10^{10} K/s for ns [121] laser ablation are reported in the literature. Research reporting the presence of NP in a very early phase of the vapor bubble supports this nucleation hypothesis [132, 133]. Moreover, it was reported that changes in the cavitation bubble dynamic do not influence primary particles' size distribution [134]. However, in most cases, bimodal size distributions were reported [135] in the early stage of the bubble dynamic [136]. The bimodality indicates that rapid nucleation cannot be the only mechanism for NP formation. Experimentally an explanation could not be found.

However, Sylvestre et al. hypothesized that plasma dynamics cause the formation of a larger size fraction since they observed the amount of larger particles correlating with the plasma intensity [135]. Therefore, simulation studies attempted to provide more in-depth insight into the NP dynamic and formation [127, 137]. Molecular dynamic simulation has proven to be the most promising approach for this theoretical study since atoms' dynamic behavior, the energy dissipation, and thereby the plume phase can be simulated. Shih et al. determined that the instability of the superheated metal layer is responsible for the formation of secondary NPs during ps laser ablation [127]. For ablation with pulse duration from 400 ps – 2 ns, most NPs are formed by spinodal decomposition [137]. In Fig. 5, spinodal decomposition is marked by the dotted blue line. After laser heating of the system ($D_1 \rightarrow D_2$), the system cools down ($D_2 \rightarrow D_3$). In the meta-stable regime between the binodal and spinodal curve, decomposition of the system is kinetically restrained so that decomposition and thus NP formation occurs in the two-phase regime. Additionally, due to a lower density and higher temperature in the CB, collision and coalescence lead to the disappearance of smaller NPs for ns laser pulses.

In summary, the ablation mechanism during fs and ns pulse ablation has been examined in the literature. One disadvantage of fs-laser ablation is the energy loss due to non-linear effects. Moreover, a distinct bimodality of the colloid is observed. For ns-laser ablation, on the other side, energy losses due to plasma shielding or heating occur. Therefore, an intermediate pulse duration range of several hundred ps to 2 ns are expected to be favorable for LAL. However, this pulse duration range has rarely been considered in the literature.

2.3. Manipulation of the nanoparticle properties

Apart from LAL, there is also the field of laser processing of colloids, which consists of post-processing steps after the ablation to manipulate the NP properties [29]. NPs can be manipulated concerning their size, stability, and surface chemistry. Often, these three aspects cannot be discussed individually but are connected. Laser ablation in liquids usually forms NPs from a few nm to some hundred nm [138, 139]. Laser fragmentation, on the other side, yields towards particles from 1 – 10 nm [140] and laser melting towards (sub-) micrometer particles [141–143] and can additionally reshape the NPs [144–146]. In the following, an overview of possible parameters, including the laser fragmentation in liquids (LFL) and laser melting in liquids (LML), is presented.

For size manipulation, variation of laser parameters, as well as the addition of inorganic or organic solvents to the liquid are possible. The variation of laser parameters is not restricted to the additive's potential adverse effects on the application, but it only allows a limited NP size variation.

As indicated in the previous section, the laser pulse duration determines the ablation mechanism [137] and influences the NP size distribution. A distinct bimodal NP size distribution is observed, especially for fs and short ps laser pulses [135, 147]. Whereas for NPs produced by fs and ps ablation, only reirradiation by the consecutive laser pulse occurs, irradiation with the same laser pulse is possible for ns pulses [148]. The dominant mechanisms for fragmentation are heating-melting-evaporation [149] or Coulomb explosion [150], leading to higher fragmentation efficiencies for shorter pulses and higher intensities [149].

Laser energy is absorbed by NPs in the liquid during LAL and by the cavitation bubble. Therefore, the temporal and spatial distance between the pulses is addressed in the literature. Here, the repetition rate and the scan velocity can be combined to calculate the interpulse distance. Menendez-Manjon et al. showed that the particle size of Au NPs is reduced by increasing the repetition rate from 100 to 5000 Hz at constant laser pulse energy [151] and Wagener et al. demonstrated that for increased scan velocities, the NP size increases [152]. The influence of the pulse energy at a constant repetition rate of 10 Hz on the other side was examined in [153, 154]. They found that for an increased laser pulse energy, the mean particle size decreases, attributed to LFL during LAL. One last parameter which has to be considered is the working distance between the focusing optic and the target surface. This parameter influences the diameter of the irradiated area on the target surface and thus the laser fluence. Especially from the laser fragmentation, the process's sensitivity to a focal plane shift is known since the highest efficiency is achieved just below the liquid's breakdown fluence [155]. This focal plane shift aspect has been studied in the literature for laser ablation [135, 138, 156].

Most of the studies, considering the influence of laser parameters on the NP size, are performed in a vessel where the NPs are continuously re-irradiated by the laser beam. Depending on the laser fluence, this re-irradiation can either increase or decrease the mean NP size [157]. These, in part, contradictions [139, 153] emphasize that the different process parameters cannot be discussed individually due to cross-effects by inhomogeneous energy distribution in the liquid by the focusing and scattering [158, 159]. Moreover, there is a necessity to find a parameter combining all of them.

Note that systematic control is not possible yet due to a lacking model combining these observations. Additionally, supersaturated naked atom clusters are present in the liquid, leading to ripening and growth of NP over time, which already occurs on a time scale of minutes to hours [160] and leads to a size increase for higher liquid temperatures [160, 161]. The surface chemistry has to be manipulated by additives to suppress this growth, which also quenches the NP size.

In that sense, different strategies can avoid NP growth and narrow the size distribution. First, there is the steric stabilization of NP with organic molecules. In general, smaller NPs are observed for higher stabilizer concentrations [162–164]. However, a substantial size decrease is observed when the critical micelle concentration is exceeded [165]. Additionally, the colloidal stability can be increased and the NP size reduces when the solvent polarity is high [166]. The stability increase is attributed to slower ripening kinetics [167] and a stronger electrostatic double-layer [166]. Since the organic compounds easily decompose due to the rough conditions during the laser impact and plasma formation, it is reported that for higher laser fluences, the stabilizing effect is diminished [126] and the organic stabilizers are decomposed to carbon nanostructures during irradiation [168, 169]. Moreover, few studies indicate that reactive components during decomposition evolve and interact with the ablated matter so that the NP composition differs from the bulk target composition [170, 171].

Second, electrostatic stabilization by inorganic salts is possible [172]. Here, the decomposition of the additive and alteration of the bulk is not reported in the literature. Adding anions with good polarizabilities such as chloride or bromide electrolyte concentrations before the ablation significantly increases the surface charge density [64] of the nanoparticles improving the colloidal stability and leading to the size quenching effect. In general, higher concentrations in the micromolar range lead to smaller particles [172]. Especially for Au, the size variation by additives has extensively been investigated [173] and fewer for other noble metals [67]. In general, size quenching and stabilization for Au is achieved due to the absorption of chaotropic anions, whereas cosmotropic anions lead to destabilization [174]. When the salt concentration is in the range of tens of millimolar, the repulsive forces are weakened, and particles are destabilized, called salting-out effect [175].

When comparing the organic and inorganic stabilizers, both methods reveal different advantages and disadvantages and varying stabilizing mechanisms. For salts, e.g., NaCl,

size quenching of Au is already observed within the first bubble oscillation at approximately 100 µs after laser pulse [128] leading to a smaller NP size. For a macromolecule, as PVP and its monomer N-vinylpyrrolidone, no size quenching inside the CB and only ex-situ stabilization is observed [132, 176]. Interestingly, the macromolecule's monomer effectively quenched the NP size in situ at equimolar concentrations [176] but did not provide colloidal stability.

Further possibilities of NP stabilization are in situ support of NP [177] or bioconjugation [173]. These examples already indicate that the application determines the stabilizer choice. Citrate is not suitable for biological applications due to its cytotoxicity [56] and reduces the SERS signal for laser-generated NPs [178]. Therefore, the challenge arises, especially for Ag NPs, to find a suitable stabilizer unless cleaning steps are employed. This cleaning requires centrifugation steps and demands additional resources.

Although laser-generated NPs are ligand-free [179, 180], their surface is partially oxidized [181] and thus can absorb OH/O^- species. Moreover, these oxidized species are responsible for, e.g., the catalytic activity of NPs [182]. Therefore, knowledge of the parameters determining the NP surface oxidation is essential when NP for customers with different requirements shall be produced.

During the highly reactive conditions of the plasma and liquid mixing, reactive particles [113] can form and enable the various chemical reaction. Therefore, it was found that Au and Pt NP produced in water are acting as Lewis acid and absorb OH/O^- species. This highly charged surface leads to enhanced stability of laser-generated NP compared to chemically synthesized particles [46]. Also, solvent decomposition and water splitting are observed [93, 183]. Kalus et al. found experimental evidence that gas formation might be driven by the redox reactions in the plasma-liquid interface since the gas formation correlated with the standard electrode potential [91].

For Au, e.g., surface oxidation degrees of 3 – 12 % is determined, where Au^+ and Au^{3+} are the oxidized species [46, 184, 185]. With 20 – 73 %, the surface of Pt NP is stronger oxidized [184]. Since Pt is commonly used as a catalytic material, it is important to mention that catalyst load influences the surface oxidation [186]. Marzun et al. also showed the dependence of the surface oxidation state on the support material. The synthesized colloid contained about 30 % Pd^0, which increased to 55 % and 67 % for NPs supported on carbon or TiO_2 [67]. Finally for Ag, 0 – 85 % of surface oxidation are reported [91, 184, 187].

When comparing the different results, the non-equilibrium process of fs ablation leads to slightly higher oxidized noble metal species. This rapid cooling of the plume for ultrashort pulses [114, 121] leads to particle freezing in a non-equilibrium state (see Tab. 1). For noble metals, this would also mean that oxidized species are already formed during their emergence and are subsequently reduced. Coulomb explosion is also more prone to occur during fs ablation [188, 189], which underlines this hypothesis. On the contrary, for ns laser

ablation, the higher plasma temperatures, longer lifetime, and lower cooling rates resemble less harsh conditions. Possibly, the measurement of the amount and composition of the formed gasses can give more in-depth insight [91, 92]. Also, UV irradiation leads to a higher amount of oxidized species, which supports the hypothesis that the non-equilibrium oxide state for noble metals occurs due to the freezing of this state and particles reduce to the elemental form under moderate ablation conditions. However, the influence of reirradiation by high repetition rates and during batch processes of NPs has not yet been discussed. Possibly, post-heating of the pre-formed NPs due to ns pulses and higher repetition rates leads to less oxidized species [184, 190].

Tab. 1: Comparison of literature results to determine the influence of laser and process parameters during LAL on the oxidation degree for Au, Pt, and Ag.

material	reference	pulse duration	wave-length	fluence	repetition rate	additive	batch or continuous	unoxidized
Au	[46]	120 fs	800 nm	5 mJ/cm²	1 kHz	-	batch	89 %
Au	[184]	8 ns	1064 nm	64 J/cm²	10 Hz	0.1 mM KCl	batch	97 %
Au	[185]	ns	1064 nm	(80 mJ)	10 Hz	-	batch	94 – 97 %
Au	[91]	10 ns	1064 nm	280 J/cm²	10 kHz	-	cont.	93 %
Pt	[184]	8 ns	1064 nm	64 J/cm²	10 Hz	0.1 mM KCl	batch	78 %
Pt	[191]	7 ns	355 nm	3 J/cm²	-	-	batch	49 %
Pt	[191]	7 ns	355 nm	14 J/cm²	-	-	batch	58 %
Pt	[191]	7 ns	355 nm	110 J/cm²	-	-	batch	27 %
Pt	[91]	10 ns	1064 nm	280 J/cm²	10 kHz	-	cont.	70 %
Pt	[190]	8 ns	1064 nm	6.4 J/cm²	10 kHz	-	batch	84 %
Ag	[184]	8 ns	1064 nm	64 J/cm²	10 Hz	0.1 mM KCl	batch	100 %
Ag	[91]	10 ns	1064 nm	280 J/cm²	10 kHz	-	cont.	85 %
Ag	[187]	ns	1064 nm	(6.5 mJ)	5 kHz	1 mM citrate	flow	15 – 20 %

2.4. Productivity and efficiency for laser ablation in liquids

After introducing the general ablation mechanisms and presenting the influence of different parameters on the NP quality, the present section summarizes their influence on productivity. Especially when laser ablation in liquids should become an economically feasible industrial alternative, reaching high productivity is decisive [65]. The influences of the interpulse distance, the laser fluence, and the laser pulse duration are addressed in the following.

The lateral interpulse distance during LAL is determined by the laser repetition rate f_R and the scan velocity on the target surface. In general, productivity can decrease for small interpulse distances due to shielding caused by the CB generated by the previous pulse [68, 192, 193]. According to $f_R = \bar{P}/E_P$, the repetition rate connects the laser pulse energy E_P and the mean laser power $\bar{P}$. At constant pulse energy, i.e., increasing laser power, the ablation per pulse is decreased and overall ablation rate increases with increasing repetition rate [152]. Simultaneously, at fixed laser powers, i.e., decreasing laser energy, the ablation per pulse decreases, and the overall ablation rate increases with increasing repetition rate [68]. By varying the scanning speed and thus increasing the interpulse distance for ns pulses and at 4.6 mJ, the productivity increases until 75 µm and decreases again for larger distances [192], whereas for 40 – 55 ns, the optimum is found at 125 µm [194]. An intermediate distance of 100 µm is observed for 7 ps LAL [152]. Additionally, for increased distances, the productivity decrease is less distinct for ps compared to ns ablation [152]. It is assumed that an interplay between the losses due to shielding, favoring larger distances, and a beneficial influence of a heat affected zone from a previous pulse [192], favoring smaller distances, lead to the optimal interpulse distance.

The laser fluence is the most important factor of productivity adjustment and describes the pulse energy per laser spot on the ablation target surface. Thus, the fluence can be increased by increasing the pulse energy or decreasing the laser spot size. Numerous studies showed that increased laser pulse energy and laser power lead to higher productivities [32, 68, 76, 117, 195]. Fewer studies investigated the influence on the working distance and thus the ablation area [32, 76, 148]. Aggravatingly, in most of these studies, the relative focal distance is compared, where the focal plane was set to the point of maximal productivity. Here, the influence of the spatial laser energy distribution cannot be discussed. In principle, higher productivity for a lens with a shorter focal length due to smaller ablation spot diameters is expected for the same laser power [75]. However, also the possibility of optical breakdown in the liquid increases for sharper focusing, which, in turn, reduced productivity [196].

Due to the multiple and often cross-linked parameters determining productivity, a prediction model would be advantageous. A model for calculating the ablation depth was developed in the past, postulating a logarithmic dependency of the ablation depth on the laser fluence

[197]. It was later adapted to LAL [117] and is described by Eq. 3. The model also provides the possibility to estimate the ablation efficiency (see Eq. 4) [198]. There is an optimal set of parameters for each process, where the fluence dependency is of interest. The optimal fluence F_{opt} is dependent on the material threshold fluence F_{th} can be described by $F_{opt} = e^2 \cdot F_{th}$ in air [198]. Streubel et al. [68] and Kanitz et al. [117] verified this dependency for liquids and ultra-short pulse durations. For fluences lower than the optimal fluence, the maximum possible penetration depth of the energy into the material is not yet reached. On the contrary, it is exceeded for fluence higher than the optimal fluences so that the excess energy cannot penetrate the material anymore.

One drawback of this model is the pulse duration dependency of the ablation process. As shown in Eq. 3, the pulse duration is not explicitly mentioned in the equation. Implicitly, the pulse duration determined the effective penetration depth δ_{eff} and the threshold fluence F_{th}. Therefore, results from the literature determining the influence of the pulse duration on the penetration depth and the threshold fluence are discussed first.

The threshold fluence is constant if the pulse duration remains smaller than the electron-phonon coupling time t_{ep} [199, 200], which ranges from < 10 to 100 ps for metals. This range of $\tau_P < t_{ep}$ is called an ultrashort pulse regime. For longer pulses, in the range of larger than 100 ps, a dependency of $F_{th} \propto {\tau_P}^{0.5}$ is reported [199, 200]. Fig. 6 shows the explained trends, where data from literature are compared. It has to be noted that both damage and ablation threshold are shown in Fig. 6.

$$\frac{dm}{dt} \cdot \frac{1}{{w_0}^2 \cdot f_R}(F_P, \tau_P) = \frac{1}{4} \cdot \pi \cdot \rho \cdot \delta_{eff} \cdot \ln\left(\frac{F_P}{F_{th}}\right)^2 \qquad \text{Eq. 3}$$

$$\dot{m}_{spec} = \frac{dm}{dt} \cdot \frac{1}{\overline{P}} \qquad \text{Eq. 4}$$

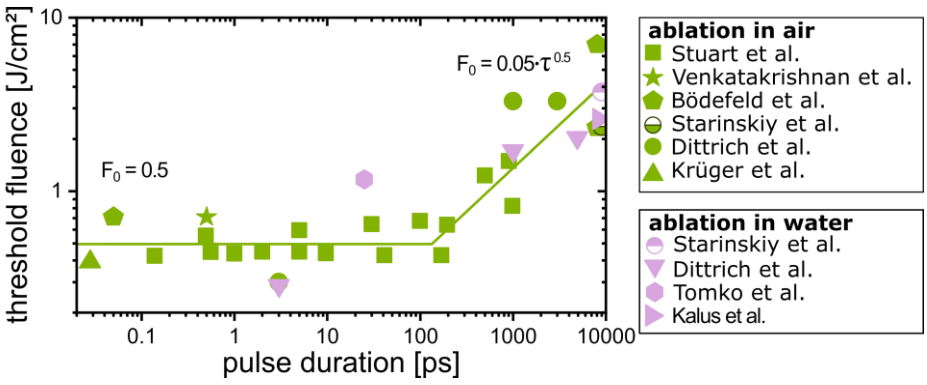

Fig. 6: Comparison of ablation threshold values reported in literature determined at different laser pulse durations for Au from various studies in air (green data points) and in water (pink data points) [70, 105, 107, 126, 199, 201–204]. The green line shows the fit for the threshold fluences determined in air.

When discussing penetration depth dependency, it is differentiated between ultra-short and short pulse regimes as well as between low and high fluence ablation. For the former condition, the penetration depth is reciprocal to the absorption coefficient $\delta_{eff} \propto \alpha^{-1}$ [205], which is valid up to approximately 0.5 J/cm² [206]. Since such low fluences, just above the threshold fluence, do not yield high NP productivities, this fluence regime is not further discussed. For fluences >0.7 J/cm² [206], the penetration depth increases proportionally to the thermal diffusivity $\delta_{eff} \propto \gamma$ [205]. Regarding the pulse duration dependency theoretically and similar to the threshold fluence trend, constant penetration depth in the ultra-short regime of $\delta_{eff} = \sqrt{D \cdot \tau_{ep}}$ is expected and $\delta_{eff} = \sqrt{D \cdot \tau_P}$ for short pulses [206–208]. As a rule of thumb, this effective penetration depth is about 10-20 times higher than the optical penetration depth [209]. These theoretical considerations are sketched in Fig. 7 by the dark green lines. However, only a few experimentally determined penetration depths can be found in the literature. For copper and steel, it is reported that in the ultra-short regime δ_{eff} slightly decreased with increasing pulse duration [198, 206, 210]. For the short regime, the penetration depth increases again [211], indicating that heat conduction becomes the dominant energy transport mechanism here. The data obtained from the literature are presented in Fig. 7 and show an increase in the penetration depth when comparing ps to ns laser ablation. In a molecular dynamic simulation, reaching from ultrashort fs and ps pulse duration to short ns pulses, it is assumed that for pulse durations > 1 ns, plasma shielding and scattering of the falling laser edge can occur. This shielding leads to a lower penetration depth for increasing ns pulses because the temporal fluence is lower for longer pulses [137]. A slight decrease is observed when comparing the experimentally determined penetration depth at 1 ns to 5 ns. Though, no clear correlation of the experimental data with the theoretical trend can be seen. Potentially, this decrease in the penetration depth is related to heat dissipation into the liquid, which occurs on the time scale of nanoseconds [212].

When comparing experimental findings for different pulse durations, a higher tendency for self-focusing for fs and ps laser ablation due to lower threshold values [213] and thermal-induced self-focusing can occur on ns time range [214]. Both lead to undesired attenuation of the laser beam. Ablation with a 1 ps laser leads to 20 − 30 times higher productivities than that obtained with a 150 fs laser duration, and with 2 ps, the maximal productivity for Au NP was found [215]. However, the maximal examined pulse duration was 200 ps [215].

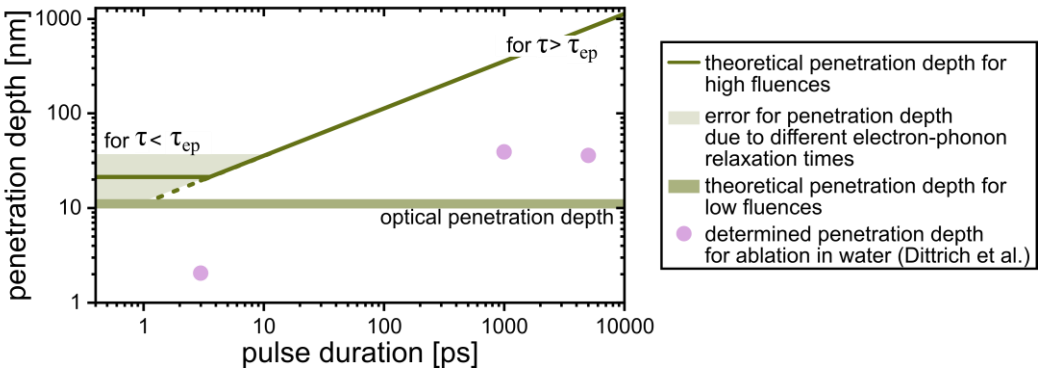

Fig. 7: Comparison of the penetration depth determined at different laser pulse durations for Au (pink circles). The green lines and areas mark the theoretical expectation for different fluences and pulse durations. [70, 98, 207, 216–220]

Also, plasma-mediated nanobubbles could be generated from plasmonic Au NPs or carbon NP using a fs laser, reducing productivity [221, 222]. The nanobubble formation is also found for ns [223] laser ablation, leading to stronger energy shielding with increasing energy input [223]. Finally, also NPs in the liquid shield the laser beam with increasing concentration [92] and increase non-linear optical effects [224]. For 10 ns LAL, plasma shielding of a single laser pulse leads to energy loss for ablation [107]. Interestingly, decreasing productivity for increasing ns pulses width and an increasing number of laser pulses is only observed in water and not in air [115].

In conclusion, several models for productivity prediction exist and may be adapted for laser ablation in liquids. However, they leak to predict the pulse duration dependency of productivity and ablation efficiency since existing models neglect different shielding effects. Thus, it is hypothesized that an optimum pulse duration-dependent productivity is located between hundreds of picoseconds to maximal ~2 ns pulse durations. In this range, it is assumed that energy losses due to non-linear optical effect, which occur mostly for fs pulses, and plasma shielding, mostly expected for >2 ns pulses, are minimized. However, experimental evidence is missing.

2.5. Scalability of laser ablation in liquid

Achieving high productivities with LAL is crucial for this synthesis's economic feasibility and is also demanded when laser-generated particles are used in applications. Especially for catalyst screenings [225] and NP-doped powder for 3d printing [226], several grams of NPs are often needed.

It would be useful for a continuous NP production if the complete target without residuals is ablated, and a constant target supply is realized [187]. In the literature, this has been addressed by the ablation of wire targets. It was shown that from thin wires to bulk target, the absorbed energy increases, but maximal ablation efficiency of a 10 ns laser was found at an intermediate wire diameter, which was attributed to local heating symmetry broken cavitation effects [187, 227, 228]. The efficiency of wire ablation is determined gravimetrically [227]. Therefore microparticles may be ripped off the target, and the real productivity is expected to be lower. Thus, the ablation of the bulk target is generally applied.

As already explained previously, a commonly chosen attempt to increase productivity is by increase laser power and fluence [68]. However, due to the limited penetration depth, the ablation efficiency decreases for high laser fluence [198]. This finding has not yet led to alternative attempts for the productivity increase for LAL. However, in laser micro-structuring, the ablation with high laser powers can lead to thermal ablation and thus reduce the structure quality [229]. Therefore, the laser beam is often split into multiple parts to reduce the power for each beam. This beam splitting leads to sharper structures and, additionally, fast processing [229, 230]. For LAL with high fluences, this strategy could be applied so that the full laser power is used and, simultaneously, the efficiency would increase. Today, the world record of LAL 4 g/h AuNP production is achieved by supersonic lateral beam displacement, allowing shielding minimized ablation at the µm-scale by Streubel et al. [68]. Recently, even 8 g/h were reached for Pt NPs [231].

As identified in the previous section, the ablation with hundreds of ps to ~2 ns pulse durations provides the opportunity of increasing the ablation efficiency by reducing shielding effects. Therefore, lasers that could meet such specifications are identified in Tab. 2, ranging from ~1 to 150 W output power.

Tab. 2: Overview of different laser types providing sub-ns laser pulses promising increased ablation efficiency due to reduced shielding during LAL (τ_P: laser pulse duration, λ: wavelength, E_P: laser pulse energy, f_R: repetition rate (maximal), $\bar{P}$: mean laser power, M^2: beam quality).

company	model	laser type	τ_P [ns]	λ [nm]	E_P [mJ]	f_R [kHz]	$\bar{P}$ [W]	M^2 [1]
Coherent	FLARE NX	passive diode-pumped solid-state laser with Q-Switch	1.5	1030	0.5	2	1[1]	<1.2
InnoLas	MAGNA EVO III	active Q-switch	0.6	1064	250	1	25 [2]	-
Dausinger & Giessen	Gigapulse Linear Amplifier	linear amplifier	1	1064	1000	1	150	-
Edgewave	GX-Serie	electro-optical Q-switched InnoSlab laser	1	1064	120	800	150	<2
Edgewave	IS-Serie	electro-optical Q-switched InnoSlab laser	1	1064	50	400	150	<2
CryLaS	MOPA 1064-650	diode-pumped passively Q-switched solid-state laser	1.6	1064	0.65	1	0.65	-
CryLaS	MOPA 1064-2000	diode-pumped passively Q-switched solid-state laser	1.6	1064	$1 \cdot 10^{-4}$	20	2	-
Onda	Onda 1064nm	Diode Pumped Solid State Laser	2	1064	0.8	100	15	-

[1]: @ 2 kHz, [2]: @100 Hz

3. Objectives

Studies and reviews have shown that LAL can meet industrial demands and provide distinct advantages over chemically produced NPs [65, 173, 232, 233]. This thesis presents the development and perspectives of a device for NP generation via LAL, which enables an automated and reproducible NP production. This includes fundamental studies on parameters affecting LAL efficiency. An overview of this thesis is illustrated in Fig. 8.

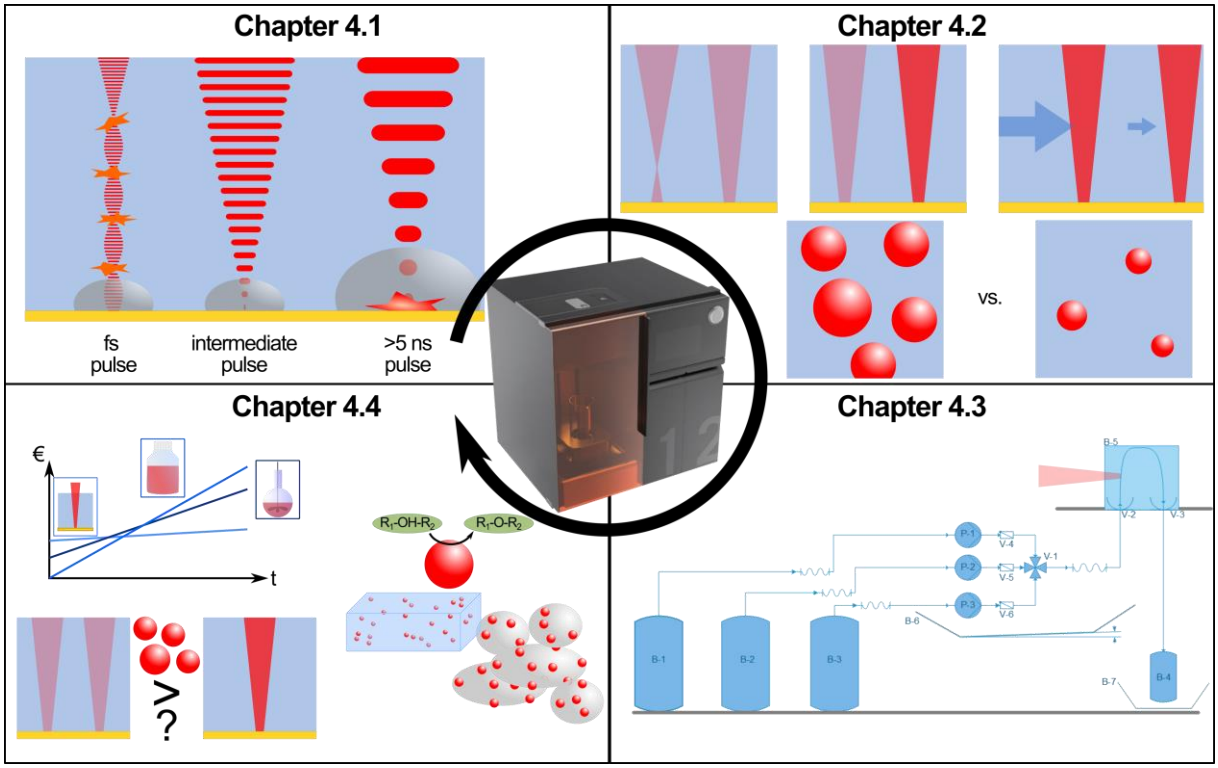

Fig. 8: Development of an automated device for colloid production via LAL in four stages. Chapter 4.1 represents the comparison of the ablation efficiency and shielding effects during LAL for different pulse durations. In chapter 4.2, the influence of laser parameters on the connection between productivity and NP size is investigated. Chapter 4.3 symbolizes the process setup and development of the automated process and chapter 4.4 the device's perspectives regarding the economic feasibility and capacities. In the center, a preliminary model of the automated LAL device is shown.

As explained in section 2.1 and 2.4, the laser-matter interaction with laser exhibiting pulse durations of 500 ps to 2 ns has rarely been investigated. However, this pulse duration regime could provide high ablation efficiency because energy losses are reduced. At the lower pulse duration range, i.e., for fs up to tens of ps pulses, non-linear optical effects cause energy losses, as described in section 2.1. On the upper pulse duration range, i.e., for pulses longer than several ns, plasma-shielding reduces the ablation efficiency. Therefore, laser ablation efficiency regarding the laser pulse duration is decisive for the suitable laser source in the automated device (Fig. 8 (1)) and will be analyzed in section 4.1.

From sections 2.3 and 2.4, it is known that both the productivity and the NP properties are influenced by laser parameters such as the laser power, laser pulse duration, and repetition rate. However, the linkage between productivity, NP size, and laser parameters has not been investigated for LAL in this intermediate pulse duration regime and is therefore discussed in section 4.2. Additionally, the process parameters for the automated device are tuned in this section, and the resulting NP quality, i.e., their size and stability, is compared to commercially available colloids (Fig. 8 (2)).

After the process parameters are optimized for the device, the process design for the automated desktop device is developed in section 4.3. Here, the flow chart is designed and used for safety and process stability analysis. Potential hazards for the user, situations resulting in reduced NP quality, and device defects are determined and counter-measures are proposed. Since the device aims to be user-friendly and easy to use, the user-device interaction and handling of possible malfunctions are presented (Fig. 8 (3)).

Lastly, the perspectives of the device are discussed in section 4.4. Here, the final pricing and the economic competitiveness compared to purchased and chemically synthesized colloids are presented. Also, the capacity of possible downstream products is estimated, and the quality of exemplary products is evaluated. For large-scale testing of, e.g., NP additive powder for 3d printing or exhaust catalysts, the capacity demands are exceeded. Therefore, beam splitting is examined to increase productivity (Fig. 8 (4)).

4. Results and discussion

4.1. Influence of the laser pulse duration on the productivity and efficiency of laser ablation in liquids

As a first step for the device development, a suitable laser source needs to be found. Therefore in the first part of this section, different possible lasers for the device are selected: One commonly used laser system for laser ablation in liquid, one high-power laser system known for high NP productivity, and a cost-efficient, low-power laser system widely used for spectroscopic analyses. The three laser classes were analyzed regarding their NP productivity and ablation efficiency. A compact, low power, ~2 ns laser class was found to provide the highest ablation efficiency. The physical phenomena for sub-ns and short (1 – 3) ns are rarely examined in the literature. Thus, in the second and third sections, the fundamental physical phenomena of the sub-ns pulse range are studied by shadowgraphy imaging (section two) and pump-probe microscopy (section three).

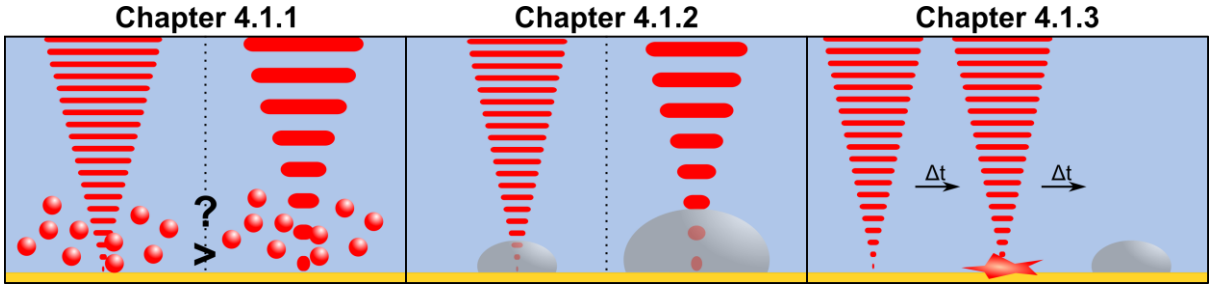

Fig. 9: Overview of the laser pulse duration effect on the productivity and efficiency of laser ablation in liquids. The influence of the laser pulse duration on the ablation efficiency is quantified (chapter 4.1.1). In the following, the energy shielding caused by the CB is analyzed (chapter 4.1.2) and the temporal evolution of plasma and vapor is determined on the ns scale (chapter 4.1.3).

4.1.1. Comparison of the productivity and ablation efficiency of different laser classes for laser ablation of gold in water and air

Sarah Dittrich, René Streubel, Cormac McDonnell, Heinz P. Huber, Stephan Barcikowski, Bilal Gökce

Published in: "Comparison of the productivity and ablation efficiency of different laser classes for laser ablation of gold in water and air, *Appl. Phys. A (2019) 125: 432*"

Abstract

In this study, we compare different laser systems used for the synthesis of nanoparticles. The productivity and ablation efficiency of laser ablation of gold in water and in air are determined for three laser systems with different laser parameters such as pulse duration and repetition rate. All experiments are performed in a fluence range of up to 20 J/cm². The highest productivity among the considered lasers is found for a high-power ps laser, which shows 12 times higher ablation rate for the ablation in air compared to ablation in liquid. Further, we find that the threshold fluence for ablation in air is up to 1.9 times higher than for ablation in water. The highest ablation efficiency, which is defined as the ablation rate divided by the laser power, can be found for a ns laser system.

Introduction

Chemically synthesized colloids, e.g. those synthesized by the Turkevich method, are characterized by nanoparticles of defined size and monomodality [24]. However, disadvantages of chemically synthesized nanoparticles (NP) are residual precursors and reactant oxidation products in the colloid [24], which have negative effects on biological application, if they are not removed by post-processing steps such as washing of the colloid [234]. Purity is also important in the field of catalysis [16] and for analytical reference materials [233]. An alternative way to generate NP is by pulsed laser ablation in liquids (PLAL) since no additives or precursors are needed for this synthesis method [235]. Further advantages of PLAL include a broad variety of possible material-liquid combinations enabling the synthesis of unique and tailored colloids [29]. Moreover, the procedure is conceptually simple, reproducible and fast [65].

Accordingly, the applications of laser-synthesized nanoparticles span a wide area including catalysis [236, 237], magnetism [169, 238–240], tribology [241] and additive manufacturing [242–245]. If PLAL should become a considerable alternative to the chemical synthesis of NP, the productivity of the process is crucial. Productivity is defined as the ablated mass per time and is given in [µg/s]. On the other hand, the efficiency of the process is described by

the power-specific productivity. This is calculated by dividing the productivity by the power input and given in [mg/(W.h)]. Both expressions are used synonymously. This value has been suggested recently by Zhang et al. and Kohsakowski et al. [29, 187]. Both, the productivity and the power-specific productivity, can be influenced by the pulse duration, repetition rate, and pulse energy on the laser side and the energy per area on the target surface, pulse overlap, and scanning speed on the process side.

The lasers, chosen in this study, exhibit comparable pulse energy, but vary in the maximal power and in the laser pulse duration. The influence of the laser pulse duration on the mechanisms of laser-matter-interaction has been discussed in the literature [104, 246, 247]. Also, empiric attempts to calculate the material removal rate by laser and ablation efficiency have been made with a simple model [248], where multiple laser pluses are applied on a target [104, 197, 206, 249]. However, a precise prediction is difficult because the simple model neglects the influence of certain factors. The model fit parameters, which are threshold fluence and effective penetration depth, are not described depending on e.g. the pulse duration [211] and wavelength [250]. Consequently, the calculation of the removal rate depends on the considered laser system.

When comparing laser ablation in air with the ablation process in a liquid, the thermodynamic characteristics and kinetics of the mechanism change due to confinement by the liquid [251]. Though this has been known for many years, there are also recent findings explaining the interaction of the cavitation bubble with the surrounding liquid and nanoparticles [127] and the influence of the surrounding liquid on the ablation mechanism [113, 118, 252, 253]. Most publications state a higher ablation rate in air [107, 113, 254], Shaheen et al., however, reported a higher ablation rate of brass in water, although they may have used fluences in the order of 100 J/cm² for their experiments, which is about a factor of 10 to 20 higher than the expected fluence for optimum ablation efficiency [255]. Sajti et al., on the other hand, compared ablation rates of α-Al_2O_3 in air and water for different distances of consecutive laser pulses, pulse energies, and repetition rates and found the ablation rate to be dependent on those parameters [194]. Also, the laser pulse duration influences the ablation rate as shown for fs and ps lasers [256, 257]. Moreover, most of the theoretical consideration and calculations concerning the ablation rate, have been performed with regard to ablation in air [197, 206].

In this work, the parameters relevant for high productivities are studied by comparing three commercially available and well-established laser systems. The laser sources deliver comparable pulse energies in the range of 100 µJ at a near-infrared wavelength but exhibit different repetition rates, average output powers, and pulse durations. The first laser system is one of the most commonly used laser-types in PLAL, a diode-pumped Q-switched nanosecond (ns) laser providing an average maximal output power of 10 W and originally intended for laser cutting and marking in industry. The second laser in this comparison is a

500 W picosecond (ps) master oscillator power amplifier system (MOPA), comprising a mode-locked oscillator and a slab-laser amplifier, that demonstrated the highest productivity in laser ablation in liquid so far [68]. The third chosen laser is a very compact passively Q-switched nanosecond laser, commonly named as micro-chip laser and usually used for spectroscopy, revealing the lowest average output power with 0.2 W.

When it comes to the use of nanoparticles in applications, it is important that with the chosen synthesis method (1) as many nanoparticles as possible can be produced with (2) as little energetic effort as possible. Hence, the first part of this paper presents the influence of the laser pulse duration on the productivity as well as the comparison of the ablation rate in water and in air for the different pulse durations. The second part describes the energetic consideration.

Methods and materials

Determination and comparison of the productivity of laser ablation for gold in water and air at different pulse durations

Two different ns lasers (Rofin Powerline E20 and CryLaS DSS1064-Q4) are compared with a ps laser (Amphos flex 500). The general data of the three laser systems are summarized in Tab. 3. The experimental setup and data for the comparison of the ablation in water and in air are given by Fig. 10 and Tab. 4.

Tab. 3: General parameters for the laser systems applied in this paper

Laser power class	Compact class	Middle class	High-end class
Laser name	CryLaS DSS-1064-Q4	Rofin Powerline E20	Amphos flex500
Wavelength [nm]	1064	1064	1030
Pulse duration [ps]	1000	5000-10000	3
Average maximal output power [W]	0.15	< 10	500
Repetition rate [Hz]	1-1200	$20\text{-}200.10^3$	$(1.2\text{-}40.5).10^6$
M^2 [1]	< 1.4	< 1.5	<1.2
Height x width x length of the ablation chamber [mm]	5 x 4 x 10	5 x 4 x 10	5 x 18 x 100
Time to scan the ablation area once [s]	0.3	0.3	0.06

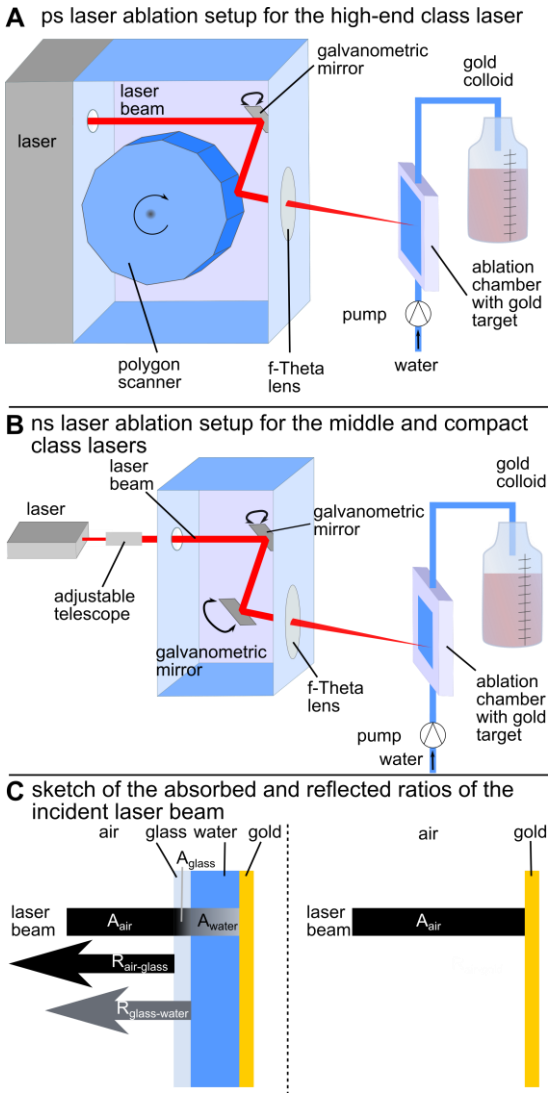

Fig. 10: Experimental setup for the high-end class (A) and the compact as well as the middle class (B) laser ablation, and a sketch illustrating the loss of laser energy for ablation in water and in air (C); the color gradient symbolizes the absorption A and the arrows the reflection R of the laser beam

Tab. 4: Experimental parameter for the determination and comparison of the productivity of laser ablation in water and air for gold at different pulse durations

Laser power class	Compact class		Middle class		High-end class	
Ablation medium	Air	Water	Air	Water	Air	Water
Maximal absorbed fluence [J/cm²]	5.5	6.3	17.4	21.0	2.3	1.3
Maximal pulse energy [µJ]	135	128	335	403	97	97
Spot diameter [µm]	79 ± 3	61 ± 5	70 ± 4	70 ± 6	120 ± 12	148 ± 14
					86 ± 8	126 ± 7
Interpulse distance [µm]	8300	8300	8300	8300	79	79
Repetition rate [kHz]	1.2	1.2	1.2	1.2	5000	5000
Nominal scanning speed [m/s]	10	10	10	10	500	500
Flow rate [mL/min]	-	5	-	5	-	510
Flow velocity [cm/s]	-	0.4	-	0.4	-	9

Both ns lasers emit at 1064 nm but differ in pulse duration, maximal repetition rate, and maximal average power. The Rofin Powerline E20 (in the following referred to as “middle class” laser) is a CW diode-pumped, actively Q-switched Nd:YVO_4 laser in end-pumping configuration. It reaches a maximum average power of 10 W and a pulse duration of 5 to 10 ns, dependent on the laser power. The repetition rate can be adjusted up to 200 kHz and the maximum pulse energy of 403 ± 2 µJ is reached at a lower repetition rate. The CryLaS DSS1064-Q4 (in the following referred to as “compact class” laser) provides maximal pulse energy of 128 ± 1 µJ and a pulse duration of 1 ns. The latter is a passively Q-switched, diode-pumped micro-chip laser, therefore the repetition rate of 1.2 kHz cannot be adjusted freely, but depends on the laser configuration and pump power. Both lasers exhibit an almost TEM_{00} mode with an M^2 smaller than 1.5.

Since the laser beam diameter has an influence on the irradiated liquid volume and the beam diameter on the target surface, an adjustable telescope is used to set the diameter to approximately 4.4 mm, measured at $1/e^2$ intensity level. An f-Theta lens with a focal distance of 100 mm is used to focus the laser beam on the target surface. Before each experiment, the working distance is varied until the point of maximal productivity is found, which is considered as the distance of a maximum spot intensity and focal distance. All the following experiments are performed at this focal distance. The laser spot diameter on the target surface at the focal distance in water amounts to 61 ± 5 and 70 ± 6 µm for the CryLaS DSS1064-Q4 and the Rofin Powerline E20, respectively. The values are determined by measuring the spot diameter on the target surface. All ns laser experiments are performed in a liquid flow chamber at a flow rate of 5 mL/min, a repetition rate of 1.2 kHz. In order to place the laser pulses on separated spots on the sample to avoid laser beam shielding by the cavitation bubble a nominal scan velocity of 10 m/s was selected, leading to a distance between the centers of two consecutive laser spots, also known as interpulse distance, of 8.3 mm, which is large compared to the spot diameter. It has to be mentioned, that the same area is irradiated multiple times during the experiments to simulate conditions under long term ablation. To vary the laser fluence, the average laser power is adjusted between 30 mW and the maximal laser power with an error of less than 1 % by measuring with a power meter (FieldMaxII-TOP, Coherent Inc.).

The ps MOPA laser system (in the following referred to as “high-end class” laser) provides a pulse duration of 3 ps and a maximal output power of 500 W. The high-end laser consists of a mode-locked ps oscillator, followed by a pulse-picker and slab laser crystal amplifier. The ps oscillator is operating at typically few a 10 MHz repetition rate at an average power of a few Watts leading to pulse energies of typically 100 nJ. The pulse-picker reduces the repetition rate of the seeder oscillator pulse train to 5,000 kHz, before it is amplified to an average power of 500 W in the side-diode pumped slab laser crystal corresponding to a pulse energy of 100 µJ. Because of the comparably high average output power and

repetition rate, the flow rate is set to 510 mL/min and the effective scanning speed is increased to 484 m/s realized with a polygon scanner. This results in an interpulse distance on the sample surface of about 97 µm. The beam diameter on the target surface has an elliptical shape with the major and minor diameter of 148 ± 14 and 126 ± 7 µm. Thus, a pulse overlap of 35 % occurs on the target.

The material removal rates for the ablation in water for all three lasers are determined spectroscopically by UV-VIS extinction measurements. Since this is only applicable for nanoparticles with approximately the same size [258], a calibration for each laser was prepared by correlating the gold nanoparticles interband absorption at 380 nm with the gravimetrically determined mass productivity. In case of laser ablation in air, the material removal rate is determined gravimetrically after an ablation time of 5 minutes for both ns lasers and after 10 seconds for the high-end class laser. Each experiment is carried out three times to calculated the average of the values and the standard deviation.

As shown by Streubel et al. for liquid flow setups, the productivity stays constant with the ablation time and the quality of the colloid is not influenced, so that it is possible to extrapolate and compare the ablation rate [32]. The focal distance is changed to the position of maximal productivity in air. Laser spot diameters on the target surface amount to 79 ± 3 and 35 ± 2 µm for the CryLaS DSS1064-Q4 laser and the Rofin Powerline E20 laser, respectively. For the Amphos flex 500 laser, an ellipse with a major and minor diameter of 120 ± 12 and 86 ±8 µm is determined.

For the data evaluation, the peak energy is converted to the laser peak fluence according to Eq. 5. To give a better comparison between laser ablation in air and in water, the reflection of the laser beam at the chamber entrance and absorption by water is considered Fig. 10 C. The reflection at the water-gold and air-gold interface is not taken into account because it has been reported in literature that a change in morphology lowers the reflectivity and increases energy absorption [259, 260]. However, when assuming full absorption of the laser energy, the real absorbed fluences will be lower. The values of the absorption and reflectivity are given in Tab. 5 [217, 261, 262]. The values of the optical glass are taken from data sheets provided by SCHOTT North America, Inc.

$$F_P = \frac{8 \cdot E_P}{\pi \cdot d^2} \quad \text{Eq. 5}$$

$$\dot{m} = \frac{1}{16} \cdot f_R \cdot \pi \cdot \delta_{eff} \cdot d^2 \cdot \rho \cdot \ln\left(\frac{F_P}{F_{th}}\right)^2 \quad \text{Eq. 6}$$

where:

F_P: peak fluence [J/cm²]
E_P: peak energy [J]
d: spot diameter [µm]
$\dot{m}$: productivity [µg/s]
f_R: repetition rate [Hz]
δ_{eff}: effective penetration depth [nm]
ρ: density [g/cm³]
F_{th}: threshold fluence [J/cm²]

Tab. 5: Values of the absorption (A) of the different media and the reflection (R) at the different layer interfaces, calculated by the Fresnel formula

	1064 nm	1030 nm
A_{air}	Neglected	Neglected
A_{water}	0.261	0.213
$R_{air\text{-}glass}$	0.041	0.041
$R_{glass\text{-}water}$	0.004	0.004

The simple ablation model of Raciukaitis et al. [197] is given by Eq. 6, which required the threshold fluence and the effective penetration depth to be fit. However, for a range of fluences between the threshold fluence and the optimal fluence, which equals the threshold fluence times e², also a linear plot can be applied, as an approximation. In this case, the threshold fluence can be determined as the intercept of the linear fit with the x-axis.

Efficiency of laser ablation of gold in water

The laser power, repetition rate and distance between the ablation target and the focusing optics are varied to determine the point of maximal mass productivity. The final parameters are provided in Tab. 6. The parameters not mentioned in the table remain the same as described in the previous section and given by Tab. 4. The experimental setup remains the same as depicted in Fig. 10. The resulting productivity of these experiments are divided by the average laser output power to calculate the power-specific productivity, or i.e. ablation efficiency in [mg/(W.h)], of the lasers.

Tab. 6: Experimental parameter for determination of the maximal productivity and ablation efficiency of laser ablation of gold nanoparticles in water

Laser power class	Compact class	Middle class	High-end class
Pulse duration [ps]	1000	5000	3
Average maximal output power [W]	0.15	5	500
Repetition rate [kHz]	1.2	15	5000
Pulse energy [µJ]	130	330	100
Maximal absorbed fluence [J/cm²]	2.5	6.7	0.3
Interpulse distance [µm]	8300	670	97

Results and discussion

Determination and comparison of the productivity of laser ablation of gold in water and air at different pulse durations

In Fig. 11, the fluence-dependent productivity for gold in water for the high-end (Fig. 11 A), compact (Fig. 11 B), and middle (Fig. 11 C) class laser is presented. As expected, decreasing the laser fluence leads to a drop in the productivity [68] for all lasers. Moreover, the high-end class laser provides the highest absolute productivity with nearly 1700 µg/s. Linear extrapolation from 10 s experiment to one hour should be done with care, but would result in 6 g/h and is significantly higher than previously published for the same laser system (4 g/h) [68]. This deviation can be explained by an optimized focal position, a lowering of the pulse overlap from about 67 % to 35 % due to a lower repetition rate, and increased maximal pulse energy (from 50 to 100 µJ). The lowest productivity is reached with the compact laser class with 1.7 µg/s at about 8 J/cm², whereas the middle class reached maximal productivity at about 20 J/cm² (Fig. 11 C).

According to Chichkov et al. [206], for a laser pulse duration τ_P smaller than a critical pulse duration required for electron-phonon equilibration, the threshold fluence remains independent of the laser pulse duration and is only a function of material properties. The critical pulse duration for gold is on the order of tens of ps. In the literature, a value of 100 ps is often stated [100, 103, 263]. However, theoretical calculations of the threshold fluence in this regime are still difficult, since values for the reflectivity and the coefficient of absorption differ widely in literature [98, 217, 218]. Calculation of the threshold fluence is performed by measuring the crater diameter after single pulses, according to Gamaly et al. indicate a value of 0.5 J/cm² for gold in air [105, 199]. Saraeva et al. found ablation thresholds in water after single laser pulses for fs and ps lasers between 1 and 3 J/cm² [257]. For the high-end laser class, a threshold fluence of 0.2 J/cm² was found. One aspect which has to be considered is that most experiments in the literature are performed with a plane surface. Vorobyev et al. examined the influence of the surface morphology on the absorbed energy during laser ablation and found that a rough surface increases the absorbed energy to nearly 100 % [259]. Scanning electron microscopy (SEM) images (Fig. 12) show a rough surface, which

leads to the conclusion that also for ablation in water, a change in the surface morphology results in an increase in absorbed energy and consequently to a lower ablation threshold.

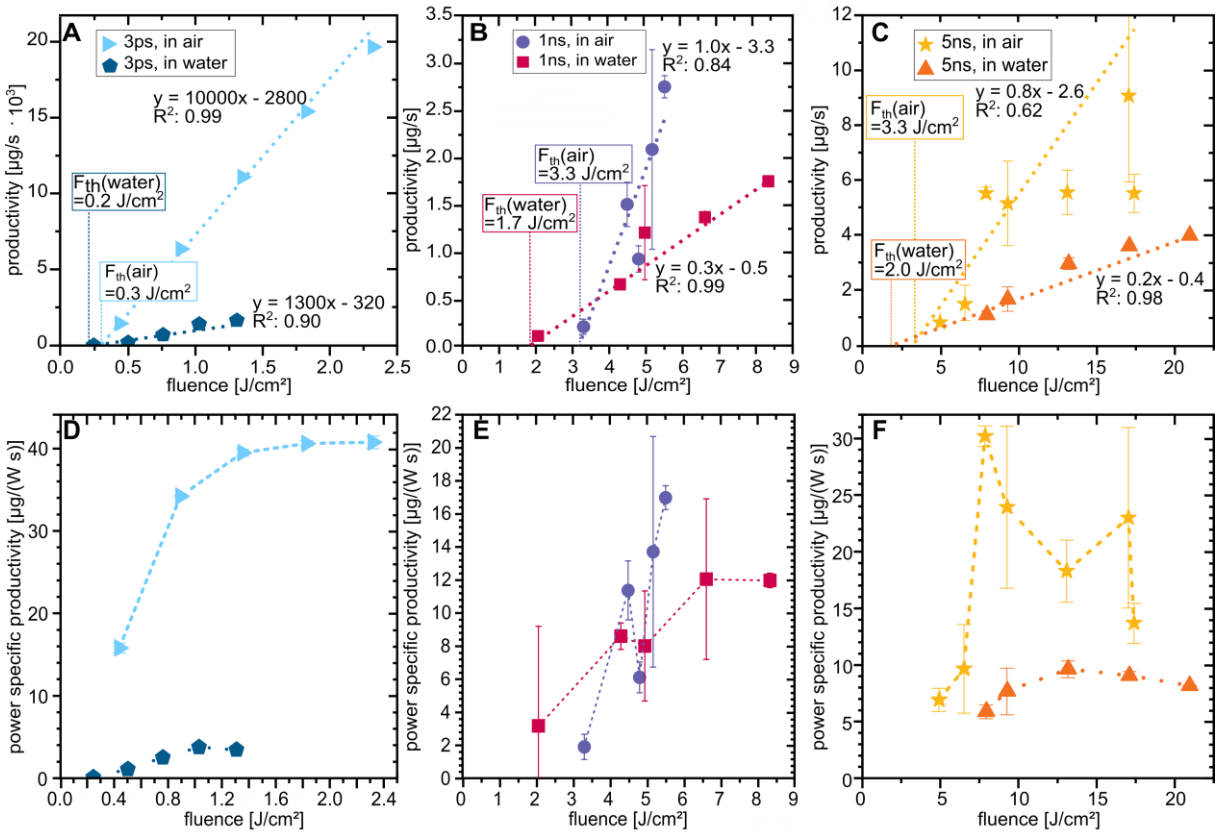

Fig. 11: The productivity for ablation in water and in air for the high-end class laser (A), the compact class laser (B), and the middle class laser (C) is shown, the lines in A-C present the linear fit where the intercept with the x-axis marks the threshold fluence; the corresponding power specific values of the same data are shown in D-F, in these cases the lines connect the data point as a guide to the eye; error bars are included in all figures and represent the statistical error.

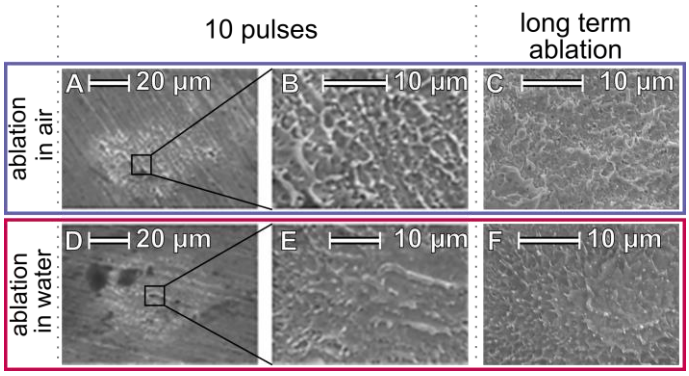

Fig. 12: SEM images of the ablated spot after 10 pulses and after long term ablation with the compact class laser are shown for ablation in air in (A) to (C) and ablation in water in (D) to (F).

When increasing the pulse duration to ns laser pulses, the electron and lattice temperature are in equilibrium and electron heat conductivity plays the dominant role for heat diffusion. As the thermal penetration depth follows the well-known square-root dependence, the thermally affected volume also scales $\propto \sqrt{\tau_P}$. Thus, for the threshold fluence (F_{th}) a square root increase with pulse duration $\propto \sqrt{\tau_P}$ is expected in this regime, too [206, 264]. According to that, the expected increase in the threshold fluence from 1 ns to 5 ns should be a factor of approximately 2.2, whereas the experimental results (Fig. 11 B) reveal a change from 1.7 to 2.0 J/cm² in the threshold fluence for the compact and middle class lasers. However, this is theoretical and only based on the one dimensional, two-temperature diffusion model [104]. In the model, energy loss due to heating perpendicular to the incident laser beam is neglected and also the interaction between the laser beam and the plasma plume is not taken into account. In literature, it has been reported, that especially for laser pulses in the range of ns a portion of the laser beam energy is absorbed by the plasma [265]. Moreover, the amount of absorbed energy is higher for longer laser pulse durations [266]. Since this effect has not been studied systematically it is hardly possible to quantify the impact of the shielding by the plasma plume. Furthermore, plasma expansion increases for higher laser energies [267]. This means, that the real absorbed laser fluence may be lower than calculated, leading to a shift of the fluence-graphs to lower fluences.

The highest power-specific ablation rate in water is determined for the compact class laser. This may be because for laser ablation in liquid not only the plasma but also the produced nanoparticles itself shield part of the laser beam [268]. The latter effect is especially relevant for high repetition rates and high productivities, as gained with the high-end class laser. Due to the ultra-high repetition rate with this laser, we have a lateral pulse overlap of about 35 % and a temporal delay of successive laser pulses of 200 ns. A calculation of the flow velocity using the values provided by Tab. 3 and Tab. 4 within the ablation chamber for ablation in liquid results in 9 cm/s. Therefore, a linear flow and no mixing of fluid elements are assumed. This rough calculation reveals that the same fluid element, which contains NP, is hit by the laser more than 15 times while moving through the ablation chamber. The real flow behavior is determined by intermixing and diffusion, which leads to a higher mean residence time and more interaction of the fluid element with the laser beam. This calculation may be an explanation for the low ablated rate per pulse and energy input for the high-end class laser in water. During the compact and middle class laser experiments, no lateral and temporal pulse overlap occurs. Furthermore, lower NP concentrations were achieved in these experiments and the NP have an approximate mean residence time of three pulses in the ablation chamber, which reduces the possibility of re-irradiation and consequently laser beam shielding. We assume that the laser shielding due to ablation products from the previous pulse is negligible.

The maximal productivity is considered to correspond to the maximal NP productivity. It has been shown in previous studies with the same laser systems and experimental conditions that gold nanoparticles synthesized in liquid are always smaller than 100 nm [32, 93]. However, note that if higher laser pulse durations (>100 ns) are used to ablate metal targets in liquids, plasma-mediated melt expulsion is also possible, leading to even larger particles [269]. Also, the particle sizes of the particles synthesized by laser ablation in air were not studied.

Although, the absorption of the laser beam in the case of the ablation in water is considered in Tab. 5, a higher ablation rate is found for ablation in air. The highest increase for the comparison of ablation in water and in air is found for the high-end class laser.

When comparing the threshold fluences, the values for ablation in air are between 1.5 and 1.9 times higher for all laser systems. In the case of ablation with the middle class laser in air, the values should be considered with caution since the data points fluctuate strongly. Therefore, we only discuss the results qualitatively. Fig. 12 shows SEM images of the gold surface in air and in water after ten pulses. Since the ablated area looks similarly rough in both cases, it is not possible to explain the lower ablation thresholds in water without further characterization.

The ablation efficiency in air and in water is shown in Fig. 11 D to F. A drop in the power-specific productivity as for example shown by Jaeggi et al. cannot be seen in our data since the maximal possible laser power is reached at this point [270]. Please recall in this context, that we measure the highest productivities for the described lasers. We do not claim to cover the whole range of fluences for the lasers classes.

The higher efficiency is found in air and the absolute highest efficiency is in case of the high-end laser class with more than 40 µg/(W.s). This value is about 11.0 times higher than for ablation with the same laser in water, whereby it increases by 1.4 and 2.4 for the compact and the middle class lasers, respectively. But it should also be considered, that for the compact and middle class lasers, the maximal levels reached in the experiments are more than 5 J/cm² lower than the optimal ablation fluence, which makes a comparison for all three lasers at that point difficult. This observation supports the hypothesis that effects reducing the energy input, such as the absorption and scattering by NP, particularly occur for the high-end class laser ablation in water, where high local NP concentrations are reached [224]. One reason for the high increase in air for this laser class can be the difference in the ablation mechanism. In the case of ablation in air, the ablation products, a mixture of vapor, atomic clusters, and droplets, are generated in a phase explosion of superheated metal and can propagate freely and rapidly away from the target. In a liquid water environment, the ablation plume is decelerated and a dense superheated molten metal layer is formed at the interface of ablation plume and water. Shih et al. simulated this for ps laser ablation of Ag at 0.6 J/cm² [113, 271] and explained the lowering in the ablation rate per pulse and energy for the

ablation in water. When comparing the ablation rate per pulse and energy input for the compact and middle class lasers, the increase from water to air is higher for the compact class laser, as already observed for the ablation in water. Since lower particle concentrations were obtained in the compact and middle class lasers experiments the shielding of the laser beam radiation by the particles is of minor importance. Moreover, the fluence for ablation with these two lasers in air is not high enough to reach the phase explosion regime.

Efficiency of laser ablation of gold in water

As indicated in Fig. 11 C, for ablation in liquid with the compact class laser, a large part of the energy is used for material ablation. If the process of laser ablation in liquid should become a viable alternative to the colloids commercially available or the chemical synthesis of colloids [65], it is crucial for the ablation process to reach a high efficiency, i.e. power-specific productivity, and productivity. For the results in this section, laser power and repetition rate were varied to reach the point of maximal productivity, accessible within the given parameter range. The productivity for the middle class laser could be increased to about 10 µg/s (Fig. 13). Since the efficiency of the different laser systems should be discussed, the power-specific productivity is shown in Fig. 13 B and the maximal values are compared in Fig. 13 C and D. The drop in the power-specific productivity was not reached, but the compared data points represent the efficiency at maximal productivity.

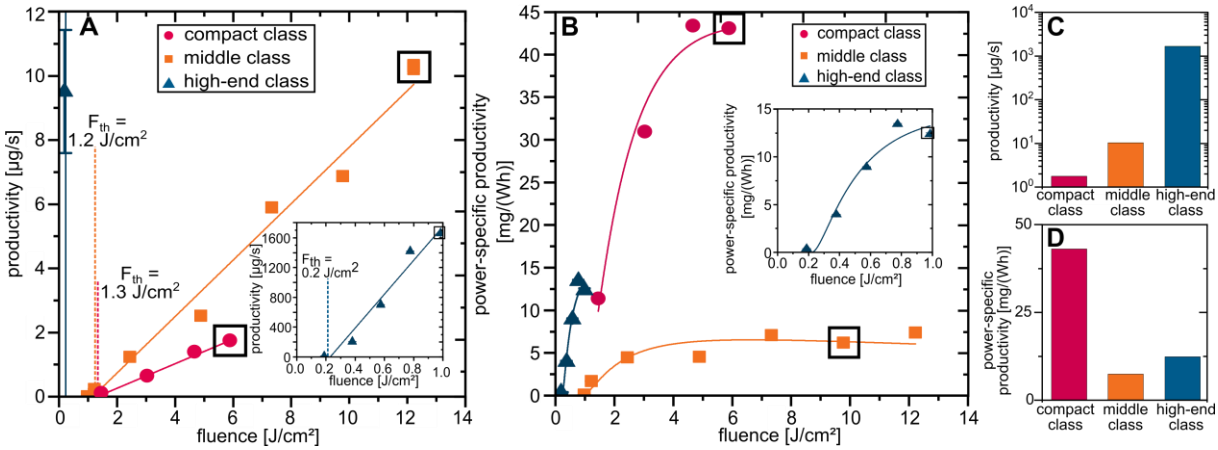

Fig. 13: Maximal fluence dependent productivity for the three laser classes (A) and the corresponding fluence dependent power-specific productivity (B), the maximal values for the productivity (C) and the power-specific productivity (D) are compared; the values used for C and D are marked with squares in A and B; the lines in A and B connect the data points as a guide to the eye; error bars are included in all figures and represent the statisticial error.

In literature, it has been stated that lasers with lower pulse duration, especially when comparing sub-ns to fs lasers, provide higher ablation rates [210]. This is indicated in Fig. 13 C. As expected, the compact class laser providing the lowest average output power

reached the lowest productivity (Fig. 13 C) but the highest ablation efficiency (Fig. 13 D). As previously discussed, it can be assumed that for the chosen parameters most of the ablated mass forms NP. With this assumption, it can be concluded, that NP produced with the compact class are produced with the lowest average power input.

As can be seen in Fig. 13 B all three laser systems (nearly) operate at the optimal fluence. As discussed in section\,\ref{prod}, different effects lower the efficiency of the high-end class laser. When comparing the results for the middle class laser system operating at lower (Fig. 11) and higher (Fig. 13 A and B) absolute productivities, it can be seen that the experiments were performed in comparable fluence ranges and for both experiments, the value of optimal fluence was reached. When comparing the ablation efficiencies for both experiments, a lower value is found for the experiment with the higher absolute ablation rate, although no pulse overlap occurs in both experiments. It has been reported in literature [154, 272], that with high repetition rates a higher part of the laser beam energy is absorbed by the NP which is in agreement with the experimental results for the middle class laser.

Conclusion

The fluence-dependent productivity, threshold fluence, and ablation efficiency of PLAL of gold were determined for ablation in water and in air for three different laser power classes operating at different pulse durations. All experiments were performed in a fluence range of up to 20 J/cm². Although the reflection and absorption of the laser energy by the water were taken into account, the maximal ablation rate in air is higher than for ablation in water. This effect cannot be explained by a difference in the surface structure of the ablated targets. Partially, this effect can be correlated to shielding by the produced NP and larger re-deposition of the material in the liquid environment. Also, shielding due to the plasma plume must be taken into account, especially for ns laser pulses. However, further investigations are needed to understand the higher ablation rate in air compared to ablation in water.

Furthermore, the threshold fluence for the ablation in water is lower compared to ablation in air. Effects like changes in reflectivity and morphology do not explain this observation, therefore further investigations are required.

When comparing the efficiency of the three different lasers operating at parameters providing the maximal absolute productivity in the chosen fluence range, the compact class laser system, providing maximal 0.15 W output power, reached the lowest absolute productivity and the highest ablation efficiency. It is assumed that the largest part of ablated mass results in NP formation. Previous studies showed that at the chosen conditions only a minor part of the ablated mass forms µm particles. It was concluded that the shielding of the laser energy because of the higher repetition rate of the middle and high-end class lasers causes the drop in ablation efficiency. As a consequence, a high ablation efficiency is reached for a low repetition rate (1.2 kHz in our case) while reaching sufficient pulse energies.

4.1.2. Examination of plasma and nanoparticle shielding during laser ablation in liquids at 1 ns pulse duration

S. Dittrich, S. Barcikowski, B. Gökce

Published in: “Plasma and nanoparticle shielding during pulsed laser ablation in liquids cause ablation efficiency decrease, *Opto-Electronic Advances*, 4 (1), 20007201 – 20007215 (2021).”

Abstract

Understanding shielding cross-effects is a prerequisite for maximal power-specific laser ablation in liquids (LAL). However, discrimination between cavitation bubble (CB), nanoparticle (NP), and shielding, e.g., by the plasma or a transient vapor layer, is challenging. Therefore, CB imaging by shadowgraphy is performed to better understand the plasma and laser beam-NP interaction during LAL. By comparing the fluence-dependent CB volume for ablations performed with 1 ns with reports from the literature, we find larger energy-specific CB volumes for 7 ns-ablation. The increased CB for laser ablation with higher ns pulse durations could be a first explanation of the efficiency decrease reported for these laser systems having higher pulse durations. Consequently, 1 ns-LAL shows superior ablation efficiency. Moreover, a CB cascade occurs when the focal plane is shifted into the liquid. This effect is enhanced when NPs are present in the fluid. Even minute amounts of NPs trapped in a stationary layer decrease the laser energy significantly. However, this local concentration in the sticking film has so far not been considered. It presents an essential obstacle in high-yield LAL, shielding already the second laser pulse that arrives. Hence, measures to lower the NP concentration on the target must be investigated in the future.

Introduction

Since the 1990s, laser ablation has evolved into a promising nanoparticle (NP) synthesis method [28], rapidly growing since about 10 years [29], and today even attracting industrial attention [225, 273]. By enabling the production of a wide variety of material-liquid combinations [169, 240, 274] of ligand-free NPs [275] in a g/h scale [32], laser-generated particles became of high interest for the fields of catalysis [181], biomedicine [276], cancer therapy [277], 3d printing [226, 243, 245], and analytical chemistry [232, 233].

A high NP productivity, i.e., the mass of nanoparticles produced per time, is required to make laser ablation in liquids an economically feasible production method for colloid production [65], especially for two of the fields mentioned above: catalysis and 3d printing. As described by [278], NP productivity is proportional to $(\ln(F))^2$, where F is the laser fluence, while the

maximal power-related productivity is found at a fluence of $e^2 \cdot F_0$, with F_0 being the material-dependent threshold fluence [278]. Often reports indicate that high-power laser ablation operates far above this optimal fluence range [68, 70, 198]. This model described in [278] was initially developed to describe the laser ablation in air [197] with the pulse duration-dependency of the productivity being indirectly considered by the penetration depth [98, 207, 216–220] and the threshold fluence [70, 105, 107, 126, 199, 201–203]. Later, it was shown that the model is also able to describe the productivity of laser ablation in liquids [68]. However, for ablation in liquids, not only the pulse duration-dependent penetration depth and threshold fluence need to be considered by the model, but also the interaction of the laser beam with the liquid and the emerging NPs [91, 92]. The NP shielding effect in dependence on the laser pulse duration has not been investigated so far for nanosecond pulses. However, a productivity loss for ns pulse durations increasing from 19 to 150 ns for ablation in water is reported but could not be observed for ablation in air [115]. Although this effect was not fully understood, that study demonstrates that pulse duration-dependent shielding effects influence the productivity of laser ablation in liquids. In addition, the influence of the local NP concentration, which can significantly differ from the global concentration, has not been considered so far.

When a laser pulse interacts with a metal target, the laser energy initially heats the electrons. The excited electrons transfer their energy to the lattice by collision processes. Due to the high mass difference between electrons and the lattice, the energy transfer requires several ps. Therefore, for pulse durations below the electron-phonon coupling time of specific material, physical processes occur more or less subsequently, whereas they overlap during ablation with ns pulses [31]. As soon as a plume is formed, energy is dissipated into the surrounding liquid, leading to vapor formation at the water layer interface. These processes have extensively been studied by simulations [113, 114, 137] and experiments [95, 117]. It is reported that the cavitation bubble emerges from the vapor covering the plume [253, 279]. The energy transfer from the electrons to the lattice is material dependent and occurs in times in the order of picoseconds for metals [31].

During ablation with fs and ps laser pulses, the laser energy is converted into the plasma [117]. In contrast to sub-ps and ns, where the laser energy is partially used to sustain the plasma resulting in high plasma lifetimes [115, 116]. However, when a critical electron density in the plasma is reached, the laser beam can no longer penetrate the plasma and is reflected, resulting in decreased ablation efficiency [115]. Vogel et al. calculated that the plasma absorption coefficient decreases from sub-fs to sub-ns pulse durations for a wavelength of 1064 nm from about 800 cm^{-1} at 300 fs to 200 cm^{-1} at 10 ps due to the high electron density generated by cascade ionization [78]. For ns pulses, the absorption coefficients were not determined and the values strongly depend on the laser intensity. Moreover, for the rising edge of a ns laser pulse, the energy is mostly transmitted. However,

the free electron density raises so that during the falling edge of the laser pulse, most of the laser energy is absorbed [78]. Also, for ns ablation, laser energy is absorbed by inverse Bremsstrahlung by the plume resulting in a higher plume temperature [280] and, consequently, a longer plasma lifetime of up to 1200 ns [116]. The higher energy density and pressure within the plume cause the transformation of the laser energy into mechanical energy to be larger for ns than for ps pulses [124]. In [279], it was also found that for a pulse duration of 19 ns, the plasma exceeds the boundary of the cavitation bubble, for a pulse duration of 50 ns, the plasma boundary approximately coincides with the cavitation bubble boundary, and for 100 ns, the cavitation bubble boundary exceeds the plasma. When a critical electron density in the plume is reached, the laser beam can no longer penetrate the plume leading to lower ablation efficiencies for longer laser pulses [115], typically termed as plasma shielding. In addition, atomistic simulations revealed that for increasing pulse durations from 400 ps to 2 ns and fixed absorbed fluences, the amount of ejected material is reduced due to heat losses [137]. On the other hand, roughening of the interfacial layer between the metal and water environment, i.e., formation of a transient metal layer, occurs within the first ~2 ns [137], possibly favoring the intrapulse absorption during longer ns pulses. The energy absorbed and dissipated by these transient states is difficult to quantify due to their dependence on numerous parameters. The quantification of energy dissipation is further complicated by the temporal changes of the material surface during the laser pulse impact [107].

Although the absorbance of, e.g., gold (with an absorption coefficient of $8 \cdot 10^5$ cm^{-1}) or silver (with an absorption coefficient of $9 \cdot 10^5$ cm^{-1}) as bulk materials in the infrared spectrum range is low [217], the role of the NP concentration in the liquid is often discussed concerning the laser light attenuation and the resulting productivity decrease [225]. Also, the bubble formation around NPs has been investigated in former studies [281–287]. It was shown that for 30 nm Au NPs and a fluence of 0.3 J/cm², the bubble radius already exceeds 110 nm [283, 286], and the amount of absorbed energy is larger for smaller NPs [288]. Contrary to the cavitation bubble on the target surface, the laser pulse duration does not influence the bubble size found around the NPs [283]. However, the influence of such nanoparticle-related vapor bubbles on the target ablation process has hardly been studied since the literature mainly focused on using vapor bubbles for imaging and therapies. Kalus et al. presented attempts to quantify the energy absorption by the NPs. They found that for Au concentration of 50 mg/L, 25 % of the laser energy is absorbed [91, 92]. For vapor bubbles on the other side, a bubble radius around a 10 nm Au NP of 30 nm is observed for irradiation with a 1 ns laser at a fluence of 0.5 J/cm² [283] while for increasing laser fluences this radius even increases [288].

In this study, we perform shadowgraphy to observe the cavitation bubble dynamics during laser ablation with a 1 ns laser and compare our findings with the literature values obtained

for ablation with a 7 ns laser to gain insight into the ablation phenomena in the ns ablation regime. A laser with a pulse duration of 1 ns is chosen since it revealed the highest ablation efficiency so far. This pulse duration can be realized with high-power q-switched laser systems [289]. On the contrary, 7 ns is an interesting pulse duration since ablations performed with a laser having this pulse duration showed a significant decrease in the ablation efficiency compared to ablation with a 1 ns laser [70]. Also, pulse durations of 1 to 10 ns is the industrial standard of high-power ns lasers. Moreover, the laser beam-liquid interaction is analyzed under consideration of non-linear effects. Lastly, the extent of the NP-laser beam interaction and its effect on the cavitation bubble dynamic is demonstrated. Thereby, the NPs caught in the stationary liquid layer are used to investigate the influence of the local NP concentration on the ablation mechanism.

Methods and Materials

The experimental setup is shown in Fig. 14. For the imaging, a liquid flow chamber with a flow rate of 10 mL/min and a liquid layer height above the target of 5 mm was used. A similar setup is shown in [131]. All experiments were conducted with a silver target of 1 mm thickness and with MilliQ water. A microchip laser (CryLaS, eMOPA1064-400) with a pulse duration of 1 ns, pulse energy of about 400 µJ, and a wavelength of 1064 nm was focused with a combination of two lenses, each with a focal length of 100 mm.

For the image acquisition, an ICCD camera (Andor i-Star, DH334T-18H-13) and a Xenon flash lamp (Hamamatsu, L4633-01) were used. The image quality was improved by placing a diffusor between the lamp and the ablation chamber. Additionally, a telecentric telescope (Sill Optics, Correctal T/1.5, and Edmund Optics, 4X, 65mm CompactTL Telecentric Lens) is positioned in front of the photodetector. One image is acquired per laser shot, and maximal 100 shots are applied on one spot to avoid a pulse number dependent change in the cavitation bubble. As demonstrated in the literature, the maximal number of laser pulses applied per spot before the CB size decreases are dependent on the laser energy [260] and does not change during the first 100 shots at 20 mJ and 11 J/cm² [131]. The camera is used as a trigger in this study. It sends independent trigger signals to the flash lamp and the laser (solid black lines in Fig. 14) so that by varying the delay time difference of the laser's and the lamp's trigger signal, the temporal evolution of the cavitation bubble can be examined. However, the laser system responses with a fluctuating internal delay to the trigger signal, so that the real delay time must be determined with an oscilloscope. Therefore, simultaneously to the laser trigger signal, a signal is transmitted from the camera to the oscilloscope (green line in Fig. 14). For the laser pulse detection, the beam is split by a 10:90 beam splitter. A photodiode detects the minor part of the laser pulse, and its signal is transmitted to the oscilloscope (purple line in Fig. 14). The image acquisition time was 100 ns for all images. For the first two sections of this paper, the delay time is varied between 5 – 100 µs to

observe the lifetime of the first cavitation bubble. In the following, the volume of the cavitation bubble at its maximal expansion is calculated by measuring the bubble width and height and assuming an elliptical quasi-hemisphere. In the last section, a constant delay time of 11 µs is chosen. To ensure that all NP are removed from the liquid in-between shots, one image is acquired every three seconds.

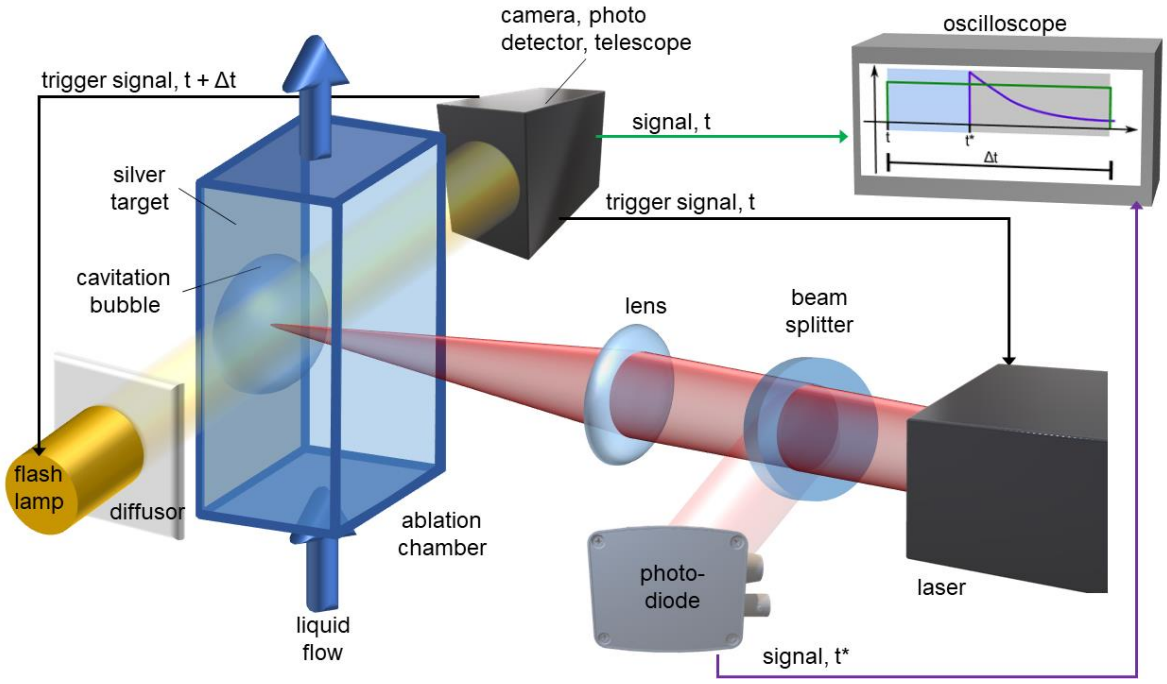

Fig. 14: Shadowgraphy setup for cavitation bubble imaging during 1 ns, Q-switched laser ablation in water; the solid black lines represent the trigger signals sent by the camera. Also, the signal of the camera and the photodiode are sent to an oscilloscope. In the exemplary oscillogram, the camera and laser pulse signals are shown. The blue-shaded area in this diagram represents the laser's response time to the trigger signal and the gray-shaded area the resulting corrected delay time, which is the time between the laser pulse and the moment of image acquisition.

In the following, the laser power will be varied by using reflective filters, and the laser power is measured with a power meter (Coherent Inc., FieldMaxII-TOP). For the fluence calculation, the spot size is determined, as described in [290]. For the variation of the focal distance, the imaging chamber is mounted on a precise micrometer stage. The productivity in this section is determined gravimetrically. For the size analyses, the NPs are stabilized with 0.1 mmol/L tetraethylammonium hydroxide (TEAH) solution and measured 18 h after production. The hydrodynamic diameter distribution is determined by an analytical disk centrifuge (CPS, DC24000). When the laser shots are performed in the colloid instead of pristine water, the concentration is also determined gravimetrically.

Results and Discussion

In the following, the CB's volume dependence on the laser fluence by varying the laser energy is compared to literature results. The differences in the CB dynamic are discussed as a possible explanation of the different ablation efficiencies for both lasers. Another way to alter the laser fluence is to change the focal spot size. Since in literature, the change in the colloidal quality for different focal distances is reported [225], we use our shadowgraphy setup to investigate possible laser-fluid interactions. Lastly, it is shown that already a µg/L NP concentration is sufficient to vary the CB size and dynamic, and how local versus global NP concentration affects cavitation.

Comparison of the cavitation bubble volume for different pulse durations

Exemplary cavitation bubble images at five different laser fluences, ranging from 0.4 to 14 J/cm², can be found in the SI (Fig. S 2). The total bubble energy is the sum of the adiabatic expansion, surface energy, and the potential energy [291]. For CBs, which usually have a radius of least several hundreds of µm, the contribution of the adiabatic expansion and surface increase are negligible, so that $\Delta E_{bubble} \approx \Delta V_{bubble} \cdot (98961\ Pa)$ can be used to calculate the bubble energy. For a bubble expansion from 0 to 0.16 mm³ 16 µJ, i.e., 4 % of the laser energy, is required. In the laser ablation setup, the laser pulse is the only energy source so that at a constant focal distance, the bubble volume is expected to scale linearly with the laser fluence or laser intensity at a fixed laser pulse duration. Since the NP productivity scales with the laser fluence [68], it may also be expected to observe a correlation between NP productivity and the cavitation bubble volume. Regardless of the laser pulse duration, the NP formation is driven by the plasma dynamics [292]. However, the linear correlation between the laser fluence and the CB volume is only observed for a limited laser fluence range of 50 – 175 J/cm² for 7 ns pulse duration in the literature (Fig. 15 B) [128]. Especially for the low fluence regime, the observed cavitation bubble volume is lower than expected, which is assigned to the plasma ignition threshold by the authors [128].

In Fig. 15 A, the fluence-dependent bubble volume is shown for 1 ns pulse duration. In the literature, the spallation regime at low fluences and the phase explosion regime at high fluences are observed with single-pulse experiments, showing a logarithmic productivity-fluence trend similar to the cavitation bubble volume-fluence plot (Fig. 15 A) [68, 246]. When comparing lasers with different pulse durations (Fig. 15 A and B), the maximal productivity for the 1 ns laser (9 mg/h) is lower than for a 7 ns laser system (35 mg/h) at the same fluence of 12 J/cm², as is the cavitation bubble volume. However, the 1 ns laser reveals significantly higher power-specific productivity than the 7 ns laser system, with 36 mg/(W·h) compared to only 7 mg/(W·h) (Fig. 15 A and B). In [70], it was shown that the 1 ns laser showed higher power-specific productivity, also called ablation efficiency, than 3 ps and 10 ns lasers. At first glance, productivity seems to be the more relevant factor since it provides the obtained NP

mass. However, the ablation efficiency gains importance when evaluating the process performance since it enables process comparison [293] and the determination of energy losses. In [131], it is hypothesized that not only the laser fluence but also the plume dynamics determine the ablation rate. Since the plume formation is stated as the starting point of the CB [279] and additionally, it is reported that for ns pulses, the laser pulse sustains the plasma [115]. It is hypothesized that when the plume absorbs more energy, the CB will grow larger. In other words, the amount of laser energy per CB volume can be considered as "lost energy" for the formation of NPs. When comparing this energy-specific cavitation bubble volume (Fig. 15 C), this is higher for the 7 ns laser, indicating that the plume absorbs a larger amount of laser energy. The higher energy-specific cavitation bubble volume for the 7 ns laser agrees with the literature result, in which larger CB [279] and lower productivities [115, 215] are observed for increasing pulse durations. The maximum energy-specific cavitation bubble volume for the 7 ns curve lies between 10 – 15 GW/cm², which coincides with the threshold intensity for optical breakdown of 12 GW/cm² for 6 ns at 1064 nm for the case that seed electrons are present in the liquid [78]. For a deeper understanding of the ablation efficiency, plasma analysis, especially in the pulse duration range from sub-ns to ns, would be required.

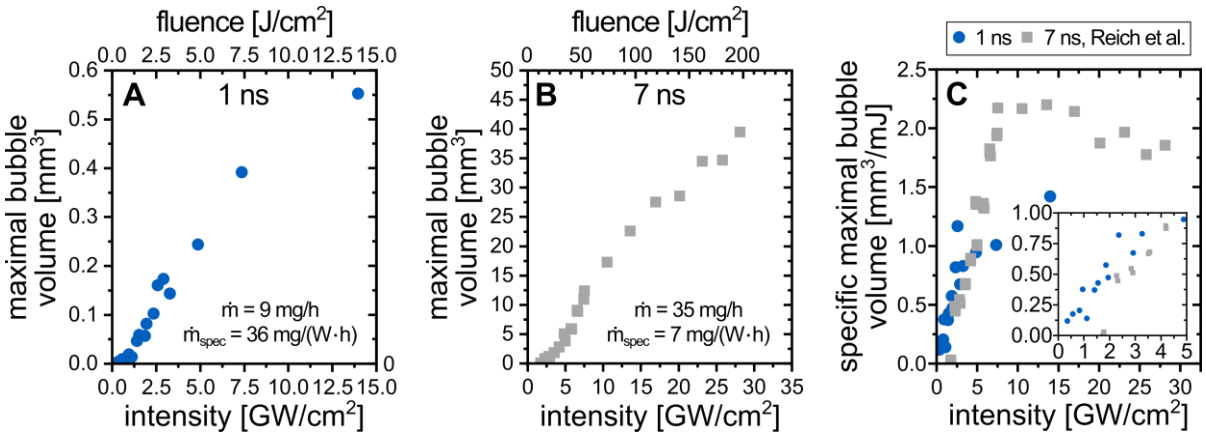

Fig. 15: The maximal cavitation bubble volume for different laser intensities are shown for a 1 ns laser (A) and a 7 ns laser (B) [128]. The productivity $\dot{m}$ and the ablation efficiency $\dot{m}_{spec}$ in B are taken from [70]. For both lasers, the productivity and ablation efficiency are determined at 12 J/cm². Moreover, the power-specific maximal CB volume is shown for both lasers (C).

In conclusion, it is hypothesized that the increased laser-plume interaction for larger pulse durations leads to larger CBs, at the expense of lower NP mass yield. Also, the laser energy transmittances already decreased during the temporal rising edge of the laser pulse for longer pulse durations (e.g., 9 ns in [107]). Consequently, both effects lead to a significantly increased ablation efficiency with decreased laser pulse duration. Simultaneously, compared

to ultrashort pulses, moderate intensities of the 1 ns laser are less prone to optical breakdown in the liquid, allowing the ablation pulse to reach the target.

Influence of the focal plane shift on the cavitation bubble dynamics

Several studies investigated the influence of the focal plane position on NP productivity and size [156, 225, 294–296]. In general, smaller NPs are observed when the laser beam is focused in the liquid layer. In contrast, higher productivities are observed when the focal plan lies slightly behind the target surface [156, 225]. One explanation is that a high laser fluence in the liquid layer leads to the fragmentation of NPs, and the consequent loss in laser energy results in lower NP productivity. By examining the CB in relation to the focal plane position relative to the target surface, it is expected to observe smaller CB sizes and smaller NPs, when the laser focus lies in the liquid layer.

Images of the emerging, maximal, and shrinking cavitation bubble at different focal distances are shown in Fig. S 3, and the whole parameter series is summarized in Fig. 16. The maximal cavitation bubble volume is observed at a target-lens distance of 54.0 mm, which does not correlate with the highest nominal laser fluence on the target surface (Fig. 16 A and B), which is found at a slightly higher target-lens distance of 54.5 mm. Moreover, during the bubble expansion phase, a smaller satellite bubble or a cascade of satellite bubbles in front of the cavitation bubble can be seen for distances between 54.0 and 54.5 mm (see the gray shaded area in Fig. 16). Streaks of microbubbles along the beam path have been observed in several ps and ns cavitation bubble studies [122, 126, 297] and have been assigned to localized boiling of the liquid induced by NPs. Vapor bubbles, which enclose NPs, already occur for fluences at around tens of mJ/cm² [298], which is well below the ablation threshold fluence of hundreds of mJ/cm² to several J/cm² [107, 195]. These vapor bubbles scatter a significant amount of laser energy since the vapor bubble is about twice as large in the radius as the present NP [286].

However, the observed bubble cascades look different from those microbubbles observed in the literature (compare Fig. S 4, Fig. S 5, and [297]). Additionally, productivity at the respective distances is examined. Interestingly, Fig. 16 C shows that the maximal productivity of 3 ng/pulse is found at 53.3 mm, where the nominal fluence on the target surface is only about a third of the maximal fluence reached in this study and the focal plane lies behind the target surface [156, 225]. Since the fluence inside the liquid layer increases with larger lens-target distances, it is considered that the laser beam interacts with the NPs in the liquid and possibly leads to a size manipulation. Moreover, for fs LAL, there is a critical maximal NP radius that will be fragmented [299]. Therefore, the change in the particle size fraction <10 nm is a good indicator of changes in the NP size distribution.

The nanoparticle size change due to the changing focal plane is shown in Fig. 16 D. Exemplary hydrodynamic size distributions can be found in Fig. S 7. Beginning at a focal

plane distance of 51.3 mm, the mass fraction of particles <10 nm slowly increases until a constant size fraction <10 nm of 45 % is reached at 54.3 mm. As already known from former studies, the NPs interact with the laser beam and lead to NP size manipulation, dependent on the laser fluence [89, 155]. Under certain conditions, for low laser fluences, nanoparticles can melt together, which is termed as laser melting in liquids [189]. A NP size decrease is observed for high fluences, up until just below the optical breakdown threshold [155], which is referred to as laser fragmentation in liquids [149].

When increasing the lens-target surface distance, the focal plane of the laser beam shifts from a virtual focal plane behind the target to a focal point in the liquid layer in front of the target, which is sketched in Fig. 16 A. At this focal distance, the point of highest laser fluence lies within the liquid layer so that the surrounding nanoparticles interact with a high-fluence laser beam, resulting in a nanoparticle size decreasing [135]. The limit for non-linear optical effects is reported to be in the range of hundreds of GW/cm² to TW/cm² depending on the laser pulse duration [78]. In the case that seed electrons, which can be ejected from the target due to the laser pulse impact, are present, the threshold intensity of optical breakdown at a pulse duration of 1 ns pulse is decreased to 10 – 20 GW/cm² [78]. NPs present in the liquid also significantly decrease this threshold [29]. The reduced breakdown threshold means that although nanosecond laser pulses are used for the presented experiments, optical breakdown can occur within the gray shaded area in Fig. 16.

When comparing the bubble cascade images to those of optical breakdown in water, they reveal similarities [124, 300]. For distances larger than 55.0 mm, the cavitation bubble size decreases drastically, and no succeeding bubbles are observed. We assume that for these distances, the area where the next bubbles occur are not visible in the image anymore since the total width of the images shown in Fig. 16 measures about 1.2 mm and the liquid layer height approx. 5.0 mm. We also observed non-hemispherically shaped bubbles with spike-like structures at their center point (examples in Fig. S 4 and Fig. S 5). Moreover, ripple-structures at the bubble's center point are observed, looking similar to the coalescence of a bubble with a fluid [301]. The observation of ripple-structures indicates the merging of succeeding bubbles to one larger bubble, which explains the larger bubble volume occurring where succeeding bubbles are observed and the abrupt bubble volume decrease at 55.0 mm distance. Here presumably, the distance between the breakdown bubble and the cavitation bubble is too large for both to touch and merge.

As expected, the NP size decreases when the focal plane is shifted into the liquid layer and, simultaneously, the CB size is drastically decreased. These observations indicate that laser energy is lost by the formation of the bubble cascade and additionally scattered at the bubble interfaces. The energy dissipated in the liquid layer could trigger NP fragmentation, whereas the reduced laser energy reaching the target surface leads to decreased NP mass yield and in the liquid layer. Despite this general trend that links fluence with CB size and NP

productivity, in detail, at conditions of maximized nanoparticle production, neither cavitation bubble volume nor the laser fluence is maximal. Moreover, bubble successions are observed for focal planes in the liquid layer indicating the NP-laser beam interaction in the liquid layer, leading to NP size reduction.

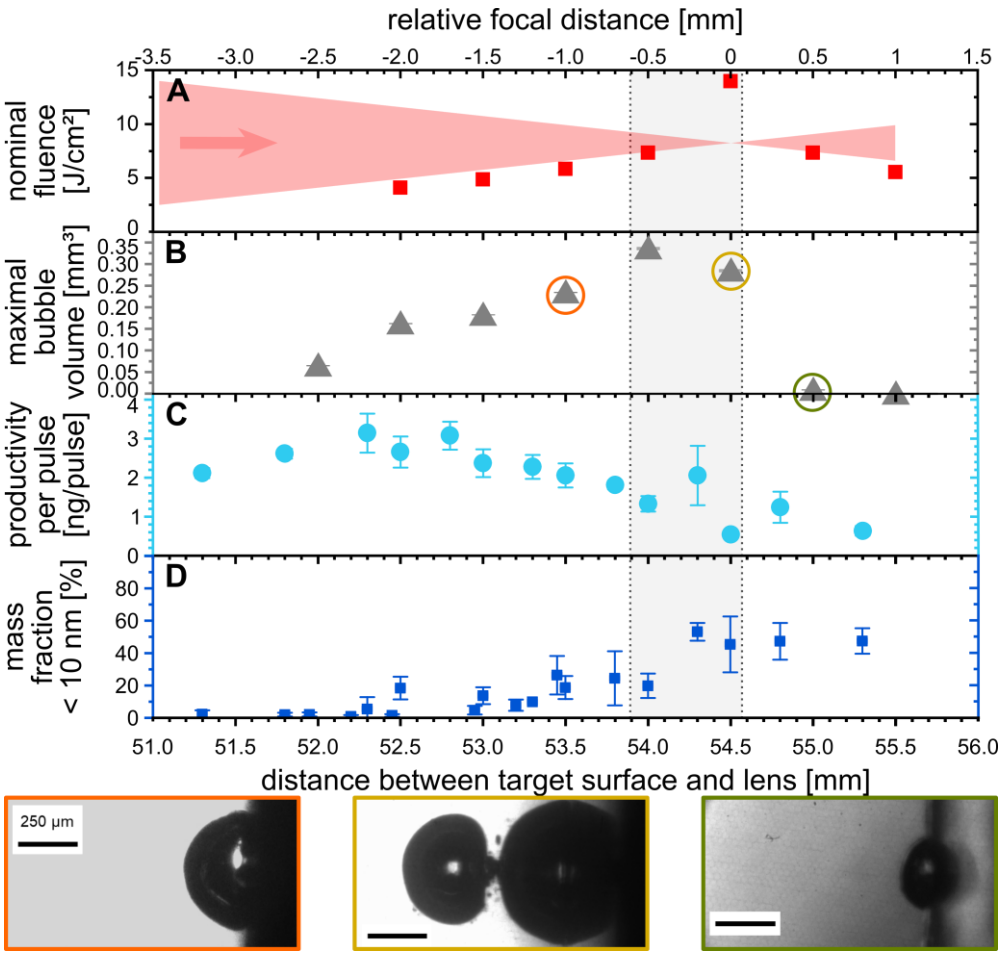

Fig. 16: The distance between the target surface and the lenses is varied for the 1 ns laser system at maximal laser power, the resulting nominal change in the laser fluence (A), the determined maximal cavitation bubble volume (B), the corresponding productivity (C), and the mass fraction of particles < 10 nm are shown. The gray area in A – D marks the focal distances where bubble cascades are observed. The exemplary images show bubbles at distances shorter than (orange), within (yellow), and larger (green) than the range where successive bubbles occurred.

Alteration of the cavitation bubbly dynamics by variation of the nanoparticle concentration in the surrounding liquid

When NPs are present in the liquid layer, it is expected that the laser energy is absorbed and scattered by the NPs. This absorption decreases the laser energy reaching the target surface so that a smaller cavitation bubble is observed. When NPs favor the optical breakdown, the energy difference between cavitation bubbles surrounded by pure water and bubbles

surrounded by colloid is expected to be larger when the intensity in the liquid layer is high, i.e., the focal plane is shifted in the liquid layer. The total bubble energy is the sum of the adiabatic expansion, surface energy, and the potential energy [291]. For gas bubbles expanding into the water at ambient pressure, it is calculated that at larger sizes discussed here, the size dependence of the surface tension plays a minor role in the energy balance and the bubble volume is linearly proportional to the bubble energy.

In the following, the volume difference between a bubble in pure water and a bubble surrounded by a colloid will be expressed as an energy difference as a rough measure to which extend the colloid possibly absorbs part of the laser energy. The corresponding results are presented in Fig. 17. It can be seen that for the same NP concentration, e.g., for 20 mg/L, the energy difference is about 16 µJ when the intensity is low in the liquid layer and increases to more than 19 µJ when the intensity in the liquid layer is increased. The bubble images in Fig. 17 also show the bubble cascade for the latter case, indicating the laser beam interaction with the NPs and liquid and even stronger when the focal plane lies in the liquid layer.

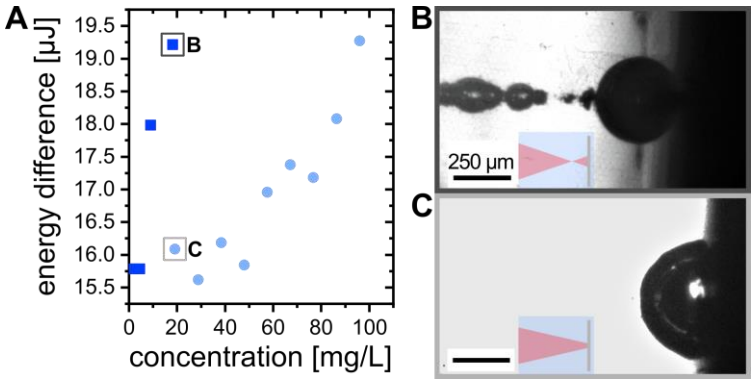

Fig. 17: Energy difference of CBs surrounded by colloid compared to the respective CB surrounded by water at different colloid concentrations and with the focal plane shifted into the liquid layer (dark blue squares) as well as the focal plane virtually shifted behind the target (light blue circles) (A). Images show exemplary CBs with the focal plane shifted into the liquid layer (B) and virtually shifted behind the target (C) at a NP concentration of approximately 20 mg/L as marked by the squares in A.

As expected, the absorbed amount of laser energy scales with the NP concentration. However, the question of the extent of shielding by local and minute NP concentration arises. Hence, experiments comparing two consecutive pulses under different conditions are performed to achieve minimal local NP concentrations and show the extent of the laser beam-particle interaction. In laser ablation flow chambers with typical flow channel diameters of 5 mm and flow rates in the order of 10 mL/min, the Reynolds numbers are so low that laminar flow conditions are ruling the flow profiles. According to the film theory [302], during

laminar flow over a plate, a stationary film with the thickness $\delta_c = {}^{D_{AB}}/_{\beta}$ is formed. Where D_{AB} is the diffusion coefficient, estimated by the Stokes–Einstein equation, of a component *A* within the fluid *B* and β is the mass transfer coefficient. For NPs of 30 nm, a diffusion coefficient of $1.5 \cdot 10^{-11}$ m²/s is calculated (see SI). The mass transfer coefficient can only be estimated using an empirical equation consisting of the Sherwood and Reynolds number resulting in $5.4 \cdot 10^{-6}$ m/s so that the film thickness measures 2.7 µm. At the given experimental conditions of 0.5 Hz and 10 mL/min, the productivity is 1 ng/pulse and a bulk concentration of 3 µg/L is achieved. It is assumed that the local NP concentration is the same since the NP mix in the bulk liquid after the CB collapse and those in contact with the walls are trapped in the formed stationary layer. Consequently, the layer is only enriched during the first and second laser pulse on a fresh surface but not during consecutive pulses.

When comparing the first and second pulse (Fig. 18), microbubbles appear around the cavitation bubble. In the ns study from Letzel et al., satellite bubbles were observed [131]. The authors hypothesized that the crater formation due to the hole drilling could cause satellite bubble formation [131]. In another study, re-deposited nanoparticles sticking to the target were explicitly not excluded as an origin of the satellites [127]. Here, we provide an indication that NPs caught in the stationary liquid layer could be the source of these satellite bubbles.

Former studies showed that for a constant laser pulse energy, the cavitation bubble size depends on the number of laser shots on the respective spot [260]. Presumably, due to the intensified coupling of the light into the material by incubation of defects or surface roughening, the bubble size increases for the first shots until about the tenth pulse [260]. It then decreases once the depth of the drilled hole (500 µm in the study of Letzel et al. [131]) limits the cavitation bubble expansion and the shape of the cavitation bubble transforms from hemispherical to almost spherical [260]. For the given experimental parameters, constant bubble size is determined after about 15 pulses (Fig. S 6). In order to exclude these CB bubble size changes caused by a material modification, the comparison of consecutive bubbles after the 25th and the 26th laser pulse is chosen, since here a constant bubble size is reached.

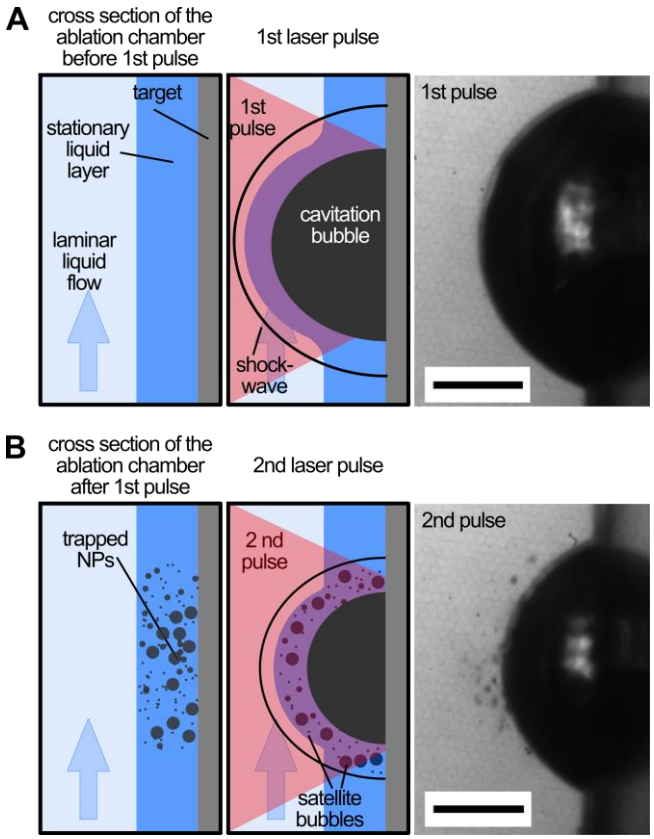

Fig. 18: The sketches illustrate the stationary liquid layer above the target and the first cavitation bubble of an image sequence (A). The formed NP are partially trapped in the stationary layer leading to satellite bubble formation, as shown in the sketch, and observed experimentally (B); please note that the sketches in the middle are not depicted on the correct time scale for the sake of the message, the scale bar measures 250 µm.

Fig. 19 shows these two bubbles, and, as can be seen in Fig. 19 A, the sizes of the two consecutive bubbles differ by about 15 % within the steady bubble size regime. The experiment runs under liquid flow conditions and a low repetition rate, where the hydrodynamic residence time is low and the time sufficient to remove the NPs inside the liquid from the laser beam path before the next pulse. In laminar flow conditions, the NPs in the main flow channel can easily be removed from the bulk liquid, but not from the stationary film. This film and the enclosed NPs will stay in front of the target, even at flow conditions.

In this study, the liquid is entirely removed from the ablation chamber, the target rinsed, dried, and the chamber filled with freshwater between the 25th and 26th pulse to probe the effect of NP present in this layer. A bubble size increase of about 140 % is observed (Fig. 19 B) and leads to the conclusion that even minimal amounts of NPs inside the stationary film lead to a significant decrease of the cavitation bubble volume, presumably due to energy extinction by the trapped NPs. Moreover, at the 25th pulse (Fig. 19 B), smaller satellite bubbles surrounding the cavitation bubble in a hemispherical shape can be observed but are not observed after manually refreshing the stationary liquid (26th pulse). Previous studies

assumed that the confinement of the cavitation bubble by the ablation crater leads to material ejection from the bubble into the surrounding [131]. We can now specify that the crater confinement alone does not lead to material ejection from within the cavitation bubble. Instead, nanoparticles are caught in the stationary liquid layer.

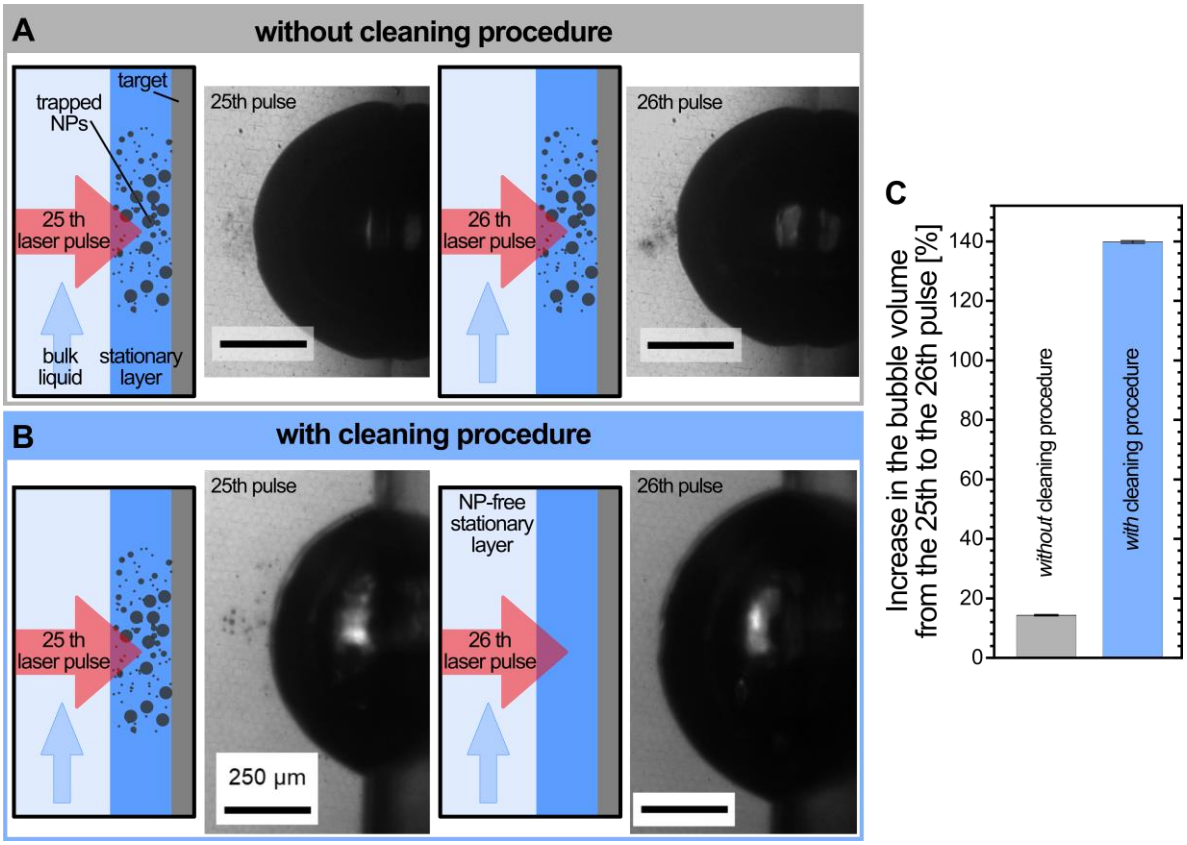

Fig. 19: The influence of the NP in the stationary liquid layer is examined by comparing the CB size of consecutive laser pulse with and without a cleaning procedure in between. After 25 laser pulses, the stationary liquid layer is enriched with NP, and a constant cavitation bubble size is reached (A); when the ablation chamber and target are rinsed between two consecutive pulses, a NP-free stationary liquid layer is generated, leading to the formation of an increased cavitation bubble and the absence of satellite bubbles (B), the comparison of the volume increase between the 25th and 26th pulse for A and B is plotted in C.

The occurrence of satellite bubbles was also shown for ps laser pulses in [127], where it is associated with the jetting of micro-droplets into the dense water region above the cavitation bubble. In MD simulation, the jetting of larger NPs from the cavitation bubble into the surrounding liquid was only seen for ps laser pulses but not for ns laser ablation, where the NPs are caught in the cavitation bubble until its collapse [137]. This simulation emphasized the previous hypothesis that the observed satellite bubbles for ns pulses result from NPs captured in the stationary liquid layer. In literature, hemispherical shockwave propagation was observed before the cavitation bubble expands [122, 303]. Former studies already

reported the formation of microbubbles along the laser beam path as a result of NP interaction with the incident laser beam [122]. However, in our case and as shown by [131], microbubbles form around the cavitation bubble. Therefore, it is assumed that particles act as seeds for shockwave energy dissipation by the vaporization of the liquid around the NPs.
In conclusion, it is found that the interaction of the NPs with the laser beam is stronger when the focal plane is shifted into the liquid layer and for high NP concentrations in the liquid. Additionally, it is observed that even the minute amount of NPs produced with one single laser pulse is sufficient to shield about (0.4±0.002) % of the laser energy, completely change the bubble morphology, and causes the satellite bubbles during ns laser ablation in liquids.

Conclusion

In the past years, multiple cavitation bubble studies were performed, focusing on its dynamics and connection with the nanoparticle formation mechanism. However, hardly any study thoroughly examined the influence of different energy distribution channels such as temporal or spatial energy distribution (i.e., pulse duration or focusing and defocusing) of the laser beam or absorption by nanoparticles.
In general, for different temporal energy distributions, a significantly larger cavitation bubble for longer pulse durations, i.e., ≥7 ns, is observed, presumably due to an enhanced laser-plume-interaction. It is assumed that longer pulse durations sustain the ablation plume, which gains more energy, which in turn is released in larger CBs, and favors temporally dependent intrapulse absorption by a transient metal layer. Consequently, less energy is converted into mass ablation, so that the ablation efficiency is decreased for higher ns pulse durations and found to be highest for a 1 ns laser.
When keeping the temporal energy distribution constant and changing spatial energy distributions by varying the focal distance, it was found that the point of highest fluence and maximal bubble volume do not coincide. In a regime where the focal point is slightly above the target surface, a succession of bubbles and a decreased NP size are observed, strengthening the hypothesis that NPs are fragmented. However, the extent to which fragmentation in the liquid, the changed fluence on the target surface, plasma dynamics, or the laser-induced cavitation bubble dynamics contribute to the size modification cannot be quantified and further explanations cannot be excluded. Additionally, the resulting energy loss leads to reduced productivity, which is further emphasized because, with higher NP concentrations in the liquid, the energy decrease is even more substantial.
The cavitation bubble imaging experiments were performed in a liquid flow chamber with flow velocities sufficient to remove NPs from the chamber's main flow channel in-between laser pulses. However, satellite bubbles were observed at each cavitation bubble after the first one, which indicates the presence of NPs in a stationary liquid layer on the target surface. The incident beam causes vapor bubble formation around the NPs and therefore leads to a

larger fraction of scattered laser light. Removal of the NP-enriched stationary liquid layer leads to a bubble volume increase of 140 %.

Overall, these results point to two future measures: First, cavitation and satellite bubble imaging experiments must be planned carefully and take local NP concentrations into account to understand LAL dynamics. Second, it was found that short laser pulses are required but not sufficient for a high ablation efficiency. NPs trapped in a stationary liquid layer, which has so far not been considered, presents an obstacle in high-yield LAL. Hence, effective measures to lower the local NP concentration just in front of the target are demanded.

4.1.3. Influence of the pulse duration on the productivity and ablation efficiency

S. Dittrich, M. Spellauge, S. Barcikowski, H. P. Huber, B. Gökce

“Picosecond resolved pump-probe microscopy revealing the mechanism of high power-specific productivity of sub-ns laser ablation in liquid“
(to be published)

Abstract

Laser ablation in liquid (LAL) provides a versatile and safe nanoparticle (NP) production method. However, due to laser-liquid interactions, different energy dissipation channels, such as linear and non-linear absorption by the liquid as well as scattering by NPs and cavitation bubbles, lead to a reduced amount of laser energy available for NP production. This energy extinction results in a decreased ablation rate compared to laser ablation in air. In former studies, high power-specific productivity, i.e., ablation efficiency, was observed for an intermediate pulse duration of 1 ns. It is now shown that pulse durations ranging from several hundreds of ps to 2 ns enable efficient LAL since the laser beam shielding by the ablation plume is reduced. Pump-probe microscopy images revealed that the vapor expansion in liquids starts to differ from vapor expansion in air at about 2 ns. Additionally, non-linear effects are less prone for intermediate pulse durations compared to fs pulses. Accordingly, pulse durations in the range of several hundred ps to 2 ns enable highly efficient NP production due to reduced vapor shielding.

Introduction

Laser ablation in liquids (LAL) is a versatile method for the synthesis of nanoparticles (NPs) that enables the production of ligand-free colloids [29, 180]. Compared to chemically synthesized colloids, particles generated by LAL exhibit a better signal-to-noise ratio for laser desorption ionization mass spectrometry [233], are suitable as reference materials for nano-toxicological assays [173] and enable the decoration of microparticles for 3d printing [226, 304].

Another advantage of LAL is the possibility to produce alloy NPs from pressed micro powder targets, even if an element miscibility gap exists [305]. For fully miscible elements, a composition gradient is observed for chemically synthesized NPs, presumably due to their different redox potential [306]. This elemental segregation in an outer layer and a core was also observed for laser-generated NPs [307]. However, the yield of solid-solution particles can be increased by applying picosecond (ps) laser pulses [307]. Especially in the field of

catalysis (e.g., AuPt [305, 308], AuAg [274, 306], PtPd [309], high entropy alloys [310]) or for biomedical applications (e.g., AuAg [311]), alloy NPs present a promising perspective.

Although laser-generated particles show advantages compared to chemically synthesized NPs, only a few commercial distributors offer laser-generated NPs. A possible reason is that LAL is more expensive than chemically synthesized NPs for productivities smaller than 550 mg/h [65]. Productivities higher than 550 mg/h can be achieved by LAL, however only with high power laser systems (>200 W) [65], which emphasized the importance of increasing the efficiency during LAL. It was found that the efficiency, which we define as the ablated NP mass per time in [g/h] (productivity) divided by the laser power in [W], varies strongly. It was shown that the efficiency is maximal for laser systems operating at a pulse duration of one nanosecond (ns) when compared with a few ps or higher than 5 ns [70]. Additionally, a decrease in productivity with increasing ns pulse duration is observed in the literature [115, 215], which could not be explained yet.

In contrast to ablation in air, the laser beam's interaction with the liquid medium needs to be considered for LAL. Therefore, different additional channels of energy losses occur due to the liquid environment, such as linear and non-linear absorption, interaction of the laser beam with NPs, and energy extinction caused by the ablation plume.

LAL performed with ultrashort laser pulses ranging from tens of femtoseconds (fs) to a few ps is often accompanied by an optical breakdown and non-linear effects such as the optical Kerr effect [95]. For a laser wavelength of 1064 nm, threshold fluences for optical breakdown of 1 – 13.5 J/cm² for ps and 100 – 300 J/cm² for ns were measured by Vogel et al. [78]. Dittrich et al. found the highest ablation efficiency for a 3 ps laser at about 1 J/cm² and for ns lasers between 5 – 10 J/cm² [70]. Consequently, optical breakdown only contributes to the laser energy loss during ps experiments in this study. On the contrary, if laser fluences above the breakdown threshold are applied, the resulting energy loss is dependent on multiple parameters. Vogel et al. measured the transmission through the breakdown volume for different pulse durations at a fluence of six times the optical breakdown threshold fluence. The transmission was approximately 50 % for pulse durations <300 fs, maximal 80 % for a pulse duration of 3 ps, and lower than 10 % for pulse durations exceeding 5 ns [78]. For LAL with ns pulse durations, the threshold intensity is not exceeded so that non-linear absorption as an energy dissipation channel can be excluded for longer ps and ns pulse durations.

The linear optical effects like the absorption of the laser energy by the water layer are inevitable for laser ablation in liquid. Due to the reflectance at the optical window of the ablation chamber entrance, the absorption of the glass, reflectance at the water-glass interface, absorption by the water, and reflection at the water-metal interface as illustrated in [70], more than half of the laser energy is dissipated before reaching the target surface.

Additionally, for all ablation processes in liquid, shielding effects by the emerging NPs, and persistent microbubbles [91–93] must be considered. In the literature, there are attempts to

account for the shielding effect of the NPs, which is dependent on the NP concentration. Even at low concentrations of 50 mg/L, 25 % of the laser energy was shielded by the NPs [91, 92]. Since single pulse experiments are performed in the present study, the NP and microbubble shielding can be neglected. Next to energy shielding by the NPs, they can lower the threshold fluence for the optical breakdown of the liquid for ns pulses [78]. For a 1 ns pulse duration and a wavelength of 1064 nm, a breakdown threshold of pure water is 100 J/cm². By impurities in the liquid, this threshold can be reduced to ~20 J/cm² [78].

In the literature, the early laser-matter interaction has been studied via pump-probe microscopy (PPM). Starinsky et al. observed that already during the irradiation of Au in water with a 10 ns pulse, the target surface is fully covered with a vapor layer, and nucleation-induced scattering shields the target from the laser energy [107]. Also, for fs laser pulses, where the laser pulse and the following mechanical material response are temporally separated, pump-probe experiments are conducted [95]. However, examinations of the early ablation process were so far only performed for <500 fs [95] and >9 ns [107], so that investigation for an intermediate pulse duration range of hundreds of ps to 8 ns are missing. Next, the laser beam can be shielded by the forming vapor on the target surface and, later, the cavitation bubble. In a 9 ns laser study, the shielding at an early stage of the laser pulse was investigated [107]. Here, approximately 0.3 ns after the laser pulse emittance, scattering of the laser pulse, first by critical opalescence later by nucleation induced scattering, starts. This effect is dependent on the laser intensity and the laser pulse duration.

In a former study, LAL at pulse durations of 1 ns was considerably more efficient than LAL with pulse durations of a few ps and pulse durations exceeding 5 ns [70]. Following [107], we form the hypothesis that, compared to longer ns laser pulses, laser beam scattering does not occur, which leads to lower energy losses. At first, we quantify the losses of laser energy during LAL compared to ablation in air for different pulse durations. Afterward, for the pulse duration range with the lowest energy losses, the formation of a vapor layer and the consecutive cavitation bubble are examined by PPM of gold (Au) surrounded in air and water. The early vapor formation is observed with 100 ps resolution after the impact of a 650 ps laser pulse. In the last step, we additionally analyzed the response of silver (Ag) and platinum (Pt) to identify the material dependency of the vapor formation.

Methods and Materials

Ag, Au, and Pt bulk samples with a thickness of 1 mm and a purity >99.99 % were used throughout the experiments. The samples were embedded in a resin matrix and subsequently sanded and polished. An arithmetic average surface roughness R_a (see Eq. 7) [312] of approximately 10 nm was achieved, ensuring a smooth optical surface for the applied imaging techniques. All experiments were performed under ambient air conditions or in deionized water with a liquid layer height of 4 mm.

$$R_a = \frac{1}{n}\sum_{i=1}^{n}|y_i| \qquad \text{Eq. 7}$$

where n is the number of intersections with the profile at the mean line and y the measured peak height.

Fig. 20 a depicts the experimental pump-probe microscopy (PPM) setup. A laser source (picoloAOT, InnoLas Laser) simultaneously emitted pump- and probe-pulses with a repetition rate of f_{rep} = 500 Hz. The pump-pulses that induced the ablation process were centered at the fundamental wavelength of 1064 nm with a pulse duration of 650 ps (FWHM). Frequency-doubled probe-pulses used for illumination were centered at 532 nm with a pulse duration of 600 ps (FWHM).

A glass plate (GP) partially reflected the pump-pulses onto a photodiode (DET10A2, Thorlabs), which served as a trigger source for temporal synchronization. A mechanical shutter (LS6S2TO-NL, Uniblitz Electronics) then selected a single pulse from the pulse train, which was guided through a half-wave-plate (HWP) polarization beam splitter (PBS) combination to adjust the pulse energy. Finally, the single pump-pulse was focused onto the sample surface at an incidence angle of 35° by a plano-convex lens with a focal length of f = 75 mm. An elliptical laser spot on the sample surface with a minor beam waist radius of $w_{0,min}$ = (12 ± 1) µm and a major beam waist radius of $w_{0,maj}$ = (15 ± 1) µm was measured with a focal beam profiler (MicroSpotMonitor, Primes). The peak fluences Φ_0 were calculated by:

$$\Phi_0 = \frac{2 \cdot P}{\pi \cdot w_0^2 \cdot f_{\mathrm{rep}}} \qquad \text{Eq. 8}$$

The average laser output power P was measured after the focusing lens using a power meter (PS10Q, Thorlabs). Note that all peak fluences mentioned throughout this manuscript refer to incident peak fluences in air.

The delay time Δt of the probe-pulse regarding the pump-pulse was introduced with a motorized delay line, allowing Δt to be adjusted between -1 ns and 8.5 ns. After passing a quarter-wave-plate (QWP) PBS combination, the probe-pulse imaged the ablation process at normal incidence onto a CCD camera (pco.pixelfly usb, PCO). The beam was focussed through a long working distance microscope objective (50x, NA = 0.42; M Plan Apo 20, Mitutoyo) and a tube lens (TL). A bandpass filter (BPF) centered at (532 ± 5) nm was located in front of the camera to suppress undesired pump- and plasma-radiation. The shutter and camera were temporally synchronized to the trigger signal with a delay-generator (DG645, Stanford Research Systems).

For each Δ*t,* the sample was laterally translated to a pristine surface, where a sequence of three images was acquired. The first image was recorded 5 s before the pump-pulse (reference image, R_0). Afterward, the ablation process was imaged at the desired Δ*t* ($R(\Delta t)$). Finally, a picture was taken 5 s after pump-pulse impact (infinity image, R_{inf}), which gives access to the reflectivity when the ablation process has finished and the produced crater reached its equilibrium depth. Subsequently, the relative surface reflectivity change $\Delta R/R_0$ was calculated for each pixel (Eq. 9).

This process is illustrated in Fig. 20b at a delay time Δ*t* of 8 ns after irradiation of Au in water with an incident fluence of 8 J/cm^2. All $\Delta R/R_0$ curves presented throughout this manuscript were averaged over an area of 20 x 20 pixels, located in the center of the irradiated region.

$$\frac{\Delta R}{R_0} = \frac{R(\Delta t) - R_0}{R_0} \qquad \text{Eq. 9}$$

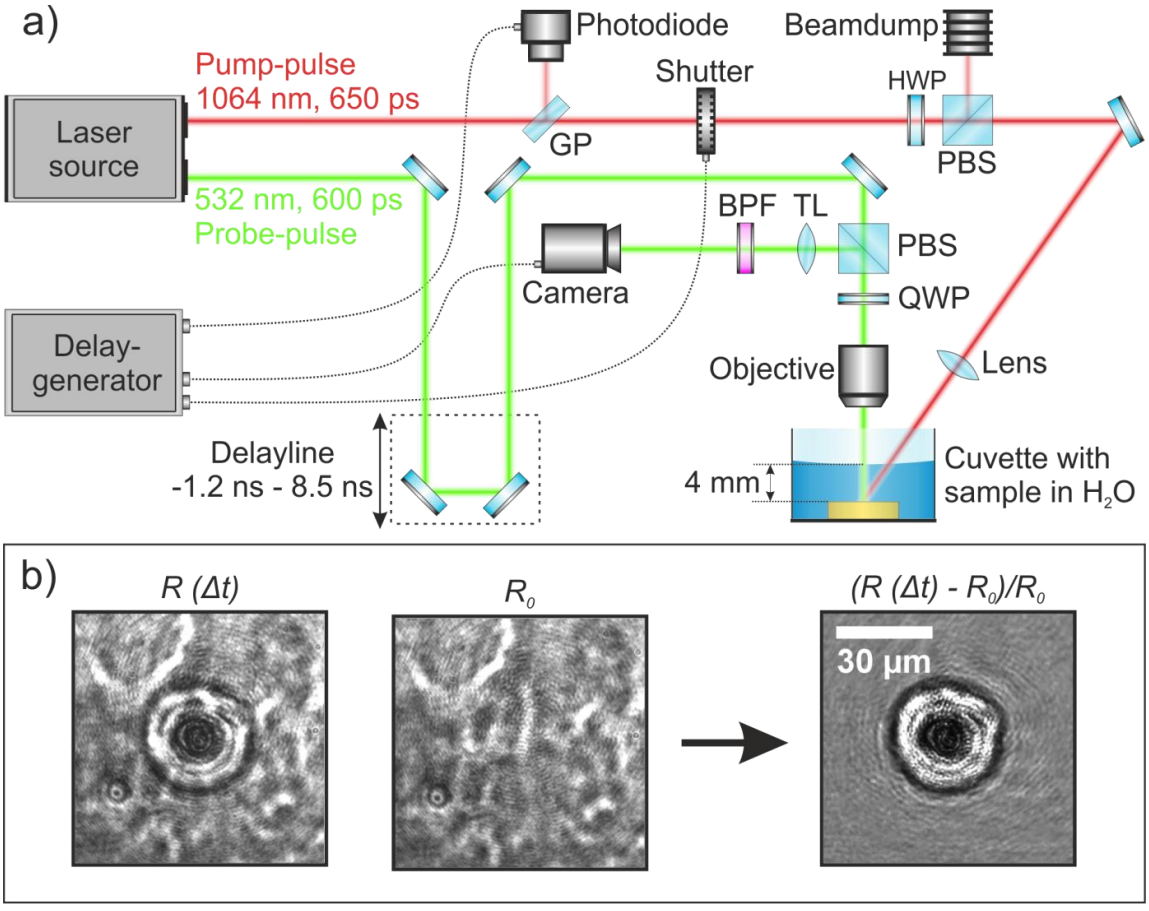

Fig. 20: (a) Pump-probe microscopy setup for the ablation in water. For the analysis of the ablation mechanism in air, the setup is the same except for the cuvette. (b) Image post-processing. The first image is taken of the unirradiated surface 5 s before the pump pulse arrives and is used for measuring the initial sample reflectivity R_0. The second image is taken at a selected delay time Δt and used to determine the time-dependent reflectivity R(Δt). These two images are used to calculate a difference image.

Results and Discussion

In the introduction, different mechanisms leading to laser energy loss during LAL are illuminated. However, the quantification of these mechanisms is challenging due to their dependence on multiple parameters. In [70], the efficiencies for different pulse durations are presented. However, the origin remained ambiguous. Comparing the ablation efficiencies obtained in [70] for gold once in ambient air and once immersed in water for a given laser pulse duration gives the efficiency loss caused by the liquid environment (compare solid bars in Fig. 21). The energy extincted by linear absorption in the liquid and reflectance at the layer interfaces can be calculated. For this calculation, the optical properties listed in [70] are taken. The corrected ablation efficiency under consideration of the linearly absorbed energy is shown in Fig. 21 by the dashed bars. It can be seen that the same ablation efficiency is reached for the ablation in air and water with the 1 ns laser (17.0 ± 0.7 µg/(W·s) and 17.1 ± 0.4 µg/(W·s), respectively), when absorption and scattering caused by the liquid layer are considered. For the ps laser ablation, the efficiency loss is largest during LAL (4.97 ± 0.1 µg/(W·s)) and 90 % lower than in air (40.7 ± 0.8 µg/(W·s)). Since these results are obtained by multipulse experiments, presumably, extinction caused by the formed NPs leads to the low efficiency in water. With a breakdown threshold fluence of about 1 J/cm² for 3 ps pulses [78] and a fluence of 1 J/cm² for the 3 ps ablation [70], optical breakdown is expected to occur. For the ablation with a 7 ns laser, the absorption corrected efficiency decreases from 19.7 ±5.0 µg/(W·s) in air to 13.7 ± 1.1 µg/(W·s) in water, which equals a decrease of 30 %.

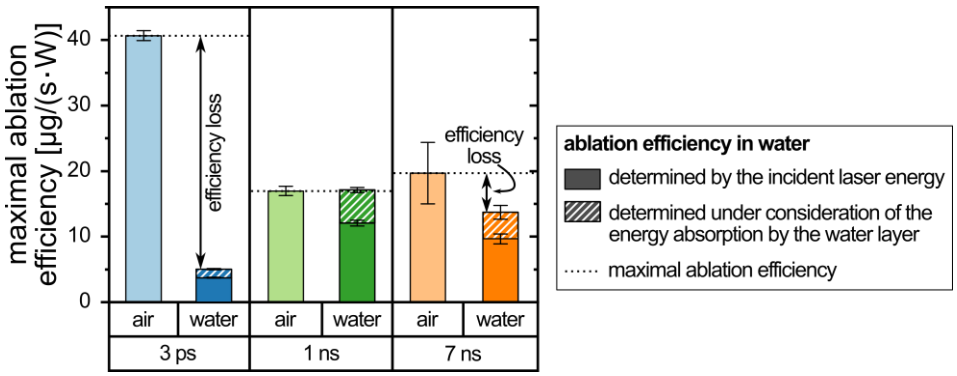

Fig. 21: Maximal ablation efficiency for the ablation of gold in air (light-colored, solid bar) and water (dark-colored bar) for lasers of 3 ps (blue), 1 ns (green), and 7 ns (orange) pulse durations with data from [70] where the ablation efficiency is calculated with the incident laser energy (dark-colored, solid bar) and under consideration of energy extinction by the water layer (dark-colored, dashed bar).

Following the observation from Starinskiy et al. [107], it is hypothesized that for pulse durations of several hundreds of ps to 1 ns, the laser pulse is shorter than the starting time

for vapor layer and plume formation so that the amount of extincted laser energy is minimized. We performed time-resolved PPM measurements of Au in air and water with a 650 ps laser as a pump- and probe- pulse source at an irradiated fluence of 8 J/cm², which lies a factor of 4 – 5 above the ablation threshold of Au in water [70], to prove this hypothesis (Fig. 22).

From the resulting PPM images (Fig. 22a), the reflectivity, determined at the center of the images (Fig. 22b), and the area of expanding reflectivity change are derived (Fig. 22c) for pulses on Au in water and air. First, it is observed that the surface reflectivity in air and water do not differ (Fig. 22b). For 500 fs PPM, the reflectivity change was more extensive in air than in water [95]. However, this could be attributed to the higher amount of laser energy, reaching the target for ablation in air since filamentation occurred for pulses in water. For ns ablation on the ns scale, the reflectivity change in water is more extensive than in air due to supercritical water layer formation and emerging vapor layer [107]. The time scale of the supercritical water layer formation is dependent on the laser fluence. The formation starts already during the 9 ns laser beam's rising edge or fluences near the damage threshold [107]. Since, in our experiments, the threshold fluence is exceeded about 4 – 5 times [70], a very early vapor formation, i.e., reflectivity decrease, would be expected.

Next, it is observed that the area of laser modification in air and water starts expanding at the same time delay (~ 0 ns). For irradiation in water, this area expands for 2 ns until it equals the final sport size of 167 µm². For irradiation of Au immersed in water, however, the area of changed reflectivity increases continuously within the observed time range and exceeds the final spot area of 120 µm² 2 ns after the surface changes start (Fig. 22a, c). Within these first 2 ns, after the laser impact, a high velocity of about 6000 m/s is observed for pulses in air and water, which results in a Mach number (Ma) of 18 and 4, respectively (Fig. 22d). In the literature, the supersonic adiabatic plasma expansion [313] is reported. The shockwave velocity was found to be dependent on the laser pulse duration, the pulse energy [124] and the focusing conditions [314]. After reaching the final spot diameter, the spot area remains constant for Au in air, whereas it starts to expand with 1700 m/s continuously for the experiments in water (Ma > 1). The shockwave propagation between 0.2 – 2 µs after the laser pulse measured 1700 m/s for Cu (8 ns pulse width, 68 J/cm² [315]), or for silica (50 fs pulse width, at ten times the threshold fluence [129]) in the literature. At a very early stage of the cavitation bubble formation, it moves with the speed of the shockwave [316], which explains the observation of Mach cones at early stages (50 fs pulse width, 1.58 J/cm² [129], 8 ns pulse width [317], 13 ns pulse width [318]). In the literature, for the ablation of Ti with a fluence of 68.5 J/cm², the detachment of the shockwave from the bubble is observed between a delay time of 20 – 52 ns [319] and between 6 – 27 ns at 29.8 J/cm² [303]. Further investigations using shadowgraphy show the difference in the temporal evolution of ablation of epoxy-resin in air and water for delay times >10 ns [320].

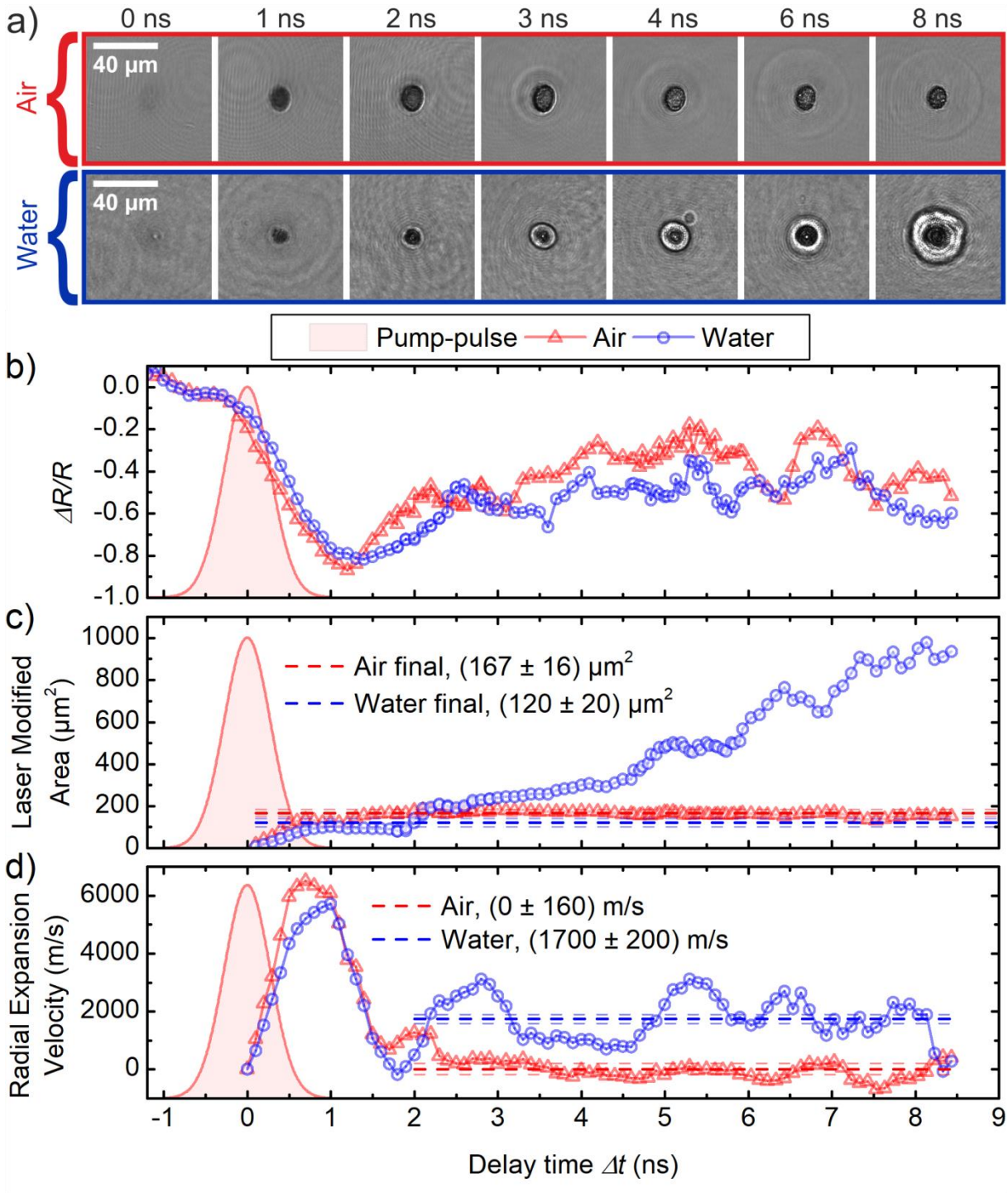

Fig. 22: Exemplary microscopy images at different delay times are displayed (a). Time-dependent change in the relative reflectivity (b) and the spot area (c) in the Au target surface for PPM in air (red) and water (blue) at 8 J/cm². Additionally, the velocity of the observed surface changes in air and water is calculated (d). The horizontal lines in (c) and (d) mark the final spot area and velocity, respectively.

Later, the cavitation bubble expansion is drastically decreased to, e.g., 50 m/s at a delay time of 0.5 – 5.0 µs [123]. All observations combined lead to the conclusion that we observe a supersonic expansion for the first 2 ns of ablation of Au in water. Since, in this time frame,

the reflectivity change, laser modified area, and radial expansion velocity are identical for the ablation in water and air, we assume similar processes occurring, such as material modification and plume expansion. The laser beam energy loss is presumably equal for water and air in this time frame. Only after delay times >2 ns, the vapor layer has detached from the shockwave and, at this early stage, propagated with sonic velocity for the first 9 ns of the ablation process. Consequently, the ablation efficiency for ablation in air and water, under consideration of absorption by the liquid, is equal as long as the laser pulse is over before the detachment of the vapor layer occurs. This detachment starts 2 ns after the laser pulse maximum.

Since the absorption is a material-dependent property, it is assumed that the material response to the laser pulse is also material-dependent, i.e., the higher the absorption at the laser wavelength, the faster the material response is expected. Therefore, we additionally analyzed the material response for Ag and Pt samples within the first 9 ns. The laser modified area changes (Fig. 23a) start first for the Pt sample (0 ns), revealing the largest final spot area of 584 µm. For Ag and Au (Fig. 22c), the surface change starts at 0.2 ns and exhibit a smaller final spot area than Pt. This order coincides with the metals' absorption coefficients at 1064 nm, which are $8.99 \cdot 10^5$ cm^{-1} for Ag [217], $8.22 \cdot 10^5$ cm^{-1} for Au [217], and $13 \cdot 10^5$ cm^{-1} for Pt [220]. In the literature, it is observed that a coating, which increased the absorptivity, causes stronger stress waves in the sample material and leads to a faster shockwave and vapor expansion [321], which supports our observations. Although the energy absorption for the three materials is different, the radial expansion velocity is 1700 m/s for all three materials (Fig. 23c), also for the ablation of Cu wires in water (8 ns, 68 J/cm²), 1700 m/s are observed [315]. It is slightly slower with 1200 m/s for Pd in acetone (250 fs, 7 J/cm²) [123]. These observations show that an optimal laser pulse duration range exists and depends on the material specific absorption at the selected laser wavelength. For materials with absorption coefficients at about 10^6 cm^{-1}, the maximal efficiency is found for laser pulses of several hundred ps to 3 – 4 ns.

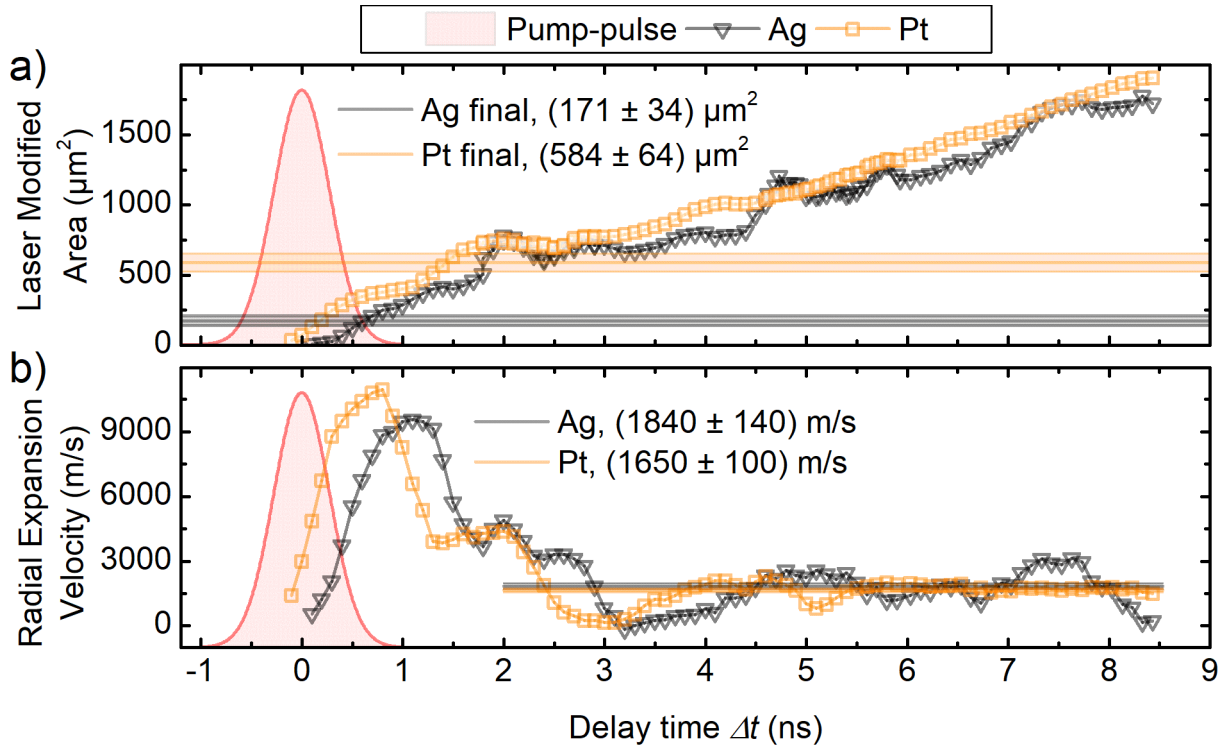

Fig. 23: Time-dependent change in the spot area (a) in the target surface for PPM for Ag (gray) and Pt (yellow) targets at 8 J/cm². The velocity of the observed surface changes for Ag and Pt in water at 8 J/cm² (b). The horizontal lines in (a) and (b) mark the final spot area and velocity, respectively.

Conclusion

Pump-probe microscopy reveals insight into ablation mechanisms for targets immersed in air and water. For the first 2 ns after the laser impact, the surface and reflectivity changes for samples in air and water are identical, leading to the assumption that the vapor formation starts after the laser pulse has ended. Therefore, plasma and vapor shielding are negligible for ablation with a pulse duration of several hundred ps to 3 – 4 ns. Consequently, the reduction of shielding effects during the laser pulse irradiation increases the ablation efficiency observed for these intermediate pulse durations.

For Ag, Au, and Pt ablation in water, the vapor is presumably attached to the shockwave and both expand with supersonic velocity within the first 2 ns. Afterward, the vapor detaches from the shockwave is propagated with sonic velocity for at least 7 ns. The time at which the area modified by the laser starts to expand, and the size of the final spot area scale with the material absorption coefficient at the selected laser wavelength. Consequently, the pulse duration range for maximal ablation efficiency is dependent on the material absorption coefficient.

4.2. Adjustment of nanoparticle productivity and properties during the automated laser ablation

A suitable laser system was identified in the previous section. For the application of NPs, knowledge of the colloid quality is essential since it strongly influences the particle properties and thus their application, e.g., catalytic activity. As indicated in the fundamentals sections 2.3 and 2.4, both the NP properties and productivity are influenced by the laser system and process parameters. However, there is less knowledge of how both are connected. Therefore, in the first section, the productivity and NP size control by laser parameter variation are determined, and the influence of the colloid quality on the catalytic performance is emphasized. Then, in the second section, the variability of the process parameters, their impact on the productivity and colloid quality are analyzed, and data for the preparation of material data sheets are collected. The focus lies on the focal plane shift, the flow rate adjustment, and the ablation and colloid storage time. As was presented in the fundamentals, the different process parameters cannot be considered individually but are connected. The volume-specific energy dose is introduced as a process variable that summarizes the influence of the laser power, the focus position, and the liquid flow rate on the NP size. Regarding the colloid stability, Au and Pt NPs reach good stabilities in 0.1 mM sodium chloride solution, whereas Ag NPs in 0.1 mM trisodium citrate are not stable. Therefore, since citrate ions negatively influence different applications, the stabilization of Ag in tetraethylammonium hydroxide and different citrate concentrations is examined in section three. Lastly, in section four, the reproducibility and robustness of the NP properties produced under the conditions determined in the previous sections are determined, statistically evaluated, and compared to commercial standards.

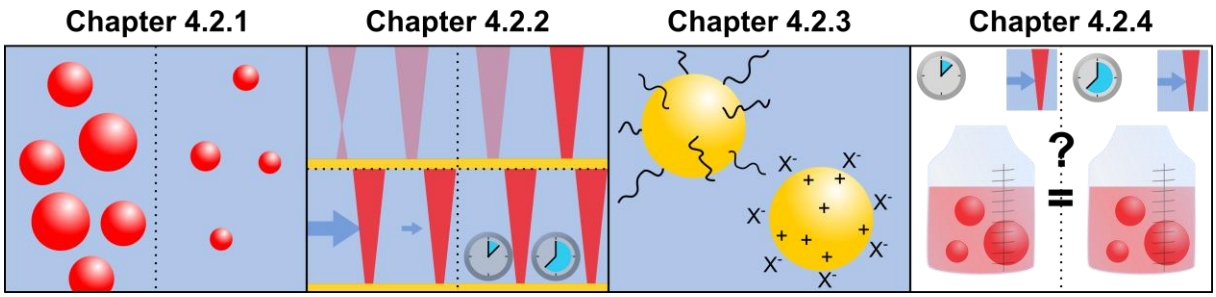

Fig. 24: Overview of the measures for NP productivity and property adjustment with the automated device. In chapter 4.2.1, the general relation between NP productivity and size is examined. The optimal laser parameters for the automated device are determined in chapter 4.2.2. The influence of different stabilizers on the Ag NP properties is analyzed in chapter 4.2.3. Last, the reproducibility of the automated NP production is validated in chapter 4.2.4.

4.2.1. Influence of the process parameters on nanoparticle productivity and size

S. Dittrich, S. Kohsakowski, B. Wittek, C. Hengst, B. Gökce, S. Barcikowski, and S. Reichenberger

Published in: “Increasing the Size-Selectivity in Laser-Based g/h Liquid Flow Synthesis of Pt and PtPd Nanoparticles for CO and NO Oxidation in Industrial Automotive Exhaust Gas Treatment Benchmarking, *Nanomaterials* (2020) 10: 8”

Abstract

PtPd catalysts are state-of-the-art for automotive diesel exhaust gas treatment. Although wet-chemical preparation of PtPd nanoparticles below 3 nm and kg-scale synthesis of supported PtPd/Al2O3 are already established, the partial segregation of the bimetallic nanoparticles remains an issue that adversely affects catalytic performance. As a promising alternative, laser-based catalyst preparation allows the continuous synthesis of surfactant-free, solid-solution alloy nanoparticles at the g/h-scale. However, the required productivity of the catalytically relevant size fraction <10 nm has yet to be met. In this work, by optimization of ablation and fragmentation conditions, the continuous flow synthesis of nanoparticles with a productivity of the catalytically relevant size fraction <10 nm of >1 g/h is presented via an in-process size tuning strategy. After the laser-based preparation of hectoliters of colloid and more than 2 kg of PtPd/Al2O3 wash coat, the laser-generated catalysts were benchmarked against an industry-relevant reference catalyst. The conversion of CO by laser-generated catalysts was found to be equivalent to the reference, while improved activity during NO oxidation was achieved. Finally, the present study validates that laser-generated catalysts meet the size and productivity requirements for industrial standard operating procedures. Hence, laser-based catalyst synthesis appears to be a promising alternative to chemical-based preparation of alloy nanoparticles for developing industrial catalysts, such as those needed in the treatment of exhaust gases.

Introduction

For the treatment of exhaust gases of internal combustion engines, platinum group metals (PGM) supported on γ-Al_2O_3 are used as standard automotive catalysts [322, 323] for CO and NO oxidation. Here, it is essential to understand the activity and stability of such catalysts depending on their composition and particle size under realistic testing conditions [324]. The γ-Al_2O_3 support provides the advantages of a high BET surface and temperature stability under hydrothermal aging [325]. In literature, the discussion of the optimal particle

size is still ongoing and partially contradictory. For instance, Boubnov et al. compared catalysts with a Pt nanoparticle (NP) size in the range of 1.2–10 nm and found an optimal particle size of approximately 2 nm for the CO conversion [19] in line with the literature [326, 327]. However, results differ in the case of NO oxidation. For one, the highest activities were found at particle sizes of ~5 nm [19] and about 20 nm [328]. Graham et al. reported an increased activity for a decreased NP size and a maximal conversion rate at about 9 nm [329]. Thirdly, Xue et al. found the lowest light-off (LO) temperature and the highest maximum conversion rate to be at about 6 nm [330]. Aggravatingly, even if there would be a scientific agreement on the optimal particle size for a distinct reaction, the size of NPs does not remain constant during the lifetime of the automotive catalyst. Temperature changes during operation potentially lead to Ostwald ripening and, with further increasing temperature, coalescence [331–333]. Platinum nanoparticle catalysts are especially prone to these degradation processes because of the high mobility of platinum atoms under a reactive CO atmosphere [327], such that Ostwald ripening was observed in heated in situ transmission electron microscopy (TEM) studies in synthetic air [332]. Also, several research groups have reported a higher tendency of Pt NPs to form oxidized species, which reduces the adsorption of O_2 [23, 328, 334–337] and CO [338] and, thus, decreases catalytic activity [19, 334, 339]. Even though pure Pt shows the highest catalytic activity for oxidation reactions, alloying of Pd into Pt has been shown to suppress the Pt NP growth significantly [22, 23, 333] by trapping mobile platinum atoms at PdO sites [327, 329]. Hence, due to their better long-term stability, PtPd alloy nanoparticles are the current standard catalyst used in automotive exhaust after-treatment applications [340].

The elemental distribution (e.g. core-shell or solid solution) and alloy formation in chemical reduction methods are, amongst other factors, linked to the reduction potential differences of the mixed precursors [341, 342]. Therefore, laser ablation of mixed powder or alloy targets in liquid has emerged as a promising alternative to yield alloy nanoparticles (e.g., NiMo [343], AuPt [305, 308], PtCo [344], AuAg [274, 306], PtPd [309]). Generally, NPs with homogeneous elemental distributions are obtained by laser ablation synthesis of colloids when fully miscible compositions are being used [181]. Laser-generated colloids are free of surfactants, i.e., organic ligands, and electrostatically stabilized by high surface charge density due to partial oxidization and adsorption of anions added in micromolar concentrations [67]. Opposed to organic ligands, the inorganic ions do not decompose into carbon, which would cover the catalytically active surface, during calcination. The barrier-less adsorption of the surfactant-free nanoparticles yields heterogeneous catalysts in quantitative efficiency, which are highly active even without heat treatment [17, 27, 67]. The advantages and disadvantages of different heterogeneous catalysts are described e.g., in [345]. Furthermore, the presence of lattice strains in laser-generated nanoparticles and its favorable implication in electrocatalytic reaction has recently been reported for CuZn NPs

[346]. It can be assumed that lattice strains are also produced during the formation of other metal NPs due to the fast cooling conditions in the ablation plume [137].

Laser ablation in liquid has been shown to be economically favorable compared to chemical reduction synthesis when the nanoparticle productivity exceeds a material-specific value (0.5 g/h in the case of Au) [65]. Far higher productivities of 4 g/h were achieved by employing high-power 500 Watt picosecond laser ablation of platinum [68] and 1.6 g/h with a medium-power nanosecond laser system that provides the highest power-specific mass productivities of 13 mg h^{-1} W^{-1} [293]. Recently, even a power-specific productivity of more than 43 mg h^{-1} W^{-1} was found for low-priced 1 ns, 0.15 W compact lasers [70], inspiring the parallelized application of several small-scale lasers. Nevertheless, the laser pulse duration affects the nanoparticle formation pathways [137], typically causing broad size distributions in nanosecond laser synthesis [293] and bimodal nanoparticle size distribution in picosecond laser synthesis, which are typically around 5 nm and >20 nm, respectively [127]. Apart from the total nanoparticle mass productivity that is commonly discussed in the literature, the productivity of the catalytically important size fraction <10 nm is only ~30–60% of the overall productivity [293]. Hence, size quenching of laser-generated nanoparticles by in situ deposition on support particles added during laser ablation in liquid (LAL) [347, 348] and post-processing steps has become well established. The in situ size quenching strategy is limited to well dispersed support materials at low concentration in order to avoid scattering of the incoming laser light or excitation of the support material potentially triggering cross-effects by changing its structure/composition. In case of the latter strategy of post-processing, the desired size fraction (<10 nm) is either extracted from the initial colloid, e.g. by continuous tubular centrifugation [293, 349], or the larger fraction (>20 nm) is fragmented into smaller particles by laser fragmentation in liquid [188, 275, 350]. Tubular centrifugation has recently been shown to match the output flow rates of laser ablation (hundreds of mL/min), allowing it to be coupled to the ablation process downstream [349]. While laser fragmentation leads to a quantitative yield of nanoparticles <<10 nm, the throughput depends on the laser repetition rate and fluence [149]. Overall, literature shows that laser-generated NPs are not only of high interest as a catalytic material for exhaust gas treatment but also for the selective electrochemical reduction of CO_2 [346] and the oxygen reduction reaction [181, 344, 351, 352].

To that end, instead of only improving the overall mass-productivity, as done in previous scale-up oriented publications [68, 293], this study aims to specifically scale the laser ablation process regarding the mass yield of the desired small nanoparticle fraction <10 nm. Herein, a high power ps-laser system suitable for g/h-scale nanoparticle synthesis was used to demonstrate the increased mass yield of the small particle size fraction, despite the fact that focusing the laser into the liquid decreases overall productivity. This strategy allowed for g/h-scale production and high yield of the catalytic size fraction <10 nm for the first time. To

benchmark the heterogeneous catalysts gained from PtPd nanoparticles synthesized under the developed g/h conditions (regarding <10 nm size fraction), 2 kg of laser-generated PtPd/Al_2O_3 catalysts were prepared via adsorption of laser-generated nanoparticles to Al_2O_3. Honeycomb cordierite template structures were wash-coated with the catalyst, then core samples of automotive cordierite catalyst carriers were drilled out and used for catalytic runs. The performance and stability of these exhaust gas catalysts were tested in reference reactions of CO and NO oxidation within an industrial testing environment. It will be shown for the first time that the laser-generated catalysts prepared on the kg-scale show a comparable CO oxidation and even higher NO oxidation activity and stability when compared to a wet-chemically prepared reference catalyst and literature values, in an industrial test setting.

Methods and Materials

Pulsed Laser Ablation in Liquid

The size selectivity of the laser ablation synthesis was optimized by focal distance and laser parameter optimization in short time experiments, aiming at the parametrization of the in-process laser fragmentation-coupled laser ablation. In the second step, longer ablation times were applied, and the particle size-optimized colloids were supported on alumina (Puralox SCFa-90, Sasol, Germany)-and wash-coated on the catalyst carrier for oxidation catalysis testing. In the size selectivity studies, the Pt NPs were fabricated by employing a 500 W ps laser (Amphos flex500, Trumpf GmbH & Co. KG, Germany) in a continuously operating liquid flow setup, as described in [68] and sketched in Fig. 25A.

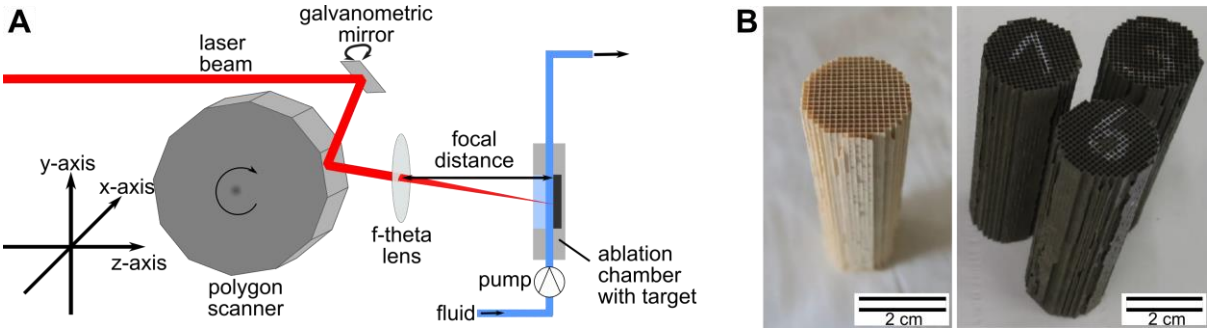

Fig. 25: (A) Experimental setup of the laser-based continuous synthesis of colloidal nanoparticles (NPs); the laser beam is moved by a galvanometric mirror (slow axis), with supersonic lateral speed by a polygon scanner (fast axis) and focused by an f-theta lens on the metal target placed in the flow chamber. (B) Blank (left) and wash-coated (right) cordierite carriers with 3 wt.% laser-generated PtPd NP/Al2O3 catalysts.

To maximize the yield of platinum nanoparticles with a diameter below 10 nm, the distance between the target and the focusing lens (100 mm f-theta lens) was optimized between

−2 mm and +2 mm, with 0 mm defined as focal distance of highest ablation rate. Here, a µm-precise translation stage was used while the applied laser pulse energy was held constant at 83.6 µJ with a 5 MHz repetition rate and 5 ps pulse duration. Laser fluence and laser intensity calculations can be found in the Supplementary Information (SI, Tab. S 6). To maximize the ablation efficiency and nanoparticle productivity, the laser beam was scanned with a nominal scan velocity of 500 m/s in the vertical direction using a polygon scanner system. High scanning rates are required to bypass the cavitation bubble while using MHz repetition rates and to minimize scattering of subsequent laser pulses by emerging cavitation bubbles [152]. Water containing 30 µM KOH for size quenching by electrostatic interaction [160] was constantly pumped through the ablation chamber at a flow rate of 360 mL/min to maintain steady-state conditions with a constant particle concentration and size. In the size control experimental series, ablation was conducted for a total time of 2 min, while sample collection started 30 s after the ablation process was initiated. This way, the ablation rate and, hence, productivity can be determined by differential gravimetry of the target before and after ablation. To investigate the effect of in-process laser fragmentation on the productivity of nanoparticles below 10 nm normalized to the number of applied laser pulses, the focal distance was set to +1 mm in the second experimental part. Consequently, the geometric focal plane was about 1 mm in front of the target and also inside the liquid under these conditions. At a fixed laser output power of about 400 W, the applied pulse energies were varied between 263 and 42 µJ by adjusting the repetition rate of the laser between 1.5 and 10 MHz. To that end, the overall nanoparticle productivity, as well as the productivity of nanoparticles below 10 nm, were evaluated as a function of the laser fluence (pulse energy) at a constant laser power. The hydrodynamic nanoparticle diameter was characterized by an analytical disk centrifuge (CPS DC24000, CPS Instruments Inc., Netherlands). This in-process strategy, aimed to influence the particle size, was validated for laser ablation of a Pt (AGOSI Allgemeine Gold- und Silberscheideanstalt AG, Germany) and PtPd alloy target ($Pt_{0.66}Pd_{0.33}$ molar composition, 3.66:1 by mass).

Preparation of PtPd Catalysts and Catalytic Testing

For catalytic testing, NPs were prepared under conditions of high nanoparticle productivity, referring to the size fraction <10 nm, and laser parameters set to 400 W, 5 ps, 1.5 MHz, and 3.0 J/cm^2. The colloid was centrifuged using a continuously operating tube centrifuge (LE GP, Carl Padberg Zentrifugenbau GmbH, Germany) to remove the particle fraction >15 nm, in line with [293]. The large nanoparticle fraction is retained by a PTFE foil, removed from the foil, and then re-dispersed. Thus, three different catalysts were prepared from the laser-generated particles: the size-optimized monodisperse smaller NPs (later referred to as “supernatant”), the re-dispersed larger NPs (“re-dispersed”), and the non-centrifuged bimodal sample (“raw colloid”). Additionally, a “reference” catalyst, was prepared using an established

wet impregnation process. The Feret diameter of more than 100 particles per sample was measured with ImageJ. The resulting data were fitted by a log-normal distribution.

Surfactant-free, laser-generated colloidal nanoparticles are easily adsorbed on a catalyst support by tuning between the diffusion-deposition and dielectrophoretic deposition regime via pH adjustment during stirring [181]. For the exhaust catalyst preparation from the laser-based $Pt_{0.66}Pd_{0.33}$ NP colloids, the γ-Al_2O_3 white wash coat was mixed with the respective laser-generated nanoparticle colloidal suspension with pH adjustments according to general procedures [17, 67, 353]. The quantitative adsorption of nanoparticles was verified as a transparent, nanoparticle-free supernatant. The mass load of $Pt_{0.66}Pd_{0.33}$ NPs on γ-alumina, which was also used for the reference catalyst preparation, was set to 2.5–3 wt.%. The mass load was confirmed by inductively coupled plasma optical emission spectrometry (ICP-OES) measurements (see Fig. S 8 and Tab. S 7). The sample prepared from the supernatant obtained a slightly smaller mass-load of 2.23 wt.%. For the reference catalyst, the platinum and palladium precursor solutions were added in calculated amounts following a standardized industrial recipe. Examples of wash-coated cordierite carriers with 3 wt.% laser-generated PtPd NP/Al_2O_3 catalysts are shown in Fig. 25B. In all cases, the wash coat load was 100 g/L. The catalysts were calcined at 550 °C for 2 h.

Catalytic tests were performed with three laser-generated NP catalysts with different PtPd NP sizes and the wet-chemically prepared reference. CO and NO oxidation were investigated in the temperature range of 75–500 °C with a temperature ramp of 15 K min^{-1}. The reaction gas contained 500 ppm CO, 167 ppm H_2, 600 ppm (as C_1) C_3H_6, 200 ppm (as C_1) C_3H_8, 60 ppm (as C_1) C_7H_8, 140 ppm (as C_1) $C_{10}H_{22}$, 150 ppm NO, 10% H_2O, 13% O_2, and 5% CO_2 with the balance N_2 at a space velocity of 37,500 h^{-1}. To simulate the long-term performance and evaluate the catalyst stability, the catalyst-coated cordierite carriers were also tested in a second run after hydrothermal aging at 750 °C for 16 h.

Results and Discussion

Determination of Laser Parameter Influence on the Nanoparticle Size Fraction <10 nm

The focal plane position is an essential scaling parameter for the nanoparticle productivity in laser ablation [29]. Herein, the focal position determines the nominal laser fluence applied to the target surface, where the lower fluence limit is given by the ablation threshold fluence. In turn, the upper economically feasible limit is generally constrained by the limited penetration depth of the laser light into the material or the decomposition of the liquid due to non-linear effects (e.g. filamentation) when exceeding the required threshold intensity. The latter is on the order of hundreds of GW/cm² to TW/cm^2 [78, 354] for ps pulses in water and is substantially lowered if nanoparticles are present in the beam path. To that end, when changing the distance between the focusing lens and target (see sketches in Fig. 26C) the highest laser fluence and the focal plane, respectively, are either located inside the liquid

medium or on the target surface. In the case of the focal plane shift, a maximal intensity of about 230 GW/cm² and, in the case of pulse energy variation**,** a maximal intensity of approximately 460 GW/cm² were reached in these experiments. Although the lower thresholds of colloids compared to pure water are likely to be exceeded in our experimental conditions, the calculation of these complex concentration- and size-dependent effects are out of the scope of the present application-oriented study and will not be discussed further. Moreover, clear trends related to pulse energy and focal distance variation were observed.

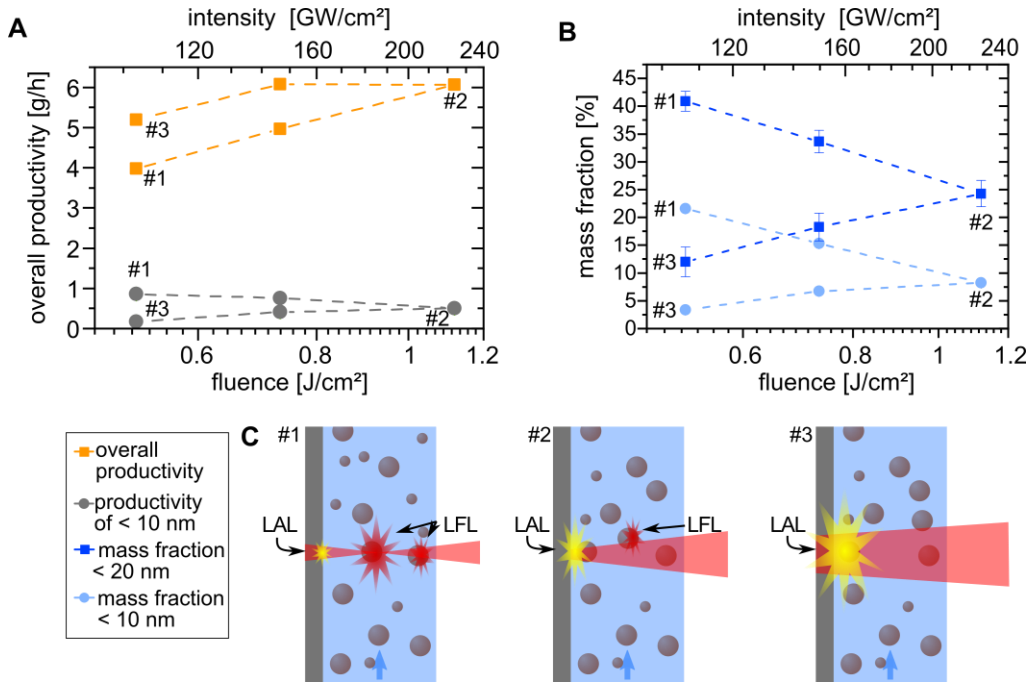

Fig. 26: Influence of the applied laser fluence due to the change in the focal plane position on (A) the overall productivity (orange squares) and the productivity of the mass fraction of platinum particles smaller than 10 nm (gray circles) and (B) the mass fraction of NP <20 nm (blue squares) and <10 nm (light blue circles). (C) The sketches are related to the three different focal positions and indicate the change of laser ablation in liquid (LAL) and laser fragmentation in liquid (LFL) during focal plane shift.

When the laser spot lied inside the liquid (Fig. 26C, #1), the effective laser fluence on the platinum target surface was low. Shifting the focal plane towards the target surface increased the laser fluence on the surface, reaching its maximum when the focal plane was located directly on the target surface (Fig. 26C, #2). Note that a maximum laser fluence does not naturally coincide with a maximum in nanoparticle productivity, as theoretically predicted by Neuenschwander et al. [198] and experimentally proven by Streubel et al. [68], while maximum productivity correlates with an optimal laser fluence on the target surface [68, 198]. Further reduction of the distance between the lens and target virtually shifted the spot behind the target, so that the fluence on the target surface decreased again (Fig. 26C, #3). Interestingly, although the laser fluences of points #1 and #3 were nominally equal, the

overall ablation rate was higher when the laser spot was virtually located behind the target. Waag et al. recently observed similar results for the picosecond laser ablation of nickel in water and found a decrease of the target temperature and an increased nanoparticle yield (ablation-cooling) in a similar case to that of position #3 and vice versa in the case of position #1 [156]. Complementing the discussion of Waag et al., in our study, we additionally suggest that a fragmentation process occurred in the case of #1. This is supported by the significantly increased mass fraction of particles <10 nm at #1 and consequently higher productivity of the mass fraction <10 nm, reaching more than 0.8 g/h (see Fig. 26B). In turn, in the case of #3, the relative yield and absolute productivity of small particles were significantly lower. Here, the laser-induced fragmentation was strongly reduced as the fluence inside the liquid layer was the smallest for #3 (see Fig. 26A, C). Post-irradiation effects of nanoparticles generated by previous pulses are likely since the average residence time of the nanoparticles inside the flow chamber is in the range of 1.5 s, which equals $7.5 \cdot 10^6$ laser pulses per volume element at the given repetition rate of 5 MHz. Hence, laser fragmentation is as expected more pronounced when the laser spot is located inside the liquid (#1). In turn, due to the fragmentation process, less laser energy reaches the target so that the overall platinum nanoparticle productivity is lower in #1 compared to #3 although similar nominal laser fluences are being applied.

For the ablation of the $Pt_{0.66}Pd_{0.33}$ target, the same trend in the productivity of total mass as well as the catalytically relevant nanoparticle size fraction below 10 nm was found (Fig. S 9). Interestingly, when comparing the maximal ablation rate for Pt and $Pt_{0.66}Pd_{0.33}$, the ablation rate correlates with the material density [91] so that a similar volume-related ablation rate of about 0.27 cm³/h was found for both (see Fig. 26 and Fig. S 9).

To verify the beneficial effect of in-process laser fragmentation on the productivity of smaller particle size fractions, the applied laser fluence was held constant, while the mean residence time of NPs in the irradiated volume was varied from 0.7–2.6 s by varying the liquid flow rate and using the $Pt_{0.66}Pd_{0.33}$ ablation target. By increasing the flow rate, a lower mean residence time of the NPs in the ablation chamber and, thus, a lower in-process laser fragmentation effect should be expected. In other words, a higher fraction of particle sizes below 10 nm is expected when the flow rate is decreased, as the mean residence time and number of post-irradiating laser pulses are increased (from $3.7 \cdot 10^6$ to $12.8 \cdot 10^6$ pulses per volume element). The experiments were conducted at position #1 (Fig. 26C) where high fluences were applied into the liquid and laser fragmentation was expectedly pronounced. As indicated in Fig. 27, the NP mass fractions (<10 nm and <20 nm) in the liquid correlate with the residence time, validating that in-process laser fragmentation triggered a significant increase in size selectivity of the laser synthesis process, although absorption cross-section and absorption efficiency of the platinum nanoparticles were low at infrared laser wavelengths [355].

With the previously described effect of focal distance and residence time on the size-selected nanoparticle productivity, the following question arises: how do the laser fluence (proportional to pulse energy at constant spot diameter) and the repetition rate affect the size fraction <10 nm? For the given laser system, due to $\bar{P} = E_P \cdot f_R$, the repetition rate (f_R) and laser pulse energies (E_P) are anti-proportional at a constant mean laser power ($\bar{P}$). Again, the working distance at position #1 was chosen as the highest productivity of the mass fraction <10 nm found at this position (see Fig. 26A). The total productivity change as well as the size-selective productivity of mass fractions of <10 nm and <20 nm particles with increasing pulse energy (laser fluence) are summarized in Fig. 28, respectively. Note that the overall ablation rate decreases although the ablation rate per pulse increases (Fig. S 10A). In contrast to the initial expectation, the productivity of NPs <10 nm (Fig. S 10B) remained constant at about 1.2 g/h, while the overall productivity decreased with increasing laser fluence and decreasing repetition rate (Fig. 28). The latter observation agrees well with results from Streubel et al., where the optimal laser fluence for high repetition rate (10 MHz) is in the range of 0.3–0.4 J/cm^2, similar to the fluence used at 10 MHz in this study (0.37 J/cm^2) [68]. In turn, for the lowest repetition rate and highest fluence (1 MHz and ~2.4 J/cm^2) in Fig. 28, the fluence is about two times higher than the optimal value found by Streubel et al. for the same repetition rate (~1.2 J/cm^2) [68]. Although the absolute production rate of the Pt NPs <10 nm did not change (compare Fig. S 10B), their relative mass fraction in Fig. 28 significantly increased with laser fluence by a factor of more than two (compared to the same conditions at #1 in Fig. 26B).

Apart from the effect of laser fluence discussed, the decrease in the repetition rate also comes along with an increase of the lateral interpulse distance so that the pulse overlap is lowered [152]. When calculating the lateral pulse overlap from the repetition rate, focal diameter, and scan velocity, subsequent pulses obtained an overlap of about 65% for the highest repetition rate of 10 MHz at a fluence of 0.4 J/cm². For the smallest repetition rate of 1.5 MHz at 2.3 J/cm², no overlapping of consecutive pulses is expected. This difference in pulse overlap is sketched in Fig. 28.

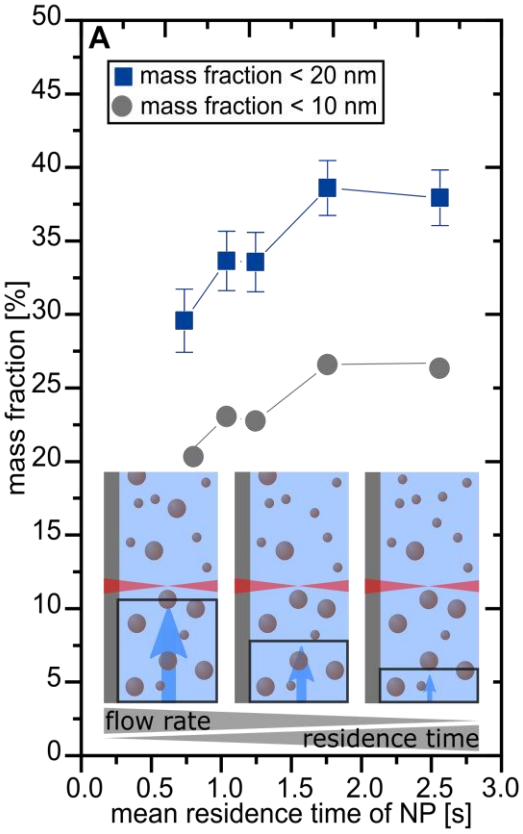

Fig. 27: Variation of the mean residence time and the resulting mass fraction of particles <10 nm (gray circles) and <20 nm (blue squares); the sketches show how the irradiated volume decreases with increased residence time.

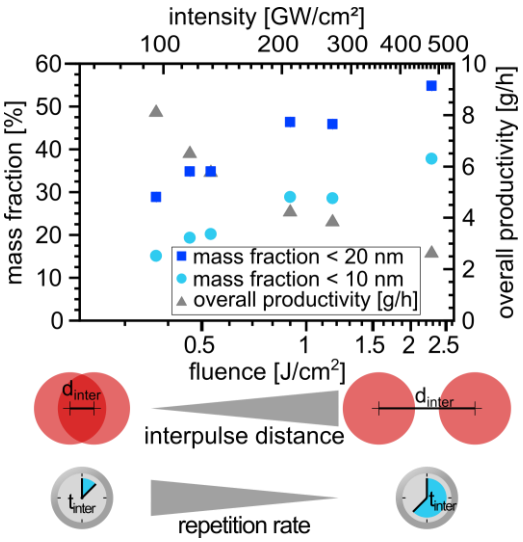

Fig. 28: Influence of laser fluence on the mass fraction of Pt NPs <10 (light blue circles) and <20 nm (blue squares) and the overall productivity (gray triangles). The sketch below the graph indicates the change in the lateral interpulse distance d_{inter} as well as the repetition rate (inverse temporal interpulse distance t_{inter}) with changing pulse energy at constant laser power.

Moreover, the interpulse delay (sketched in Fig. 28), which is the time between two consecutive pulses, changed from 100 ns at 0.4 J/cm² to 700 ns at 2.3 J/cm². Due to these short time scales and the high scanning speed, the interaction of subsequent laser pulses with the cavitation bubble is unlikely. Our results indicate that a short temporal delay between two subsequent laser fragmentation pulses is beneficial to increase the yield of fragmentation. Note that fluence and interpulse delay are directly proportional so that one laser pulse fired every 700 ns with 2.3 J/cm^2 nominally delivers the same cumulative energy to nanoparticles present in the laser's pathway as seven pulses every 100 ns with 0.4 J/cm^2. These observations emphasize that both the repetition rate and laser pulse energy are determinants for NP size control, particularly for MHz lasers with hundreds of nanosecond pulse delays. It is worth mentioning in this context that Plech et al. recently investigated the structural kinetics of picosecond laser fragmentation of colloidal nanoparticles in situ at time-resolved 80 ps resolution X-ray scattering. The authors reported that 54 nm Au spheres were fragmented into significantly lower particle sizes of 2–3 nm and were detected within 30 ns. Growth of the fragmented particles was observed during the first hundreds of nanoseconds, being arrested on the microsecond time scale if anions were added before laser fragmentation [356]. This indicates that the LFL process (at least of 54 nm Au) could take hundreds of nanoseconds to be completed. In other words, the interpulse delays should be long enough to allow conversion of the educt NPs into fragmented products, avoiding energy input into particles that are about to downsize from the previous pulse. Looking beyond these short time scales, barrier-less growth of the resulting ultra-small primary fragments has been observed for Pt nanoparticles after laser fragmentation, which could be suppressed (or at least slowed down) by the addition of anions [160]. Both studies [160, 356] point out that particle growth quenching by anions is a perspective to further increase the yield of small particles and that the interpulse delay effects need further investigation, especially for the MHz repetition rate LFL.

Moreover, further study is also suggested for the variation of the fluence by changing the repetition rate and the pulse energy and whether high productivity of the desired mass fraction (high fluences) or high overall productivity (low fluences) is more reasonable for the application in mind. As has been systematically shown here, both can be optimized by adjusting the focal distance (located slightly in front of the target) and the laser fluence at maximum power, enabling g/h productivity. Our findings show that for the used high power (400 W) MHz-ps-laser system, the mean productivity for the catalytically important size fraction of Pt NPs <10 nm was found to be about 1.2 g/h, while the mass fraction selectivity towards small particles was freely adjustable between 5% and 40%. This size selectivity was realized by balancing between the in-process fragmentation (downsizing) and ablation (overall productivity) particle formation pathway. Further improvement of the mass fraction

under a g/h-scale premise, e.g., via wavelength adaption and anion concentration variation, may be subject to follow-up studies.

Examination of the Catalytic Activity of Laser-Generated PtPd Nanoparticles

To evaluate the catalytic activity of nanoparticles synthesized under these established conditions and tested in an industrial environment, laser-generated alloy $Pt_{0.66}Pd_{0.33}$ NPs were synthesized with 2.7 g/h overall and 0.9 g/h <10 nm productivity. The laser-generated nanoparticles were synthesized with the focal plane in the liquid, resulting in about 32 wt.% of <10 nm particles (see Fig. S 9). Through centrifugation, both fractions were separated at a 10 nm cut-off diameter to prepare catalysts containing only particles <10 nm, >10 nm, or the initial mixture of both before centrifugation (see Fig. S 11 to Fig. S 13 for more information on the NPs). In this way, NP size effects on the catalytic activity of nanoparticles stemming from the same process may be studied in addition to benchmarking with chemically prepared particles. Subsequently, the NP were supported on γ-Al_2O_3 with 3 wt.% load. Additionally, a reference catalyst was prepared by a wet-chemical approach. Fig. 29A shows the number-weighted particle size distribution of the heterogeneous catalyst after the supporting step, as measured by TEM. The wet-chemical reference catalyst obtained a mean particle size of 2.5 nm (“reference”), whereas the laser-generated catalyst based on the raw colloid without post-processing steps achieved an average particle size of 8.1 nm (“raw colloid”). In comparison to the raw colloid, the catalysts generated with the optimized laser-generated monodisperse small particle fraction (“supernatant”, after centrifugation) and the separated big particle fraction (“re-dispersed”, after centrifugation) resulted in sizes of 4.4 and 18 nm, respectively.

The catalytic test results for the CO oxidation are shown in Fig. 29B. Tab. 7 summarizes the temperatures at which 50% of the CO was converted during the temperature increase (temperature of 50% conversion, T_{50}CO) for fresh and aged states. The fresh laser-based catalyst bearing the small particle fraction showed the best performance of all catalysts with a T_{50}CO of 97 °C, compared to 117 °C for the wet-chemically synthesized reference. Due to the larger NP size, the catalyst made of the raw colloid delivered comparable activities in the first (T_{50}CO value around 168 °C) and the second runs, indicating good stability.

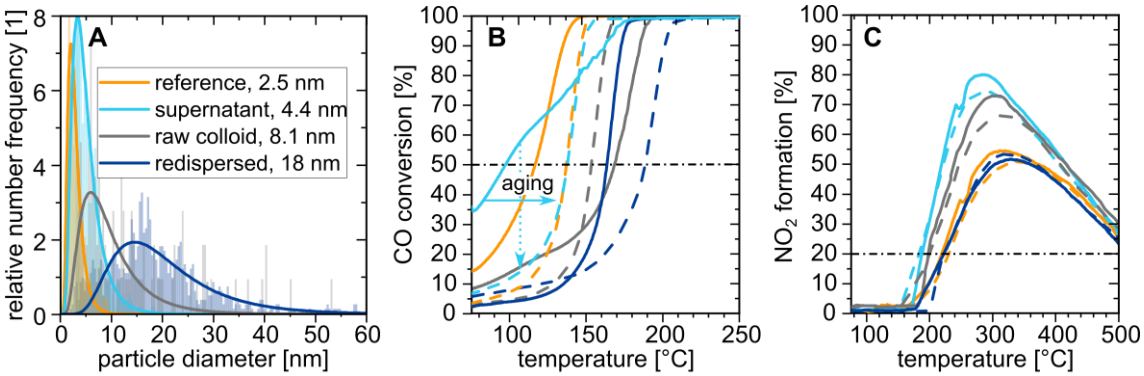

Fig. 29: (**A**) Size distribution of the alumina-supported PtPd NPs, where the bars are the result of the transmission electron microscope (TEM) image analysis, and solid lines are the resulting log-normal fits; temperature-dependent (**B**) CO and (**C**) NO oxidation of the different PtPd catalysts. Solid lines present the first conversion run, the dashed lines are the conversion after hydrothermal aging, and the horizontal, black dotted-dashed line are the conversion at 50% and 20%, respectively. In **B**, the conversion rate change after aging is marked by two arrows, where the trend indicated by the solid arrow is valid for all curves, and the trend marked by the dotted arrow is only found for the small-sized catalysts.

The T_{50}CO for the reference and laser-generated small particle fraction catalysts exhibited increases by 20 K and 41 K in the run after hydrothermal aging, respectively. The disappearance of the shoulder in the first run possibly indicated absence of defects on the NP surface. For both larger-sized catalysts, the shoulder in the first catalytic run cannot be seen, which agrees with [181] that surface defects especially occur on small NPs. Note that it has recently been reported that laser-generated (palladium) nanoparticles have a higher catalytic activity than chemically prepared ones due to high defect densities caused by the kinetic-controlled nature of the synthesis process [351], at least before aging. Despite this increase in the T_{50}CO and catalytic activity, the laser-based and reference catalysts revealed a similar activity after aging. Therefore, both catalysts appear to converge into similar final states. Grunwaldt et al. compared the CO/NO oxidation performance and hydrothermal aging of Pt/Al_2O_3 catalyst from five different preparation methods, where a superior hydrothermal resistance of the laser-generated catalyst at 500 °C was shown. However, due to small initial interparticle distances, the particle size distribution increased considerably at high temperatures [324].

Fig. 29C displays the plot of NO oxidation with maximal possible NO_2 formation of 100%, the temperature at 20% conversion (T_{20}NO), as well as the maximal conversation of NO. For the NO oxidation, the chemically prepared catalyst showed the strongest aging behavior with an increase in the T_{20}NO of about 11 K. The activity of the small particle size catalyst (supernatant) on the other side was resistant to hydrothermal treatment, displaying the best overall activity of the tested catalysts with a T_{20}NO of about 183 °C after aging. All size-dependent catalytic activities after aging are illustrated in Fig. 30. Additionally, the catalytic

results from other studies with comparable synthesis methods, reaction gas composition, and catalyst loading are described below and in Fig. 30.

Although an optimal NP size could be determined for CO and NO oxidation from Fig. 30, it should be noted that the aging behavior of the different catalysts is not presented. In some of the presented studies, e.g. [329], aging has been used to alter the particle sizes. By comparing the size dependency of the NO_2 formation for the different studies, it can be suggested that laser-generated particles perform equally well in CO and NO oxidation, similar to chemically prepared catalysts. When comparing the maximal conversion after aging, all laser-generated samples showed a higher maximal conversion of NO and yield of NO_2. Thus, these catalysts possess a significantly higher selectivity in NO conversion, which is hypothetically linked to the particular defect-rich surface of the laser-generated PtPd nanoparticles [181, 346]. The influence of different crystal structures of laser-generated Pd catalysts was experimentally demonstrated and theoretically explained by density functional theory calculations [351]. In our work, for the first time, the results in Fig. 30 indicate benchmark performance of the laser-generated catalysts in both CO and NO oxidation. Yet, it should be noted that the potential contribution of the crystal structures or defect density of laser-generated compared to chemically synthesized catalysts requires further study.

In summary, the performance of a chemically prepared reference catalyst and three different laser-generated catalysts during NO and CO oxidation were examined and compared with literature. Results reveal that small-sized catalysts are prone to aging during CO oxidation but the small-sized laser-generated catalysts show comparable conversion rates with the reference catalyst. During NO oxidation, laser-generated catalysts, although larger than the reference catalyst, display higher conversion rates, even after hydrothermal aging. The reason for the higher activity of laser-generated NPs will be investigated in a future work.

Tab. 7: Comparison of the T50CO and T20NO for the fresh and aged catalysts.

.	T_{50}CO (°C)		T_{20}NO (°C)		maximal NO conversion (%)	
	fresh	aged	fresh	aged	fresh	aged
reference, 2.5 nm	117	137	219	230	55	51
supernatant, 4.4 nm	97	138	188	183	80	74
raw colloid, 8.1 nm	168	153	198	200	73	66
re-dispersed, 18 nm	163	188	222	223	52	54

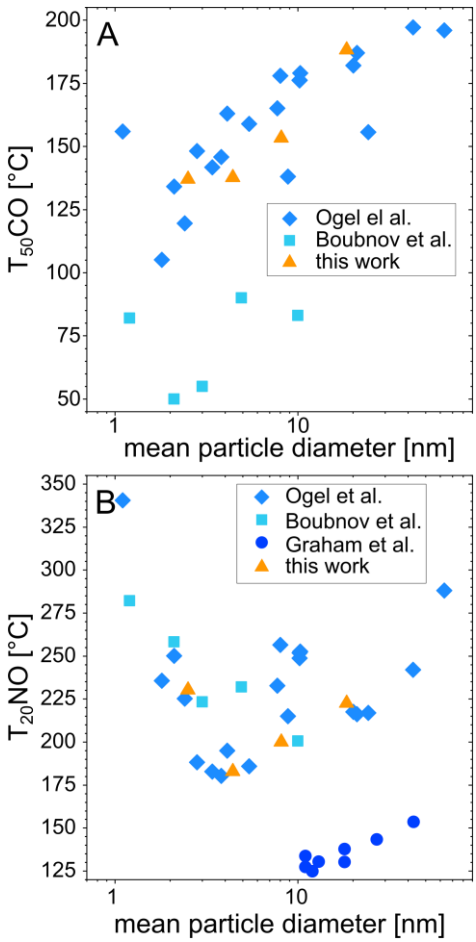

Fig. 30: Size dependency of the (**A**) CO and (**B**) NO conversion of laser-generated catalysts; the orange triangles represent the conversion temperatures determined in this work and the blue data points are taken from the literature [19, 324, 329, 357].

Conclusion

The development of automotive diesel oxidation catalysts in an industrial environment requires syntheses which deliver supported alloy nanoparticle wash coats, e.g. PtPd/Al_2O_3, in kg-scale. Coating honeycomb cordierite carriers with the wash coats allows catalytic testing under standard exhaust gas treatment conditions. The employed nanoparticle syntheses need to operate at the g/h-scale to meet the demanded quantities of heterogeneous catalysts. For example, 1 kg of 3 wt.% PtPd supported on alumina requires about a week (30 h of 1 g/h) laser synthesis. Considering that nanoparticle sizes below 10 nm are required to enable high catalytic activity, the operation conditions that allow the g/h-scale laser synthesis of colloidal Pt nanoparticles <10 nm were investigated by tuning the size selectivity of the continuous high-power laser ablation method. It was determined that the tuning of in-process fragmentation during laser ablation is the main parameter to meet the requirements for industrial catalyst screening studies.

When shifting the focal plane of the laser beam into the liquid layer slightly above (1 mm) the ablation target, the mass yield of NP sizes <10 nm and the absolute productivity of this

fraction significantly increased. This downsizing effect can be explained by an increased mean laser energy deposited in the liquid volume containing nanoparticles produced by previous laser pulses. Consequently, when the laser beam focus was located within the liquid, a higher fragmentation rate of the undesired larger Pt nanoparticle size fraction occurred, which increased the mass yield of nanoparticles below 10 nm. By increasing the laser fluence while maintaining the laser spot slightly in front of the target, the mass fraction of the small-size NP fraction increased. Moreover, reducing the volume flow rate or, in other words increasing the residence time by a factor of five, improved the mass-share of Pt nanoparticles <10 nm by more than 25%. Under these conditions, the laser fragmentation also appeared to benefit from increased temporal pulse delay, at least for the investigated MHz repetition rate scale, supported by recent literature findings on the structural kinetics of laser fragmentation. This interesting temporal effect on pulsed laser fragmentation deserves further dedicated studies. Overall, the optimized parameters allowed a continuous laser synthesis of 1.2 g/h Pt and 0.9 g/h $Pt_{0.66}Pd_{0.33}$ nanoparticles <10 nm, respectively, referring to the mass of particles below 10 nm. This equals to about 2.4 kg of 0.3 wt.% alumina-supported catalyst in an 8 hour shift. After colloidal deposition of laser-generated PtPd alloy particles on alumina and coating of cordierite carriers with the former, CO/NO oxidation performance tests were conducted under conditions relevant for applications. The performance of the laser-generated catalysts was equal to that of the industrial reference and results from the literature. The laser-generated NPs even showed superior NO conversion behavior with better resistance against hydrothermal aging compared to the chemically prepared reference catalyst. The origin of the higher resistance and conversion rate may be related to the reported higher compressive strains found in laser-generated Pd nanoparticles, but this estimation requires a deeper defect-based investigation of the catalyst before and after aging as well as by analytical operando studies in the future.

4.2.2. Influence of ~2 ns laser ablation in liquid process parameters on the nanoparticle properties for gold, silver, and platinum

Wholesome parameter studies for ~ 2 ns laser are missing in the literature, although this laser pulse duration promises high-efficiency LAL. Therefore, the influence of the focal position and the liquid flow rate on the productivity are examined. Subsequently, the laser beam focusing, the pulse energy, and the liquid flow rate are combined to the volume-specific energy dose, and its influence on the NP size is analyzed. Lastly, the impact of ablation time and storage time on the NP properties is examined.

Focal position and target thickness

In laser ablation in liquid, the productivity increase has been one of the main challenges in recent years [273], which was successfully addressed by increasing the laser power [32, 68]. However, the laser power usually scales with the purchase price of the laser system [358]. A more cost-efficient approach for increasing productivity is the decreasing of the laser spot size in the target surface and, thus, and increasing the fluence on the target surface [206, 359]. The fluence increase can be realized by applying stronger focusing conditions or varying the target position relative to the focal plane [360]. However, this shifting of the focal plane does influence not only the productivity but also the NP size. When shifting the focal plane from behind the target into the liquid layer, the NP size decreases [294, 295], which is attributed to an increased fragmentation rate due to the point of highest fluence in the liquid layer [225] and often at the expense of NP productivity [225]. The optic chosen for focusing the laser beam determines the minimal achievable spot diameter for a Gaussian beam according to Eq. 10, and the Rayleigh length according to Eq. 11 [361]. Here, w_0 is the beam waist, λ the laser wavelength, and f the lens' focal length. The former determines the maximal fluence and, consequently, the maximal productivity, and the latter the divergence of the laser beam waist around the focal plane. For larger Rayleigh lengths, the deviation of the laser beam diameter from the optimal diameter is lower. Thus, the fluence change due to a focal plane shift is weaker.

$$w_0{}' = \lambda \cdot f \cdot \pi^{-1} \cdot {w_0}^{-1} \qquad \text{Eq. 10}$$

$$z_R' = {w_0}'^2 \cdot \pi \cdot \lambda^{-1} \qquad \text{Eq. 11}$$

For the studied automated LAL device, based on a compact ~ 2 ns laser, the maximal laser power is limited to 500 mW. The distance between the focusing optic and the ablation chamber is kept constant during the ablation process. Consequently, material removal leads

to an increased distance between the lenses and the target surface. This distance is measured between the lenses' center and the ablation target surface and will be referred to as lens-target distance in the following. When choosing and adjusting the focusing optic for the automated device, two aspects need to be considered. On the one hand, the laser spot should be as small as possible to enable high NP productivity. On the other hand, the Rayleigh length should be as large as possible to ensure minimal productivity drift for increasing lens-target distances. This time-dependent productivity drift was demonstrated by Labusch et al. [360]. In this study, the productivity decreased to zero after 412 min but remained constant when the target position was adjusted during the experiment.

For the automated LAL device, possible lens-target distance is determined by the range where at least 90 % of the maximal productivity is reached. This range then determines the maximal possible target thickness. Thus, a large Rayleigh length of the lenses allows thicker targets and enables longer production times with the same target. However, according to Eq. 10 and Eq. 11, smaller spot sizes are achieved using lenses with a short focal length, leading to a shorter Rayleigh length. Consequently, for the automated device, aiming at several hours of continuous LAL, a compromise between intense focusing and long ablation times needs to be found.

In a preliminary study (appendix 8.2.3), a combination of two lenses with a focal length of 100 mm each and combined 50 mm shows the best result regarding productivity, target thickness, and price. This setup is adapted to the eMOPA1064-500 laser system (CryLaS GmbH, Berlin, Germany). Additionally, the NP size and colloid stability in dependency on the focal distance are examined to set the optimal target thickness and lens-target distance of the device. The thickness and distance are determined by measuring the extinction for Ag, Au, and Pt colloids at different lens-target distances and normalizing the results to the maximal extinction.

The colloids' maximal extinction is found for a lens-target distance of 52.0 – 52.5 mm for all three materials (Fig. 31), which is larger than the theoretical focal distance of 50 mm of the lenses. This deviation can be explained considering the refraction difference in air and water and the lens setup. A focal distance for ablation in air is shifted to larger distances due to laser beam refraction. Calculations result in a distance of the center of the lenses and target surface of 51.9 mm in air and 53.1 mm in water to achieve the highest laser fluence (see appendix Fig. S 16), which agrees well with the experimental determination of the laser fluence (see inset in Fig. 31 A). However, this distance is different from the distance of highest productivity, which can be explained by the optimal material-specific laser fluence for material removal [198]. Also, the variation of the optimal focusing distance for Ag, Au, and Pt is connected to their different ablation thresholds, which gives the optimal fluence for ablation according to $F_{opt} = F_0 \cdot e^2$ [198]. Similar ablation threshold fluences for Ag and Au of 3.7 J/cm² for single pulses and 9 ns pulse duration are reported [107]. Since multiple pulses

and short pulse durations are applied in this case, the threshold fluence is expected to be significantly lower [114, 362]. Moreover, the thermal conductivity of Pt is about 4.5 times lower than of Au, leading to a lower threshold fluence than for Au and Ag [107].

In Fig. 31, the concentrations of at least 90 % of the maximal concentration are marked by the horizontal, green areas. The respective lens-target distances are marked (vertical green lines in Fig. 31 B). Subsequently, the maximal target thickness is the difference between the maximal and minimal marked lens-target distance. Especially for Pt, the lens-target distance covers a broad range from 51.3 – 52.8 mm. Generally, the limits are chosen to be identical for all three materials, whereby Au reveals the smallest range and limits the target thickness to 0.5 mm. The initial lens-target distance is set to 52.0 mm for the automated device and approaches 52.5 mm due to material removal during the ablation process.

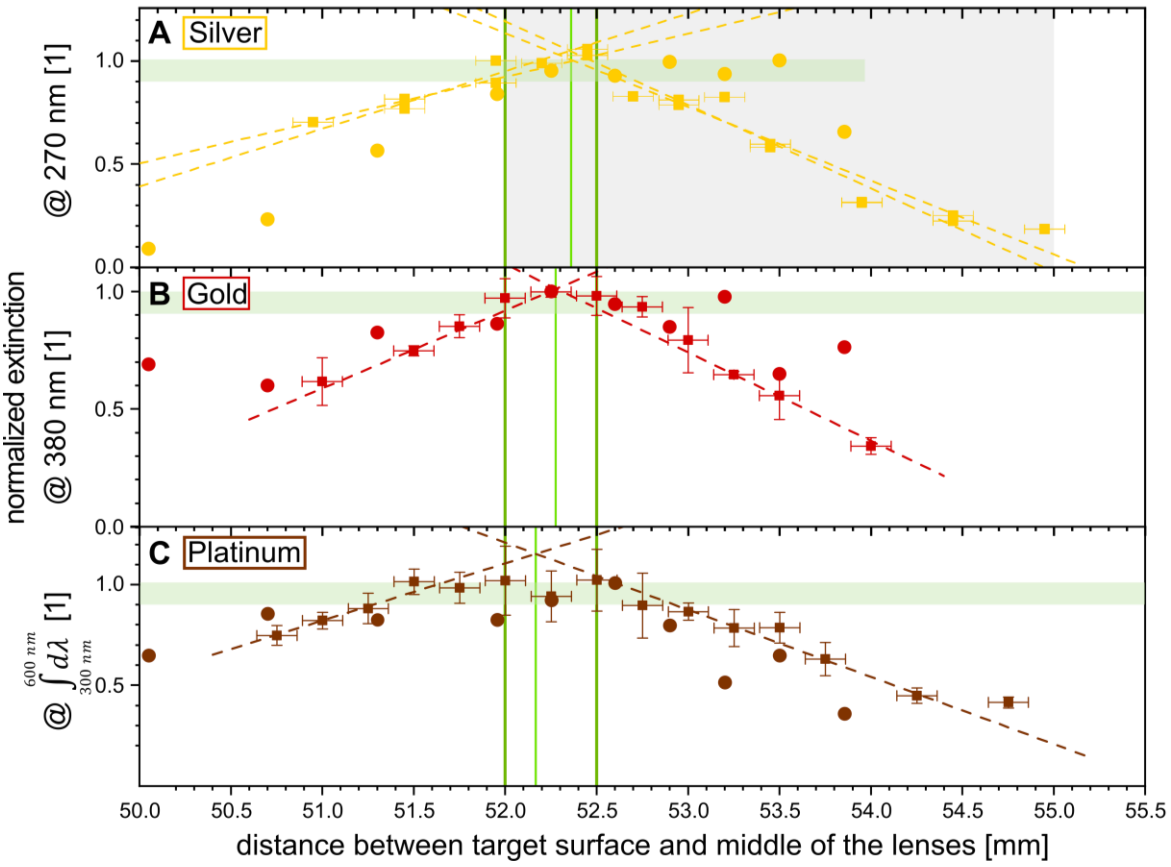

Fig. 31: Influence of the lens-target distance on the colloid extinction for Ag (A), Au (B), and Pt (C). The maximal extinction for each material is marked by the light green vertical line, and the green shaded areas mark extinctions of at least 90 % of the maximal extinction; the gray-shaded area in A is analyzed concerning the laser fluence for the distance in Fig. 33; the dark green vertical lines mark the determined minimal and maximal lens-target distances for the automated LAL device; the circles symbolize results obtained with the final setup, whereas squares mark results from preliminary studies.

For the ablations with a fully automated device, the targets need to be positioned in capsules. Their dimensions are set to 10 x 5 x 0.5 mm (length x width x thickness) so that the maximal material for ablation with one capsule is fixed. The resulting capsule capacities are summarized in Tab. S 9 in the appendix.

The NP hydrodynamic mass-weighted size distribution is analyzed within the chosen lens-target distance since a constant colloid quality, i.e., NP size, should be ensured throughout a target capsule lifetime. For comparison, the colloid quality, the fractions of NPs <10 nm and <20 nm, and the NP diameter of the size distribution peak are extracted from the size distribution (see appendix section 8.1). As shown in Fig. 32, the mass fraction <10 nm and <20 nm (A-C), as well as the mass-weighted peak maximum (D-F), only vary within the standard deviation of the measurement between 52.0 and 52.5 mm, proving high robustness of the automated LAL. The inset in Fig. 31 shows that the focal plane of the laser lies behind the target surface in this range. Thus, the interaction between the laser beam and the emerging NPs is minimized [225]. The laser fluence on the target surface changes from 5.8 to 7.5 J/cm² within the 0.5 mm range (see section 4.1.2). In the same range, the mean fluence in the liquid layer ranges from 0.77 to 0.93 J/cm², and the fluence at the chamber entrance measures less than 0.1 J/cm². The difference between the fluence on the target surface and the mean fluence are explained in the appendix (section 8.1).

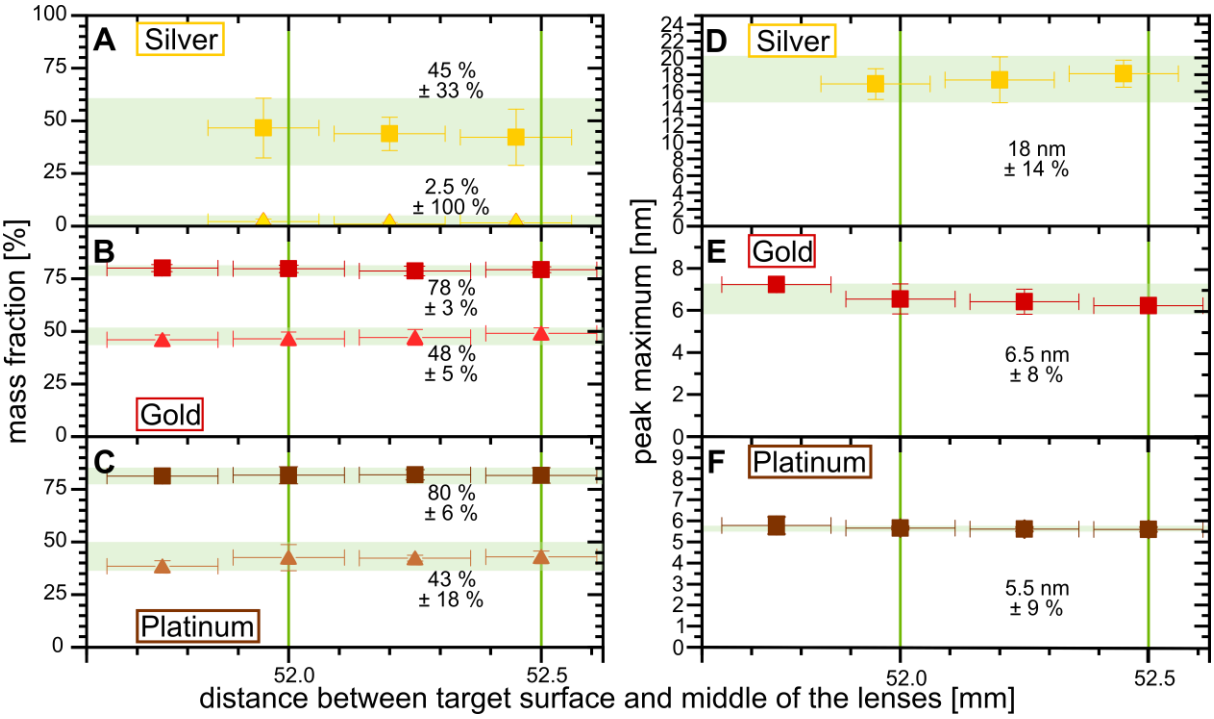

Fig. 32: Influence of the lens-target distance on the mass fractions (A-C) <10 nm (triangles) and <20 nm (squares), and the peak maximum (D-F) for Ag (A, D), Au (B, E), and Pt (C, F); the green shaded areas mark the maximal size variation for lens-target distances between 52.0 and 52.5 mm, which are marked by the green vertical lines.

In [298], the threshold fluence for the NP size-dependent fragmentation of Au NPs with ns laser pulses is calculated. Accordingly, for a particle radius of approximately 5 nm (see Fig. S 17), a fluence of more than 0.03 J/cm² is required. In Fig. 33, the spatially mean fluence profiles for focal distances of 52.0 and 52.5 mm are shown. Although the mean fluence for 52.0 mm is lower than for 52.5 mm, a broader beam area exceeds the threshold fluence. For 52.5 mm, this area is decreased by 25 %. Moreover, the flow velocity in these experiments was set to 600 µm/ms and a repetition rate of 1000 Hz, i.e., an interpulse duration of 1 ms, was applied. Thus, except for a small fraction of particles sticking to the stationary layer in front of the target [82], most particles are probably not re-irradiated by the subsequent laser pulse so that the NP size remained independent of the lens-target distance.

As shown in section 4.2.1, the size decrease of NP by adjusting the focal distance in the liquid layer is possible. However, the productivity drops to about 66 % of its maximum [70]. Since the automated device's absolute productivity is already lower compared to other lasers used for LAL, NP downsizing by variation of the laser parameters is not recommended in this case. If the size needs to be adjusted for a specific application, centrifugation [293], laser fragmentation [149], or variation of the stabilizer concentration [173] should be chosen.

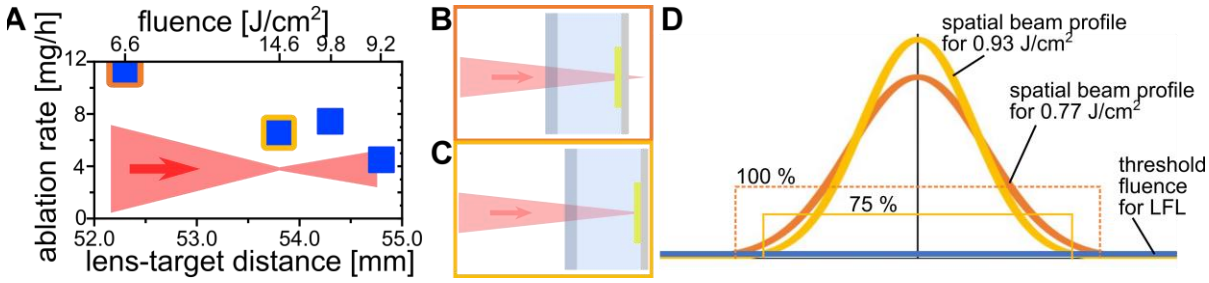

Fig. 33: Variation of the ablation rate in dependence of the lens-target distance and the resulting fluence on the target surface change caused by the distance variation (A). The schemes in B and C show the focal plane position regarding the target surface for two distances. The spatial beam profiles for these positions are indicated by the scheme in D. Fluences refer to the mean fluence in the liquid layer. The blue line marks the threshold fluence for fragmentation of Au NPs.

In conclusion, a target of 0.5 mm thickness provides the best compromise between constant productivity, NP size, and a long capsule lifetime for the automated device. Moreover, the initial lens-target distance should be set to 52.0 mm for Ag, Au, and Pt. Thus, at least 90 % of the maximal colloid productivity is ensured for all metals. This distance is validated with the final setup (see circles in Fig. 31). The same target distance for all three materials allows using the same capsule and can decrease production costs. Measurements of the hydrodynamic diameter show that the particle sizes for the three metals do not change

significantly, which means that it is possible to provide a constant particle quality during the capsule lifetime.

Liquid flow rate

For the production of NPs via laser ablation in liquids, the most simple experimental setup is the ablation in a beaker or other vessel where the target is positioned at its bottom and covered by the liquid [240]. However, during the ablation process, the NP concentration increases, leading to shielding of the laser beam by the NPs [363, 364] by absorption, scattering, and reflection. Consequently, less laser energy reaches the target surface leading to decreased NP productivity. Since laser beam shielding is caused by the laser beam interaction with the NPs, their properties depend on the ablation time [37, 187]. Consequently, the colloid throughput for these batch chambers is limited and their capacity is lower than for liquid flow chambers [187]. A deceive factor for achieving a high NP productivity $\dot{m}$ within the flow chamber is the flow rate $\dot{V}$. When the flow rate increases, the productivity increases [365] to the cost of lower NP concentration c [32]. At low flow rates, on the other side, the laser beam is shielded by the high NP concentration [363, 364] and persistent micrometer-sized bubbles (PBs) [91, 93]. In the following, a model for the flow-dependent concentration and productivity is introduced, and screening effects are discussed.
The NP concentration in dependence of the flow rate is expected to approach zero for an infinitely high flow rate. The NP concentration increases continuously for a decreasing flow rate and reaching a maximal finite concentration when the flow rate, in turn, is zero. The maximal concentration is mainly determined by the laser power and the material-specific ablation rate. Therefore an exponential decay with the general form of Eq. 12 is chosen as a fit function.

$$c(\dot{V}) = c_0 \cdot exp(-\varepsilon \cdot \dot{V}) \qquad \text{Eq. 12}$$

where

c_0: concentration at zero flow $\left[\frac{mg}{L}\right]$

ε: shielding factor $\left[\frac{min}{mL}\right]$

In turn, the productivity is expected to approach zero for a flow rate of zero since the high NP concentration shield the laser beam. At the beginning of the ablation process, NPs are formed until the final concentration is reached. Here, the productivity and concentration at steady-state conditions are discussed. The productivity reaches its maximum, which is determined by the laser power and the material-specific ablation rate, for an infinitely high flow rate. Therefore, the productivity is fit by the integral $\int c \cdot d\dot{V}$, where the integration constant is the maximal productivity (see Eq. 13).

$$\dot{m}(\dot{V}) = \frac{c_0}{\varepsilon} \cdot exp(-\varepsilon \cdot \dot{V}) + \dot{m}_\infty \qquad \text{Eq. 13}$$

where

$\dot{m}_\infty$ maximal productivity at an infinite flow rate $\left[\frac{mg}{h}\right]$

The experimental results and fits are shown in Fig. 34 and summarized in Tab. 8. It can be seen that for the concentration fit, good correlations ($R^2 \approx 0.9$) are obtained. However, the productivity deviated for the calculated fit, especially for flow rates higher than 1 mL/min. This behavior was not observed in literature so far [32, 365]. For comparing the flow condition in different ablation chambers, it is necessary to compare the flow velocity. In the presented study, the flow velocity ranged from (0.133 –16.7)·10^{-3} m/s. In contrast, Streubel et al. [32] examined the productivity at 1.9 – 4.8 m/s. In any liquid flow LAL chambers published so far, small Reynolds numbers (Re) results indicate laminar flow conditions. By putting the internal, molecular momentum, and the external flow momentum in relation, the Reynolds number reflects the flow's hydrodynamic stability. A smaller number indicates that induced vortices can be calmed down again by the molecular momentum so that the flow conditions remain laminar. Since the Bodenstein number (Bo) of the given setup is high (>1·10^9), back-mixing of the NPs in the ablation chamber is unlikely, and the stationary concentration layer [82] is 50 – 90 nm thick (see appendix section 8.2.4). Moreover, the Fourier number (Fo) is close to zero (Fo <2·10^{-8}), indicating flow conditions close to an ideal plug flow.

However, the tube length necessary to develop the final flow profile z_{in} exceeds the chamber length by one order of magnitude, indicating that the core flow is turbulent. For the presented study, a tube length of 10 mm before the ablation zone allows the development of the final flow condition (z_{in} = 0.2 mm). With a Reynolds number of 1 – 52, full laminar flow conditions are assumed with low NP back mixing (Bo >1·10^6, Fo <2·10^{-5}). The stationary concentration layer thickness is one order of magnitude larger (1 – 15 µm) than at flow conditions reported by Streubel et al. [32]. Within the stationary concentration layer, the NP concentration is higher than in the bulk liquid and the particle can only escape this layer by diffusion [366]. The thicker layer for the presented study could lead to a higher amount of laser beam shielding [82, 204], resulting in a deviation of the expected and determined productivity.

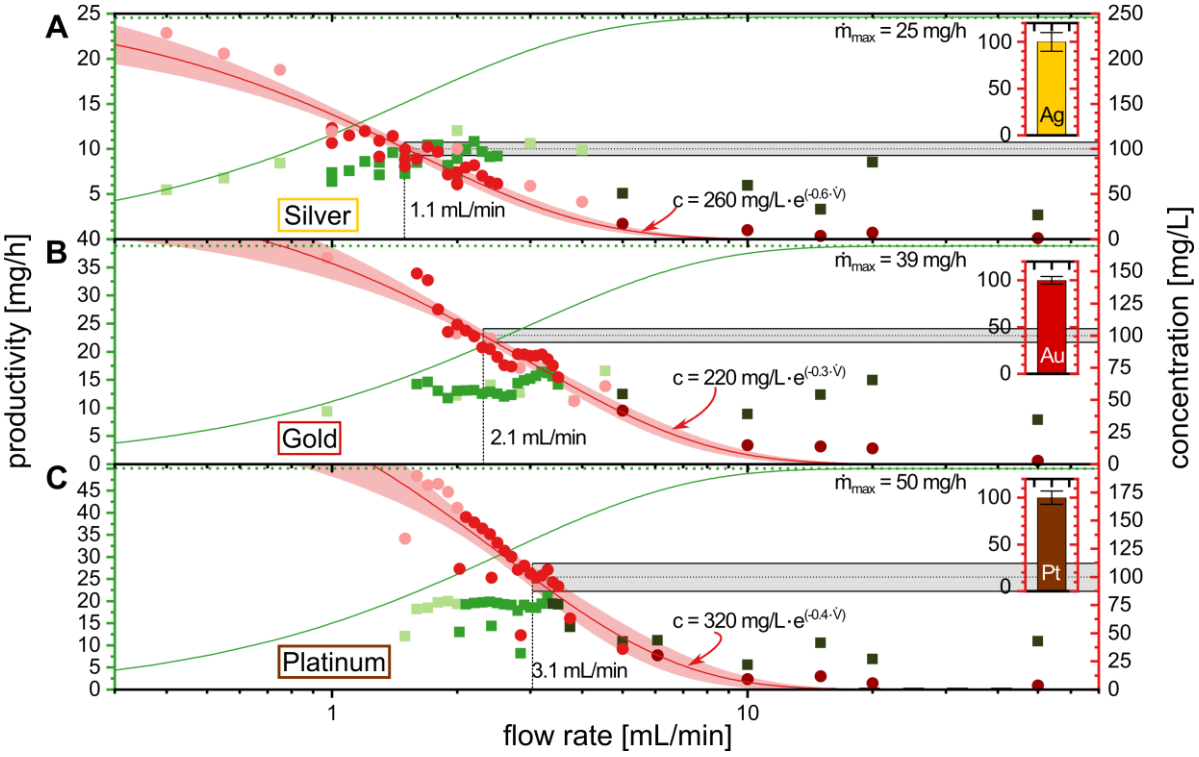

Fig. 34: Flow rate dependent concentration (right, red axis) and productivity (left, green axis) for Ag (A), Au (B), and Pt (C) NPs, where the horizontal dotted gray line mark a concentration of 100 mg/L, the vertical line the respective flow rate and the insets give the final colloidal concentration at the determined flow rate.

Tab. 8: Summary of the flow rate dependent concentration and productivity fit parameter and the determined flow rate for the automated, compact LAL device

	concentration at zero flow $\left[\frac{mg}{L}\right]$	shielding factor $\left[\frac{min}{mL}\right]$	maximal productivity at infinite flow rate $\left[\frac{mg}{h}\right]$	R^2 [1]	flow rate to achieve a concentration of 100 mg/L $\left[\frac{mL}{min}\right]$
Ag	260	0.6	25	0.91	1.1
Au	220	0.3	39	0.93	2.1
Pt	320	0.4	50	0.88	3.1

However, these considerations only explain the difference between literature results and the presented study, but not the increasing deviation of measured and calculated productivity in Fig. 34. For the calculated values, the interaction of the CB is not taken into account. Therefore, the influence of the fast expansion and induced pressure changes of the CB on the flow conditions shall be discussed. Initial CB expansion velocities of up to 40 m/s were reported in the literature [134]. In section 4.1.2, an expansion velocity of 25 m/s was found in the first 20 µs. When assuming that the CB accelerates the surrounding fluid during its

expansion and taking the CB expansion velocity instead of the liquid flow rate, Reynolds numbers larger than 10^5 are calculated, indicating highly turbulent flow conditions.

Linear stability analysis provides a semi-empirical attempt to predict the transition from laminar to turbulent flow. However, the developed models often require knowledge of, e.g., the wave propagation velocity, which is not easy to determine. For the discussion, if CB can induce turbulent flow in the ablation chamber, a model introduced by Jordinson for flow over a flat plate [367] is taken. Here, with the help of an indifference curve (see Fig. 35), it can be estimated if a stable (white area in Fig. 35) or unstable (blue area in Fig. 35) regime is reached for a given flow condition (Reynolds number) and momentum of a disturbance ($f_R \cdot \delta_l / v_\infty$). For the latter case the flow condition will change to turbulent flow. For the case of CB in an ablation chamber, the wave frequency f_R is assumed to be equal to the repetition rate (1000 Hz) since this represents the frequency of possibly newly induced vortexes. The displacement thickness δ_l is the amount to which streamlines are displaced by the boundary layer to the direction of the flow core. For turbulent flow it is hardly calculateable, therefore, the CB height at the respective time is taken (250 µm). Since the CB additionally provides a phase boundary layer, this assumption gives the lower limit of δ_l. Lastly, the free stream velocity v_∞ is set to the CB expansion velocity of 25 m/s. With an impact of the disruption of 0.01 and a Reynolds number around the CB of 120 000, an instable regime is reached due to the CB expansion and collapses. Assuming a smaller CB height for ps pulses of Streubel et al. of maximal 100 µm [68], a repetition rate of 10 MHz and a CB expansion velocity of 25 m/s results in an impact of the disruption of 40 and a Reynolds number around the CB of 120 000, corresponding to the stable regime in Fig. 35. The vortexes induced by CB lead to back mixing and longer residence time of NP in the chamber. Thus, higher laser beam shielding leads to an increasing deviation of productivity from the ideal productivity for increased flow rates.

Due to the ultra-fast CB expansion (100 – 200 ms [131, 136]), the fast processes' influence on the flow condition due to inertia remains elusive. There are only a few simulations, which calculate the pressure and temperature change in the surrounding of the CB [368]. Dabir-Moghaddam et al. also calculated the velocity change of the fluid surrounding a CB induced in calm water, which exceeds 100 m/s in this case [368] and equals an acceleration of more than 1.10^6 m/s². For a more in-depth insight into the highly dynamic and complex flow conditions during laser ablation, computational fluid dynamic (CFD) simulations are recommended. For laser ablation-induced CB, CFD simulation results published so far are not sufficient. However, CFD simulations of CBs induced in water close to a solid boundary can provide a first insight into the dynamic of laser ablation-induced CB: Lechner et al. demonstrated that the CB collapse influences locally high flow velocities (here ~ 800 m/s), which influence the surrounding flow dynamics [369]. Also, pressures of >100 bar were

calculated [369], even at a distance of 400 µm from the bubble center [370]. Consequently, also for LAL, the flow behavior in the ablation chamber cross-section could be entirely turbulent. Additionally, imaging of persistent bubbles (PB) shows that PB and NP quickly mix within the complete liquid layer above the target. Therefore, the simple film theory and laminar flow assumptions need to be advanced for laser ablation under liquid flow [82, 93].

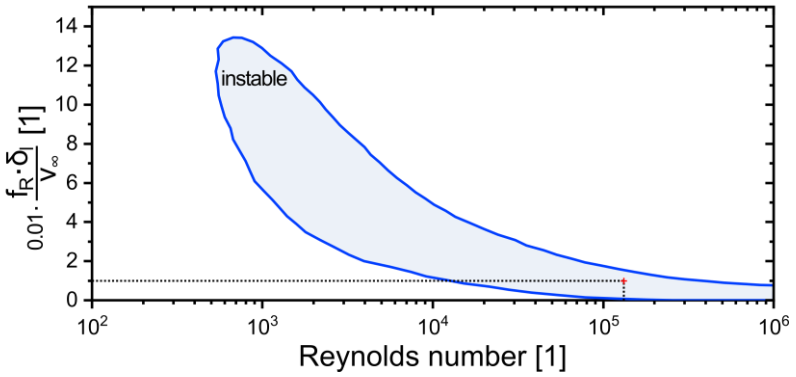

Fig. 35: Indifference curve determined by Jordinson for liquid flow over a flat plate, adapted from [367]. The blue area marks the regime where small disruptions induce the transition from laminar to turbulent flow. The red dot depicts the momentum of disturbance for the Reynolds number achieved in this section's ablation experiments.

In summary, for the desired concentration of 100 mg/L, productivities of around 10, 13, and 20 mg/h are measured for Ag, Au, and Pt NPs at flow rates of 1.1, 2.1, and 3.1 mL/min, respectively. Consequently, power-specific productivities of 20, 26, and 40 mg/(W·h) are reached, which is higher than 10, 18, and 13 mg/(W·h) for Ag, Au, and Pt NPs at a flow rate of 100 mL/min achieved by Kohsakowski et al. [293]. The higher power-specific productivity in this study indicates a higher ablation efficiency compared to former studies.
Non-laminar flow conditions caused by CB induced vortexes limit the productivity of LAL. The momenta of disturbance increase for higher flow rates so that vortex formation is more prone. This observation means that for higher flow rates, the deviation between the expected and measured productivity increases.

Volume-specific energy dose

The previous sections discussed the influences of the focal plane shift, the pulse energy, and the liquid flow rate individually. Here, these parameters are evaluated and combined into one parameter. Therefore, the mean laser fluence through the liquid layer at different focal distances is calculated by the mean value theorem (see appendix, section 8.1 and Eq. 14) and divided by the fluid's average flow velocity. This parameter gives the energy dose per liquid volume and is referred to as volume-specific energy dose. Since the particle size distribution differs for ps and ns laser ablation [137, 371], the NP size produced with the

Amphos flex 500 (see section 4.2.1) and the eMOPA1064-500 for different relative volume-specific energy doses are compared. A kinetic approach is chosen to describe the influence of the volume-specific energy doses on the NP size <10 nm w_{10} (Eq. 15 and Eq. 16).

$$I_{0,spec} = \frac{1}{\bar{v}} \cdot \frac{F(z_1) - F(z_0)}{z_1 - z_0} \quad \text{Eq. 14}$$

$$\frac{dw_{10}}{dI_{0,spec}} = l \cdot w^n \quad \text{Eq. 15}$$

$$w_{10} = \left(\left(c - l \cdot I_{0,spec} \right) \cdot (n-1) \right)^{1/(1-n)} \quad \text{Eq. 16}$$

where:

$I_{0,spec}$: volume-specific energy dose $\left[{}^{GJ}/_{cm^3} \right]$

$\bar{v}$: average flow velocity $[{}^{m}/_{s}]$

w_{10}: mass fraction of particles <10 nm [%]

l: reaction rate constant

n: order of reaction [1]

c: integration constant

Usually, the NP size distribution is broader for fs and ps laser pulses than for ns pulses [371, 372]. For all volume-specific energy doses, the ns laser ablation produces a larger size fraction of NP <10 nm (Fig. 36). For both fits (Eq. 17 and Eq. 18, summarized in Tab. 9), a reaction order of -3 is determined, where the negative sign indicates that particles <10 nm are formed due to the laser irradiation. Moreover, this shows that the initial particle volume, and not the number of particles, influence the degree of fragmentation, as reported in the literature [299]. Here, a fragmentation threshold is given in dependence of the initial NP radius [188]. The reaction rate for the ns size adjustment is about seven times larger than for ps pulses, indicating a more efficient size decrease. Coulomb explosion [373] and a heating-melting-evaporation [356] are mechanisms discussed for NP size fragmentation. The former is mostly assigned to ps pulses and the latter to ns fragmentation [374].

However, each mechanism's contribution to fragmentation, especially for different pulse duration, is not yet fully understood [149]. Consequently, the cause of the higher in-process fragmentation efficiency for ns pulse in Fig. 33 cannot be fully explained. One hypothesis is that the size decrease for ns pulse is more efficient and starts for lower volume-specific energy doses since the fragmentation threshold for Au NP for ns is in the range of tens of MW/cm² [188]. In contrast, the threshold is one order of magnitude larger for ps pulses [188].

Aggravatingly, for the initial colloid, the larger NP size fraction produced with ns pulse is smaller than for ps, further decreasing the fragmentation threshold for ns pulses [371, 372].

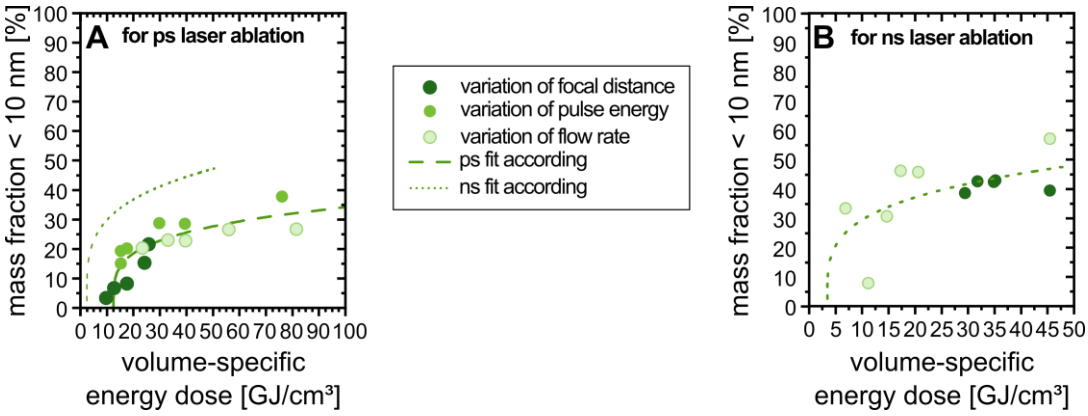

Fig. 36: Dependency of the mass fraction of NP <10 nm on the volume-specific energy dose and the resulting pseudo-kinetic fit for Pt for (A) ps laser ablation and (B) ns laser ablation, for comparison, the ns fit is added in A.

w_{10} for ps laser ablation:

$$w_{10}(I_{0,spec}) = \left(-195 \cdot 10^3 + 15.6 \cdot 10^3 I_{0,spec}\right)^{0.25} \quad \text{Eq. 17}$$

w_{10} for ns laser ablation:

$$w_{10}(I_{0,spec}) = \left(-391 \cdot 10^3 + 115 \cdot 10^3 I_{0,spec}\right)^{0.25} \quad \text{Eq. 18}$$

Tab. 9: Fit parameter of the pseudo kinetic approach for the volume-specific energy dose-dependent particle size of Pt for a ps and a ns laser system

	ps laser ablation	ns laser ablation
order of reaction	-3	-3
reaction rate constant	3 895	28 700
integration constant	48 730	97 230
R^2	0.8	0.4

Ablation time

For the NP production in batch processes, the NP concentration and the NP size depend on the production time [187]. Since the NP concentration increases with the ablation time, the probability of reirradiation increases fragmentation [363, 364]. For the continuous flow process, however, the ablated mass increases linearly with the production time, i.e., the productivity remains constant [32, 360], resulting in a concentration independent of the process duration. Regarding the NP size during the continuous process, research mainly focused on the size evolution during the NP formation process [127, 137, 352]. However, Waag et al. observed an ongoing increase in the colloidal temperature [156], which

influences the particle motion, stability, and size. Additionally, for the high power laser irradiation, it needs to be considered that the reflectivity of the emerging critical water layer and plume drastically differ from the bulk properties [100, 107]. For the automated LAL, a constant colloidal concentration, size, and stability should be guaranteed over the whole production process, even at prolonged ablation times. Therefore, the difference in productivity and colloid quality of an unablated and a, e.g., by LAL, roughened target needs to be determined. Additionally, long term effects, such as the temperature increase, must be analyzed. Lastly, the change of the NP properties after storage is examined.

The productivity difference for new and roughened targets for a five-minute ablation is shown in Fig. 37 A and the particle size change in Fig. S 18 (appendix, section 8.2.5). Regarding the particle size for ablation with a new and used target, no notable change within the first 300 s can be detected (see Fig. S 18). Also, no significant productivity difference is found for Ag and Pt. In contrast, the productivity drops from 18 ± 2.7 mg/h, when using a roughened target, to 9.9 ± 1.2 mg/h for a new Au target. The continuous extinction measurement during the ablation of a new target (in Fig. 37 B), as a measure of productivity, shows that after about 500 s, the level of a roughened target is reached. The target surface is scanned about 3 – 4 times within 500 s. The question arises why the difference is highest for Au, where the bulk medium's reflectivity is highest for Ag. Since the optical properties can drastically change under laser irradiation, the reflected laser power for the three materials in dependence of the applied laser pulses per spot is measured with the eMOPA1064-500 under an incidence angle of 45° (see Fig. 38). Here, an initial reflectivity of 45, 22, and 34 % are detected for Ag, Au, and Pt, respectively. After the target is irradiated for the first time, Au reflectivity is decreased to 7 %, whereas for Pt two, and Ag four runs are necessary. The literature reported that micro- and nanostructures formation enhances absorption of light for Au after ~ 100 shots/spot [259]. Therefore, scanning electron microscopy (SEM) images of the unirradiated and irradiated surfaced of the three metals are taken (see appendix section 8.2.5, Fig. S 11). However, no significant structural difference between the metals can be observed. It was also reported that the cavitation bubble size depends on the number of laser pulses per target spot [260]. Here, it is shown that for 7 ns pulses, about 20 pulses on Ag and only about three pulses on Au are necessary to reach the final cavitation bubble size. However, for 12 ps pulses after only two pulses for both materials, the final CB size is reached. For multi-pulse fs laser ablation, increased absorption due to laser-induced periodic surface structures (LIPSS)/ripple formation [375, 376] appearance in dependence of the applied laser fluence [259, 377] and also a decreased reflectance due to the surface structuring [378, 379]. Au shows a lower theoretical threshold fluence of 5.2 J/cm² and, thus, at the given fluence of 12 J/cm², a lower ablation rate than Ag (F_{th} = 2.7 J/cm², F_{th}(Pt) = 3.3 J/cm²) [260, 380]. However, due to its lower ultimate tensile stress (100 MPa for Au [381], 170 MPa for Ag [381] and 125 –150 MPa for Pt [382]), incubation effects in water are

stronger for Au [383], so that the ablation rate increases strongest within the first 3 – 4 pulses per spot.

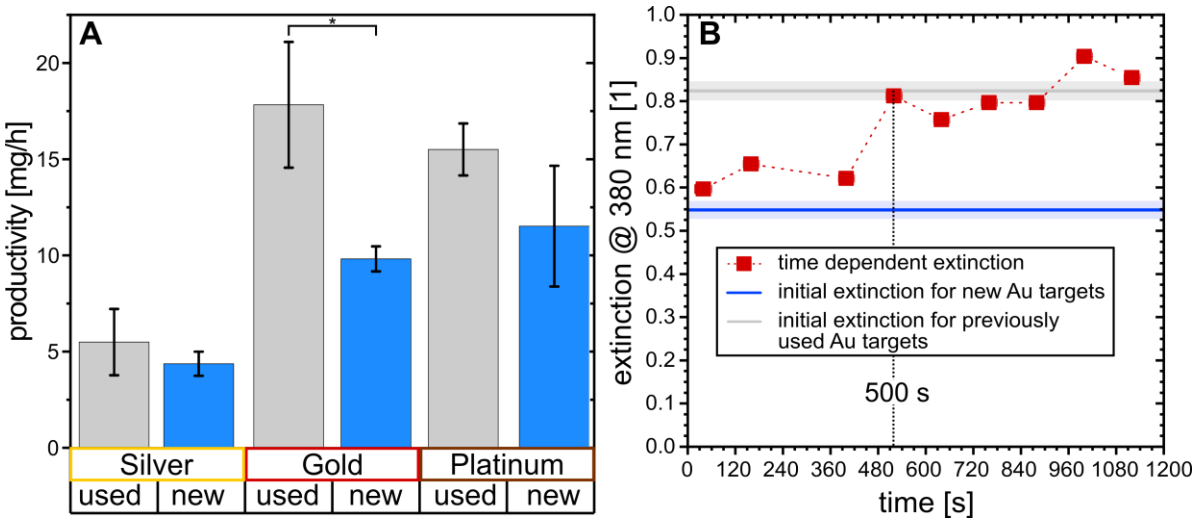

Fig. 37: Productivity of Ag, Au, and Pt when ablating new (blue) or previously used (gray) targets (α = 0.05) with a fluence of 12 J/cm² (A). The time-dependent extinction for the ablation with a new Au target is shown (B). The horizontal blue line marks the initial extinction of a new target, and the gray line the extinction of a previously used target. The shaded areas correspond to the standard deviation determined in A.

For the automated device, the previous results mean that whether a new or roughened target is used for an ablation does not make a significant difference for Ag and Pt. For Au, however, the target either needs to be roughened before the first usage, or the Au colloid produced within the first 500 s needs to be discarded, or a minimal production time needs to be set for the first usage. For the latter case, the mean productivity in dependence of the total production time with a new target is shown in Fig. 39. A minimal first production time with a new target of 23 min is required to reach at least 90 % of a roughened target's productivity on average.

In summary, a new Au target shows significantly (>40 %) lower productivity compared to a roughened target, presumably due to the strong incubation of Au. The lower productivity of new Au targets can be solved by putting a roughened Au target in the capsule, discard the Au colloid produced within the first 500 s, or setting a minimal ablation time to 23 minutes for the first ablation with a new Au capsule.

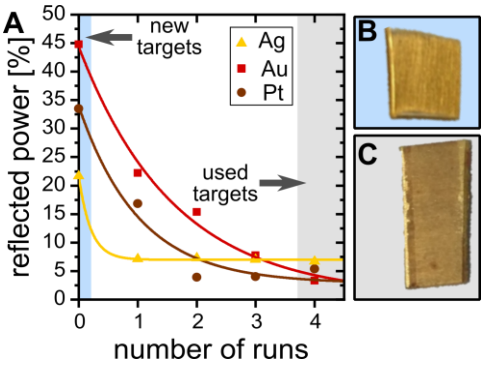

Fig. 38: Reflectivity change at a wavelength of 1064 nm depending on the number of scan runs (A) for Ag (yellow triangles), Au (red squares), and Pt (brown circles). Photographs of a new Au target (B) and an Au target after four runs (C).

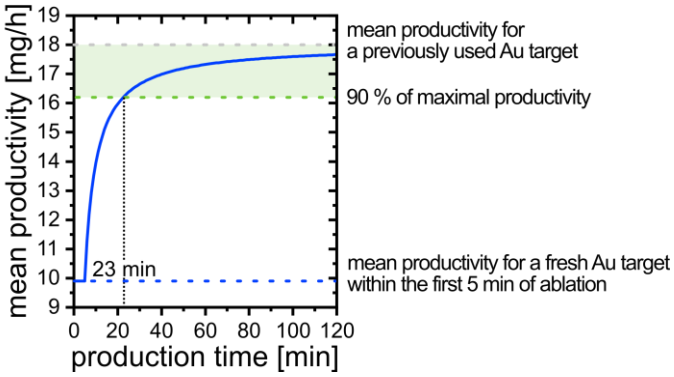

Fig. 39: Calculated mean productivity of an Au colloid produced with a new ablation capsule dependent on the respective production time (solid blue line). The green shaded area marks the productivity between 90 % of the productivity reached with a roughened target and maximal productivity.

As shown in Fig. 37 and Fig. S 20 (appendix), the target surface quality only influences the first 500 s of ablation. When considering a longer ablation time (see Fig. 40), a decrease in productivity is observed within the first 1.5 h of ablation for Ag and Pt. Additionally, a slight drift to lower productivities observed between 1.5 – 8 h for Ag, Au, and Pt. However, this drift lies within the confidence band of the respective flow rate. As shown in section 0, productivity increases to a maximum and decreases again for increasing lens-target distances. For the ablations in Fig. 40, new targets are used in all cases, and the initial target-lens distance was set to 52.0 mm. Therefore, productivity is expected to increase with the beginning of material removal until the distance of maximal productivity is reached, i.e., when half of the target is ablated. The shift of the ablation plane does not explain the long-term productivity trend. In the previous part, the flow rates required for 100 mg/L were determined for each material (Fig. 34) and are applied for these experiments. The confidence intervals for the respective fits show the fluctuation of the concentration for the chosen flow rate and are marked in Fig. 40 (green area). The extinction tends to exceed the upper confidence band initially, whereas

it tends to fall below the lower confidence band in the second half of the long-term ablation of Ag, Au, and, Pt.

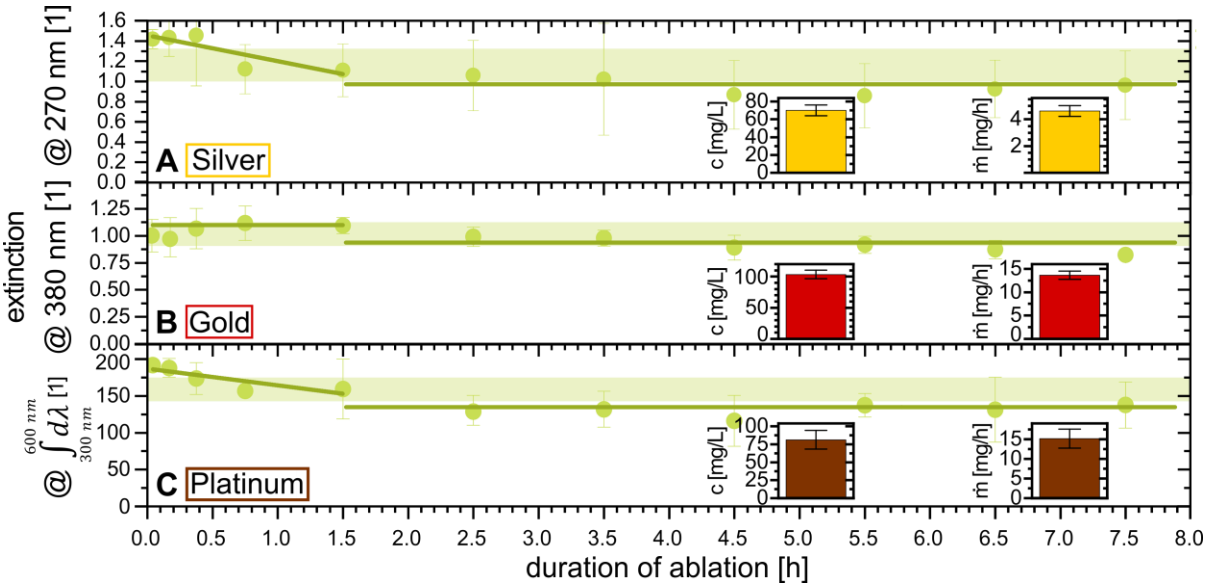

Fig. 40: Extinction of Ag (A), Au (B), and Pt (C) during 8 h ablation. Separate fit for the time range of 0 – 1.5 h and 1.5 – 8 h are depicted as solid green lines. The shaded areas mark the confidence bandwidth at the set flow rate (Fig. 34). The insets in each penal show the mean concentration and productivity determined gravimetrically after 8 h of ablation.

Additionally, the target temperature change during the ablation is measured to explain the time-dependent extinction decrease. Waag et al. reported that the target and colloid temperature increase continuously over the ablation time, influencing the NP size and colloidal stability [156]. Additionally, it is hypothesized that heat accumulation in the target can favor the material removal process, especially for high repetition rate ps laser ablation [384, 385]. Fig. 41 shows the increase of temperature at the ablation target backside from 21.5 °C to 25.2 °C within the first 1.5 h resulting in a mean heat flux of 2.5 °C/h and to 26.5 °C within 8 h. The final mean heat flux between 4 h and 8 h measures 0.2 °C/h. Moreover, the target temperature continuously increases and does not reach a steady-state within 8 h. Therefore, the time-dependent heat flux is calculated according to $\dot{Q} = \frac{\partial T}{\partial t}$. The detailed calculation is explained in the appendix (section 8.2.5). In summary, the Ag target at the front size is less than 1 °C warmer than the measured temperatures at the target backside. A mean liquid temperature of 20°C at the chamber inlet and 22 °C at the chamber outlet is measured. The heat flux through the Ag target is less than 1.6 mW and about 0.5 mW from the target surface into the liquid layer. The heat transfer coefficient is low (5.6 $W \cdot m^{-2} \cdot K^{-1}$) due to the low flow velocity ($0.36 \cdot 10^{-3}$ $m \cdot s^{-1}$ for Ag) (see appendix 8.2.5 “Calculation of Ag target heating”). Therefore, the highest temperature is found at the target

frontside and the NPs caught in the stationary laminar layer are affected by this temperature increase.

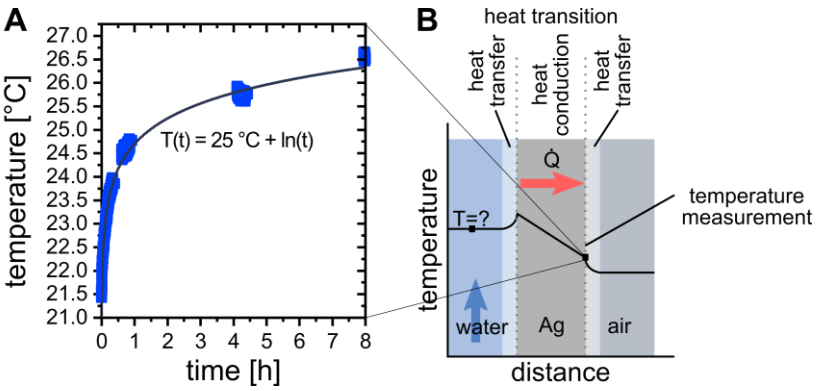

Fig. 41: Increase in the target temperature measured on the ablation target backside over an 8 h ablation for an Ag target (blue squares). The gray line represents the fit (A). The scheme illustrates the heat flow temperature profile through the water layer, Ag target, and ambient air (B).

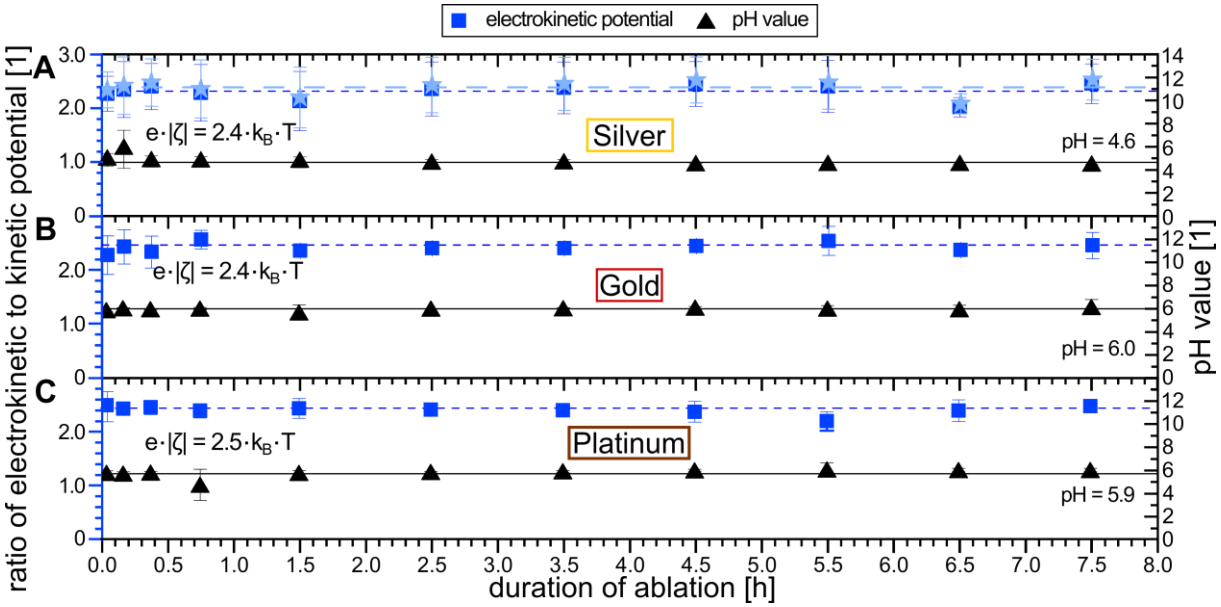

Fig. 42: Electrokinetic potential and the pH value of the citrate stabilized Ag (A), Au (B), and Pt (C) colloids during 8 h of continuous ablation. For the calculation of the electrokinetic potential, a temperature of 25°C is assumed. Since the temperature development during the ablation is measured for Ag (see Fig. 41), the electrokinetic potential is also calculated with the current colloid temperature in this case (light blue data points and fit in A)

A slight shift in the temperature could potentially affect NP stability, i.e., increase their kinetic potential (Fig. 42), and thus favor aggregation and agglomeration (Fig. 43). Neither the electrokinetic potential of the NPs nor the colloid's pH value change during the 8 h ablation. For all three samples, the electronic repulsion overweighs their kinetic potential by a factor of more than two, even when the temperature increase during the ablation is considered (see

Fig. 42 A), which indicates stability. Due to the formation of OH^- surface adsorbates on the NPs [173], a low pH value of 4.6 is measured for the Ag colloids indicating an insufficient amount of the stabilizer sodium citrate. The stabilization of Ag colloid will be examined in more detail in section 4.2.3.

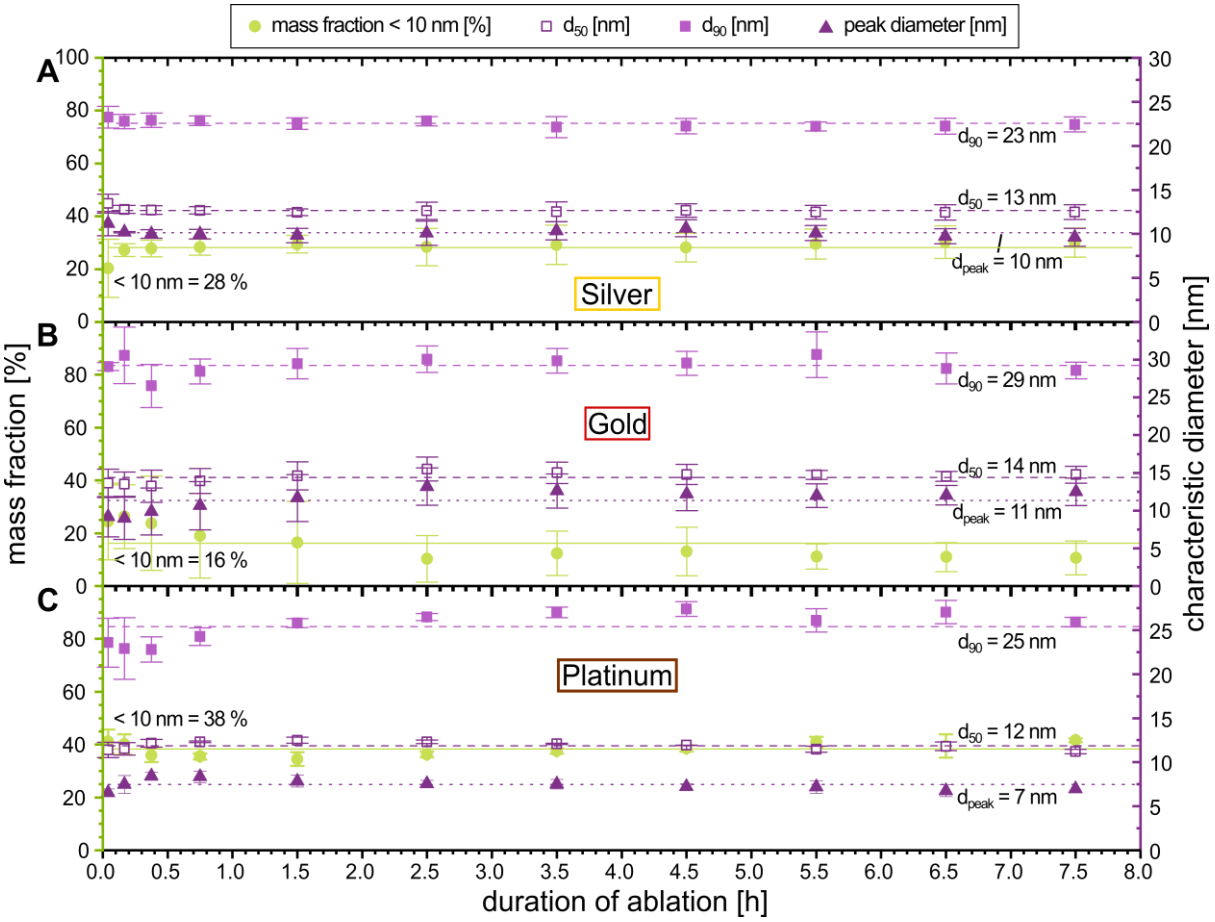

Fig. 43: The size variation of Ag stabilized with citrate (A), Au (B), and Pt (C) during long time ablation of 8 h is characterized by the NP mass fraction <10 nm (green squared) and different characteristic diameters (purple symbols). These diameters are the peak diameter of the size distribution (triangle) and the diameters marking the 50 (open square) and 90 % (solid square) cut-off. The lines are the result of a constant fit between 1.5 h – 8 h.

Regarding the NP size, fluctuations of up to 45 % are observed for all materials within the first 1.5 h. The influence of the temperature on the NP size can be seen in detail when the size change within the first minutes of the ablation is determined (see Fig. S 18, appendix). For Ag and Au, the NP size increases, whereas it remains constant for Pt. Between 1.5 – 8 h, regardless of the increasing temperature, NP size remains constant.

Fig. 44 depicts the difference in the colloidal quality, i.e., NP concentration, size, and stability, for the first 1.5 h and between 1.5 and 8 h of ablation. For all three materials, the NP concentration for the first 1.5 h of ablation is significantly higher than for the following 6.5 h (Fig. 44 A). For Ag and Au, the size fraction <10 nm decreases after 1.5 h by 10 %,

respectively (Fig. 44 B), and for Au also the larger NPs are increased from 15 to 16 nm, resulting in a larger d_{90} diameter (Fig. 44 C). The size distribution of Pt is not affected by the ablation time. Regarding the Zeta potential, no significant difference for the first 1.5 h of ablation and afterward is found for any material (Fig. 44 D). Additionally, with a zeta potential of ~ -60 mV, all colloids are very stable (Fig. 44 D).

NP properties for material data sheets are determined for the particles obtained after 1.5 h of ablation. In the following, the first 1.5 h of ablation will be called run-in time since variations in the concentration and NP size are high in this time range. For the automated device, the run-in time of 1.5 h would mean that 100, 190, and 280 mL of Ag, Au, and Pt colloid are discarded per production process if a high reproducibility is desired. There is no clear hint whether a heated stationary liquid layer or a heated target material is responsible for the run-in behavior of the ablation process. Experiments with heated targets or targets cooled throughout the experiment (e.g., with a Peletier element) could be performed to elucidate the temperature-effect on the NP quality.

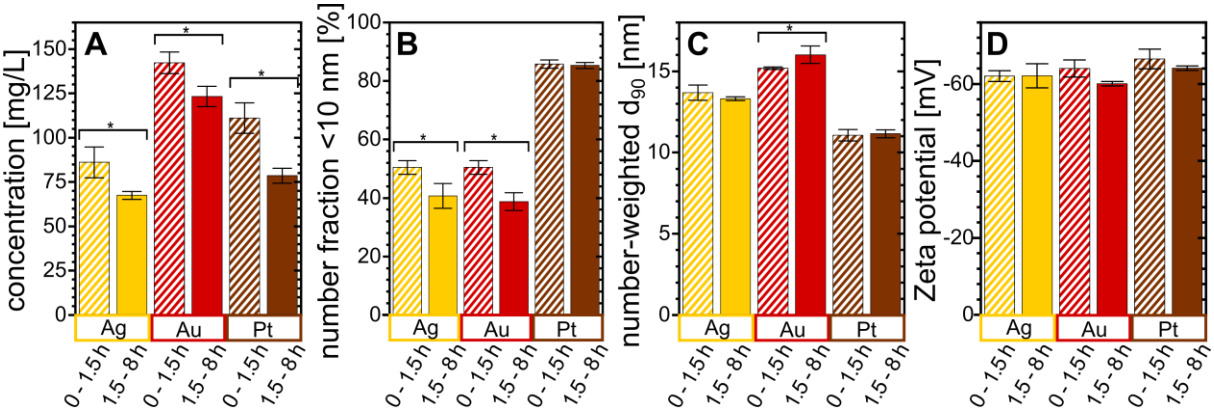

Fig. 44: Comparison of the mean concentration determined via extinction measurement (A) and the number-weighted particle fraction <10 nm (B), the d_{90} diameter (C), and the Zeta potential for Ag (yellow), Au (red), and Pt (brown) for different time intervals during 8 h ablation (α = 0.05).

Moreover, the storage stability of the produced colloids is analyzed. Therefore, the colloid is stored for 28 days at 25 °C. As a thermodynamically meta-stable system, NPs will continue to grow until a uniform NP size is reached. A kinetic approach describes the particle growth. The time shortly after production has been fit by kinetic equations of barrierless coalescence of particles and the long time ripening by a combination of barrierless coalescence and Ostwald ripening [160, 167].

After 28 days at 25 °C, no aggregations are found for Ag, Au, and Pt. Fig. 45 shows how the hydrodynamic particle size, the zeta potential, and the optical properties change within the storage time. The NP concentration, determined by optical spectroscopy, decreased after 28 days (Fig. 45 A), although no material precipitated over time. Since the extinction within the

interband absorption is proportional to the number frequency of the NPs, the decrease in the concentration is a sign that the number concentration decreases. This increase in the particle size can be seen by the SPR peak shift, from 400 to 410 nm, towards a higher wavelength for Ag (Fig. 45 B) and the increase in the characteristic diameters (Fig. 45 E). On the other hand, Au and Pt NP size do not significantly differ before and after the storage time.

Assuming van't Hoff conditions, i.e., a doubling of reaction rate per 10 K increase, the produced Au and Pt colloids are expected to be stable for four months at 5 °C. The stability for Ag will be further examined in the next section (4.2.3).

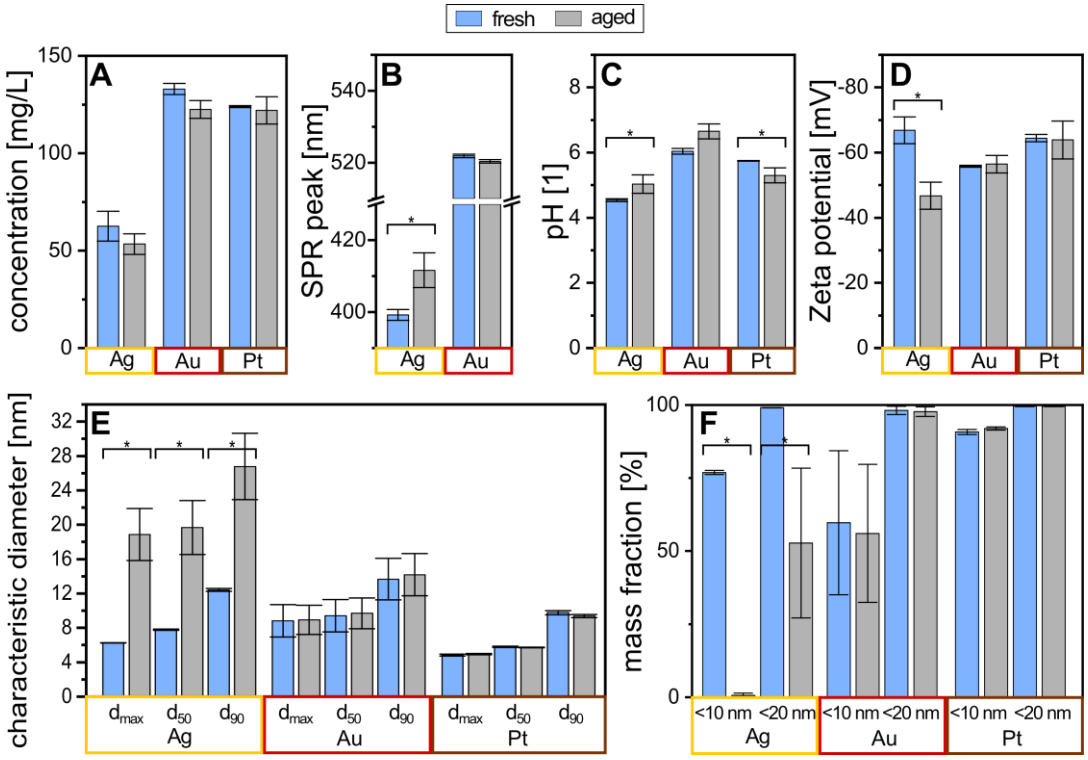

Fig. 45: Changes in the colloid concentration determined by UV-Vis spectroscopy (A), SPR peak (B), pH value (C), Zeta potential (D), the peak d_{max}, and 50 and 90 % cut-off diameter d_{50} and d_{90} (E), and the mass fraction <10 nm and <20 nm (F) after 28 days for Ag, Au, and Pt.

In summary, the time effect concerning the target condition, production time, and colloid storage are investigated. First, only for the usage of a new Au target, but not for Pt or Ag, a significant decrease in productivity is observed, which can be explained by the incubation effect. It is recommended to use pre-roughened Au targets for the automated LAL device. Second, a productivity decrease within the first 1.5 h of ablation is observed. Within the time frame, also the NP size fluctuates stronger than afterward. For Ag ablation, a heating rate of 2.5 °C/h is found for the first 1.5 h and decreases to 0.2 °C/h. The first 1.5 h of produced colloid should be discarded to ensure constant colloid properties and high reproducibility over the ablation time. In future investigations, the influence of preheating or cooling the ablation target on NP productivity can be investigated. Third, initial tests on the long-term stability of

the produced Ag colloids indicate that a further in-depth study is necessary to thoroughly estimate their shelf life. Au and Pt colloids were stable for 28 days stored at 25 °C, indicating a shelf life of four months at 5 °C.

4.2.3. Increasing the long-term stability of silver colloid

As demonstrated in the previous chapter and reported in the literature, Ag NPs are prone to ripening [167]. Since, e.g., the production of 100 mL with the automated LAL device of Ag takes more than 1.5 h, the particle size should not change on this short time scale. The user might also store residual colloids, produce the colloid ahead, or need even higher amounts, which might take one workday in production. Therefore, also on a longer time scale, the NP size must not change. Here, the short term, i.e., 18 h, size consistency of Ag NP ablated in 0.1 mmol/L sodium citrated and tetraethylammonium hydroxide (TEAH) is discussed. Furthermore, the long term stability over 28 days is determined for sodium citrate solutions of 0.1, 0.25, 0.5, and 1.0 mmol/L.

For short-term stability, the NP size is analyzed from the production start to 18 h, mimicking the storing overnight (see Fig. 46). For citrate, a peak diameter of 6 nm is found. In contrast, the TEAH-stabilized Ag NP peak diameter rapidly increases from 7 to 13 nm after 1 h and 27 nm after 18 h, indicating an insufficient stabilization. TEM images of the TEAH-stabilized sample reveal a distinct bimodality of the colloid, favoring fast Ostwald ripening [386]. Moreover, irregular, non-spherical NP shapes like triangles are observed. The formation of triangle- or polygon-shaped particles was found during the reduction of silver nitrate at low reduction rates [387]. Ostwald ripening is the dominant mechanism in the presence of ions or dissolved crystals [388], which explains the strong influence of Ostwald ripening on the Ag NP growth. Since TEAH-stabilized NPs already change significantly on a short time scale, further shelf-life tests are not conducted.

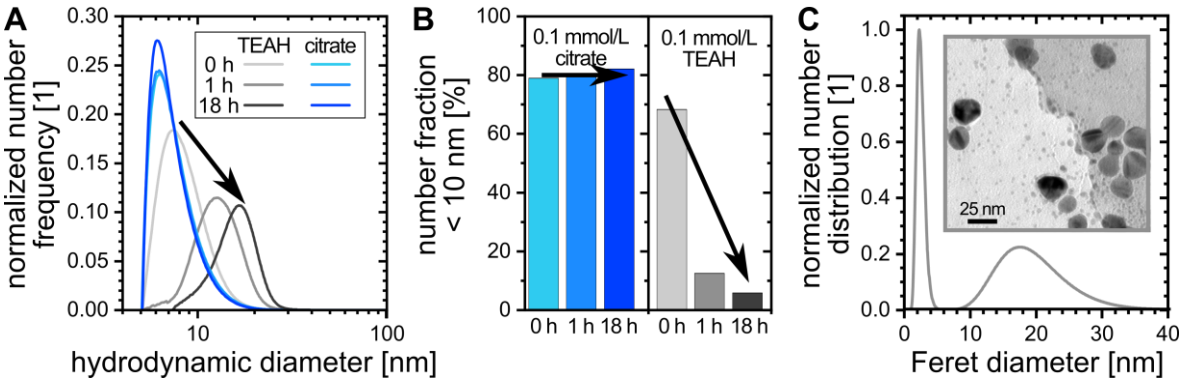

Fig. 46: Size-dependent normalized number frequency (A) and change in the number fraction of nanoparticles <10 nm (B) in dependence of the time passed since the ablation process. Results are shown for citrate- (blue) and TEAH-stabilized (gray) colloids. For the TEAH-stabilized colloid 18 h after production, the Feret diameter and an exemplary TEM image are depicted (C).

Although the short-term measurement for citrate-stabilized Ag NPs shows no changes, the peak diameter increases from 6 to 19 nm within 28 days (see Fig. 45). Therefore, the long-

term stabilization with three higher citrate concentrations is analyzed (see Fig. 47). The size distribution for NP produced in 0.1 mmol/L citrate solution show a broad (PDI of 2) but no distinct bimodal size distribution, which explains the slower aging compared to TEAH (Fig. 47A and C). Additionally, TEM images reveal that the size fraction >20 nm decreases with higher citrate concentration (Fig. 47 C – F). Therefore, the NP growth over 28 days is slowed down for higher citrate concentrations (Fig. 47 B).

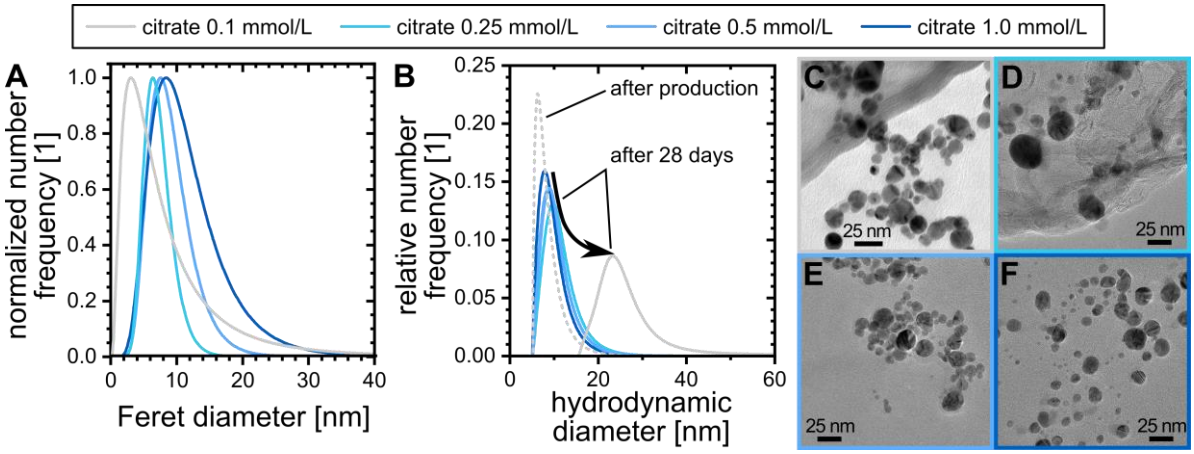

Fig. 47: Comparison of the log-normal fitted Feret (A) and hydrodynamic (B) number-weighted size distribution for Ag NPs produced with different citrate concentrations of 0.1, 0.25, 0.5, and 1.0 mmol/L and exemplary TEM images (C – F). For all experiments, the flow rate was set to 1.1 mL/min, samples were taken after 15 min of ablation, and measured 18 h after the ablation process.

In summary, significant post-processing growth of TEAH-stabilized Ag NPs is observed already 1 h after production. The production of 100 mL Ag colloid takes about 1.5 h resulting in a broad and strongly time-dependent NP size distribution. Therefore, TEAH is an unsuitable additive for the automated LAL device. With increasing citrate concentration from 0.1 to 1.0 mmol/L, the peak diameter shift over 28 days is reduced from 17 to 2 nm. A concentration of 0.25 mmol/L is sufficient to reduce the peak diameter shift to 4 nm for the time of 28 days. Therefore, a minimal citrate concentration for the automated device of 0.25 mmol/L is recommended for Ag. However, for possible applications of Ag NPs, it needs to be kept in mind that 0.25 mmol/L citrate already leads to surface coverage $>5 \cdot 10^{15}$ molecules (ligand)/m² (NP), which could have a negative influence on the application [179].

4.2.4. Reproducibility and robustness of the automated laser ablation process

The temporal consistency of the process, as examined in section 4.2.2.4, and low batch-to-batch variability are required for a reliable device. Therefore, the long-term ablations (section 4.2.2) and five additional reproducibility tests are executed for each material and taken to determine the expected values and specification ranges for the material data sheets (MDS) (appendix sections 8.2.6.2, 8.2.6.3, and 8.2.6.4). Ten experiments per material with process times ranging from 15 min to 4 h are performed for data validation in the next step. These results are compared to the expected values and specification ranges from the MDS to validate these.

In Fig. 48, the MDS values (shaded area and circle) are compared with the data validation experiments (box plot) for Ag, Au, and Pt, respectively. The results from the validation experiments meet the specification of the MDS. The colloid quality is further assessed by comparing the reached specification to commercially available colloids. Therefore, commercially available chemically and laser-generated colloids of about the same NP size are chosen. For the comparison, the specifications from the MDS of the commercial colloids are taken. The results are presented in Tab. 10. The PDI for Au is larger for the automated device than for commercial colloids. One possible solution may be to increase the stabilizer concentration since it was shown that the size of Au NPs can be adjusted freely from 7 to 25 nm by adjusting the stabilizer concentration [173]. As discussed in section 4.2.2, the size adjustment by flow rate variation is only possible to the cost of productivity losses and longer production times. Moreover, since higher NP concentrations will be achieved in this case, the probability of agglomeration increases and demands higher stabilizer concentrations.

In summary, the automatically produced Ag and Au colloid qualities are within the set data sheet specifications and, except for the polydispersity index, match the specifications of commercially available colloids given in their MDS. The stabilizer concentration can be adjusted to achieve more narrow NP size distributions. For the Pt colloids, excellent colloid qualities are met, which even meet commercial distributors' specifications.

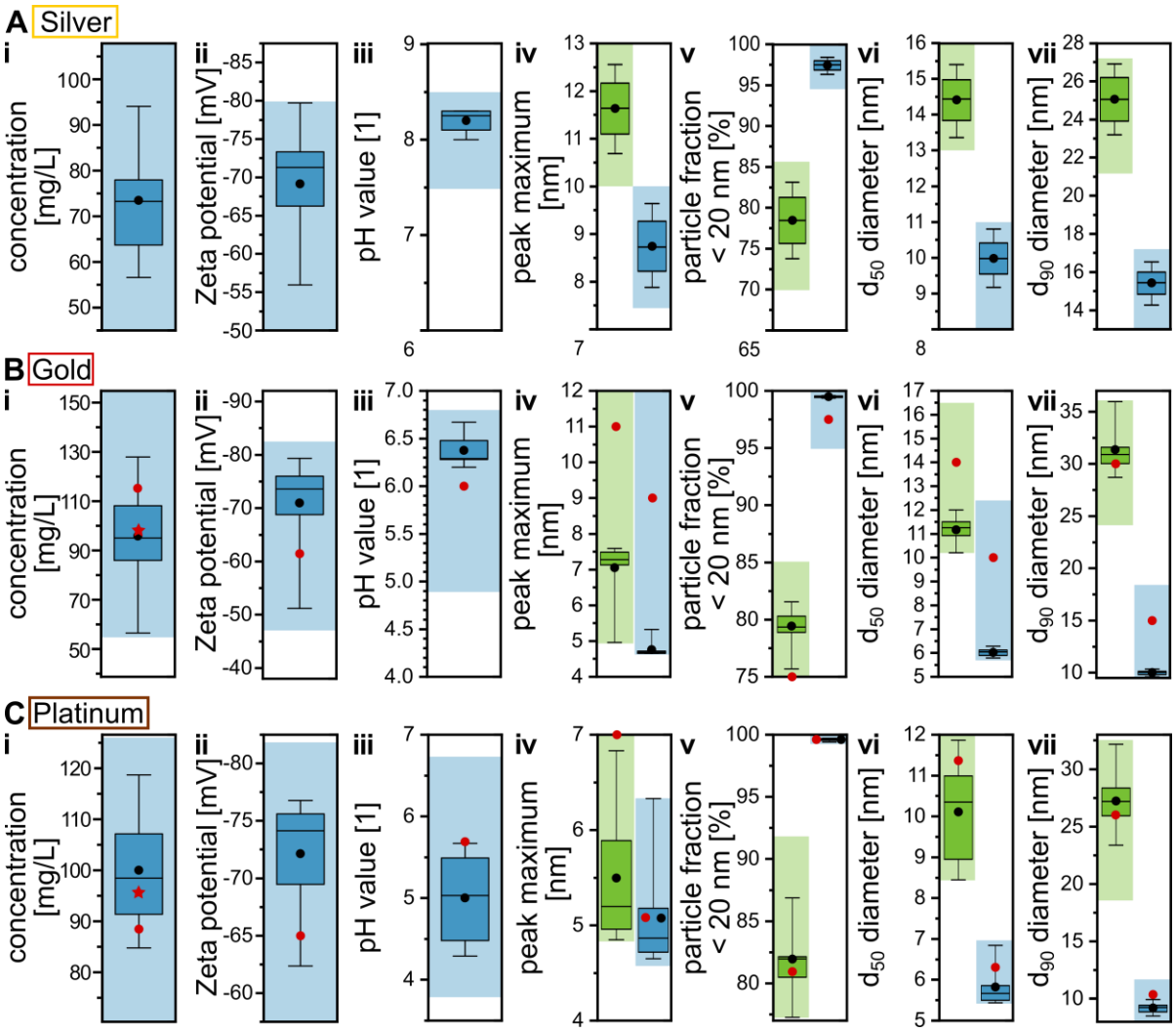

Fig. 48: Diagrams for Ag colloid stabilized with 0.25 mmol/L citrate (A), Au (B), and Pt (C) depict the data ranges (shaded areas) and mean values (red circles) determined by the long-term and reproducibility studies. The boxplot represents the results of ten LAL runs (15 min – 4h) with the mean values (black circles) and medians (horizontal lines in the boxes). In (i), the star represents the gravimetrically measured concentration and the circle the concentration base on extinction measurements. In (iv – vii), the green dataset (left) refers to the mass-weighted and the blue dataset (right) to the number-weighted size distribution.

Tab. 10: Traffic light system for evaluating the colloid quality produced by the automated device. For this comparison, the mean values shown in Fig. 48 are taken. The flow rate was set to 1.1, 2.1, and 3.1 mL/min for Ag, Au, and Pt, respectively. Ag is stabilized with 0.25 mmol/L sodium citrate and Au and Pt with 0.1 mmol/L sodium chloride.

	mass concentration	Zeta potential	pH value	primary peak diameter (TEM)	Specific surface (TEM)	Polydispersity Index (TEM)	SPR peak	Optical density	commercial reference colloid
Ag	●	●*	●	●	●	●	●	●*	[389–391]
Au	●	●	●	●	●	●	●	●	[392–395]
Pt	●	●*	●	●	●	●	○	●	[396, 397]

○: no evaluation possible, ●: out of the MDS specification, ●: meet specification in MDS but should be improved to compete with commercial colloids, ●: meet MDS specification and can compete with commercial colloids, *: no specification was given for commercial colloids

4.3. Validation of the process safety and stability

The realization of a safe and reliable process is essential to construct a user-friendly device and meet the customers' demands. Therefore, in the first section of this chapter, possible hazards for the user and consistent product quality are identified by a preliminary hazard analysis, and counter-measures are determined. Afterward, a proof of principle for the chosen sensors is presented, and each sensor's threshold values are given in the second section. In the third section, a decision chart illustrates the malfunction determination and user-device interaction.

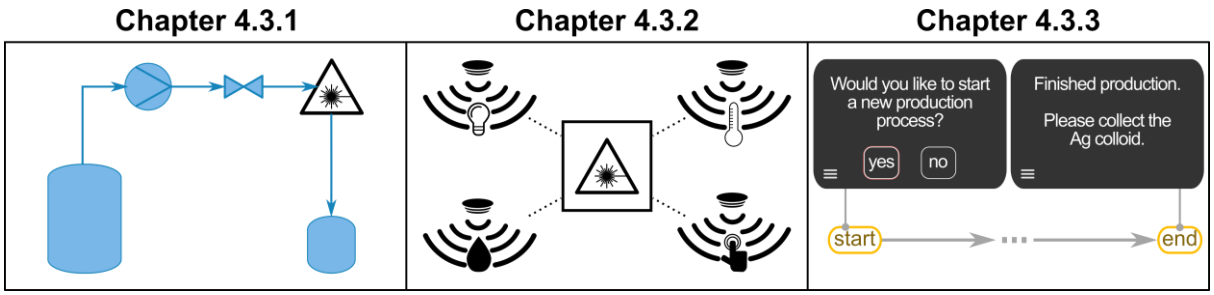

Fig. 49: Overview of process safety measures. Possible hazardous scenarios are determined with the help of a preliminary hazard analysis in chapter 4.3.1. Sensors are selected and implemented in chapter 4.3.2 to avoid these scenarios. A decision chart describing the user-device interaction is presented in chapter 4.3.3.

4.3.1. Preliminary hazard analysis of the automated ablation process

The piping and instrumentation diagram (PID) is designed to show the interaction between the different items of the device, determine necessary safety measures and prepare an equipment list. The PID (Fig. 50) is constructed following the DIN EN ISO 10628 and ISO 3511, with the exception that control units (labeled with “E” for electronics) are included [398, 399]. Including the control units, ensure a complete safety evaluation of the device, as explained later in this section. The equipment list can be found in the appendix (Tab. S 12).

In Fig. 50, all items in contact with liquids are colored blue, electronic control units are yellow, and beam guiding items are green colored. The tanks B-1, B-2, and B-3 contain stabilizer solutions, which will be the solvent for the produced colloid. The fluids are pumped from the lower to the upper level of the device using a piezoelectric micropump (P-1, P-2, P-3). One-way check valves (V-4, V-5, V-6) are installed behind each pump so that reflux and intermixing of the different fluids due to the cross valve V-1 is prevented. The removable ablation chamber B-5 is connected to the device’s fluid system by a valved quick-coupling (V-2), which ensures liquid hold back in the ablation chamber when the chamber is removed, protecting the user and device from dripping liquids. The ablation chamber's outlet is a 3d printed nozzle (V-3), from which the liquid flows into the collection vessel (B-4). The containers B-6 and B-7 are collecting trays for liquids. The irradiation for the ablation process is emitted by the laser (O-1). The two mirrors (O-2, O-3) are positioned perpendicular and moved to realize beam movement on the ablation target. Before entering the ablation chamber, the laser beam is focused by two lenses (O-4). The device's central control unit is a microcomputer (E-1) responsible for controlling, and processing the user input. Further sub-control units are responsible for communication with the micropumps (E-2), laser control (E-3), and movements of the mirrors (E-4).

A preliminary hazard analysis (PHA) is performed to identify malfunctions and possible hazards for the user. For example, if the fluid tanks (B-1 B-2, or B-3) is empty and without any safety measures, air would be pumped through the tubes and the ablation chamber. Consequently, no colloid is produced, and the laser damages the ablation capsule. Implementing a liquid level sensor can prevent the process from starting if the liquid level is insufficient. For the full analysis, see Tab. S 13 (appendix). The results leading to the implementation of sensors into the device’s setup are presented in the following. In total, five different kinds of sensors are applied in the device: liquid level sensors (L-01 to L-04), a humidity sensor (M-01), two optical sensors (O-01, O-02), a contact sensor (I-01), and a temperature sensor (T-01).

The liquid level sensors L-01 to L-03 are responsible for registering the current state of the sensor attached to the liquid tanks B-1 to B-3 and the process is stopped when a threshold for the lower liquid level in the tank is reached. Simultaneously, the user is informed by an

alarm on the display. Moreover, the sensors detect if a liquid tank is not in place, avoiding ablation in air and thus ensuring a safe process and constant process quality. The next liquid level sensor (L-04) stops the process when an upper liquid level is exceeded. This sensor is attached to the collecting tray B-7, which collects rinse water and spilled colloids, thereby protecting the device interior from water damage. Contrary to L-01 to L-04, the humidity sensor (M-01) is meant to detect minimal amounts of liquid and sets of an alarm if a critical signal intensity is reached. This sensor is positioned in the collecting tray B-6, into which water from leaks at the pump and valve connections drips. This tray is also slightly tilted so that the liquid is collected in one corner. The detection of small amounts of liquid is crucial at this position for two reasons. First, leakage at the pumps leads to a reduced liquid flow rate and changes the NP quality. Second, liquid, especially NaCl in the device's interior, can corrode the device case. Damaging of the electronic components is avoided by placing all control units above the liquid tanks and tubing.

The optical sensor (O-01) is placed behind the ablation target, initiates an alarm, and interrupts the process if the IR irradiation threshold is exceeded. Increased IR irradiation would indicate that either no target is inserted in the ablation chamber or the target is damaged. In the former case, irradiation can lead to damages at the ablation chamber or the device interior, and in the latter case, constant colloidal quality is no longer guaranteed. The other optical sensor (O-02) measures the colloidal extinction at the chamber's exit. Thus, possible malfunctions of the laser source, scanner, or fluid system can be determined. The contact sensor (I-01) is responsible for detecting if the ablation capsule is inserted correctly and be realized by Electrically Erasable Programmable Read-Only Memories (EEPROMs). EEPROMs can also save information about the material within the capsule and the number of left ablations. Finally, the laser temperature is monitored by the temperature sensor (T-01) to avoid overheating of the laser source.

For optimizing the device setup, the tubing between V-1 and V-2 should be minimized and ideally eliminated to avoid contamination with a different stabilizer leading to colloidal impurity and decreased stability. An ablation chamber with three different fluid inlets is designed to overcome this insufficiency (Fig. 51 A). Depending on the material within the chamber, one of the three inlets will be closed. For example, for Au, the entrances for water and the sodium chloride solution are opened and connected to the respective socket mounted in the device. This design makes V-1 and V-4 – V-6 obsolete but requires three quick coupling valves like V-2 and an altered ablation chamber design.

For the prototype, the liquid tanks B-01 – B-03 are inserted by the user, and, thus, he or she is responsible for positioning the tubing in the fluid tank correctly. To avoid user mistakes, the tanks, including the tubing, could permanently be placed in the trays. Next to the tubing inlet, a second cap at the top of the tank enables the user to refill the vessels without moving them or removing the tubing (Fig. 51 B).

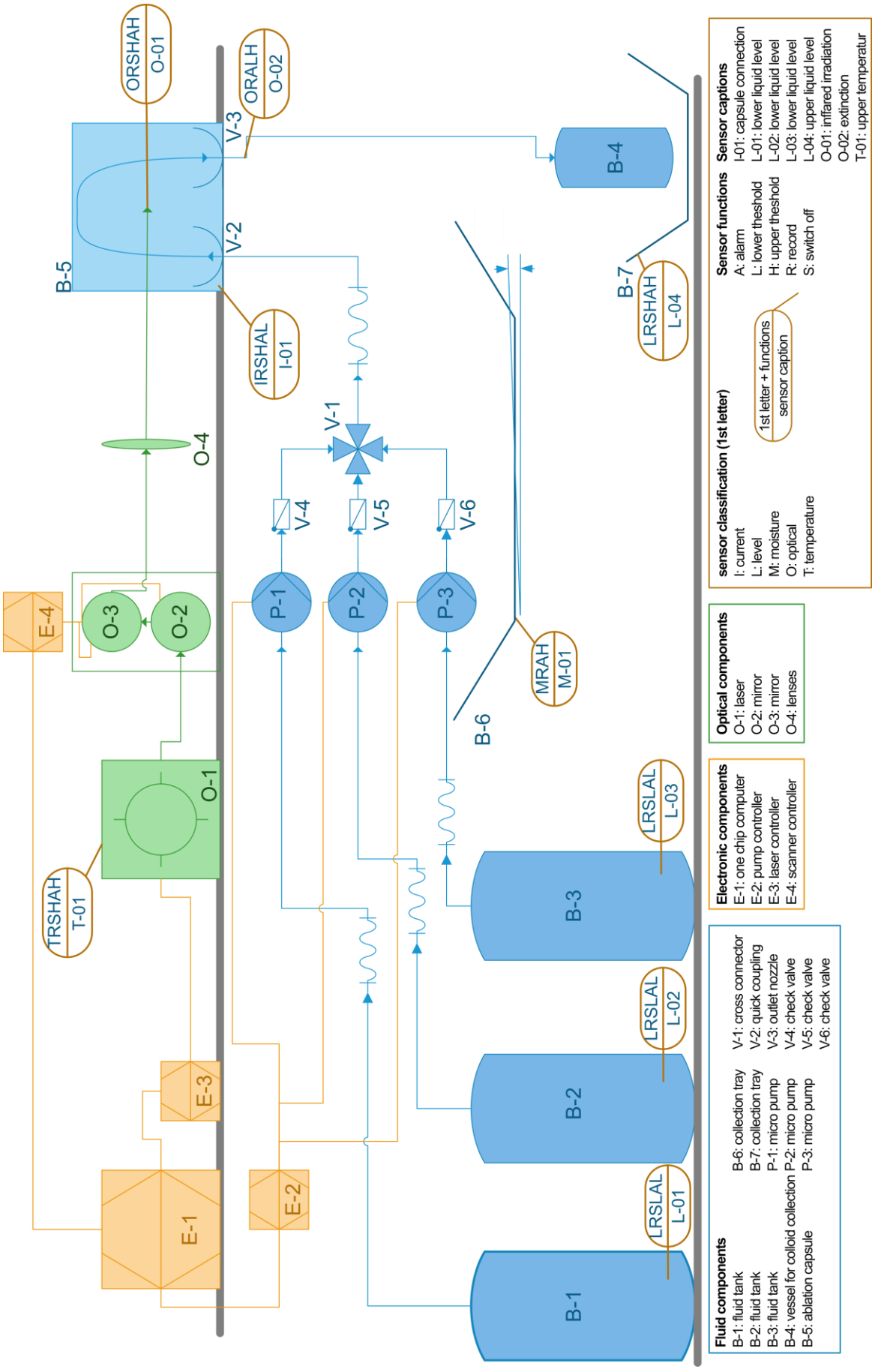

Fig. 50: PID of the automated device. Components in contact with the liquid are depicted in blue, electrical components in yellow, and optical equipment in green.

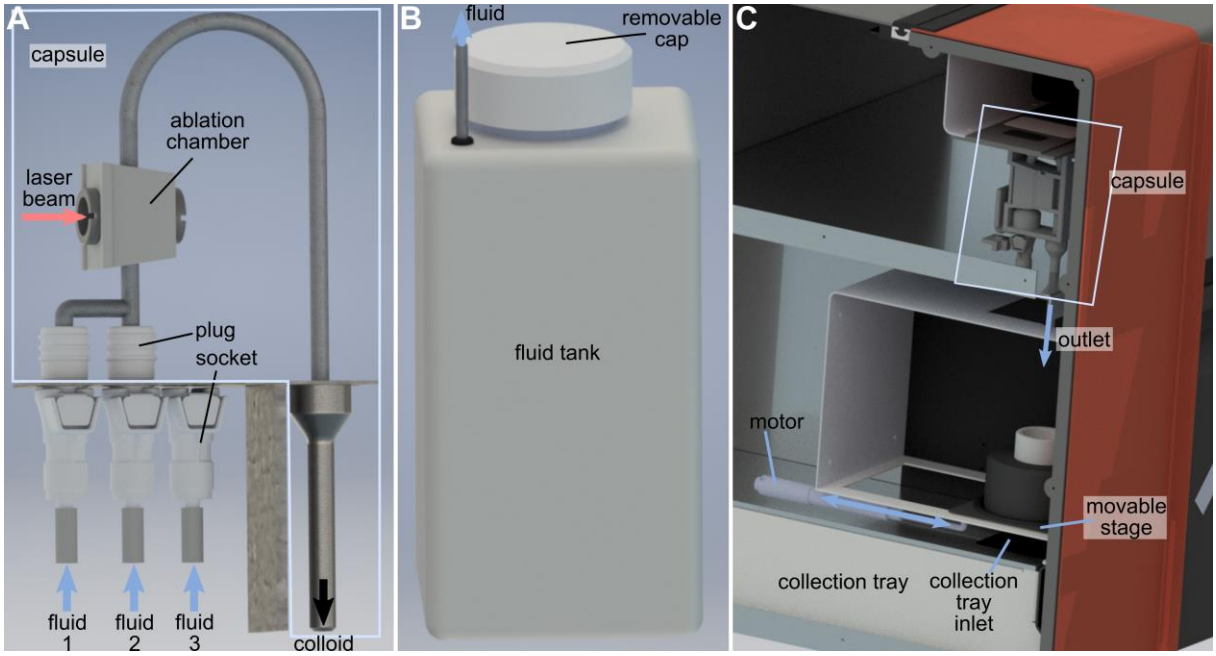

Fig. 51: Scheme for an optimized fluid entrance into the ablation chamber, to avoid contamination of colloids with other stabilizer solution (A), of an optimized fluid tank with a removable cap for fluid refilling (B), and an outlet modification to allow automated flushing and colloid collection (side blende is removed to enable insight into the device's interior) (C)

Moreover, the fluid outlet, flushing process, and the necessity for a run-in period of the ablation can be optimized. When the users wish to start the colloid production process, they insert the capsule and start the process. Then, the fluid system (Fig. 50, blue components) is flushed with the stabilizer collected by B-7. During the following run-in period of ablation, the produced colloid is also collected by B-7. For the product collection, the user is finally prompted to provide the colloid collection vessel B-4. However, if the necessity for the run-in time is due to the temperature increase of the ablation target (see section 4.2.2), the ablation process should only stop for a short time. About 1.5 h after starting the process, the user must be present at the device to insert vessel B-4. If the user is distracted from this step, either all colloid goes to waste, i.e., flows into B-7. If the process does not automatically stop or if the process is automatically stopped after the run-in time, the user would have to start the process again. Both scenarios are user-unfriendly, and an automated vessel change after the run-in time can achieve a higher convenience. Since V-3 and the outlet nozzle are permanently connected to the capsule, it is impossible to add an automated valve at the outlet. Another possibility would be using an automated stage above B-7 (see Fig. 51 C). Here B-4 would be positioned by the user before the process is started. The electric stage moves so that the fluid flows into B-7. After the flushing process and the run-in period, if it cannot be avoided (see section 4.2.2), the stage moves again, and the fluid is collected in B-4 without the user's interference.

In summary, a PID of the device is created, and a PHA is performed. Thus, the necessity of different sensors is determined. The optimization for the fluid movement, the liquid tank handling, and the sample collection are also proposed.

4.3.2. Selection and adjustment of sensors

The sensors to avoid critical malfunctions identified in the previous section will be introduced and tested for their effectiveness in the following.

The concentration sensor O-02 consists of a light-emitting diode (LED) emitting 470 nm and a corresponding detector (photoresistor) positioned on the opposite of the LED. The colloid containing tube is positioned in between (Fig. 52) so that the emitted light is partially extincted by the colloid. Since the emitted light intensity of LEDs varies with their operating temperature, it is necessary to provide a run-in period of 60 min (appendix, Fig. S 22).

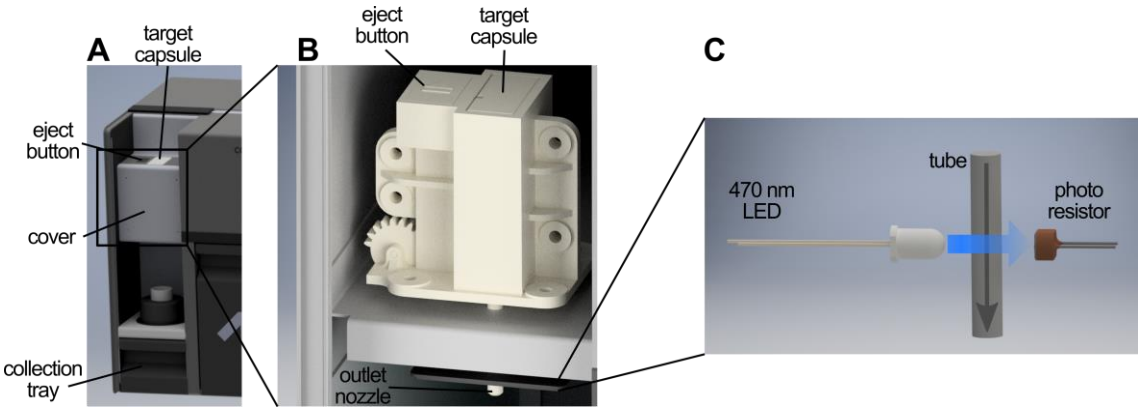

Fig. 52: The target inset and colloid outlet (A) and a close up of the capsule mounting with the concentration sensor positioned at its outlet is shown. Panel C shows the composition of the colloid concentration measurement.

For evaluation of the sensor's usability, the sensitivity, i.e., the sharpness between the colloids, water, and air signals, the response to concentration changes, and temporal consistency, is analyzed. The detector signal distribution for Ag, Au, Pt, water, and air are shown in Fig. 53. The mean signals of the colloids (0.260 – 0.285), water (0.220), and air (0.245) can be distinguished from one another. However, although the mean values for the colloids are significantly different (0.285 for Ag, 0.275 for Au, and 0.260 for Pt), the data range overlaps for Ag (0.235 – 0.330), Au (0.225 – 0.310), and Pt (0.240 – 0.290) is large. In conclusion, the sensor can detect if water, air, or colloid, in general, flows through the tube. For the differentiation between Ag, Au, and Pt, many data points or, i.e., a long measuring period is necessary. The best concentration-signal dependency is found for Au (Fig. 54). With a central emitted wavelength of 470 nm, this is the transitioning region between inter- and intraband absorption for Au, but the particle size-dependent intraband absorption for Ag, which could explain the strong fluctuation for the Ag calibration (Fig. 54 A). However, Pt does not show an interband absorption and a comparably weak intraband absorption at 470 nm, which leads to strongly fluctuating signals (Fig. 54 C). Considering the time-dependent

sensor signal over 6 h (Fig. 55), the values for Ag, Au, and Pt often overlap and do not reach a constant level.

Since the sensor O-02 should determine process-related concentration deviation, e.g., due to laser or pump damage, and respond within minutes, the selected concentration measurement is not suitable. Changing to a diode with a different wavelength does not lead to an improvement, as the spectra of at least two of the colloids overlap for most of the wavelength range from 200 to 900 nm (Fig. S 23). Instead of determining the concentration by a single wavelength, a broadband emitter and a corresponding detector can be used.

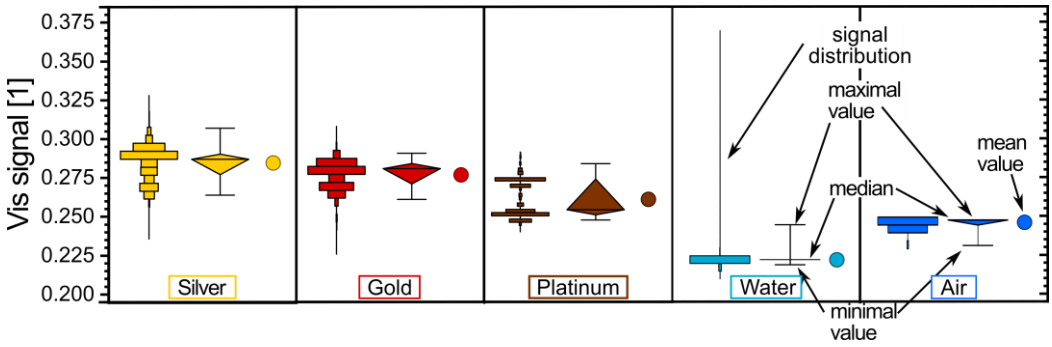

Fig. 53: Sensor signal distributions for Ag (yellow), Au (red), Pt (brown), water (light blue), and air (dark blue) are shown as bars. The corresponding boxplots are depicted in a diamond shape and the mean value as a circle. The whiskers of the boxplot range from 1 % to 99 % of the detected values.

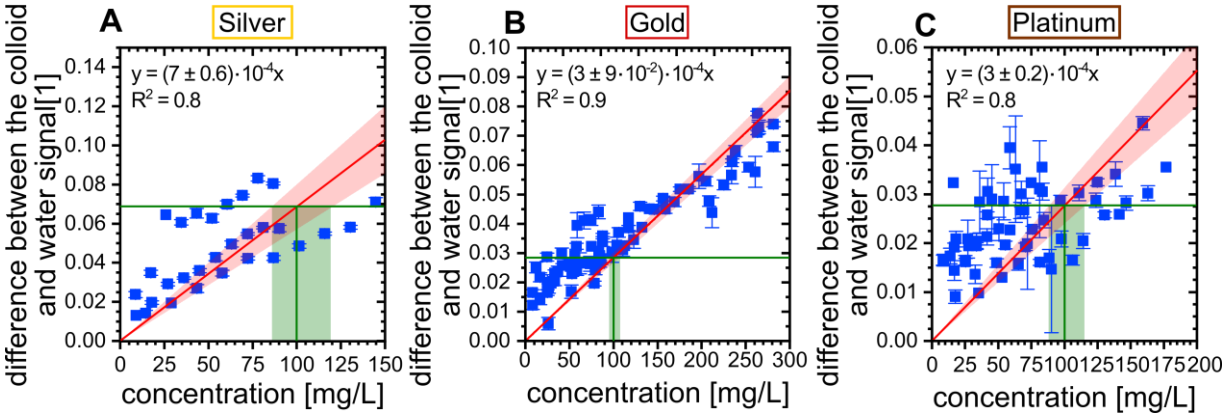

Fig. 54: Calibration of the concentration sensor O-02 for Ag (A), Au (B), and Pt (C). A linear fit is depicted as a red line with a 95 % confidence interval (red shaded area). The expected differences between the colloid and water signal for a concentration of 100 mg/L are shown as horizontal green lines and the corresponding error range according to the confidence interval of the fit as the green shaded area.

In conclusion, sensor O-02 can distinguish between water, air, and colloid in general. Bubbes produced during the ablation process do not disturb the sensor signal (compare Fig. 53 and Fig. 55). The sensitivity regarding leakage detection is dependent on the measuring interval.

With the interval set to 2 s, a minimal amount of approximately 0.1 mL of air is required until the sensor detects the leakage. However, the sensor is not sufficient for determining and monitoring the concentration of the colloids. The setup can verify the target monitoring O-01 and the liquid level detection L-01 – L-03. In the former case, no target can be ablated, and thus, only water is detected by O-02, and in the latter case, no water, and consequently no colloid, is pumped so that O-02 detects air.

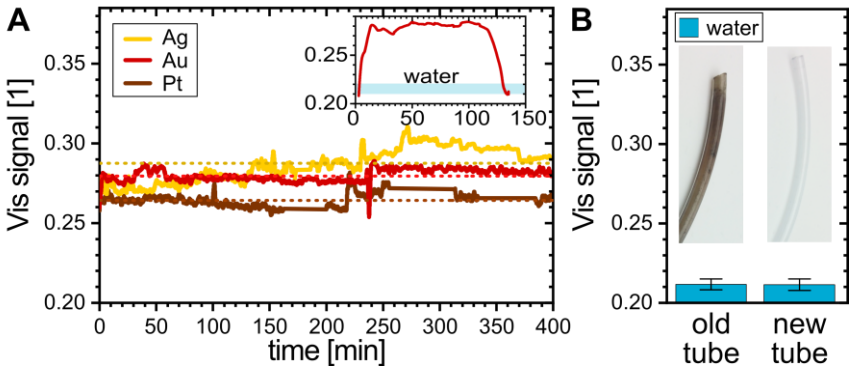

Fig. 55: Sensor signals for Ag (yellow), Au (red), and Pt (brown) colloids over more than 6 h (A). The respective mean signal is depicted as a horizontal dotted line. The inlay of panel A shows an exemplary run where the colloid production is started at 0 min and stopped at 100 min for Au. Influence of the tubes (left: extensively used, right: new) on the sensor signal (B).

The liquid level sensor ensures that air does not enter the fluid system and negatively influences the colloidal quality by detecting a minimal amount of liquid within in tank and stopping the process if there is a risk of draining. A contactless capacitive sensor is selected for this measurement since sensors positioned inside the fluid tank potentially contaminate the fluid and vice versa. The contamination occurs if particles from the sensor diffuse into the liquid or from another liquid if the sensor is not cleaned correctly in-between. As shown in Fig. 56 B and C, the sensor is positioned on the outside of the fluid tank at the height corresponding to the minimal amount of fluid for one ablation process.

Fig. 56 shows that if the sensor patch is at the same height or lower than the liquid level, its signal is maximal (Fig. 56 B) and decreases to zero if the liquid level falls below the sensor patch (Fig. 56 C). When the user initiates the ablation process, the liquid level sensor signal should be maximal. If its signal is below, not enough liquid for the process is left in the fluid tank and the user is advised to refill the tank. If the user can select between different colloid amounts, further liquid level sensors must be put at the corresponding position. The liquid level sensor signal should be higher than 75 % of the maximal signal, i.e., >1.2, to account for transitioning liquid levels.

Next to detecting a lower liquid level in B-1 – B-3, the sensor is used to monitor an upper liquid level in B-7. Before the production, the residual collection tray volume should be

sufficient to collect the cleaning water before and after the process and the colloid if the vessel is broken, missing, or knocked over. Since the dripping tray for the prototype is produced of metal, the sensor cannot adhere to the vessel wall. For the final device, it is recommended to select a plastic collection tray, e.g., made of PE. Thus, the sensor can be positioned at the inner slot wall. In contrary to the detection of a liquid level, in this case, the initial sensor value should be at the minimum when the user initiates the process, i.e., the sensor signal must not be higher than 0.1. Otherwise, the user will be warned and requested to empty the tray.

All in all, the chosen capacitive sensor enables the contactless monitoring of the liquid level in the fluid tanks and the collection tray. It was shown that the sensor responds fast to a change in the liquid level. If the collection tray is made of plastic, the same sensor can detect the liquid level in the collection tray B-7.

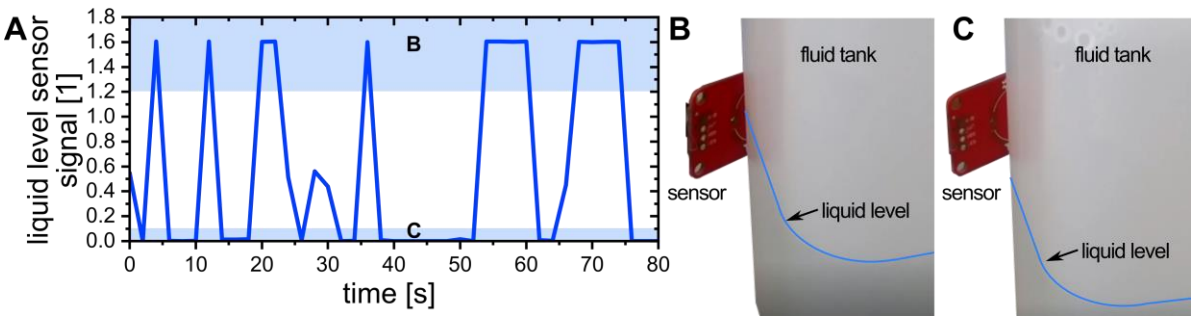

Fig. 56: Time-dependent signal of the liquid level sensor (A) when the liquid level fluctuates between a height above (B) and below (C) the sensor patch. These states correspond to the photographs in B and C, where the blue line marks the current liquid level in the tanks.

An initial analysis of the weak points reveals that connections between different fluid components are likely to break and leak liquid in the device housing. Therefore, a collecting tray (B-6) equipped with a leakage sensor M-01 is positioned underneath the pumps and valves. Dripping liquid is collected in one corner of the tray, where the leakage sensor is placed by tilting the collecting tray. This setup is capable of detecting leakage of already 10 µL (Fig. 57). For higher amounts of liquid, the signal increases steadily. Note that the signal is not proportional to the liquid volume, as can be seen at 60 s when spreading the fluid over the sensor leads to a signal increase. Since the sensor is positioned in one corner of the tray, the leaking liquid is not necessarily detected immediately, and small amounts could not be detected at all. Therefore, the sensor must give a warning when already a signal of 0.05 is reached. Further conductive sensors can be positioned in the trays. In theory, leakage detection by a capacitive sensor is also possible. In this case, the metal tray must be electrically insulated from the rest of the device and connected to the sensor patch. The conductive tray works as an enlargement of the sensor patch. It is shown that a conductivity

sensor capable of detecting microliters of liquid. A threshold of 0.05 of the process abortion is determined to prevent the device's interior from damage.

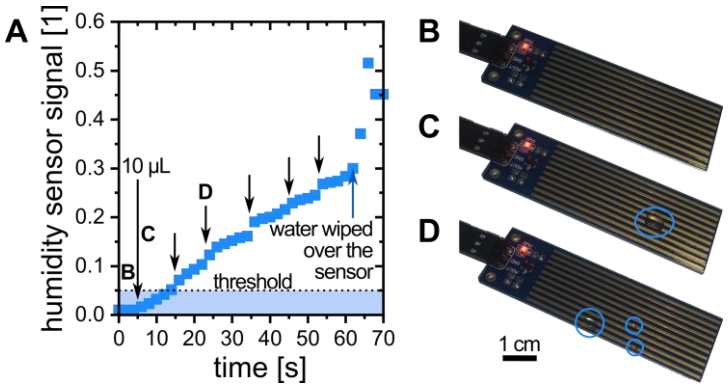

Fig. 57: The humidity sensor signal over time (A). The black arrows indicate the points where additional 10 µL of Milli Q water is dipped on the sensor, and the blue arrow where the liquid already on the sensor is spread over its surface. The photographs B-D show the sensor with none, one, and three droplets corresponding to the marked arrows in A.

An intact target is crucial for achieving the desired concentration. Also, parts of the capsule are ablated by scattered irradiation if the target is broken, leading to precipitation of the NPs and an unreliable colloid quality. Thus, target integrity is essential for reliable colloid production. During multiple ablation processes with one capsule, the passed ablation time of the target is determined by electrical sensor I-01. Thereby, the device estimates if enough target material is left to complete the process before the ablation process starts. Additionally, an IR detecting diode detects the scattered irradiation behind the ablation target.

For detecting a target breakdown, the IR diode is positioned in the capsule behind the target (see Fig. 58 A). The ablation chamber backside consists of an optical window with high transmissibility in the infrared spectrum. Thus, low amounts of the laser irradiation passing through the target are absorbed or scattered by the chamber backside, and a sensitive measurement can be assured. An example of the IR signal measurement is when the target is damaged during ablation (Fig. 58 B). At the beginning of the ablation, the detected amount of IR irradiation fluctuates around 800. As shown by the inset, the target is still intact at this point so that the detected signal is assigned to scattered irradiation passing by the target's sides. Between 18 – 22 s, the signal decreases to 150 due to the increased conductivity of the diode. The inset in Fig. 58 B shows that the first holes can be observed in the target. A signal threshold of 200 is selected to enable an early breakdown detection of the target. All in all, an IR diode positioned behind the target allows reliable detection of the target breakdown. A minimal threshold value of 200 is identified for aborting the ablation process to prevent damaging the automated device during the ablation process.

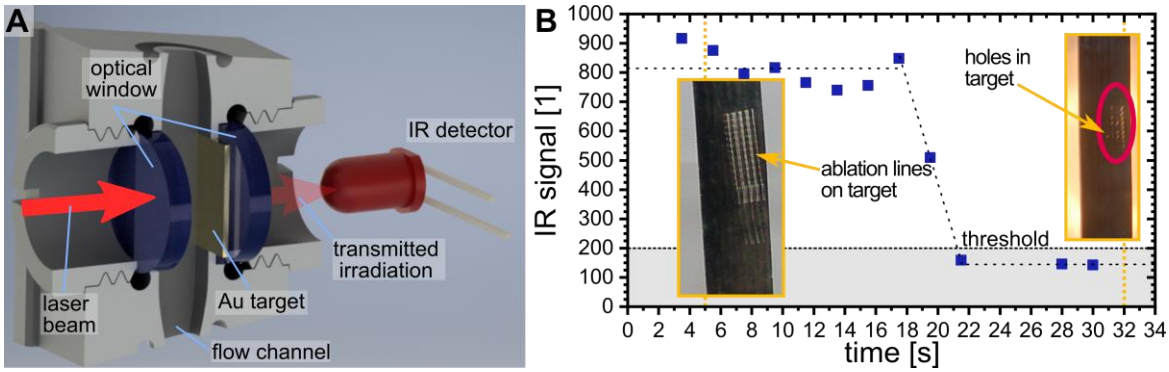

Fig. 58: Scheme of the ablation chamber cross-section shows the setup for target breakdown monitoring (A). Time-dependent IR sensor signal (B). A 100 µm Ag foil is used, starting with an un-irradiated foil. The photographs show the target condition after 5 s and 32 s of laser irradiation; the picture after 32 s is shot with transmitted light to make the holes visible (red circle).

A summary of all chosen sensors, as well as evaluations, are given in Tab. 11. The majority of selected sensors ensure the desired function of the device. However, minor insufficiencies are identified (orange dot in Tab. 11) and discussed. The leakage detection sensor M-01 can detect drops of 10 µL. However, it needs to be examined if the fluid, dripping into the collection tray B-6, reaches the sensor with sufficient velocity. If not, it is recommended to use more leakage sensors at different positions in the collection tray B-6 or to use a capacitive sensor or a combination of both. The concentration measurement O-02 can only distinguish between air, water, and a colloid in general. For quality control of the device, a time-dependent concentration measurement for Ag, Au, and Pt is essential. A measurement with multiple wavelengths may be suitable for the concentration measurement while also providing the option of monitoring the NP size.

Tab. 11: Summary of the selected sensors by task and principle of measurement, their threshold values for detection of malfunctions, and an evaluation of the eligibility of the chosen sensor

No. in Fig. 50	sensor task	physical principle of the measurement	threshold values	evaluation
L-01 – L-03	ensure a minimal fluid level in liquid tank B-1 – B-3	capacity difference for air and water	>1.2	●
L-04	ensure that a maximal fluid level B-7 is not exceeded	capacity difference for air and water	<0.1	●
M-01	check of leakage	conductivity	>0.05	●
O-01	detection of target breakdown	inner photoelectrical effect	<200	●
O-02	differentiate water, air, and colloid	light extinction	water: 0.215 – 0.225 air: 0.230 – 0.250 colloid: 0.250 – 0.290	●
	differentiate between Ag, Au, and Pt	light extinction	-	●
	enable determination of the colloid concentration	light extinction	-	●

●: the sensor is not suitable for the task ●: the sensor is suitable, but the setup can be improved to achieve higher reliability ●: the sensor is suitable

4.3.3. Decision chart for process monitoring and handling of malfunctions

After the device setup and possible hazardous scenarios are discussed in section 4.3.1, and the suitability of different sensors are tested individually in section 4.3.2, the interaction of the individual sensors and the user's interaction with the device is presented in the following.

The ablation process is shown in Fig. 59 as a decision chart and starts when the user initializes a new ablation process. When the user is asked to select the desired colloid material, the capsule contact sensor checks if the correct capsule is inserted and otherwise requests the user to remove the capsule and insert the correct one. Afterward, the user is asked to choose the required colloid volume, and the sensor signals are checked (Fig. 60). If all sensors signals are within specifications, the user confirms the selection and starts the automated process. If errors occur during the sensor check, an error message is displayed, and the user is requested to act accordingly, e.g., refill the fluid tank if the amount of liquid in B-1 is insufficient for the process. After the user’s confirmation, the sensors are rechecked. If all sensor signals meet the specification, the user is informed about the ablation start and the remaining process time is shown on the display.

The laser is now turned on and the 10 min warm-up phase is initiated, after which the flushing process with the respective stabilizer solution starts. As determined in section 4.2, the current process setup needs 1.5 h to reach steady-state conditions. If this can be solved in the future, the following process part is obsolete and is therefore marked gray in Fig. 59. At the beginning of the run-in period, the laser starts emitting, however, the initial colloid is discarded. During the run-in time, sensors are checked every 10 s and the process continues if all signals match the specifications. After 1.5 h, the electrical stage is moved so that the vessel B-4 collects the colloid. After the final process time is reached, the laser is shut off, the stage is moved, and the flushing process with water is initiated for 5 min during which the user can collect the colloid.

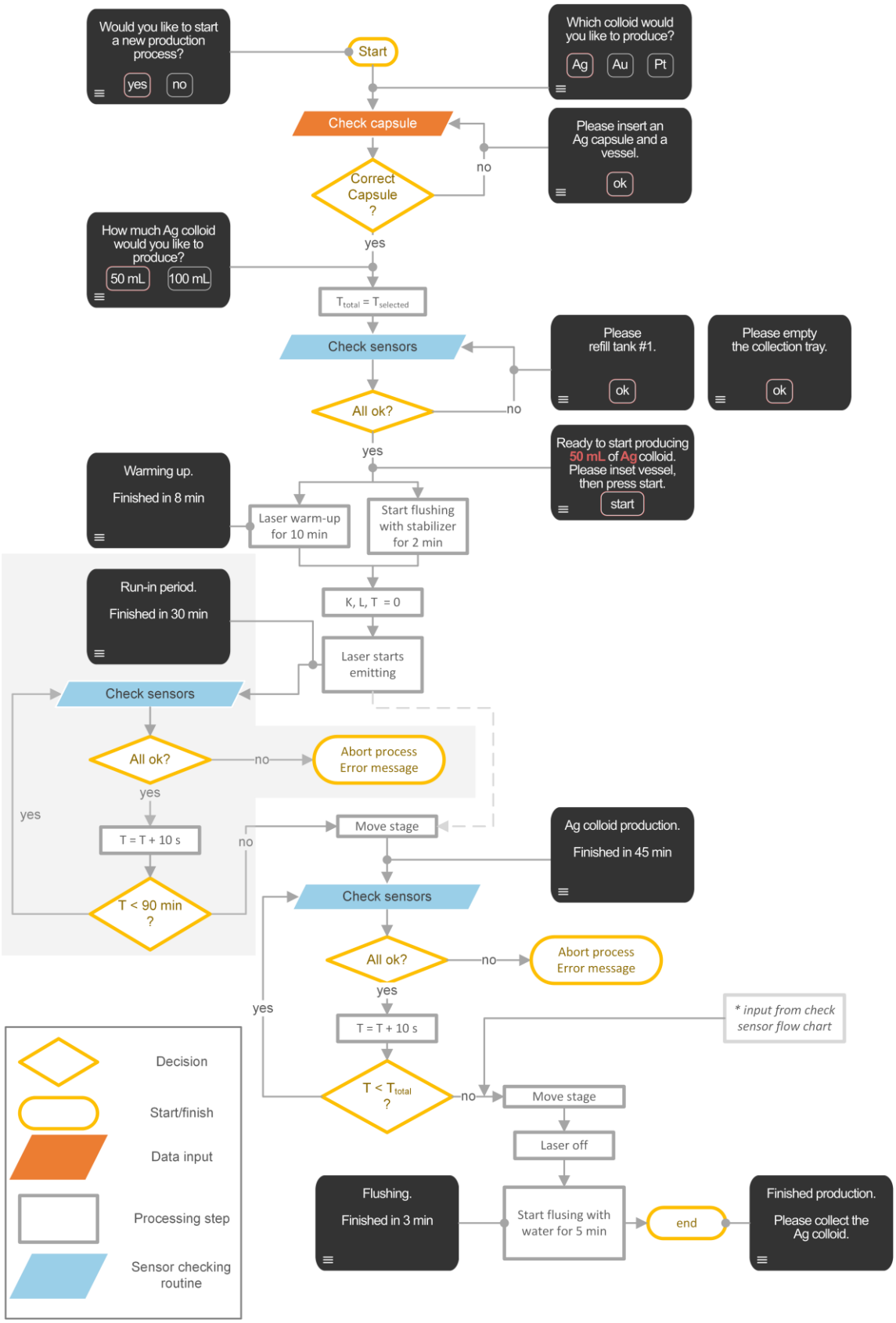

Fig. 59: Decision chart for automated colloid production. The black boxes represent possible messages for user-interaction. The gray shaded area is the process part for a run-in period. It is obsolete (dashed line as an alternative path) if future investigations can eliminate the run-in period. The variables K, L, T are used for monitoring time steps and the number of loops. The “check sensors” routine is explained in detail in Fig. 60.

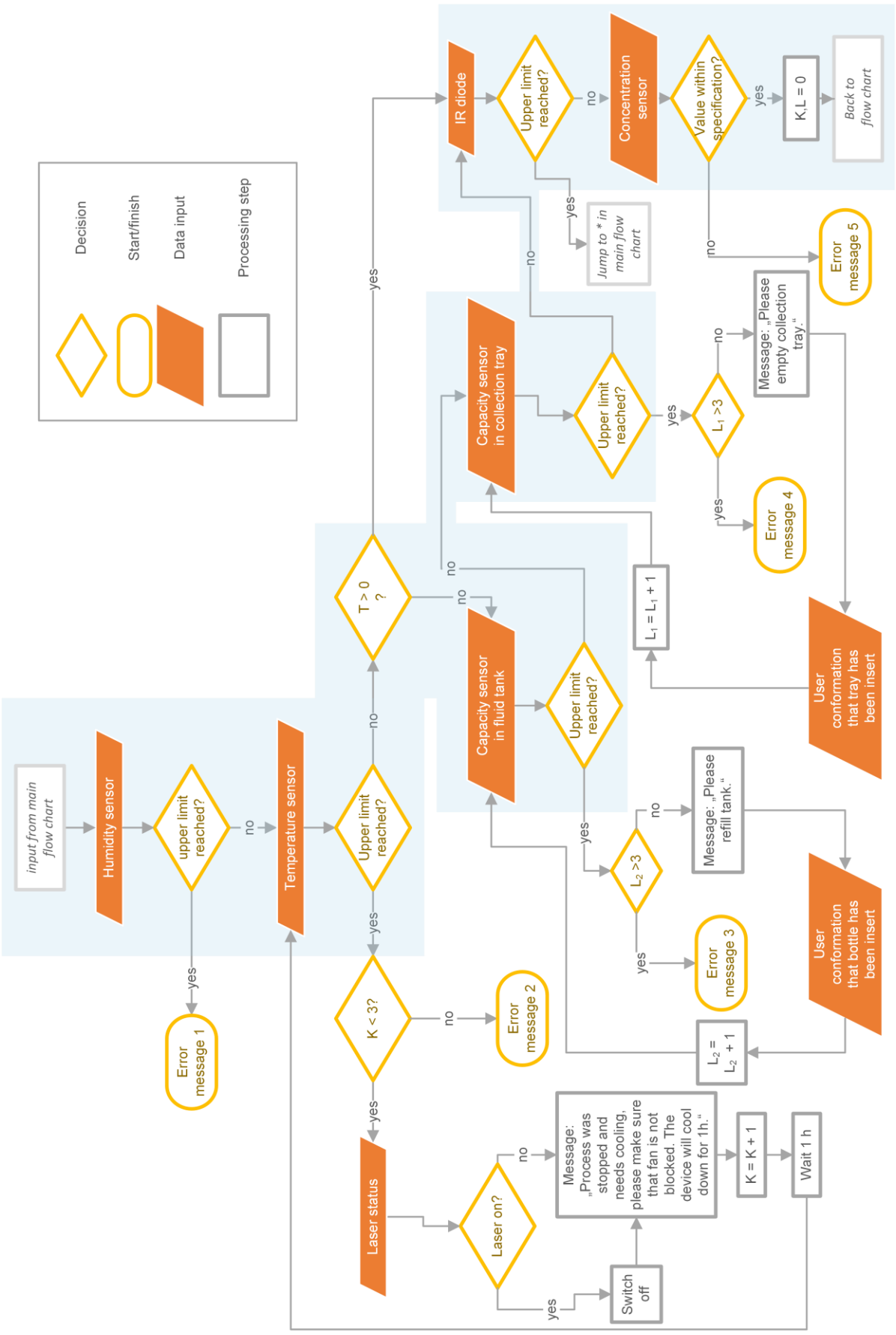

Fig. 60: Decision chart of the sensor checking routing. If a sensor signal is not within specification, the ablation process is aborted and an error message is shown (see Tab. 11). The blue shaded area shows the optimal path, where the measurements meet all criteria.

The sensor check routine is shown in Fig. 60. At first, the leakage sensor checks if the signal is out of the specification and then aborts the process and displays an error message. The leakage of the fluid system requires maintenance by a technician and the user cannot operate the device anymore. If the value is within specification, the temperature of the laser is checked. When an upper temperature limit is detected, the process is aborted. However, if the device is heated, e.g., by incoming sunlight or a blocked fan, the user received the message that the device should be put in a colder environment and blocking of the fan should be checked and removed. After an hour, the user is allowed to restart the process if the laser's temperature has dropped. However, if the temperature could not be decreased after the third attempt, maintenance by a technician is required since the laser might be damaged.

Next, all liquid levels are checked. The fluid vessels are only checked at the first checking routine since both levels are adjusted for the worst case. The IR diode checks for a target breakdown and ends the production if necessary. The user is informed that the process was aborted ahead of schedule but that the colloid quality is unaffected. Afterward, the concentration sensor checks if the specifications are met. Before the beginning of ablation, the signal for water is expected. If this criterium is not met, the pumps might be damaged. During the ablation process, the signal for colloids is expected and a deviation from the specification indicates defects of the scanning system or laser.

Due to several sensors, a reliable and automated process can be realized. Moreover, specific malfunctions can be identified depending on the sensor, not meeting the specifications (Tab. 12). This cause analysis allows preliminary diagnoses and reduces maintenance service.

Tab. 12: Overview of possible error messages, where the number corresponds to the error message number in Fig. 60.

No.	Sensor	Explanation	Cause
1	M-01 (leakage detection)	Leakage in collection tray B-6 detected	Tube connection came off or damage at pump or valve
2	T-01 (temperature sensor)	Temperature of the laser is too high	Cooling is insufficient, e.g., due to damage of the fans or the laser is damaged
3	L-01 – L-03 (liquid level in fluid tank B-1 – B-3)	Liquid level is too low for ablation or cannot be detected	The tank was not refilled or positioned by the user The sensor is damaged
4	L-04 (liquid level in collection tray B-6)	Liquid level is too high	The user did not empty the collection tray The sensor is damaged
5-1	M-02 (extinction measurement)	During flushing or colloid production, the detected signal is 0.230 – 0.250	Air is sucked into the fluid system
5-2	M-02 (extinction measurement)	During flushing, the detected signal is >0.250	Colloid flows through the system, possible malfunction of the laser controller
5-3	M-02 (extinction measurement)	During flushing or colloid production, the detected signal is <0.215	Extinction sensor is damaged
5-4	M-02 (extinction measurement)	During colloid production, the detected signal is <0.225	No colloid is produced, laser or scanner could be damaged
5-5	M-02 (extinction measurement)	During colloid production, the detected signal is >0.29	Extinction sensor is damaged, or the flow rate is too low so that colloid concentration is higher than specified

4.4. The transition from the development phase to the technology transfer phase

This section discusses the perspectives and potentials of the automated laser ablation in liquids using compact lasers. In the first section, the final device price and the capsule prices are estimated and costs for the automated ablation, commercial colloids, and chemical synthesis are compared. Moreover, the possible production capacities of different applications are calculated in section two. Therefore, exemplary catalysts, functionalized micro powders, and bio-inks are produced. Section three shows that, especially for larger-scale testings, the current device capacity reaches its limit, and a further increase in productivity might be necessary. Therefore, the beam splitting is tested for productivity and device capacity improvement.

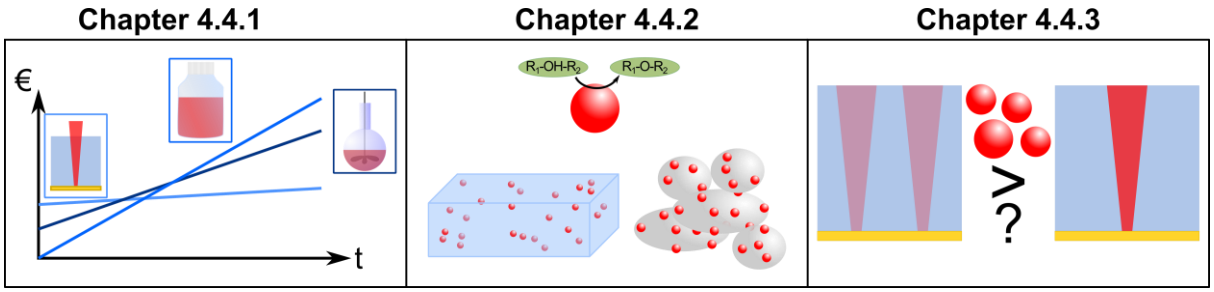

Fig. 61: Overview of measures to perform the step from development to technology transfer phase of the automated LAL device. First, the device price is estimated and its economic feasibility compared to chemically synthesized and commercially available colloids. In chapter 4.4.2, the production capacity and quality of different downstream products are determined and, in chapter 4.4.3, beam splitting as a measure of capacity increase is presented.

4.4.1. Economic feasibility of the automated laser ablation

The automated device based on a 500 mW and 1 ns laser can produce about 480 mL of Ag, 960 mL Au, and 1440 mL of Pt colloid with a concentration of 100 mg/L per workday, i.e., within 8 h. The automated colloid production can be useful for researchers, who either frequently purchase colloids from a commercial distributor or self-synthesized them. The advantages of an automated synthesis are the on-demand on-site-production compared to the purchasing and the time-saving compared to the self-synthesis. Additionally, the economic benefit of the automated device is important. In the following, the possible maximal sales price for the device, as well as the running costs, will be estimated. The resulting costs for the automatically produced colloids are compared to the purchase and chemical synthesis of Ag, Au, and Pt colloids, respectively.

First, the material costs for the device and the target capsule are estimated. The material list for the device is based on the flow chart depicted in Fig. 50. The distribution of the material costs amongst different categories and the total charges are shown in Fig. 62. A detailed overview of the material price composition (Tab. S 15), the variable costs (Tab. S 16), fixed costs (Tab. S 17), and overhead costs (Tab. S 18) can be found in the appendix. More than two-thirds of the total material costs (13500 €) consists of the laser price, followed by the case with less than 15 % and 2600 € in total. Since the laser is not yet a series model, it is expected that the laser price decreases within the next years [358]. Both the laser and case prices can be reduced if the number of sold devices increases. Additionally, the variable manufacturing costs, which are costs for logistics, packaging, and shipping, need to be considered to determine the device sales price. Lastly, fixed and overhead costs need to be considered.

For a first calculation, an annual sale of ten devices and 50 Au capsules is assumed. Since the sales of devices and capsules are only estimations and the capsule price is strongly influenced by the added amount of fixed and overhead costs, for a first calculation, the fixed and overhead costs will not be split but contribute entirely to the device price. The effect of possible changes in the fixed and overhead cost distribution will be discussed at the end of this section. The minimal net sales price and the net and gross price for the device and the capsules are summarized in Tab. 13. For this calculation, profit margins of 90 and 40 % with regard to the minimal net purchasing price are assumed so that the net sales price is the sum of both. For an exemplary calculation of the automated LAL device manufacturer’s earnings, the device's and capsuled’s calculated gross price are rounded up and shown in Tab. 14. The cost distribution of the final gross sales price for both the device and the capsules are shown in Fig. 63.

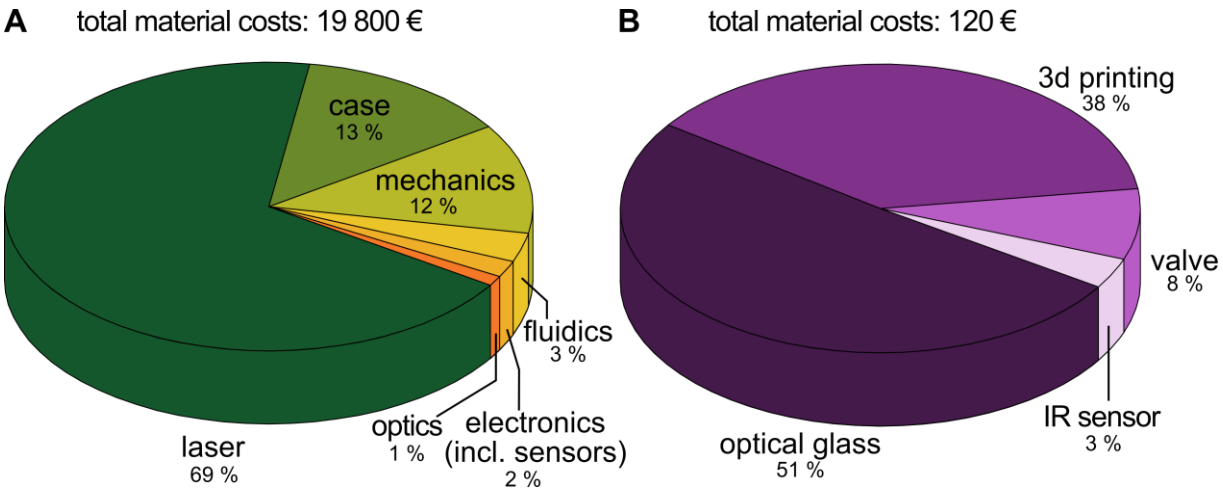

Fig. 62: Material costs divided by functional categories and the total material costs of the device (A, based on Tab. S 12) and the capsule (B, based on Tab. S 17). The target price is not included in the capsule price here.

Tab. 13: Price composition of the net minimal purchasing price of the automated device and the different capsules.*

		device	capsule (Ag)	capsule (Au)	capsule (Pt)	
	material costs per piece	19 758.35	122.84	195.44	193.44	€/piece
+	variable manufacturing costs	+ 603.35	+ 16.60	+ 16.60	+ 16.60	€/piece
+	fixed costs	+ 14 720.00	+ 0.00	+ 0.00	+ 0.00	€/piece
+	overhead costs	+ 1540.00	+ 0.00	+ 0.00	+ 0.00	€/piece
=	**minimal net purchasing price**	**= 36 621.70**	**= 139.44**	**= 212.04**	**= 210.04**	**€/piece**
+	profit margin	90 %	40 %	40 %	40 %	
=	**price (net)**	**69 581.22**	**195.22**	**296.86**	**294.06**	**€/piece**
=	**price (gross)**	**82 801.65**	**232.31**	**353.28**	**349.93**	**€/piece**
=	**sales price**	**85 000.00**	**235.00**	**360.00**	**350.00**	**€/piece**

* supplementary information: material and manufacturing costs for the device in Tab. S 12 and Fig. S 17, the material and manufacturing costs for the capsule in Tab. S 17 and Tab. S 18, the fixed and overhead costs in Tab. S 14 and Tab. S 16

Tab. 14: Earnings according to the price composition for the device and capsules with an estimated sales of 10 devices and 50 Au capsules. The trade tax rate of Essen in 2018 (480 %) is taken for calculation and a corporation is assumed as a legal business form.

		total [€/year]	device [€/piece]	capsule [€/piece]
price (gross) [€/piece]			82 800	350
sales price [€/piece]			85 000	360
earnings before taxes and interests [€]	**=**	**326 000**	32 200	80
Design licence [3% of earnings] [€]	-	9 780		
Patent licence [2% of earnings] [€]	-	6 520		
earnings before taxes, after interests [€]	**=**	**309 700**		
trade tax [€]	-	54 770		
corporate tax [€]	-	48 900		
solidarity surcharge [€]	-	2 690		
earnings after taxes and interests [€]	**=**	**203 340**		

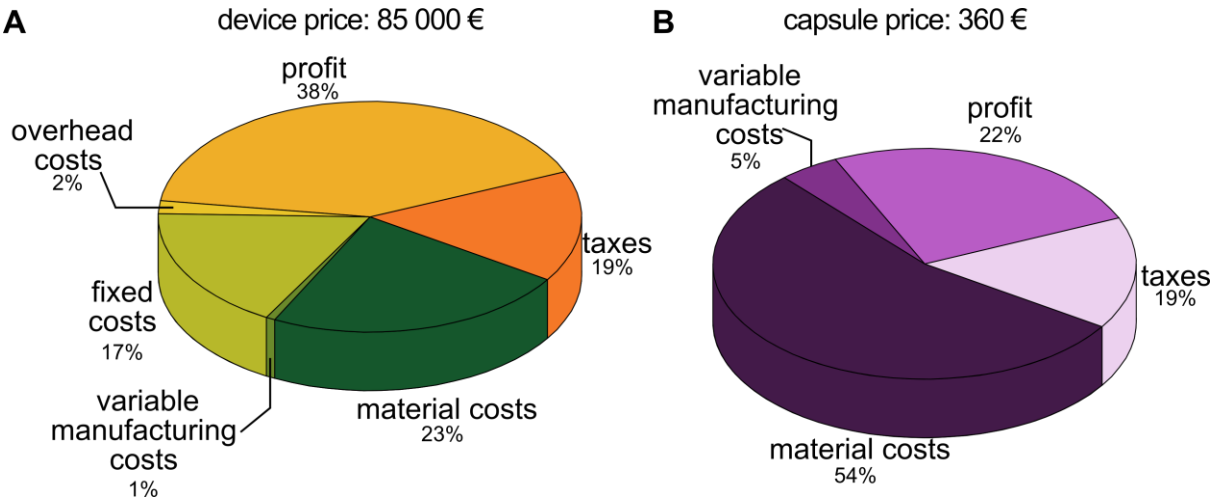

Fig. 63: Price composition of the device (A) and an Au capsule (B). The percent values represent the cost distribution of the categories among the sales price (see Tab. 13).

The colloid prices of representative information from distributors are summarized in Fig. 64. For most Ag, Au, and Pt colloids, an exponential decrease in the price per gram of NPs can be observed with the batch size, even though colloids with different stabilizers and sizes are compared. An exception from this trend is the comparatively cheap “Econix” Ag and Au colloid from nanoComposix, which has a high concentration of 5 000 mg/L and is stabilized with polyvinylpyrrolidone (PVP). For the economic comparison of the commercial and automatically produced colloid, a typical batch size of 100 mL is selected so that Ag, Au, and Pt a mean purchase price of 292, 356, and 421 €/100 mL, respectively, are determined (Fig. 64, blue shaded area). Contrary to the metal prices (Tab. 13), commercial Pt colloid is more

expensive than Au colloid, presumably, because Au colloids are more commonly used in research (Fig. 1).

The device's investment and running costs (listed in Tab. S 19 in the appendix) are compared to the purchase price of 100 mL of colloids (Fig. 65) or produced once per week. The shipping costs for commercial colloids are neglected. Next to the colloids' mean purchase price, the minimal and maximal prices in Fig. 64 are marked. The amortization time is reached when the device's cumulated costs fall below the purchase or synthesized colloid costs. For Ag, Au, and Pt, the automated production is economically more feasible than colloid purchase after 6, 5, and 4 years.

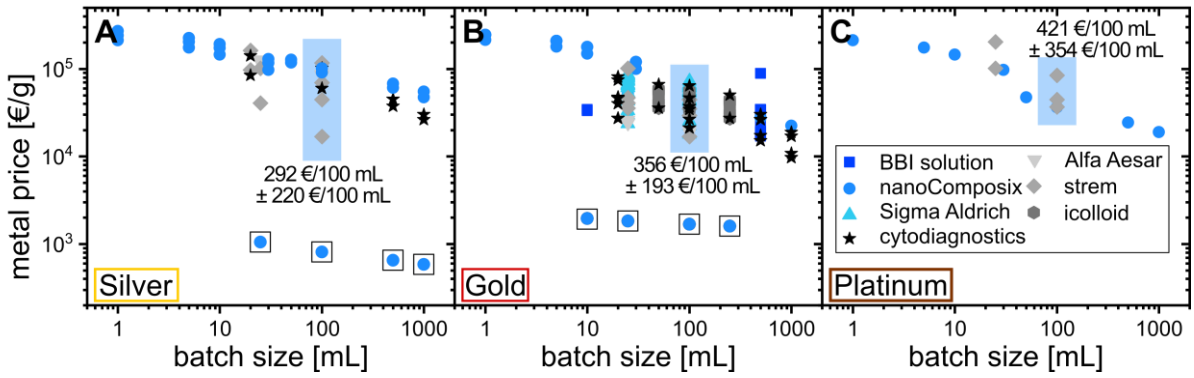

Fig. 64: Commercially available Ag (A), Au (B), and Pt (C) colloid prices for different distributors in dependency of the batch size [400–406]. NPs of different mean diameters and with various additives are included. The blue shade marks the 100 mL price window. The colloids marked by a black square are provided with a concentration of 5 mg/mL, which lead to the low material price, but are also stabilized with PVP (product line “Econix”) and are not considered for the calculation of the mean batch price (exchange rate from US$ to € is 0.9).

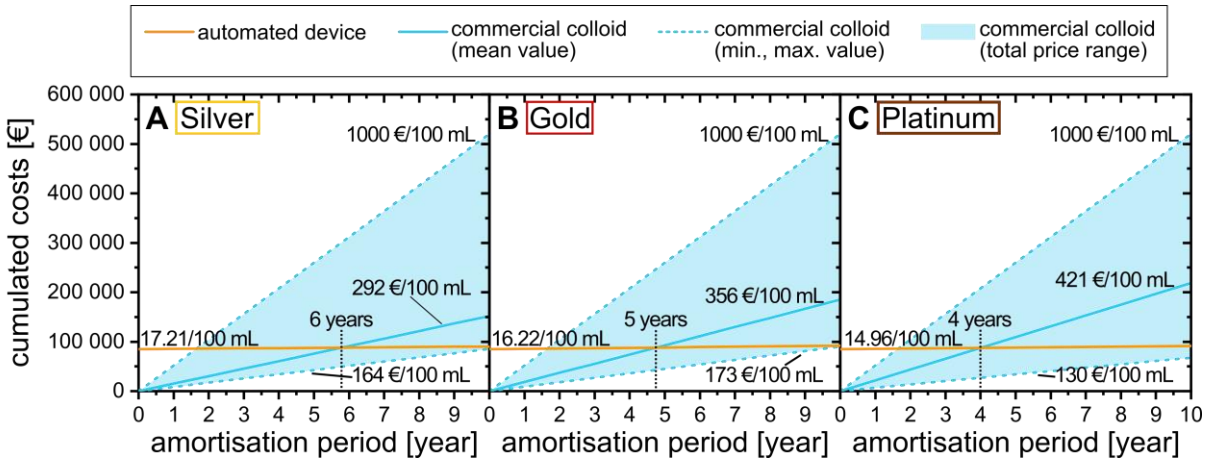

Fig. 65: Time-dependent cumulated costs for the automated device and purchased colloids for Ag (A), Au (B), and Pt (C), assuming a colloid demand of 100 mL per week. The blue shaded area depicts the total price range for all commercially available colloids and the black dotted line the break-even point.

Generally, the colloid price decreases for larger orders (Fig. 64). The amortization time and the cumulated costs for the colloids are shown in dependence of different weekly required amounts in Fig. 66 A for Au colloid. The maximal production time of the automated device for one workweek is about 7 L. In this case, the amortization time is a function of the batch size (Fig. 66 B). The typical depreciation time for laser machinery is five years [407]. Within this time, the LAL device needs to meet its economic break-even, which is 95 mL of Au colloid per week.

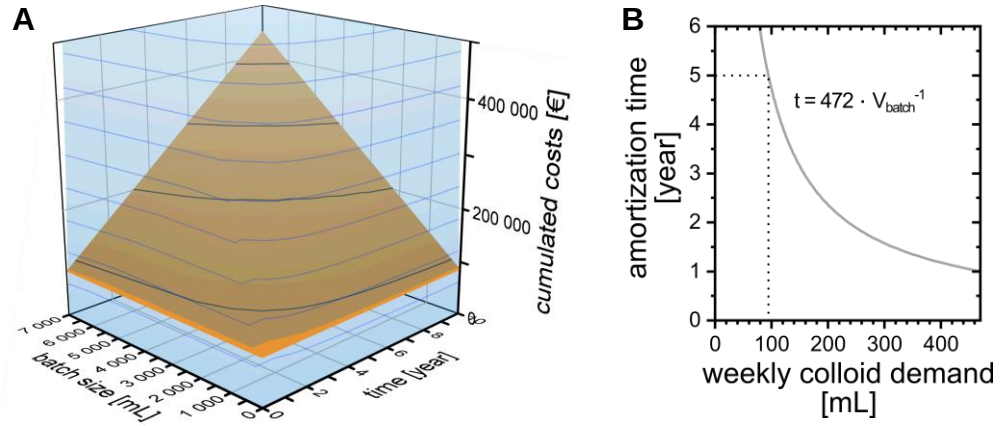

Fig. 66: Cumulated costs for Au colloids produced with the automated device (orange surface) and purchased (blue surface) in dependency of the depreciation time and the required mean weekly batch size of colloid (A). The intersection between both surfaces represents the amortization time of the automated device, dependent on the required amount of colloid (B).

Next to the colloid purchase, the device's economic feasibility is compared to the reduction-based colloid synthesis. Based on the cost calculation presented for Au colloid in [65], the time and batch size-dependent cumulated costs for automatically produced Au is given in Fig. 67. In all cases, the in-house chemical synthesis of NP is economically favorable. Both the investment and variable costs are lower for the chemical synthesis than the automated device. The net purchasing price of the device and the capsules determine the lowest possible selling price (Tab. 13). Lower running costs can be achieved with the automated device for Au and Pt if the capsule selling price is lowered (Tab. 15). Additionally, for a high demand of colloids, the laser-based synthesis can be economically more favorable (Fig. S 24). However, it is only possible to make a profit of about 30 € per capsule for Au. An alternative attempt is the reduction of the ablation chamber costs. The material costs make up the largest part of the capsule price, whereby more than half consists of the chamber printing costs (Fig. 63 B). If e.g., a recycling system of the capsules can be established, the printing costs can be minimized, and residual metal may be recycled. A subsequent market investigation must determine if the advantages of the laser-based NP synthesis and the time saving by an automated synthesis outweigh the economic disadvantage compared to the

chemical synthesis of NP. Besides, most colloid users do not have access to chemical laboratories, and chemical synthesis poses safety issues. The automated LAL deceive operates wholly sealed. Therefore, it enables colloid production in any laboratory and for untrained users.

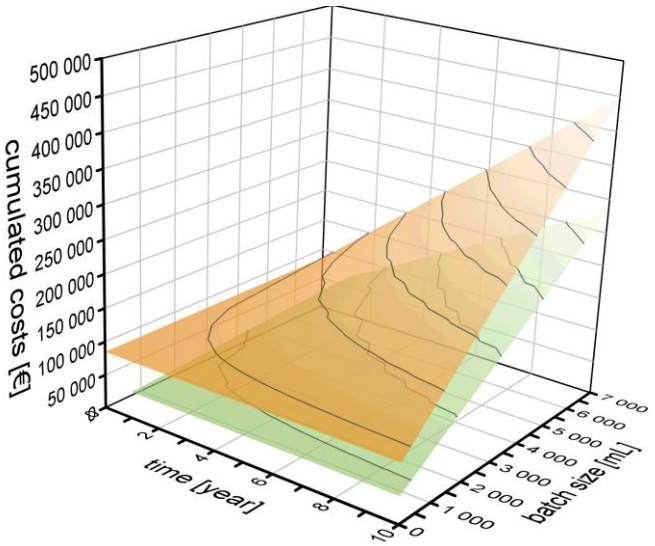

Fig. 67: Cumulated costs for Au colloids produced with the automated device (orange surface) and chemical synthesis with 100 mg/L [65] (green surface) in dependency of the depreciation time and the required mean weekly batch size.

Tab. 15: Calculation of the colloid price based on the NP synthesis by precipitation. For the laboratory and energy costs, the values determined in [65] are taken. Additional information is given in the appendix in Tab. S 20 to Tab. S 22.

	automated laser-based synthesis			chemical synthesis	
colloidal material	investment costs [€]	variable costs [€/g] *	variable costs [€/g] **	investment costs [€]	variable costs [€/g]
Ag	85 000	1194.79	708.94	39 258	407.96
Au	85 000	994.81	585.95	39 258	671.56
Pt	85 000	870.24	522.24	39 258	703.09

* contains only the capsule price as determined in Tab. 13

** based on the minimal net purchasing price in Tab. 13

This chapter demonstrated that the automated device can be sold for 85 000 € and the Ag. Au, and Pt capsules for 235, 360, and 350 €, respectively. Compared to purchased colloids, an amortization period below 6 years for all metals is estimated for a weekly colloid demand of 100 mL. For demands greater than 480 mL/week, the amortization time even decreases below one year. Compared to the chemical synthesis of colloids, the automated device is economically less favorable. However, the NPs are of higher purity, alloy NPs are easily produced, and time-saving for the laboratory employees is achieved. Moreover, the device

can be operated by untrained users and in non-chemical laboratories. Compared to the chemical synthesis of colloids, no waste or side products are produced by the automated LAL device. A subsequent market research study must investigate if the automated device is a considerable alternative for research groups or companies working with metal colloids.

4.4.2. Downstream production of functional materials with the automated device

Laser ablation in liquids enables the production of ligand-free NPs [275] with a broad variety of material-liquid combinations [240, 274, 408] including alloys such as AuPt [305, 308], AuAg [274, 306], and PtPd [225, 309]. Laser-generated NPs are of high interest in the field of catalysis [17], biomedicine [276], cancer therapy [277], 3d printing [226, 243, 245], and analytical chemistry [232, 233], with each field having different demands for NP characteristics and amounts. The NP quality, i.e., the size and the reproducibility of the process, has been addressed in section 4.2. The focus of this section lies in the testing of further material-liquid combinations and downstream processing of the NPs. Additionally, the current production rate of different colloids and downstream products are investigated in the following. An overview of the versatile NP materials and applications is depicted in Fig. 68.

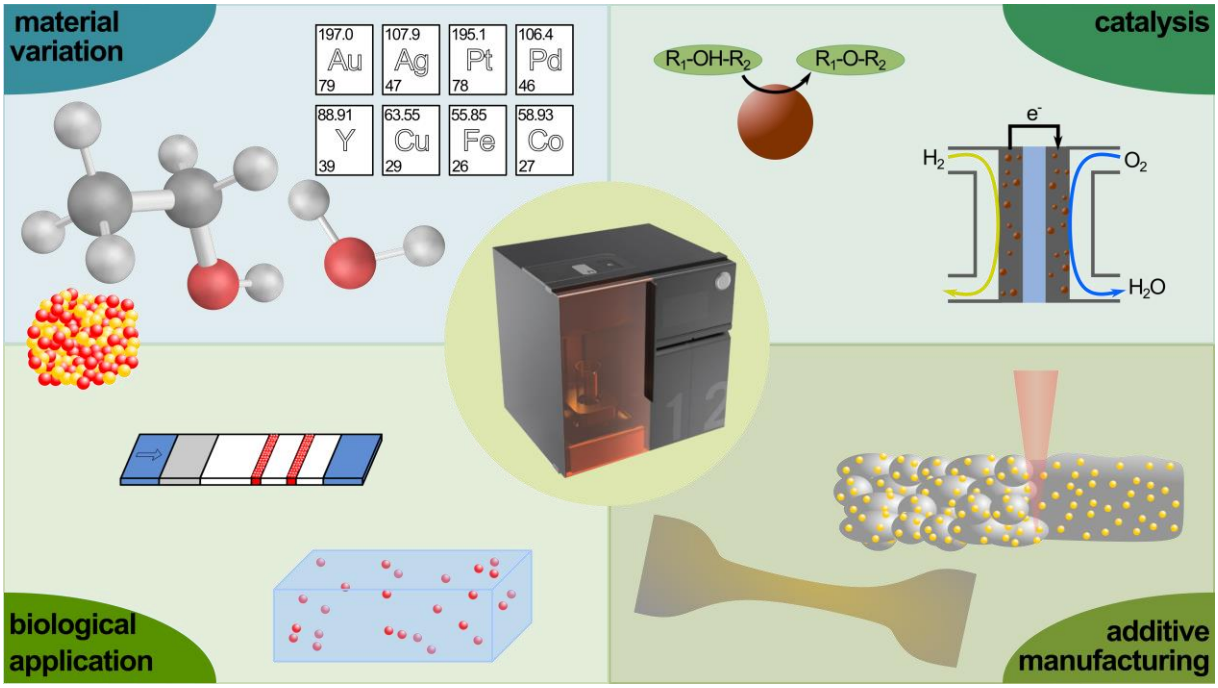

Fig. 68: Fields of application and variety of material-liquid combinations, which can be addressed with the automated device for LAL. The material-liquid variety (upper left) is wide for LAL. In contrast, the production of noble metal NPs in water or ethanol is most common and the synthesis of alloy NPs (here AuAg is indicated) is possible. In catalysis (upper right), NPs are used for reduction reactions, water splitting, or as active materials in fuel cells. The support of (polymer) micro-powders with NPs enables the development of functional materials for additive manufacturing (lower right). Examples of biological applications (lower left) are the embedding of NPs in a bio-matrix to produce wound patches or the NP functionalization to develop lateral flow assays.

In the field of additive manufacturing, micro powders are decorated with NPs. This decorating allows to either alter the powder characteristics, e.g., the laser beam absorption [409] or color [226], or the properties of 3d printed objects, like the increase the compression strength [245] or avoid solidification shrinkage [410]. The use of laser-generated Ag [226], yttrium-iron garnet (YIG) [245], or Zr [410] NPs is reported in the literature to achieve the desired property modification. With the automated device, the process-coupled decoration of polyamide 12 (PA12) powder with Ag (Fig. 69) and YIG (Fig. 70) NPs is performed. From previous experiments, it is known that Ag and YIG colloids can be produced with a productivity of 10 and 22 mg/h, respectively. The PA12 powder is dissolved and continuously stirred while the produced colloid flows into the powder solution until 0.1 and 1.0 wt.% for Ag or YIG, respectively, with respect to PA12, is reached. The experimental setup is shown in Fig. S 25. After the ablation process is finished, the solution is stirred for additional 5 min, then filtered and dried as described in [243]. The extinctions of a sample and supernatant are measured to determine the support efficiency, i.e., the reduction of the extinction at the SPR peak in the supernatant (Fig. 69 A and Fig. 70 A). For the decoration of PA12 with Ag, a support efficiency of more than 99 % and with YIG of 95 % are determined. The homogeneous deposition of NPs [226] is validated by SEM images (Fig. 69 D and Fig. 70 D). A mass load of Ag on PA12 of 0.11 wt.% is determined with energy-dispersive X-ray spectroscopy (EDX), which agrees well with the desired load of 0.1 wt.%.

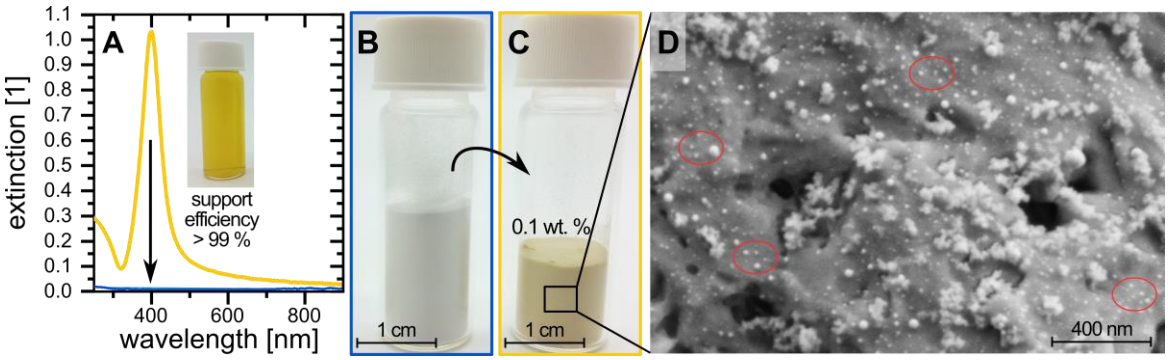

Fig. 69: Extinction spectra of the Ag colloid (yellow) and the supernatant after supporting of PA12 powder (blue) (A). Photographs of the PA12 powder before (B) and after the supporting step (C). NP distribution PA12 is examined by SEM (D). The red circles mark exemplary NPs.

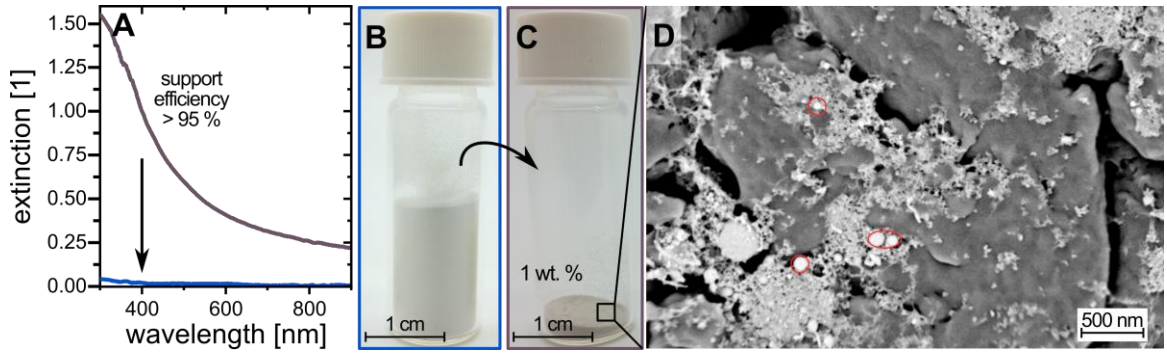

Fig. 70: Extinction spectra of the YIG colloid (brown) and the supernatant after supporting of PA12 powder (blue) (A). Photographs of the PA12 powder before (B) and after the supporting step (C). NP distribution on PA12 is examined by SEM (D). The red circles mark exemplary NPs.

Similar to the preparation of 3d printing material, catalysts can be prepared. Typical support micro powders are oxides like Al_2O_3 [411], TiO_2. [412], and CeO_2 [413], and carbon [17]. The catalytic properties of these materials are determined by the selected NP material [322] and the support powder [414, 415]. In this section, TiO_2 decorated with Au NPs (Fig. 71) and TiO_2 with Pt NPs (Fig. 72) is prepared, which can be applied as photocatalysts [416, 417].

The production and analysis are similar to the preparation of the 3d printing powders. As shown by UV-Vis extinction spectroscopy, support efficiencies >98 % are achieved (Fig. 71 A and Fig. 72 A). For both catalysts, it was aimed for a mass load of 1 wt.% of NP. EDX measurements show that for Au/TiO_2 1.1 wt.% and Pt/TiO_2 0.9 wt.% are reached. SEM images reveal that particles are aggregated for the Au NP on the TiO2, whereas a homogeneous NP distribution is achieved for Pt/TiO_2. The UV-Vis spectrum of the Au colloid used for the catalyst preparation reveals a primary particle index >8 and does not indicate the NP aggregation [172]. The pH value needs to be adjusted between the isoelectric point of Au (pH < 1.5 [418]) and TiO_2 (pH > 4.0 [418]) to obtain quantitative support. As shown in [226] for the supporting of Ag on PA12 powder, there is a regime of unstable colloid for an intermediate zeta potential, i.e., when the pH value is not reduced fast enough. In this intermediate regime, agglomeration of Au NP might occur during the catalyst preparation.

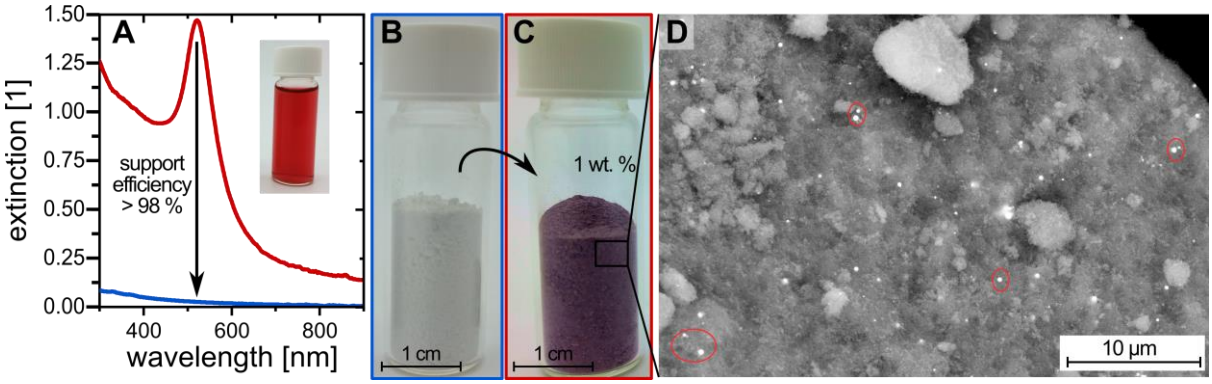

Fig. 71: Extinction spectra of the Au colloid (red) and the supernatant after supporting of TiO_2 (blue) (A). Photographs of TiO_2 powder before (B) and after the supporting step (C). NP distribution on TiO_2 is examined by SEM (D). The red circles mark exemplary NPs.

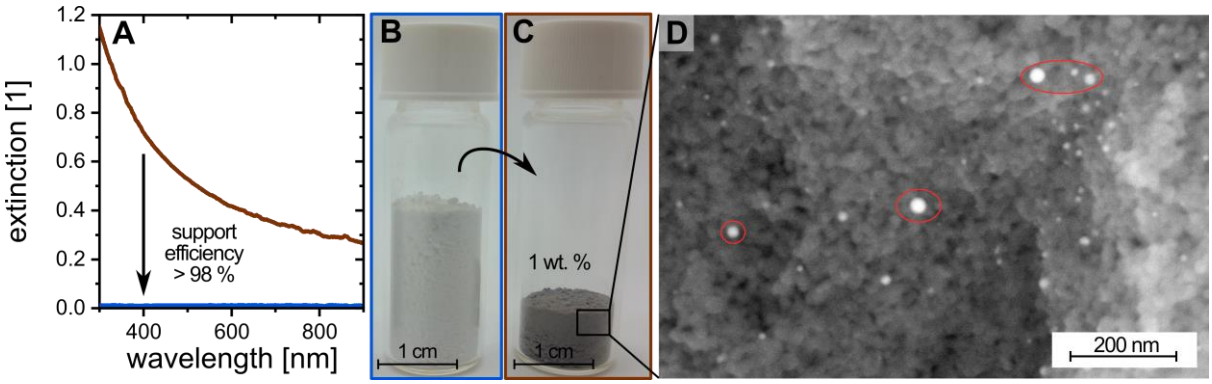

Fig. 72: Extinction spectra of the Pt colloid (brown) and the supernatant after supporting of TiO_2 (blue) (A). Photographs of TiO_2 powder before (B) and after the supporting step (C). NP distribution on TiO_2 is examined by SEM (D). The red circles mark exemplary NPs.

In contrary to the decoration of carriers with NPs for catalysts and 3d printing, NPs can also be embedded in matrices such as poly(methyl methacrylate) (PMMA) [419], thermoplastic polyurethane (TPU) [420], and alginate [421]. Especially, TPU and alginate are of interest for biomedical applications for the production of implants intended for long-term use [422] or the usage as tissue healing patches [423, 424]. The addition of Au or Pt NPs improves the cell adhesion on the nanocomposite so that foreign body reactions to the implants are reduced [8, 425]. Here, the continuous laser ablation of Au in an alginate solution is conducted. The colloid is gelated and the patch is analyzed by confocal microscopy images (Fig. 73). A homogeneous NP distribution and concentration of 1.4 wt./vol.% in the alginate patch are obtained.

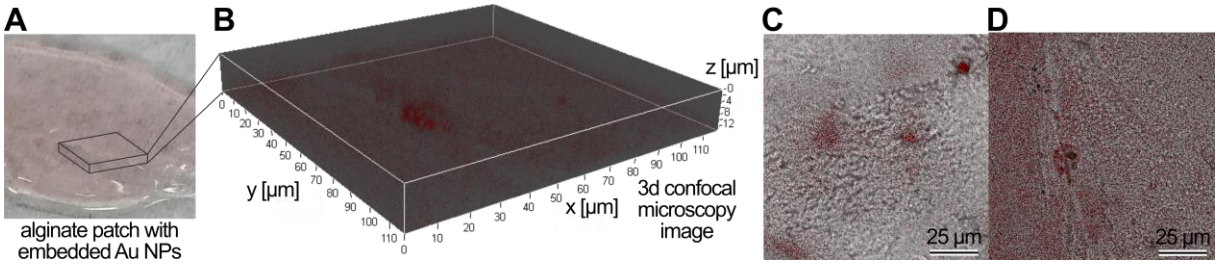

Fig. 73: Continous laser ablation of Au is performed with a 1.5 wt./vol. % alginate solution. Afterward, the colloid is gelated using 25 mg/mL $CaCl_2$ solution to obtain an alginate patch (A). 3d (B) and 2d (C, D) confocal dark-field microscopy images showing the distribution of Au NPs (red dots) in the alginate matrix.

Next to Au NPs, particles with wound healing or antibiotic effects [426, 427] can be added to the alginate matrix. Primarily Ag^+ ions released by Ag NPs are known for their cytotoxicity [5], scaling with increasing NP concentration. However, the viability of human cells is also reduced and only allows a very narrow concentration range [428]. An alternative attempt for an Ag^+ ion release reduction is the alloying with Au [311]. As expected for $Au_{50}Ag_{50}$ alloys [274], the SPR peak shifted proportionally to the metal content (Fig. 74). Moreover, the alloy formation is confirmed by high-resolution-TEM images.

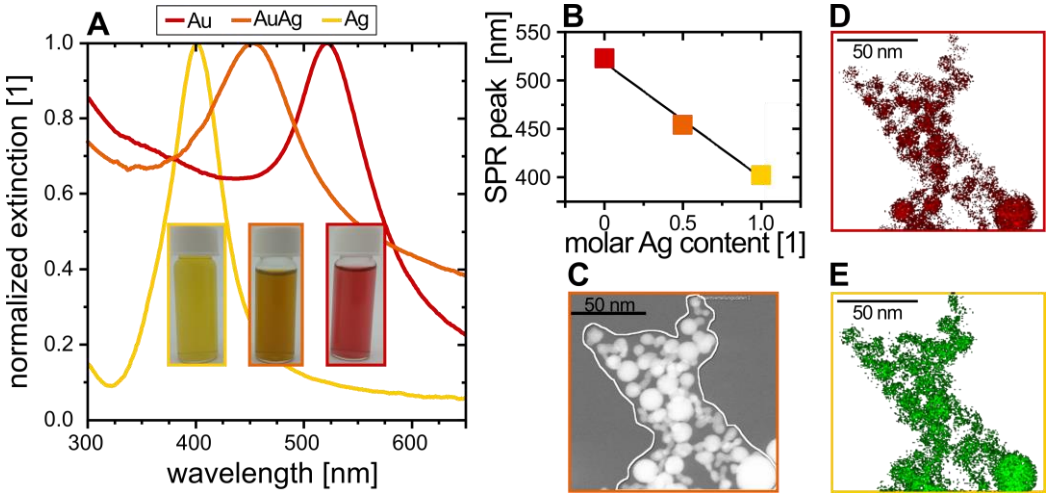

Fig. 74: Extinction spectra of the Ag (yellow), AuAg-alloy (1:1, orange), and Au (red) colloid and the inlays show photographs of the colloids (A). The SPR peak shifts proportional to the molar metal content (B). EDX image of the AuAg-alloy NPs (C), as well as the Au and Ag distribution in the alloy particles, are shown in D and E, respectively.

Contrary to the previously discussed noble metals, copper is cheaper by a factor of 50 000. Therefore, Cu has attracted attention as a catalytic material [429, 430] and for the development of biosensors [431, 432]. With a low standard electrode potential of less than 0.52 V [380], up to 80 % of Cu is oxidized during the ablation in water due to formed reactive oxygen species [433]. For Cu ablated in ethanol, the UV-Vis spectrum is shown in Fig. 75.

The peak at 590 nm is assigned to the formation of elemental Cu NPs [434, 435]. When ablating in organic solvents, the NP surface is covered with an amorphous carbon layer [435]. When CuO is formed, the SPR peak broadens and shifts to higher wavelengths [436, 437]. In consequence, the ablation of Cu in ethanol leads to the formation of elemental Cu NPs.

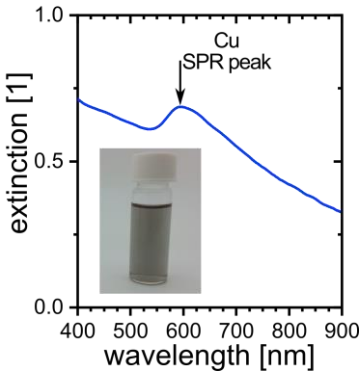

Fig. 75: Extinction spectra of copper ablated in ethanol.

An overview of the downstream NP products with the respective productivity with the automated device is presented in Tab. 16. The determination of tensile properties, the examination of the powder melting, and flow behavior have proven to be a standard testing procedure in additive manufacturing. For the tensile properties testing, standardized samples are required with an approximate volume of 2000 mm³. With an estimated powder density of 0.5 g/cm³, 16 samples can be printed within a working day of Ag/PA12 powder production. For differential scanning calorimetry and thermogravimetric analysis, less than 0.1 g of powder is sufficient. The analysis of the flow behavior and rheological properties, up to 30 g powder, i.e., 3 h of production, are required per measurement. To conclude, for rough screening of possible additive manufacturing materials, the automated device's productivity is sufficient.

In catalysis, a preliminary catalyst screening sample amount is strongly dependent on the considered reaction. For electrochemical reactions, loadings of <6 $\mu g_{NP}/cm^2_{electrode}$ [343] are required resulting in a demand of <0.1 mg (unsupported) NPs for an electrode surface of 14 cm². The needed amount can be synthesized with the device within a few minutes and, thus, enables the testing of multiple different samples. In the case of a fuel cell catalyst, testing cells with an electrode area of 16 cm² are available, so that 3 mg of NP and 15 mg of supported powder are required [17], which can be realized with the device within is less than 15 min. Third, the micro powders decorated with NPs are used to impregnate carriers, where, for example, the PtPd/Al_2O_3 load per carrier was about 3 wt.%. With a carrier mass of about 500 g, 15 g of supporting material is needed, requiring nearly three working days for one sample.

Tab. 16: Summary of possible NP application and the reached NP and modified material productivity with the automated device

Field of application	downstream material	NP productivity	Amount of NP additivation	Productivity of the modified material
additive manufacturing	Ag supported on PA12	10 mg/h	0.1 wt. % [226]	10.0 g/h
	YIG supported on PA12	22 mg/h	1.0 wt. %	2.2 g/h
	YIG supported on oxide-dispersion strengthened alloys [1]	22 mg/h	0.08 wt. % [245]	27.5 g/h
catalysis	Au supported on TiO_2	13 mg/h	1 wt. % [418]	1.3 g/h
	Pt supported on TiO_2	20 mg/h	1 wt. % [353]	2.0 g/h
	Pt supported on Al_2O_3	20 mg/h	3 wt. % [225]	0.7 g/h
	Pt supported on C	20 mg/h	20 wt. % [17]	0.1 g/h
biomedical application	Au embedded in alginate	8.2 mg/h	1.5 wt./vol.% [421]	60 mL/h
	Au embedded in TPU [1]	2.0 mg/h[2]	1.5 wt./vol.%	10 – 15 mL/h
material variation	production of AuAg NPs	13 mg/h	>100 mg_{NP}/L_{Fluid}	60 mL/h
	Cu ablated in EtOH	6.1 mg/h	>100 mg_{NP}/L_{Fluid}	60 mL/h

[1] not conducted within this thesis

[2] based on at least four times lower productivity for ablation of Au in TPU [420]

For the production of wound patches based on alginate, the NP productivities are sufficient and enable the production of about 600 cm² of Au doped alginate per working day. For TPU, more than 100 cm of tubings (assuming 4 mm diameter and 0.5 mm wall thickness) per working day can be produced within one hour, assuming the four times lower productivities than alginate [420].

In summary, the automated device can produce downstream products for additive manufacturing, catalysis, and biomedicine. It was also shown that the synthesis of NPs in organic liquids is possible. An estimation of the required material demands for different application showed that testings on a laboratory scale are possible in all considered cases.

4.4.3. Increasing the ablation efficiency and productivity by beam-splitting

The current productivity of the automated LAL device with a compact laser is not sufficient for an industrial scale testing of downstream materials. One possibility would be using a laser with a higher power, which, however, leads to an increased device sales price. Another option would be to make better use of the available laser power. As demonstrated in section 4.1.1 and the literature [68, 198], the most efficient ablation is reached at $F_{opt} = e^2 \cdot F_{th}$, however, most high power lasers reach higher fluences, therefore, operate at fluences higher than the optimal fluence and do not reach their maximal possible efficiency. Therefore, the further increase of the laser fluence in the automated device is not efficient. In the field of laser surface structuring, beam splitters are applied, since high laser powers lead to decreased material quality and in addition the process throughput is increased [229, 230, 438, 439]. It is examined if the laser beam splitting can improve overall NP productivity when lasers operating at their maximal power would run at fluences higher than the optimal fluence.

The setups for the regular ablation and ablation using a beam splitter are shown in Fig. 76 A and B. A two-parted beam is achieved using a 50:50 beam splitter, whereas multiple, in this case 11, beams are obtained using a diffractive optical element.

When ablating using one laser beam, the productivity $\dot{m}$ and power-specific productivity $\dot{m}_{spec} = \dot{m}/\bar{P}$ can be calculated according to Eq. 6 (Fig. 76 C, D). The expected productivity and efficiency can be calculated with the determined fluence on the target surface F_1. Here, the x-axis is labeled total fluence since this value refers to the cumulated fluence in each ablation process. For the ablation with one laser beam, this coincides with the fluence determined on the target surface. In contrast, for the ablation with multiple beams, this is the sum of all individual fluences, i.e., for a two-parted beam, the laser power and laser fluence on the target surface for each beam are halved (F_2). Since the ablation fluence is changed, the fluence-productivity dependency changed so that Eq. 6 can be written in a more general form, namely Eq. 19 and Eq. 20. The number of beams required to reach the maximal productivity is dependent on the cumulated laser fluence of the ablation process (Fig. 76 C). The power-specific productivity curve is independent of the number of beams since it refers to the cumulated fluence and evaluates the efficiency of the overall ablation process (Fig. 76 D). The experimentally determined productivity shows that for laser fluences until 10 J/cm², the highest productivity is reached when operating with the unsplit beam. For laser fluences until 18 J/cm², the highest productivity is achieved with two beams. The ns laser Rofin Powerline E20 (9 W) reaches a fluence of 9 J/cm², i.e., the maximal productivity for Au ablation is reached with only one laser beam. The same applies to the compact laser currently used in the automated LAL device, running at ~5 J/cm².

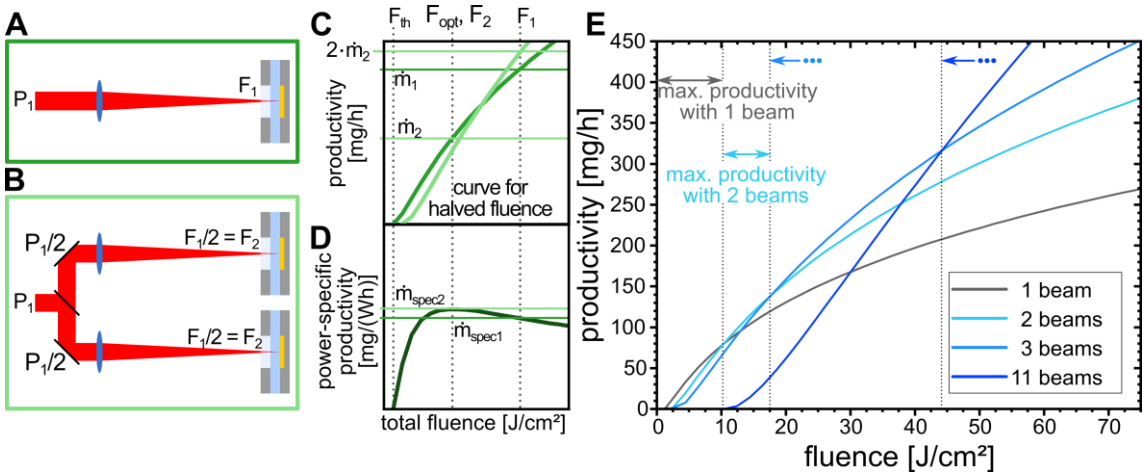

Fig. 76: Schematic setup for ablation without (A) and with a beam split in two (B). With the laser power P_1 of the incident laser beam and the spot size on the target surface, the fluence plotted in schemes C and D is calculated. The fluence-dependent productivity for both setups is shown in C. Here, the productivity $\dot{m}_2$ can either be calculated by considering the halved productivity when determining the curve (light green curve) and calculate with the original fluence F_1 or by taking the initial curve (dark green) and calculate with the halve fluence F_2. The overall productivity is twice what is calculated for one ablation process. Since the power-specific productivity (D) refers to the incident laser power, the curve is identical for both setups. However, the efficiency is determined at the fluences F_1 and F_2 at the target surface. Au productivity curves are calculated with the fluence on the target surface to illustrate the range of maximal productivity in dependence of the number of split beams in E (following the light-green curve in C). Moreover, the fluence ranges where the respective number of beams reached the highest productivity are marked.

$$\dot{m}_N = \frac{1}{16} \cdot f_R \cdot \pi \cdot \delta_{eff} \cdot d^2 \cdot \rho \cdot \ln\left(\frac{F_{P,total}/N}{F_{th}}\right)^2 \cdot N \qquad \text{Eq. 19}$$

$$F_{P,total} = F_{P,single} \cdot N \qquad \text{Eq. 20}$$

where

$F_{P,total}$: cumulated fluence $\left[J/cm^2\right]$

$F_{P,single}$: fluence determined on the target surface $\left[J/cm^2\right]$

N: number of beams [1]

According to $F_{opt} = e^2 \cdot F_{th}$ [198], the fluence at which the higher productivity is reached using a beam splitter is a function of the material-dependent threshold fluence. For a more general form of Fig. 76 E, the productivity lines' intersections are calculated according to Eq. 21. For a given maximal laser fluence and a given material threshold fluence, the optimal number of laser beams can be determined (Fig. 77 A). As already mentioned, Au productivity is highest for ablation with one laser beam., which is also valid for Pt due to its higher

threshold fluence. The threshold fluence for Ag is the lowest (0.54 J/cm²) and ablation with two beams yields increased productivity. These hypotheses are supported by experimental results (Fig. 77 C). The Innolas SpitLight DPSS 250-100 laser reaches a fluence of 66 J/cm². With a threshold fluence of Au of 0.3 J/cm³, ablation with eleven beams leads to a productivity increase of 60 % compared to ablation with one beam (Fig. 77 B).

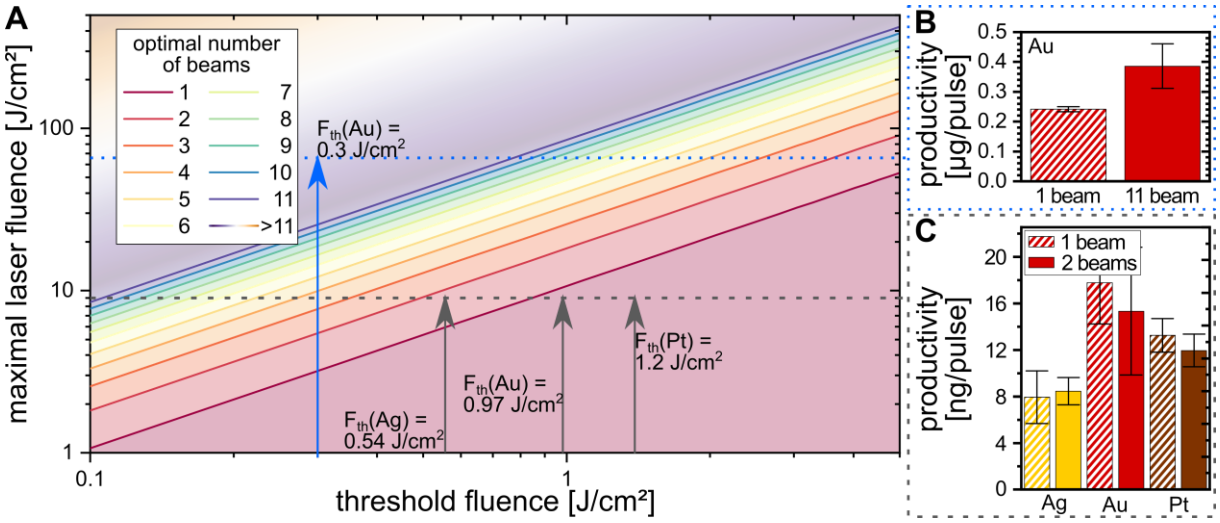

Fig. 77: Dependency of the number of laser beams leading to maximal productivity on the maximal laser fluence and material-dependent threshold fluence (A). Areas of different colors mark the ranges for different optimal numbers of laser beams. The difference in the overall productivity for the Innolas SpitLight DPSS 250-100 (blue) with one and eleven beams (B) and the Rofin Powerline E20 (gray) for ablation with one and two beams (C) for Ag (yellow), Au (red), and Pt (brown).

$$\dot{m}_N = \dot{m}_{N+1} \qquad \text{Eq. 21}$$

For materials with low threshold fluences or lasers reaching high fluences, beam splitting can significantly increase ablation efficiency. In these cases, the splitting of the laser beam also leads to increased overall productivity. For Ag, Au, and Pt, laser fluences of 6.0, 10, and 13 J/cm², respectively, are necessary to improve laser ablation in liquids by laser beam splitting. For future investigations, the laser power-specific prices of different commercially available laser systems should be considered to determine the most economical setup for multiple-beam laser ablation in liquid.

5. Summary and conclusion

Commonly, colloids are either purchased or chemically synthesized, which come with certain drawbacks. For example, for the purchase of colloids, delivery times reach up to several weeks and costs easily exceed 30 €/mL of colloid. In turn, chemical colloid synthesis has the drawback of being time-consuming, produce waste, require well-trained personnel, and colloids require cleaning before usage. Moreover, certain alloys or material-liquid combinations are not offered by distributors or cannot be chemically synthesized. The NP production via LAL enables the generation of solid-solution alloy NPs even when the bulk materials exhibit a broad immiscibility gap. Also, the synthesis of, e.g., ignoble metal NPs in unoxidized form is possible. However, the costs of laser-generated NPs are strongly influenced by labor costs determined by the material's productivity. Especially for materials with low mass productivity but required in large amounts, e.g., oxides, LAL is economically often not favorable. Lowering the labor costs by automating the ablation process and increasing productivity presents a solution to this challenge.

For the development of an automated desktop-sized device for NP production via LAL, the laser pulse duration-dependency of the productivity is examined and a suitable laser for the device is selected in the first step. Second, the process parameters are adapted for the automated device and the reproducibility of the method is evaluated. In the third step, the process is developed and potential hazards are eliminated. Lastly, the perspectives of the device are illuminated.

In the first chapter, a dependence of the ablation efficiency on the pulse duration is observed. Since plasma shielding is assumed to cause this difference, the energy distribution for ablation with ns lasers is compared and the first 10 ns of ablation are analyzed. The ablation efficiency and productivity of lasers with 3 ps, 1 ns, and 7 ns laser pulse durations are analyzed. Although the reflection and absorption of the laser energy by the water are taken into account, the ablation rate in air is higher than in water for all three lasers. Partially, this effect can be correlated to a shielding effect by the produced NPs. Also, shielding due to the plasma plume and non-linear effects must be taken into account. The former is assigned to longer ns laser pulses and the latter to fs and ps laser pulses. The highest efficiency for LAL is reached for an intermediate pulse duration of ~2 ns laser.

For a further investigation of the shielding phenomena during the ~2 ns laser ablation, cavitation bubbles imaging is used. A significantly larger cavitation bubble for longer pulse durations is observed, presumably due to an enhanced laser-plasma-interaction. Longer pulse durations sustain the ablation plume, which gains more energy, which in turn is released in larger CBs. However, the ablation efficiency is decreased for higher ns pulse durations as less energy reaches the target surface. Next to the temporal energy release, the spatial energy distribution in the liquid is varied by changing the focal distance. Surprisingly,

the point of highest fluence and maximal bubble volume do not coincide. A succession of bubbles and a decreased NP size are observed in a regime where the focal point is slightly above the target surface. The resulting energy loss leads to reduced productivity. Lastly, evidence is found that NPs are enriched in a stationary layer on the target surface, potentially leading to satellite bubbles during ns laser ablation.

The early phase (10 ns) of the ablation process is analyzed by pump-probe microscopy. Comparing the processes in air and water reveals vapor formation in the liquid about 2 ns after the laser pulse. This comparison provides evidence that vapor shielding is negligible for laser pulses shorter than this critical duration, resulting in the increased ablation efficiency for intermediate (several hundred ps to ~2 ns) pulse durations. Therefore, a laser within this pulse duration range is selected for the development of the automated device.

In the second chapter, the influence of the process parameters on both the NP productivity and size is determined. Based on this, the process parameters for the automated LAL device are adjusted to reach maximal productivity and the reproducibility of the ablation process is evaluated.

Shifting the focal plane of the laser beam into the liquid layer increases the mass yield of Pt NP sizes <10 nm and the total productivity of this fraction significantly. This downsizing effect can be explained by increased mean laser energy deposited in the liquid volume containing nanoparticles produced by previous laser pulses. Consequently, when the laser beam focus was located within the liquid, a higher fragmentation rate of the undesired larger Pt nanoparticle size fraction occurred, which increased the mass yield of nanoparticles below 10 nm. Increasing the laser fluence while keeping the focal position in the liquid layer, the mass fraction of the small-size NP fraction increases. Reducing the volume flow rate or, i.e., increasing the residence time, improves the mass-share of Pt nanoparticles <10 nm.

This NP productivity-property linkage is transferred to the automated device. First, the distance between the lenses and the unablated target surface should be set to 52.0 mm for Ag, Au, and Pt. A target of 0.5 mm thickness is the best compromise between a constant colloid quality and a long capsule lifetime for the automated device. Additionally, hydrodynamic diameter measurements show that the particle sizes for the three metals do not change significantly within this focal range. As a colloid concentration of 100 mg/L is desired, the flow rate must be adequately determined for each material. Finally, productivities of around 10, 13, and 20 mg/h are measured for Ag, Au, and Pt at flow rates of 1.1, 2.1, and 3.1 mL/min, respectively, comprising the desired concentration. Power-specific productivities of 20 – 40 mg/(W·h) are reached with the compact laser, which is twice as high as reported in the literature. Analysis for the ablation chamber flow conditions indicated that cavitation bubble-induced vortexes cause nonlinear flow conditions. These turbulences limit productivity at high flow rates. The influence of the focal distance, liquid flow rate, and laser

energy on the NP size are summarized by the volume-specific energy dose, which a pseudo-kinetic model describes.

Lastly, the time effect concerning the target condition, production time, and colloid storage are considered for the automated device. First, only for the usage of a new Au target, a significant decrease in productivity is observed, which is connected to the incubation effect of Au. For Ag and Pt, this effect is not observed. It is recommended to use pre-roughened Au targets for the automated device. Second, a productivity decrease within the first 1.5 h of ablation is observed. Within the time frame, also the NP size fluctuates stronger than afterward. During Ag ablation, a heating rate of 2.5 °C/h is found for the first 1.5 h. Either colloid produced within the first 1.5 h should be discarded to ensure a consistent colloid quality and reproducibility, or target cooling could be applied. Third, at a storage temperature of 25 °C, Au and Pt, each stabilized with 0.1 mmol/L NaCl, and Ag colloids, stabilized with 0.25 mmol/L sodium citrate, are at least stable for 28 days.

Reproducibility tests of the automated device demonstrated low batch-to-batch variability regarding the concentration and properties of the colloids. Also, the colloids meet the typical specifications set by international colloid distributors.

In the third chapter, the process is developed, the implementation of sensors eliminates potential hazards and assures process stability. The different kinds of sensors are tested and threshold values are set. The determination of malfunctions and user interaction of the device is presented in a decision chart to ensure a safe and user-friendly process.

In the fourth chapter, the perspectives of the device are discussed. Therefore, the device price is estimated and compared to the costs for other colloids. With the final setup, the productivities of possible downstream products are determined, and productivity increase is presented.

A device price of 85 000 € is determined and the running costs are dominated by the capsule prices, which are 235, 360, and 350 € for Ag, Au, and Pt. Compared to the purchase of colloids, the device's amortization period lies below 6 years for all metals at a production rate of 100 mL/week. For demands greater than 480 mL/week, the amortization time even decreases below one year. Compared to the chemical synthesis of colloids, the automated device is economically less favorable. However, the NPs are of higher purity, alloy NPs are easily produced by untrained users in any laboratory, and reproducibility is guaranteed.

Potential customers of the device can be research facilities in additive manufacturing, catalysis, and biomedicine. It is essential that the device produce the required amounts for these applications. Exemplary downstream products from each field are produced, and it is shown that the synthesis of alloys and NPs in organic liquids is possible. An estimation of the required material demands for different applications showed that testing on a laboratory scale is possible in all considered fields.

For users in an industrial environment, an increase in NP productivity may be demanded. Due to the penetration depth-limited fluence-productivity dependency, the increase of laser fluence is only feasible until the optimal fluence is reached. Therefore, for lasers reaching fluences far higher than $e^2 \cdot F_0$ splitting of the laser beam leads to increased overall productivity.

6. Outlook

Future investigations from a fundamental perspective and an economic point of view are recommended.

From a fundamental point of view, the flow conditions during the ablation process require further consideration. They are presumably at least in part turbulent due to cavitation bubbles. CFD simulations can provide a more profound knowledge of the flow conditions during LAL. Moreover, film theory predicts a stationary liquid layer on top of the target surface, which was confirmed in this thesis and where temperature and NPs accumulate. To this date, less is known about how this layer influences the ablation mechanism and the NP properties. The heat distribution in the stationary and bulk liquid, in general, can be simulated by CFD simulations coupled with heat equations.

The automated device can be improved by eliminating the run-in time. This period is presumably connected to heat effects so that preheating or cooling of the ablation target can potentially eliminate this period. Also, the production of variable NP sizes is not possible yet, but desired, e.g., for catalyst synthesis. At the low laser power of the current laser (< 500 mW), a significant size reduction by variation of the laser parameters is not possible with the device. Here, three different solutions can be tested to realize an in-process size adjustment. First, the laser can be substituted with a laser exhibiting higher power. Compact lasers are available at four times higher powers today. Second, a different laser for fragmentation can be added to the device with 355 or 532 nm wavelength increasing its dimensions. However, a desktop-sized setup would still be possible. Third, the stabilizer concentration adjustment would provide a possibility that does not require changes in the device setup and is therefore easily tested. However, stabilizer (concentration) changes should always be done concerning the NP application. The next development steps should be discussed with research institutions to achieve a user-friendly device and meet the customers' needs. The thriving questions are the mean expected colloid consumption, required quality of NPs, preferred liquid, as well as the desired downstream applications. The device's further development should focus on either upscaling of the device, adapting the device to organic liquids and ablation of, e.g., ceramic materials, or developing modules for the device enabling automated downstream processes, for example, the addivation of micropowders.

Lastly, the economic efficiency of the device could be increased with another laser system. Tab. 2 summarizes possible alternative laser systems with pulse durations in the range of 500 ps to 2 ns. For a follow-up study, it is recommended to take the prices of different commercially available laser systems into account and determine the most economical setup for laser ablation in liquid for optimized ablation parameters, including beam splitting.

7. References

[1] M. Loos, *Carbon Nanotube Reinforced Composites: Nanoscience and Nanotechnology*, CNR Polymer Science and Technology (2015).

[2] D. J. Barber, I. C. Freestone, An Investigation of the Origin of the Colour of the Lycurgus Cup by Analytical Transmission Electron Microscopy, Archaeometry, 32 *(1)*, 33 – 45 (1990).

[3] J.-W. Rhim, L.-F. Wang, Y. Lee, S.-I. Hong, Preparation and characterization of bio-nanocomposite films of agar and silver nanoparticles: laser ablation method, Carbohydrate polymers, 103, 456 – 465 (2014).

[4] A. Schwenke, P. Wagener, A. Weiß, K. Klimenta, H. Wiegel, L. Sajti, S. Barcikowski, Laserbasierte Generierung matrixbinderfreier Nanopartikel-Polymerkomposite für bioaktive Medizinprodukte, Chemie Ingenieur Technik, 85 *(5)*, 740 – 746 (2013).

[5] J. Boenigk, D. Beisser, S. Zimmermann, C. Bock, J. Jakobi, D. Grabner, L. Groβmann, S. Rahmann, S. Barcikowski, B. Sures, Effects of silver nitrate and silver nanoparticles on a planktonic community: general trends after short-term exposure, PloS one, 9 *(4)*, e95340 (2014).

[6] S. Grade, J. Eberhard, P. Wagener, A. Winkel, C. L. Sajti, S. Barcikowski, M. Stiesch, Therapeutic Window of Ligand-Free Silver Nanoparticles in Agar-Embedded and Colloidal State: In Vitro Bactericidal Effects and Cytotoxicity, Adv. Eng. Mater., 14 *(5)*, B231-B239 (2012).

[7] L. Yang, L. Chen, Y.-C. Chen, L. Kang, J. Yu, Y. Wang, C. Lu, T. Mashimo, A. Yoshiasa, C.-H. Lin, Homogeneously alloyed nanoparticles of immiscible Ag-Cu with ultrahigh antibacterial activity, Colloids and surfaces. B, Biointerfaces, 180, 466 – 472 (2019).

[8] C. Hess, A. Schwenke, P. Wagener, S. Franzka, C. Laszlo Sajti, M. Pflaum, B. Wiegmann, A. Haverich, S. Barcikowski, Dose-dependent surface endothelialization and biocompatibility of polyurethane noble metal nanocomposites, Journal of biomedical materials research. Part A, 102 *(6)*, 1909 – 1920 (2014).

[9] L. Kankate, A. Turchanin, A. Gölzhäuser, On the release of hydrogen from the S-H groups in the formation of self-assembled monolayers of thiols, Langmuir the ACS journal of surfaces and colloids, 25 *(18)*, 10435 – 10438 (2009).

[10] S. Petersen, S. Barcikowski, In Situ Bioconjugation: Single Step Approach to Tailored Nanoparticle-Bioconjugates by Ultrashort Pulsed Laser Ablation, Adv. Funct. Mater., 19 *(8)*, 1167 – 1172 (2009).

[11] C. Streich, L. Akkari, C. Decker, J. Bormann, C. Rehbock, A. Müller-Schiffmann, F. C. Niemeyer, L. Nagel-Steger, D. Willbold, B. Sacca, C. Korth, T. Schrader, S. Barcikowski, Characterizing the Effect of Multivalent Conjugates Composed of Aβ-

Specific Ligands and Metal Nanoparticles on Neurotoxic Fibrillar Aggregation, ACS nano, 10 *(8)*, 7582 – 7597 (2016).

[12] G. A. Posthuma-Trumpie, J. Korf, A. van Amerongen, Lateral flow (immuno)assay: its strengths, weaknesses, opportunities and threats. A literature survey, Analytical and bioanalytical chemistry, 393 *(2)*, 569 – 582 (2009).

[13] V. Morandi, F. Marabelli, V. Amendola, M. Meneghetti, D. Comoretto, Colloidal Photonic Crystals Doped with Gold Nanoparticles: Spectroscopy and Optical Switching Properties, Adv. Funct. Mater., 17 *(*15*)*, 2779 – 2786 (2007).

[14] V. L. Kumar, R. S. S. Siddhardha, A. Kaniyoor, R. Podila, M. Molli, S. M. Kumar, K. Venkataramaniah, S. Ramaprabhu, A. M. Rao, S. S. Ramamurthy, Gold Decorated Graphene by Laser Ablation for Efficient Electrocatalytic Oxidation of Methanol and Ethanol, Electroanalysis, 26 *(8)*, 1850 – 1857 (2014).

[15] N. Thielecke, K.-D. Vorlop, U. Prüße, Long-term stability of an Au/Al2O3 catalyst prepared by incipient wetness in continuous-flow glucose oxidation, Catalysis Today, 122 *(*3-4*)*, 266 – 269 (2007).

[16] S. Gu, J. Kaiser, G. Marzun, A. Ott, Y. Lu, M. Ballauff, A. Zaccone, S. Barcikowski, P. Wagener, Ligand-free Gold Nanoparticles as a Reference Material for Kinetic Modelling of Catalytic Reduction of 4-Nitrophenol, Catal Lett, 145 *(*5*)*, 1105 – 1112 (2015).

[17] S. Kohsakowski, R. Streubel, I. Radev, V. Peinecke, S. Barcikowski, G. Marzun, S. Reichenberger, First PEM fuel cell based on ligand-free, laser-generated platinum nanoparticles, Applied Surface Science, 467-468, 486 – 492 (2019).

[18] A. Jindal, K. Tashiro, H. Kotani, T. Takei, S. Reichenberger, G. Marzun, S. Barcikowski, T. Kojima, Y. Yamamoto, Excellent Oxygen Reduction Reaction Performance in Self-Assembled Amyloid-β/Platinum Nanoparticle Hybrids with Effective Platinum–Nitrogen Bond Formation, ACS Appl. Energy Mater., 2 *(9)*, 6536 – 6541 (2019).

[19] A. Boubnov, S. Dahl, E. Johnson, A. P. Molina, S. B. Simonsen, F. M. Cano, S. Helveg, L. J. Lemus-Yegres, J.-D. Grunwaldt, Structure–activity relationships of Pt/Al2O3 catalysts for CO and NO oxidation at diesel exhaust conditions, Applied Catalysis B: Environmental, 126, 315 – 325 (2012).

[20] S. Wu, J. Liu, Z. Tian, Y. Cai, Y. Ye, Q. Yuan, C. Liang, Highly Dispersed Ultrafine Pt Nanoparticles on Reduced Graphene Oxide Nanosheets: In Situ Sacrificial Template Synthesis and Superior Electrocatalytic Performance for Methanol Oxidation, ACS applied materials & interfaces, 7 *(*41*)*, 22935 – 22940 (2015).

[21] J. Zhang, G. Chen, D. Guay, M. Chaker, D. Ma, Highly active PtAu alloy nanoparticle catalysts for the reduction of 4-nitrophenol, Nanoscale, 6 *(4)*, 2125 – 2130 (2014).

[22] X. Auvray, L. Olsson, Stability and activity of Pd-, Pt- and Pd–Pt catalysts supported on alumina for NO oxidation, Applied Catalysis B: Environmental, 168-169, 342 – 352 (2015).

[23] C. Carrillo, T. R. Johns, H. Xiong, A. DeLaRiva, S. R. Challa, R. S. Goeke, K. Artyushkova, W. Li, C. H. Kim, A. K. Datye, Trapping of Mobile Pt Species by PdO Nanoparticles under Oxidizing Conditions, The journal of physical chemistry letters, 5 *(*12*)*, 2089 – 2093 (2014).

[24] J. Turkevich, P. C. Stevenson, J. Hillier, A study of the nucleation and growth processes in the synthesis of colloidal gold, Discuss. Faraday Soc., 11, 55 (1951).

[25] G. Frens, Particle size and sol stability in metal colloids, Kolloid-Z.u.Z.Polymere, 250 *(7)*, 736 – 741 (1972).

[26] G. Frens, Controlled Nucleation for the Regulation of the Particle Size in Monodisperse Gold Suspensions, Nature Physical Science, 241 *(*105*)*, 20 – 22 (1973).

[27] J. Zhang, G. Chen, M. Chaker, F. Rosei, D. Ma, Gold nanoparticle decorated ceria nanotubes with significantly high catalytic activity for the reduction of nitrophenol and mechanism study, Applied Catalysis B: Environmental, 132-133, 107 – 115 (2013).

[28] A. Fojtik, A. Henglein, Laser ablation of films and suspended particles in a solvent formation of cluster and colloid solutions, Berichte der Bunsengesellschaft für physikalische Chemie, 97 *(2)*, 252 – 254 (1993).

[29] D. Zhang, B. Goekce, S. Barcikowski, Laser Synthesis and Processing of Colloids, Chemical Reviews, 117 *(*5*)*, 3990 – 4103 (2017).

[30] H. Zeng, X.-W. Du, S. C. Singh, S. A. Kulinich, S. Yang, J. He, W. Cai, Nanomaterials via Laser Ablation/Irradiation in Liquid: A Review, Adv. Funct. Mater., 22 *(7)*, 1333 – 1353 (2012).

[31] A. Kanitz, M.-R. Kalus, E. L. Gurevich, A. Ostendorf, S. Barcikowski, D. Amans, Review on experimental and theoretical investigations of the early stage, femtoseconds to microseconds processes during laser ablation in liquid-phase for the synthesis of colloidal nanoparticles, Plasma Sources Sci. Technol., 28 *(*10*)*, 103001 (2019).

[32] R. Streubel, G. Bendt, B. Goekce, Pilot-scale synthesis of metal nanoparticles by high-speed pulsed laser ablation in liquids, Nanotechnology, 27 *(*20*)*, 1 – 9 (2016).

[33] P. G. Kuzmin, G. A. Shafeev, V. V. Bukin, S. V. Garnov, C. Farcau, R. Carles, B. Warot-Fontrose, V. Guieu, G. Viau, Silicon Nanoparticles Produced by Femtosecond Laser Ablation in Ethanol: Size Control, Structural Characterization, and Optical Properties, J. Phys. Chem. C, 114 *(*36*)*, 15266 – 15273 (2010).

[34] Y. Jiang, P. Liu, Y. Liang, H. B. Li, G. W. Yang, Promoting the yield of nanoparticles from laser ablation in liquid, Appl. Phys. A, 105 *(4)*, 903 – 907 (2011).

[35] R. Intartaglia, K. Bagga, M. Scotto, A. Diaspro, F. Brandi, Luminescent silicon nanoparticles prepared by ultra short pulsed laser ablation in liquid for imaging applications, Opt. Mater. Express, 2 *(*5*)*, 510 (2012).

[36] K. S. Khashan, M. S. Jabir, F. A. Abdulameer, Carbon nanoparticles prepared by laser ablation in liquid environment, Surf. Rev. Lett., 26 *(*10*)*, 1950078 (2019).

[37] C. L. Sajti, R. Sattari, B. N. Chichkov, S. Barcikowski, Gram Scale Synthesis of Pure Ceramic Nanoparticles by Laser Ablation in Liquid, The Journal of Physical Chemistry C, 114 *(*6*)*, 2421 – 2427 (2010).

[38] K. Hiromatsu, D. J. Hwang, C. P. Grigoropoulos, *US7985367B2*.

[39] G. Compagnini, E. Messina, O. Puglisi, V. Nicolosi, Laser synthesis of Au/Ag colloidal nano-alloys: Optical properties, structure and composition, Applied Surface Science, 254 *(4)*, 1007 – 1011 (2007).

[40] S. Scaramuzza, S. Agnoli, V. Amendola, Metastable alloy nanoparticles, metal-oxide nanocrescents and nanoshells generated by laser ablation in liquid solution: influence of the chemical environment on structure and composition, Physical chemistry chemical physics PCCP, 17 *(*42*)*, 28076 – 28087 (2015).

[41] K. Hagedorn, B. Liu, A. Marcinkevicius, Intermetallic PtPb Nanoparticles Prepared by Pulsed Laser Ablation in Liquid, J. Electrochem. Soc., 160 *(2)*, F106-F110 (2013).

[42] K. D. Malviya, K. Chattopadhyay, Synthesis and Mechanism of Composition and Size Dependent Morphology Selection in Nanoparticles of Ag–Cu Alloys Processed by Laser Ablation Under Liquid Medium, J. Phys. Chem. C, 118 *(*24*)*, 13228 – 13237 (2014).

[43] D. Katsuki, T. Sato, R. Suzuki, Y. Nanai, S. Kimura, T. Okuno, Red luminescence of Eu3+ doped ZnO nanoparticles fabricated by laser ablation in aqueous solution, Appl. Phys. A, 108 *(2)*, 321 – 327 (2012).

[44] N. Krstulović, K. Salamon, O. Budimlija, J. Kovač, J. Dasović, P. Umek, I. Capan, Parameters optimization for synthesis of Al-doped ZnO nanoparticles by laser ablation in water, Applied Surface Science, 440, 916 – 925 (2018).

[45] H. Wang, O. Odawara, H. Wada, Facile and Chemically Pure Preparation of YVO4:Eu(3+) Colloid with Novel Nanostructure via Laser Ablation in Water, Scientific reports, 6, 20507 (2016).

[46] J.-P. Sylvestre, S. Poulin, A. V. Kabashin, E. Sacher, M. Meunier, J. H. T. Luong, Surface Chemistry of Gold Nanoparticles Produced by Laser Ablation in Aqueous Media, J. Phys. Chem. B, 108 *(*43*)*, 16864 – 16869 (2004).

[47] E. Giorgetti, M. Muniz-Miranda, P. Marsili, D. Scarpellini, F. Giammanco, Stable gold nanoparticles obtained in pure acetone by laser ablation with different wavelengths, J Nanopart Res, 14 *(1)* (2012).

[48] V. Amendola, G. A. Rizzi, S. Polizzi, M. Meneghetti, Synthesis of gold nanoparticles by laser ablation in toluene: quenching and recovery of the surface plasmon absorption, The journal of physical chemistry. B, 109 *(*49*)*, 23125 – 23128 (2005).

[49] A. Hahn, S. Barcikowski, B. N. Chichkov, *Influences on Nanoparticle Production during Pulsed Laser Ablation*, Berichte aus der Verfahrenstechnik, Vol. 3, Shaker, Aachen (2008).

[50] G. Compagnini, A. A. Scalisi, O. Puglisi, C. Spinella, Synthesis of gold colloids by laser ablation in thiol-alkane solutions, J. Mater. Res., 19 *(*10*)*, 2795 – 2798 (2004).

[51] R. Zamiri, B. Z. Azmi, A. R. Sadrolhosseini, H. A. Ahangar, A. W. Zaidan, M. A. Mahdi, Preparation of silver nanoparticles in virgin coconut oil using laser ablation, International journal of nanomedicine, 6, 71 – 75 (2011).

[52] M. Flores-Castañeda, E. Camps, M. Camacho-López, S. Muhl, E. García, M. Figueroa, Bismuth nanoparticles synthesized by laser ablation in lubricant oils for tribological tests, Journal of Alloys and Compounds, 643, S67-S70 (2015).

[53] S. Jendrzej, B. Gökce, S. Barcikowski, Colloidal Stability of Metal Nanoparticles in Engine Oil under Thermal and Mechanical Load, Chem. Eng. Technol., 40 *(*9*)*, 1569 – 1576 (2017).

[54] M. Lau, F. Waag, S. Barcikowski, Direct Integration of Laser-Generated Nanoparticles into Transparent Nail Polish: The Plasmonic “Goldfinger”, Ind. Eng. Chem. Res., 56 *(*12*)*, 3291 – 3296 (2017).

[55] U. Taylor, A. Barchanski, S. Petersen, W. A. Kues, U. Baulain, L. Gamrad, L. Sajti, S. Barcikowski, D. Rath, Gold nanoparticles interfere with sperm functionality by membrane adsorption without penetration, Nanotoxicology, 8 Suppl 1, 118 – 127 (2014).

[56] C. Uboldi, D. Bonacchi, G. Lorenzi, M. I. Hermanns, C. Pohl, G. Baldi, R. E. Unger, C. J. Kirkpatrick, Gold nanoparticles induce cytotoxicity in the alveolar type-II cell lines A549 and NCIH441, Particle and Fibre Toxicology, 6, 18 (2009).

[57] J. Kneipp, X. Li, M. Sherwood, U. Panne, H. Kneipp, M. I. Stockman, K. Kneipp, Gold nanolenses generated by laser ablation-efficient enhancing structure for surface enhanced Raman scattering analytics and sensing, Analytical chemistry, 80 *(*11*)*, 4247 – 4251 (2008).

[58] M. Procházka, P. Mojzeš, J. Štěpánek, B. Vlčková, P.-Y. Turpin, Probing Applications of Laser-Ablated Ag Colloids in SERS Spectroscopy: Improvement of Ablation Procedure and SERS Spectral Testing, Anal. Chem., 69 *(*24*)*, 5103 – 5108 (1997).

[59] S. Yang, W. Cai, L. Kong, Y. Lei, Surface Nanometer-Scale Patterning in Realizing Large-Scale Ordered Arrays of Metallic Nanoshells with Well-Defined Structures and Controllable Properties, Adv. Funct. Mater., 20 *(*15*)*, 2527 – 2533 (2010).

[60] P. T. Anastas, J. C. Warner, *Green chemistry: Theory and practice*, 1st ed., Oxford Univ. Press, Oxford (2000).

[61] O. Short, R. Weaver, *US3725035A*.

[62] Institut für Arbeitsschutz der Deutschen Gesetzlichen Unfallversicherung, Stoffdatenblatt-Tetrachlorogold(III)-säure (zugriff: 13.05.2020).

[63] J. J. Zuckerman, A. P. Hagen, Inorganic Reactions and Methods (1991).

[64] M. Fischer, J. Hormes, G. Marzun, P. Wagener, U. Hagemann, S. Barcikowski, In Situ Investigations of Laser-Generated Ligand-Free Platinum Nanoparticles by X-ray Absorption Spectroscopy: How Does the Immediate Environment Influence the Particle Surface?, Langmuir the ACS journal of surfaces and colloids, 32 *(*35*)*, 8793 – 8802 (2016).

[65] S. Jendrzej, B. Goekce, M. Epple, S. Barcikowski, How Size Determines the Value of Gold - Economic Aspects of Wet Chemical and Laser-Based Metal Colloid Synthesis, Chemical Physics and Physical Chemistry, 18 *(9)*, 1012 – 1019 (2017).

[66] I. Trenque, G. C. Magnano, J. Bárta, F. Chaput, M. A. Bolzinger, I. Pitault, S. Briançon, K. Masenelli-Varlot, M. Bugnet, C. Dujardin, V. Čuba, D. Amans, Synthesis routes of CeO 2 nanoparticles dedicated to organophosphorus degradation: a benchmark, CrystEngComm, 22 *(*10*)*, 1725 – 1737 (2020).

[67] G. Marzun, J. Nakamura, X. Zhang, S. Barcikowski, P. Wagener, Size control and supporting of palladium nanoparticles made by laser ablation in saline solution as a facile route to heterogeneous catalysts, Applied Surface Science, 348, 75 – 84 (2015).

[68] R. Streubel, S. Barcikowski, B. Goekce, Continuous multigram nanoparticle synthesis by high-power, high-repetition-rate ultrafast laser ablation in liquids, Optics Letters, 41 *(7)*, 1486 – 1489 (2016).

[69] R. W. Boyd, *Nonlinear optics*, 3rd ed., Elsevier/Academic Press, Amsterdam (2008).

[70] S. Dittrich, R. Streubel, C. McDonnell, H. P. Huber, S. Barcikowski, B. Gökce, Comparison of the productivity and ablation efficiency of different laser classes for laser ablation of gold in water and air, Appl. Phys. A, 125 *(*6*)*, 55 (2019).

[71] J. S. Hoppius, S. Maragkaki, A. Kanitz, P. Gregorčič, E. L. Gurevich, Optimization of femtosecond laser processing in liquids, Applied Surface Science, 467-468, 255 – 260 (2019).

[72] A. Braun, G. Korn, X. Liu, D. Du, J. Squier, G. Mourou, Self-channeling of high-peak-power femtosecond laser pulses in air, Opt. Lett., 20 *(*1*)*, 73 – 75 (1995).

[73] A. Couairon, A. Mysyrowicz, Femtosecond filamentation in transparent media, Physics Reports, 441 *(*2-4*)*, 47 – 189 (2007).

[74] M. A. Sobhan, M. Ams, M. J. Withford, E. M. Goldys, Ultrafast laser ablative generation of gold nanoparticles: the influence of pulse energy, repetition frequency and spot size, J Nanopart Res, 12 *(8)*, 2831 – 2842 (2010).

[75] A. Menéndez-Manjón, P. Wagener, S. Barcikowski, Transfer-Matrix Method for Efficient Ablation by Pulsed Laser Ablation and Nanoparticle Generation in Liquids, J. Phys. Chem. C, 115 *(12)*, 5108 – 5114 (2011).

[76] N. Bärsch, J. Jakobi, S. Weiler, S. Barcikowski, Pure colloidal metal and ceramic nanoparticles from high-power picosecond laser ablation in water and acetone, Nanotechnology, 20 *(44)*, 445603 (2009).

[77] M. H. Niemz, Threshold dependence of laser-induced optical breakdown on pulse duration, Appl. Phys. Lett., 66 *(10)*, 1181 – 1183 (1995).

[78] J. Noack, A. Vogel, Laser-induced plasma formation in water at nanosecond to femtosecond time scales: calculation of thresholds, absorption coefficients, and energy density, IEEE J. Quantum Electron., 35 *(8)*, 1156 – 1167 (1999).

[79] P. Vasa, M. Singh, R. Bernard, A. K. Dharmadhikari, J. A. Dharmadhikari, D. Mathur, Supercontinuum generation in water doped with gold nanoparticles, Appl. Phys. Lett., 103 *(11)*, 111109 (2013).

[80] C. Wang, Y. Fu, Z. Zhou, Y. Cheng, Z. Xu, Femtosecond filamentation and supercontinuum generation in silver-nanoparticle-doped water, Appl. Phys. Lett., 90 *(18)*, 181119 (2007).

[81] R. A. Ganeev, M. Baba, A. I. Ryasnyansky, M. Suzuki, H. Kuroda, Laser ablation of GaAs in liquids: structural, optical, and nonlinear optical characteristics of colloidal solutions, Appl. Phys. B, 80 *(4-5)*, 595 – 601 (2005).

[82] S. Dittrich, S. Barcikowski, B. Gökce, Plasma and nanoparticle shielding during pulsed laser ablation in liquids cause ablation efficiency decrease, Opto-Electronic Advances, 4 *(1)*, 20007201 – 20007215 (2021).

[83] I. Papagiannouli, P. Aloukos, D. Rioux, M. Meunier, S. Couris, Effect of the Composition on the Nonlinear Optical Response of Au x Ag 1–x Nano-Alloys, J. Phys. Chem. C, 119 *(12)*, 6861 – 6872 (2015).

[84] G. Fan, S. Ren, S. Qu, Q. Wang, R. Gao, M. Han, Stability and nonlinear optical properties of Cu nanoparticles prepared by femtosecond laser ablation of Cu target in alcohol and water, Optics Communications, 330, 122 – 130 (2014).

[85] O. Sánchez-Dena, P. Mota-Santiago, L. Tamayo-Rivera, E. V. García-Ramírez, A. Crespo-Sosa, A. Oliver, J.-A. Reyes-Esqueda, Size-and shape-dependent nonlinear optical response of Au nanoparticles embedded in sapphire, Opt. Mater. Express, 4 *(1)*, 92 (2014).

[86] U. Pal, E.A. Almanza, O.V. Cuchillo, N. Koshizaki, T. Sasaki, S. Terauchi, Preparation of Au/ZnO nanocomposites by radio frequency co-sputtering, Solar Energy Materials and Solar Cells, 70 *(3)*, 363 – 368 (2001).

[87] N. Pinçon, B. Palpant, D. Prot, E. Charron, S. Debrus, Third-order nonlinear optical response of Au:SiO 2 thin films: Influence of gold nanoparticle concentration and

morphologic parameters, The European Physical Journal D - Atomic, Molecular and Optical Physics, 19 *(*3*)*, 395 – 402 (2002).

[88] R. F. Souza, M. A. R. C. Alencar, E. C. da Silva, M. R. Meneghetti, J. M. Hickmann, Nonlinear optical properties of Au nanoparticles colloidal system: Local and nonlocal responses, Appl. Phys. Lett., 92 *(*20*)*, 201902 (2008).

[89] A. Dakka, J. Lafait, C. Sella, S. Berthier, M. Abd-Lefdil, J.-C. Martin, M. Maaza, Optical properties of Ag–TiO_2 nanocermet films prepared by cosputtering and multilayer deposition techniques, Appl. Opt., 39 *(*16*)*, 2745 (2000).

[90] B. Can-Uc, R. Rangel-Rojo, A. Peña-Ramírez, C. B. de Araújo, H. T. M. C. M. Baltar, A. Crespo-Sosa, M. L. Garcia-Betancourt, A. Oliver, Nonlinear optical response of platinum nanoparticles and platinum ions embedded in sapphire, Optics express, 24 *(*9*)*, 9955 – 9965 (2016).

[91] M.-R. Kalus, R. Lanyumba, N. Lorenzo-Parodi, M. A. Jochmann, K. Kerpen, U. Hagemann, T. C. Schmidt, S. Barcikowski, B. Gökce, Determining the role of redox-active materials during laser-induced water decomposition, Physical chemistry chemical physics PCCP, 21 *(*34*)*, 18636 – 18651 (2019).

[92] M.-R. Kalus, V. Reimer, S. Barcikowski, B. Gökce, Discrimination of effects leading to gas formation during pulsed laser ablation in liquids, Applied Surface Science, 465, 1096 – 1102 (2019).

[93] M.-R. Kalus, N. Baersch, R. Streubel, E. Goekce, S. Barcikowski, B. Goekce, How persistent microbubbles shield nanoparticle productivity in laser synthesis of colloids – quantification of their volume, dwell dynamics, and gas composition, Physical Chemistry Chemical Physics, 19 *(*10*)*, 7112 – 7123 (2017).

[94] O. Benavides, O. Lebedeva, V. Golikov, Reflection of nanosecond Nd:YAG laser pulses in ablation of metals, Opt. Express, OE, 19 *(*22*)*, 21842 – 21848 (2011).

[95] A. Kanitz, D. J. Förster, J. S. Hoppius, R. Weber, A. Ostendorf, E. L. Gurevich, Pump-probe microscopy of femtosecond laser ablation in air and liquids, Applied Surface Science, 475, 204 – 210 (2019).

[96] C. Guo, A. J. Taylor, Ultrafast Dynamics of Thermal and Nonthermal Structural Changes in Metals, Int. J. Mod. Phys. B, 15 *(*02*)*, 101 – 115 (2001).

[97] A. L. Dobryakov, V. M. Farztdinov, Y. E. Lozovik, G. Marowsky, Laser-Induced Nonequilibrium Electron Distribution in Metals on a Femtosecond Time Scale, J. Phys. D: Appl. Phys., 60 *(*6*)*, 572 – 578 (1999).

[98] S. Babar, J. H. Weaver, Optical constants of Cu, Ag, and Au revisited, Appl. Opt., 54 *(*3*)*, 477 (2015).

[99] J. H. Weaver, C. Krafka, D. W. Lynch, E. E. Koch, Optical properties of metals, Appl. Opt., 20 *(*7*)* (1981).

[100] J. Hohlfeld, S.-S. Wellershoff, J. Güdde, U. Conrad, V. Jähnke, E. Matthias, Electron and lattice dynamics following optical excitation of metals, Chemical Physics, 251 *(*1-3*)*, 237 – 258 (2000).

[101] W. S. Fann, R. Storz, H. W. K. Tom, J. Bokor, Direct measurement of nonequilibrium electron-energy distributions in subpicosecond laser-heated gold films, Physical review letters, 68 *(*18*)* (1992).

[102] H. E. Elsayed-Ali, T. B. Norris, M. A. Pessot, G. A. Mourou, Time-resolved observation of electron-phonon relaxation in copper, Physical review letters, 58 *(*12*)* (1987).

[103] S.-S. Wellershoff, J. Hohlfeld, J. Güdde, E. Matthias, The role of electron-phonon coupling in femtosecond laser damage of metals, Applied Physics A: Materials Science & Processing, 69 *(*7*)*, S99-S107 (1999).

[104] B. N. Chichkov, C. Momma, S. Nolte, F. von Alvensleben, A. Tünnermann, Femtosecond, picosecond and nanosecond laser ablation of solids, Applied Physiks A, 63, 109 – 115 (1996).

[105] B. C. Stuart, M. D. Feit, S. Herman, A. M. Rubenchik, B. W. Shore, M. D. Perry, Optical ablation by high-power short-pulse lasers, J. Opt. Soc. Am. B, 13 *(2)*, 459 (1996).

[106] P. B. Corkum, F. Brunel, N. K. Sherman, T. Srinivasan-Rao, Thermal Response of Metals to Ultrashort-Pulse Laser Excitation, 61 *(*25*)*, 2886 – 2889 (1988).

[107] S. V. Starinskiy, Y. G. Shukhov, A. V. Bulgakov, Laser-induced damage thresholds of gold, silver and their alloys in air and water, Applied Surface Science, 396, 1765 – 1774 (2017).

[108] P. Lorazo, L. J. Lewis, M. Meunier, Short-pulse laser ablation of solids: from phase explosion to fragmentation, Physical review letters, 91 *(22)*, 225502 (2003).

[109] D. S. Ivanov, L. V. Zhigilei, Effect of pressure relaxation on the mechanisms of short-pulse laser melting, Physical review letters, 91 *(*10*)*, 105701 (2003).

[110] D. S. Ivanov, L. V. Zhigilei, Kinetic limit of heterogeneous melting in metals, Physical review letters, 98 *(*19*)*, 195701 (2007).

[111] D. P. Korfiatis, K.-A. T. Thoma, J. C. Vardaxoglou, Conditions for femtosecond laser melting of silicon, J. Phys. D: Appl. Phys., 40 *(*21*)*, 6803 – 6808 (2007).

[112] A. Rousse, C. Rischel, S. Fourmaux, I. Uschmann, S. Sebban, G. Grillon, P. Balcou, E. Förster, J. P. Geindre, P. Audebert, J. C. Gauthier, D. Hulin, Non-thermal melting in semiconductors measured at femtosecond resolution, Nature, 410 *(*6824*)*, 65 – 68 (2001).

[113] C.-Y. Shih, C. Wu, M. V. Shugaev, L. V. Zhigilei, Atomistic modeling of nanoparticle generation in short pulse laser ablation of thin metal films in water, Journal of colloid and interface science, 489, 3 – 17 (2017).

[114] C.-Y. Shih, M. V. Shugaev, C. Wu, L. V. Zhigilei, Generation of Subsurface Voids, Incubation Effect, and Formation of Nanoparticles in Short Pulse Laser Interactions

with Bulk Metal Targets in Liquid: Molecular Dynamics Study, The journal of physical chemistry. C, Nanomaterials and interfaces, 121 *(*30*)*, 16549 – 16567 (2017).

[115] T. Sakka, S. Masai, K. Fukami, Y. H. Ogata, Spectral profile of atomic emission lines and effects of pulse duration on laser ablation in liquid, Spectrochimica Acta Part B: Atomic Spectroscopy, 64 *(*10*)*, 981 – 985 (2009).

[116] B. Kumar, R. K. Thareja, Growth of titanium nanoparticles in confined plasma, Physics of Plasmas, 19 *(*3*)*, 33516 (2012).

[117] A. Kanitz, J. S. Hoppius, M. Fiebrandt, P. Awakowicz, C. Esen, A. Ostendorf, E. L. Gurevich, Impact of liquid environment on femtosecond laser ablation, Appl. Phys. A, 123 *(*11*)*, 109 (2017).

[118] S. I. Kudryashov, I. N. Saraeva, V. N. Lednev, S. M. Pershin, A. A. Rudenko, A. A. Ionin, Single-shot femtosecond laser ablation of gold surface in air and isopropyl alcohol, Appl. Phys. Lett., 112 *(*20*)*, 203101 (2018).

[119] I. B. Gornushkin, K. Amponsah-Manager, B. W. Smith, N. Omenetto, J. D. Winefordner, Microchip laser-induced breakdown spectroscopy: a preliminary feasibility investigation, Applied spectroscopy, 58 *(*7*)*, 762 – 769 (2004).

[120] K. Saito, T. Sakka, Y. H. Ogata, Rotational spectra and temperature evaluation of C2 molecules produced by pulsed laser irradiation to a graphite–water interface, Journal of Applied Physics, 94 *(*9*)*, 5530 – 5536 (2003).

[121] D. Amans, M. Diouf, J. Lam, G. Ledoux, C. Dujardin, Origin of the nano-carbon allotropes in pulsed laser ablation in liquids synthesis, Journal of colloid and interface science, 489, 114 – 125 (2017).

[122] R. Tanabe, T. T.P. Nguyen, T. Sugiura, Y. Ito, Bubble dynamics in metal nanoparticle formation by laser ablation in liquid studied through high-speed laser stroboscopic videography, Applied Surface Science, 351, 327 – 331 (2015).

[123] A. de Bonis, M. Sansone, L. D'Alessio, A. Galasso, A. Santagata, R. Teghil, Dynamics of laser-induced bubble and nanoparticles generation during ultra-short laser ablation of Pd in liquid, J. Phys. D: Appl. Phys., 46 *(*44*)*, 445301 (2013).

[124] A. Vogel, S. Busch, U. Parlitz, Shock wave emission and cavitation bubble generation by picosecond and nanosecond optical breakdown in water, The Journal of the Acoustical Society of America, 100 *(*1*)*, 148 – 165 (1996).

[125] T. Hupfeld, G. Laurens, S. Merabia, S. Barcikowski, B. Gökce, D. Amans, Dynamics of laser-induced cavitation bubbles at a solid–liquid interface in high viscosity and high capillary number regimes, Journal of Applied Physics, 127 *(*4*)*, 44306 (2020).

[126] J. Tomko, J. J. Naddeo, R. Jimenez, Y. Tan, M. Steiner, J. M. Fitz-Gerald, D. M. Bubb, S. M. O'Malley, Size and polydispersity trends found in gold nanoparticles synthesized by laser ablation in liquids, Physical chemistry chemical physics PCCP, 17 *(*25*)*, 16327 – 16333 (2015).

[127] C.-Y. Shih, R. Streubel, J. Heberle, A. Letzel, M. V. Shugaev, C. Wu, M. Schmidt, B. Gökce, S. Barcikowski, L. V. Zhigilei, Two mechanisms of nanoparticle generation in picosecond laser ablation in liquids: the origin of the bimodal size distribution, Nanoscale, 10 *(*15*)*, 6900 – 6910 (2018).

[128] S. Reich, P. Schönfeld, A. Letzel, S. Kohsakowski, M. Olbinado, B. Gökce, S. Barcikowski, A. Plech, Fluence Threshold Behaviour on Ablation and Bubble Formation in Pulsed Laser Ablation in Liquids, Chemphyschem a European journal of chemical physics and physical chemistry, 18 *(*9*)*, 1084 – 1090 (2017).

[129] H. Hu, T. Liu, H. Zhai, Comparison of femtosecond laser ablation of aluminum in water and in air by time-resolved optical diagnosis, Optics express, 23 *(2)*, 628 – 635 (2015).

[130] T. Tsuji, Y. Tsuboi, N. Kitamura, M. Tsuji, Microsecond-resolved imaging of laser ablation at solid–liquid interface: investigation of formation process of nano-size metal colloids, Applied Surface Science, 229 *(*1-4*)*, 365 – 371 (2004).

[131] A. Letzel, M. Santoro, J. Frohleiks, A. R. Ziefuß, S. Reich, A. Plech, E. Fazio, F. Neri, S. Barcikowski, B. Gökce, How the re-irradiation of a single ablation spot affects cavitation bubble dynamics and nanoparticles properties in laser ablation in liquids, Applied Surface Science, 473, 828 – 837 (2019).

[132] A. Letzel, B. Gökce, P. Wagener, S. Ibrahimkutty, A. Menzel, A. Plech, S. Barcikowski, Size Quenching during Laser Synthesis of Colloids Happens Already in the Vapor Phase of the Cavitation Bubble, J. Phys. Chem. C, 121 *(*9*)*, 5356 – 5365 (2017).

[133] S. Reich, J. Göttlicher, A. R. Ziefuß, R. Streubel, A. Letzel, A. Menzel, O. Mathon, S. Pascarelli, T. Baumbach, M. Zuber, B. Gökce, S. Barcikowski, A. Plech, In situ speciation and spatial mapping of Zn products during pulsed laser ablation in liquids (PLAL) by combined synchrotron methods, Nanoscale (2020).

[134] M. Dell'Aglio, A. Santagata, G. Valenza, A. de Stradis, A. de Giacomo, Study of the Effect of Water Pressure on Plasma and Cavitation Bubble Induced by Pulsed Laser Ablation in Liquid of Silver and Missed Variations of Observable Nanoparticle Features, Chemphyschem a European journal of chemical physics and physical chemistry, 18 *(*9*)*, 1165 – 1174 (2017).

[135] J.-P. Sylvestre, A. V. Kabashin, E. Sacher, M. Meunier, Femtosecond laser ablation of gold in water: influence of the laser-produced plasma on the nanoparticle size distribution, Appl. Phys. A, 80 *(4)*, 753 – 758 (2005).

[136] S. Reich, A. Letzel, A. Menzel, N. Kretzschmar, B. Gökce, S. Barcikowski, A. Plech, Early appearance of crystalline nanoparticles in pulsed laser ablation in liquids dynamics, Nanoscale, 11 *(*14*)*, 6962 – 6969 (2019).

[137] C.-Y. Shih, M. V. Shugaev, C. Wu, L. V. Zhigilei, The effect of pulse duration on nanoparticle generation in pulsed laser ablation in liquids: insights from large-scale atomistic simulations, Physical chemistry chemical physics PCCP (2020).

[138] A. V. Kabashin, M. Meunier, Synthesis of colloidal nanoparticles during femtosecond laser ablation of gold in water, J. Appl. Phys., 94 *(12)*, 7941 (2003).

[139] S. Besner, A. V. Kabashin, F. M. Winnik, M. Meunier, Ultrafast laser based “green” synthesis of non-toxic nanoparticles in aqueous solutions, Appl. Phys. A, 93 *(4)*, 955 – 959 (2008).

[140] V. Amendola, M. Meneghetti, Controlled size manipulation of free gold nanoparticles by laser irradiation and their facile bioconjugation, J. Mater. Chem., 17 *(44)*, 4705 (2007).

[141] K. Kawasoe, Y. Ishikawa, N. Koshizaki, T. Yano, O. Odawara, H. Wada, Preparation of spherical particles by laser melting in liquid using TiN as a raw material, Appl. Phys. B, 119 *(3)*, 475 – 483 (2015).

[142] X. Li, N. Koshizaki, A. Pyatenko, Y. Shimizu, H. Wang, J. Liu, X. Wang, M. Gao, Z. Wang, X. Zeng, Preparation of silver spheres by selective laser heating in silver-containing precursor solution, Opt. Express, OE, 19 *(4)*, 2846 – 2851 (2011).

[143] H. Wang, A. Pyatenko, K. Kawaguchi, X. Li, Z. Swiatkowska-Warkocka, N. Koshizaki, Selective pulsed heating for the synthesis of semiconductor and metal submicrometer spheres, Angewandte Chemie (International ed. in English), 49 *(36)*, 6361 – 6364 (2010).

[144] S. Link, C. Burda, B. Nikoobakht, M. A. El-Sayed, Laser-Induced Shape Changes of Colloidal Gold Nanorods Using Femtosecond and Nanosecond Laser Pulses, J. Phys. Chem. B, 104 *(26)*, 6152 – 6163 (2000).

[145] D. Liu, C. Li, F. Zhou, T. Zhang, H. Zhang, X. Li, G. Duan, W. Cai, Y. Li, Rapid synthesis of monodisperse Au nanospheres through a laser irradiation-induced shape conversion, self-assembly and their electromagnetic coupling SERS enhancement, Scientific reports, 5, 7686 (2015).

[146] G. González-Rubio, A. Guerrero-Martínez, L. M. Liz-Marzán, Reshaping, Fragmentation, and Assembly of Gold Nanoparticles Assisted by Pulse Lasers, Accounts of chemical research, 49 *(4)*, 678 – 686 (2016).

[147] S. Inasawa, M. Sugiyama, Y. Yamaguchi, Bimodal Size Distribution of Gold Nanoparticles under Picosecond Laser Pulses, The journal of physical chemistry. B, 109 *(19)*, 9404 – 9410 (2005).

[148] T. Tsuji, K. Iryo, Y. Nishimura, M. Tsuji, Preparation of metal colloids by a laser ablation technique in solution: influence of laser wavelength on the ablation efficiency (II), Journal of Photochemistry and Photobiology A: Chemistry, 145 *(3)*, 201 – 207 (2001).

[149] A. R. Ziefuß, S. Reichenberger, C. Rehbock, I. Chakraborty, M. Gharib, W. J. Parak, S. Barcikowski, Laser Fragmentation of Colloidal Gold Nanoparticles with High-Intensity Nanosecond Pulses is Driven by a Single-Step Fragmentation Mechanism with a Defined Educt Particle-Size Threshold, J. Phys. Chem. C, 122 *(38)*, 22125 – 22136 (2018).

[150] D. Werner, S. Hashimoto, Improved Working Model for Interpreting the Excitation Wavelength- and Fluence-Dependent Response in Pulsed Laser-Induced Size Reduction of Aqueous Gold Nanoparticles, J. Phys. Chem. C, 115 *(12)*, 5063 – 5072 (2011).

[151] A. Menendez-Manjon, S. Barcikowski, Hydrodynamic size distribution of gold nanoparticles controlled by repetition rate during pulsed laser ablation in water, Applied Surface Science, 257 *(9)*, 4285 – 4290 (2011).

[152] P. Wagener, A. Schwenke, B. N. Chichkov, S. Barcikowski, Pulsed Laser Ablation of Zinc in Tetrahydrofuran: Bypassing the Cavitation Bubble, J. Phys. Chem. C, 114 *(17)*, 7618 – 7625 (2010).

[153] Y.-H. Chen, C.-S. Yeh, Laser ablation method: use of surfactants to form the dispersed Ag nanoparticles, Colloids and Surfaces A: Physicochemical and Engineering Aspects, 197 *(1-3)*, 133 – 139 (2002).

[154] P. K. Baruah, A. K. Sharma, A. Khare, Effective control of particle size, surface plasmon resonance and stoichiometry of Cu@CuxO nanoparticles synthesized by laser ablation of Cu in distilled water, Optics & Laser Technology, 108, 574 – 582 (2018).

[155] M. Lau, S. Barcikowski, Quantification of mass-specific laser energy input converted into particle properties during picosecond pulsed laser fragmentation of zinc oxide and boron carbide in liquids, Applied Surface Science, 348, 22 – 29 (2015).

[156] F. Waag, B. Gökce, S. Barcikowski, Ablation target cooling by maximizing the nanoparticle productivity in laser synthesis of colloids, Applied Surface Science, 466, 647 – 656 (2019).

[157] K. Maximova, A. Aristov, M. Sentis, A. V. Kabashin, Size-controllable synthesis of bare gold nanoparticles by femtosecond laser fragmentation in water, Nanotechnology, 26 *(6)*, 65601 (2015).

[158] P. Boyer, M. Meunier, Modeling Solvent Influence on Growth Mechanism of Nanoparticles (Au, Co) Synthesized by Surfactant Free Laser Processes, J. Phys. Chem. C, 116 *(14)*, 8014 – 8019 (2012).

[159] F. Waag, B. Gökce, C. Kalapu, G. Bendt, S. Salamon, J. Landers, U. Hagemann, M. Heidelmann, S. Schulz, H. Wende, N. Hartmann, M. Behrens, S. Barcikowski, Adjusting the catalytic properties of cobalt ferrite nanoparticles by pulsed laser fragmentation in water with defined energy dose, Scientific reports, 7 *(1)*, 13161 (2017).

[160] S. Jendrzej, B. Gökce, V. Amendola, S. Barcikowski, Barrierless growth of precursor-free, ultrafast laser-fragmented noble metal nanoparticles by colloidal atom clusters - A kinetic in situ study, Journal of colloid and interface science, 463, 299 – 307 (2016).

[161] A. Menéndez-Manjón, B. N. Chichkov, S. Barcikowski, Influence of Water Temperature on the Hydrodynamic Diameter of Gold Nanoparticles from Laser Ablation, J. Phys. Chem. C, 114 *(6)*, 2499 – 2504 (2010).

[162] F. Mafuné, J.-y. Kohno, Y. Takeda, T. Kondow, H. Sawabe, Formation of Gold Nanoparticles by Laser Ablation in Aqueous Solution of Surfactant, J. Phys. Chem. B, 105 *(22)*, 5114 – 5120 (2001).

[163] T. Tsuji, D.-H. Thang, Y. Okazaki, M. Nakanishi, Y. Tsuboi, M. Tsuji, Preparation of silver nanoparticles by laser ablation in polyvinylpyrrolidone solutions, Applied Surface Science, 254 *(16)*, 5224 – 5230 (2008).

[164] J.-P. Sylvestre, A. V. Kabashin, E. Sacher, M. Meunier, J. H. T. Luong, Stabilization and size control of gold nanoparticles during laser ablation in aqueous cyclodextrins, Journal of the American Chemical Society, 126 *(23)*, 7176 – 7177 (2004).

[165] K. Yamada, Y. Tokumoto, T. Nagata, F. Mafuné, Mechanism of laser-induced size-reduction of gold nanoparticles as studied by nanosecond transient absorption spectroscopy, The journal of physical chemistry. B, 110 *(24)*, 11751 – 11756 (2006).

[166] R. M. Tilaki, A. Iraji zad, S. M. Mahdavi, Stability, size and optical properties of silver nanoparticles prepared by laser ablation in different carrier media, Appl. Phys. A, 84 *(1-2)*, 215 – 219 (2006).

[167] B. Gökce, D. D. van't Zand, A. Menéndez-Manjón, S. Barcikowski, Ripening kinetics of laser-generated plasmonic nanoparticles in different solvents, Chemical Physics Letters, 626, 96 – 101 (2015).

[168] T. Tsuji, T. Yahata, M. Yasutomo, K. Igawa, M. Tsuji, Y. Ishikawa, N. Koshizaki, Preparation and investigation of the formation mechanism of submicron-sized spherical particles of gold using laser ablation and laser irradiation in liquids, Physical chemistry chemical physics PCCP, 15 *(9)*, 3099 – 3107 (2013).

[169] V. Amendola, P. Riello, M. Meneghetti, Magnetic Nanoparticles of Iron Carbide, Iron Oxide, Iron@Iron Oxide, and Metal Iron Synthesized by Laser Ablation in Organic Solvents, J. Phys. Chem. C, 115 *(12)*, 5140 – 5146 (2011).

[170] S. Hamad, G. K. Podagatlapalli, S. P. Tewari, S. V. Rao, Synthesis of Cu 2 O, CuCl, and Cu 2 OCl 2 nanoparticles by ultrafast laser ablation of copper in liquid media, Pramana - J Phys, 82 *(2)*, 331 – 337 (2014).

[171] R.-D. Sun, T. Tsuji, Preparation of antimony sulfide semiconductor nanoparticles by pulsed laser ablation in liquid, Applied Surface Science, 348, 38 – 44 (2015).

[172] C. Rehbock, V. Merk, L. Gamrad, R. Streubel, S. Barcikowski, Size control of laser-fabricated surfactant-free gold nanoparticles with highly diluted electrolytes and their subsequent bioconjugation, Physical chemistry chemical physics PCCP, 15 *(9)*, 3057 – 3067 (2013).

[173] C. Rehbock, J. Jakobi, L. Gamrad, S. van der Meer, D. Tiedemann, U. Taylor, W. Kues, D. Rath, S. Barcikowski, Current state of laser synthesis of metal and alloy nanoparticles as ligand-free reference materials for nano-toxicological assays, Beilstein journal of nanotechnology, 5, 1523 – 1541 (2014).

[174] V. Merk, C. Rehbock, F. Becker, U. Hagemann, H. Nienhaus, S. Barcikowski, In situ non-DLVO stabilization of surfactant-free, plasmonic gold nanoparticles: effect of Hofmeister's anions, Langmuir the ACS journal of surfaces and colloids, 30 *(*15*)*, 4213 – 4222 (2014).

[175] F. Mafuné, J.-y. Kohno, Y. Takeda, T. Kondow, H. Sawabe, Structure and Stability of Silver Nanoparticles in Aqueous Solution Produced by Laser Ablation, J. Phys. Chem. B, 104 *(*35*)*, 8333 – 8337 (2000).

[176] A. Letzel, S. Reich, T. Dos Santos Rolo, A. Kanitz, J. S. Hoppius, A. Rack, M. P. Olbinado, A. Ostendorf, B. Gökce, A. Plech, S. Barcikowski, Time and Mechanism of Nanoparticle Functionalization by Macromolecular Ligands during Pulsed Laser Ablation in Liquids, Langmuir the ACS journal of surfaces and colloids, 35 *(*8*)*, 3038 – 3047 (2019).

[177] A. Santagata, A. Guarnaccio, D. Pietrangeli, Á. Szegedi, J. Valyon, A. de Stefanis, A. de Bonis, R. Teghil, M. Sansone, D. Mollica, G. P. Parisi, Production of silver-silica core-shell nanocomposites using ultra-short pulsed laser ablation in nanoporous aqueous silica colloidal solutions, J. Phys. D: Appl. Phys., 48 *(*20*)*, 205304 (2015).

[178] R. Intartaglia, G. Das, K. Bagga, A. Gopalakrishnan, A. Genovese, M. Povia, E. Di Fabrizio, R. Cingolani, A. Diaspro, F. Brandi, Laser synthesis of ligand-free bimetallic nanoparticles for plasmonic applications, Physical chemistry chemical physics PCCP, 15 *(*9*)*, 3075 – 3082 (2013).

[179] P. Wagener, A. Schwenke, S. Barcikowski, How citrate ligands affect nanoparticle adsorption to microparticle supports, Langmuir the ACS journal of surfaces and colloids, 28 *(*14*)*, 6132 – 6140 (2012).

[180] V. Amendola, M. Meneghetti, Laser ablation synthesis in solution and size manipulation of noble metal nanoparticles, Physical chemistry chemical physics PCCP, 11 *(*20*)*, 3805 – 3821 (2009).

[181] S. Reichenberger, G. Marzun, S. Barcikowski, M. Muhler, Perspective of surfactant-free colloidal nanoparticles in heterogeneous catalysis, ChemCatChem (2019).

[182] A. Y. Klyushin, M. T. Greiner, X. Huang, T. Lunkenbein, X. Li, O. Timpe, M. Friedrich, M. Hävecker, A. Knop-Gericke, R. Schlögl, Is Nanostructuring Sufficient To Get Catalytically Active Au?, ACS Catal., 6 *(*5*)*, 3372 – 3380 (2016).

[183] E. V. Barmina, S. V. Gudkov, A. V. Simakin, G. A. Shafeev, Stable Products of Laser-Induced Breakdown of Aqueous Colloidal Solutions of Nanoparticles, JLMN, 12 *(*3*)* (2017).

[184] H. Mateos, R. A. Picca, A. Mallardi, M. Dell'Aglio, A. de Giacomo, N. Cioffi, G. Palazzo, Effect of the Surface Chemical Composition and of Added Metal Cation Concentration on the Stability of Metal Nanoparticles Synthesized by Pulsed Laser Ablation in Water, Applied Sciences, 10 *(*12*)*, 4169 (2020).

[185] H. Muto, K. Yamada, K. Miyajima, F. Mafuné, Estimation of Surface Oxide on Surfactant-Free Gold Nanoparticles Laser-Ablated in Water, J. Phys. Chem. C, 111 *(*46*)*, 17221 – 17226 (2007).

[186] R. Siburian, T. Kondo, J. Nakamura, Size Control to a Sub-Nanometer Scale in Platinum Catalysts on Graphene, J. Phys. Chem. C, 117 *(7)*, 3635 – 3645 (2013).

[187] S. Kohsakowski, A. Santagata, M. Dell'Aglio, A. de Giacomo, S. Barcikowski, P. Wagener, B. Goekce, High productive and continuous nanoparticle fabrication by laser ablation of a wire-target in a liquid jet, Applied Surface Science, 403, 487 – 499 (2017).

[188] S. Hashimoto, D. Werner, T. Uwada, Studies on the interaction of pulsed lasers with plasmonic gold nanoparticles toward light manipulation, heat management, and nanofabrication, Journal of Photochemistry and Photobiology C: Photochemistry Reviews, 13 *(1)*, 28 – 54 (2012).

[189] D. Werner, A. Furube, T. Okamoto, S. Hashimoto, Femtosecond Laser-Induced Size Reduction of Aqueous Gold Nanoparticles: In Situ and Pump−Probe Spectroscopy Investigations Revealing Coulomb Explosion, J. Phys. Chem. C, 115 *(*17*)*, 8503 – 8512 (2011).

[190] S. Koenen, C. Rehbock, H. E. Heissler, S. D. Angelov, K. Schwabe, J. K. Krauss, S. Barcikowski, Optimizing in Vitro Impedance and Physico-Chemical Properties of Neural Electrodes by Electrophoretic Deposition of Pt Nanoparticles, Chemphyschem a European journal of chemical physics and physical chemistry, 18 *(9)*, 1108 – 1117 (2017).

[191] W. T. Nichols, T. Sasaki, N. Koshizaki, Laser ablation of a platinum target in water. III. Laser-induced reactions, J. Appl. Phys., 100 *(*11*)*, 114913 (2006).

[192] R. Sattari, C. L. Sajti, S. Khan, S. Barcikowski, Scale-up of nanoparticle production during laser ablation of ceramics in liquid media, Nanomanufacturing Conference, 49-54 (2018).

[193] M. A. Valverde-Alva, T. García-Fernández, E. Esparza-Alegría, M. Villagrán-Muniz, C. Sánchez-Aké, R. Castañeda-Guzmán, M. B. de La Mora, C. E. Márquez-Herrera, J. L. Sánchez Llamazares, Laser ablation efficiency during the production of Ag nanoparticles in ethanol at a low pulse repetition rate (1–10 Hz), Laser Phys. Lett., 13 *(*10*)*, 106002 (2016).

[194] C. L. Sajti, R. Sattari, B. N. Chichkov, S. Barcikowski, Ablation efficiency of alpha-Al2O3 in liquid phase and ambient air by nanosecond laser irradiation, Appl. Phys. A, 100 *(1)*, 203 – 206 (2010).

[195] H. Liu, F. Chen, X. Wang, Q. Yang, H. Bian, J. Si, X. Hou, Influence of liquid environments on femtosecond laser ablation of silicon, Thin Solid Films, 518 *(*18*)*, 5188 – 5194 (2010).

[196] W. Liu, O. Kosareva, I. S. Golubtsov, A. Iwasaki, A. Becker, V. P. Kandidov, S. L. Chin, Femtosecond laser pulse filamentation versus optical breakdown in H 2 O, Applied Physics B: Lasers and Optics, 76 *(3)*, 215 – 229 (2003).

[197] G. Račiukaitis, M. Brikas, P. Gecys, B. Voisiat, M. Gedvilas, Use of High Repetition Rate and High Power Lasers in Microfabrication, JLMN, 4 *(3)*, 186 – 191 (2009).

[198] B. Neuenschwander, B. Jaeggi, M. Schmid, G. Hennig, Surface Structuring with Ultra-short Laser Pulses, Physics Procedia, 56, 1047 – 1058 (2014).

[199] E. G. Gamaly, A. V. Rode, B. Luther-Davies, V. T. Tikhonchuk, Ablation of solids by femtosecond lasers, Physics of Plasmas, 9 *(3)*, 949 – 957 (2002).

[200] C. Momma, B. N. Chichkov, S. Nolte, F. von Alvensleben, A. Tünnermann, H. Welling, B. Wellegehausen, Short-pulse laser ablation of solid targets, Optics Communications, 129 *(1-2)*, 134 – 142 (1996).

[201] K. Venkatakrishnan, P. Stanley, N. R. Sivakumar, B. Tan, L.E.N. Lim, Effect of scanning resolution and fluence fluctuation on femtosecond laser ablation of thin films, Appl. Phys. A, 77 *(5)*, 655 – 658 (2003).

[202] J. Krüger, D. Dufft, R. Koter, A. Hertwig, Femtosecond laser-induced damage of gold films, Applied Surface Science, 253 *(19)*, 7815 – 7819 (2007).

[203] R. Boedefeld, J. Schreiber, H. Gessner, E. Welsch, W. Theobald, T. Feurer, R. A. Sauerbrey, Optical damage of sputtered gold films irradiated with femtosecond laser pulses, Proc. SPIE, 4347, 45 – 52 (2001).

[204] M.-R. Kalus, S. Barcikowski, B. Gökce, How the physicochemical properties of the bulk material affect the ablation crater profile, mass balance and bubble dynamics during single-pulse, nanosecond laser ablation in water, Chemistry (Weinheim an der Bergstrasse, Germany) (2021).

[205] P.T. Mannion, J. Magee, E. Coyne, G.M. O'Connor, T.J. Glynn, The effect of damage accumulation behaviour on ablation thresholds and damage morphology in ultrafast laser micro-machining of common metals in air, Applied Surface Science, 233 *(1-4)*, 275 – 287 (2004).

[206] B. N. Chichkov, C. Momma, S. Nolte, F. von Alvensleben, A. Tünnermann, Ablation of metals by ultrashort laser pulses, J. Opt. Soc. Am. B, 14 *(10)* (1997).

[207] M. Forster, L. Égerházi, C. Haselberger, C. Huber, W. Kautek, Femtosecond laser interaction with pulsed-laser deposited carbon thin films of nanoscale thickness, Appl. Phys. A, 102 *(1)*, 27 – 33 (2011).

[208] E. Matthias, M. Reichling, J. Siegel, O. W. Kding, S. Petzoldt, H. Skurk, P. Bizenberger, E. Neske, The influence of thermal diffusion on laser ablation of metal films, Appl. Phys. A, 58 *(2)*, 129 – 136 (1994).

[209] R. Le Harzic, D. Breitling, M. Weikert, S. Sommer, C. Föhl, S. Valette, C. Donnet, E. Audouard, F. Dausinger, Pulse width and energy influence on laser micromachining of

metals in a range of 100fs to 5ps, Applied Surface Science, 249 *(*1-4*)*, 322 – 331 (2005).

[210] B. Jaeggi, B. Neuenschwander, M. Schmid, M. Muralt, J. Zürcher, U. Hunziker, Influence of the Pulse Duration in the ps-Regime on the Ablation Efficiency of Metals, Physics Procedia, 12, 164 – 171 (2011).

[211] B. Neuenschwander, B. Jaeggi, M. Schmid, From fs to Sub-ns, Physics Procedia, 41, 794 – 801 (2013).

[212] S. Sakaki, H. Ikenoue, T. Tsuji, Y. Ishikawa, N. Koshizaki, Pulse-Width Dependence of the Cooling Effect on Sub-Micrometer ZnO Spherical Particle Formation by Pulsed-Laser Melting in a Liquid, Chemphyschem a European journal of chemical physics and physical chemistry, 18 *(*9*)*, 1101 – 1107 (2017).

[213] D. X. Hammer, E. D. Jansen, M. Frenz, G. D. Noojin, R. J. Thomas, J. Noack, A. Vogel, B. A. Rockwell, A. J. Welch, Shielding properties of laser-induced breakdown in water for pulse durations from 5 ns to 125 fs, Appl. Opt., 36 *(*22*)*, 5630 – 5640 (1997).

[214] R. A. Ganeev, M. Baba, A. I. Ryasnyansky, M. Suzuki, H. Kuroda, Characterization of optical and nonlinear optical properties of silver nanoparticles prepared by laser ablation in various liquids, Optics Communications, 240 *(*4-6*)*, 437 – 448 (2004).

[215] D. Riabinina, M. Chaker, J. Margot, Dependence of gold nanoparticle production on pulse duration by laser ablation in liquid media, Nanotechnology, 23 *(*13*)*, 135603 (2012).

[216] B. I. Belevtsev, Y. F. Komnik, E. Y. Beliayev, Electron relaxation in disordered gold films, Phys. Rev. B, 58 *(*12*)*, 8079 – 8086 (1998).

[217] P. B. Johnson, R. W. Christy, Optical Constants of the Noble Metals, Phys. Rev. B, 6 *(*12*)*, 4370 – 4379 (1972).

[218] K. M. McPeak, S. V. Jayanti, S. J. P. Kress, S. Meyer, S. Iotti, A. Rossinelli, D. J. Norris, Plasmonic Films Can Easily Be Better: Rules and Recipes, ACS photonics, 2 *(*3*)*, 326 – 333 (2015).

[219] R. L. Olmon, B. Slovick, T. W. Johnson, D. Shelton, S.-H. Oh, G. D. Boreman, M. B. Raschke, Optical dielectric function of gold, Phys. Rev. B, 86 *(*23*)*, 285 (2012).

[220] W. S. M. Werner, K. Glantschnig, C. Ambrosch-Draxl, Optical Constants and Inelastic Electron-Scattering Data for 17 Elemental Metals, Journal of Physical and Chemical Reference Data, 38 *(*4*)*, 1013 – 1092 (2009).

[221] R. Lachaine, É. Boulais, E. Bourbeau, M. Meunier, Effect of pulse duration on plasmonic enhanced ultrafast laser-induced bubble generation in water, Appl. Phys. A, 112 *(*1*)*, 119 – 122 (2013).

[222] D. Tan, Y. Yamada, S. Zhou, Y. Shimotsuma, K. Miura, J. Qiu, Carbon nanodots with strong nonlinear optical response, Carbon, 69, 638 – 640 (2014).

[223] S. Dengler, C. Kübel, A. Schwenke, G. Ritt, B. Eberle, Near- and off-resonant optical limiting properties of gold–silver alloy nanoparticles for intense nanosecond laser pulses, J. Opt., 14 *(7)*, 75203 (2012).

[224] G. X. Chen, M. H. Hong, T. C. Chong, H. I. Elim, G. H. Ma, W. Ji, Preparation of carbon nanoparticles with strong optical limiting properties by laser ablation in water, Journal of Applied Physics, 95 *(3)*, 1455 – 1459 (2004).

[225] S. Dittrich, S. Kohsakowski, B. Wittek, C. Hengst, B. Gökce, S. Barcikowski, S. Reichenberger, Increasing the Size-Selectivity in Laser-Based g/h Liquid Flow Synthesis of Pt and PtPd Nanoparticles for CO and NO Oxidation in Industrial Automotive Exhaust Gas Treatment Benchmarking, Nanomaterials, 10 *(8)*, 1582 (2020).

[226] T. Hupfeld, A. Wegner, M. Blanke, C. Doñate-Buendía, V. Sharov, S. Nieskens, M. Piechotta, M. Giese, S. Barcikowski, B. Gökce, Plasmonic Seasoning: Giving Color to Desktop Laser 3D Printed Polymers by Highly Dispersed Nanoparticles, Adv. Optical Mater., 2000473 (2020).

[227] G. C. Messina, P. Wagener, R. Streubel, A. de Giacomo, A. Santagata, G. Compagnini, S. Barcikowski, Pulsed laser ablation of a continuously-fed wire in liquid flow for high-yield production of silver nanoparticles, Physical chemistry chemical physics PCCP, 15 *(9)*, 3093 – 3098 (2013).

[228] S. Kohsakowski, B. Gökce, R. Tanabe, P. Wagener, A. Plech, Y. Ito, S. Barcikowski, Target geometry and rigidity determines laser-induced cavitation bubble transport and nanoparticle productivity - a high-speed videography study, Physical chemistry chemical physics PCCP, 18 *(24)*, 16585 – 16593 (2016).

[229] Z. Kuang, W. Perrie, D. Liu, P. Fitzsimons, S. P. Edwardson, E. Fearon, G. Dearden, K. G. Watkins, Ultrashort pulse laser patterning of indium tin oxide thin films on glass by uniform diffractive beam patterns, Applied Surface Science, 258 *(19)*, 7601 – 7606 (2012).

[230] G. Dearden, Z. Kuang, D. Liu, W. Perrie, S. P. Edwardson, K. G. Watkins, Advances in Ultra Short Pulse Laser based Parallel Processing using a Spatial Light Modulator, Physics Procedia, 39, 650 – 660 (2012).

[231] F. Waag, R. Streubel, B. Gökce, S. Barcikowski, Synthesis of gold, platinum, and gold-platinum alloy nanoparticle colloids with high-power megahertz-repetition-rate lasers: the importance of the beam guidance method, Appl Nanosci (2021).

[232] M. Muniz-Miranda, C. Gellini, E. Giorgetti, Surface-Enhanced Raman Scattering from Copper Nanoparticles Obtained by Laser Ablation, J. Phys. Chem. C, 115 *(12)*, 5021 – 5027 (2011).

[233] V. Amendola, L. Litti, M. Meneghetti, LDI-MS assisted by chemical-free gold nanoparticles: enhanced sensitivity and reduced background in the low-mass region, Analytical chemistry, 85 *(*24*)*, 11747 – 11754 (2013).

[234] S. K. Balasubramanian, L. Yang, L.-Y. L. Yung, C.-N. Ong, W.-Y. Ong, L. E. Yu, Characterization, purification, and stability of gold nanoparticles, Biomaterials, 31 *(*34*)*, 9023 – 9030 (2010).

[235] S. Petersen, J. Jakobi, S. Barcikowski, In-situ bioconjugation - Novel laser based approach to pure nanoparticle-conjugates, Applied Surface Science, 255 *(*10*)*, 5435 – 5438 (2009).

[236] J. Zhang, M. Chaker, D. Ma, Pulsed laser ablation based synthesis of colloidal metal nanoparticles for catalytic applications, Journal of colloid and interface science, 489, 138 – 149 (2017).

[237] F. Davodi, E. Mühlhausen, M. Tavakkoli, J. Sainio, H. Jiang, B. Gökce, G. Marzun, T. Kallio, Catalyst Support Effect on the Activity and Durability of Magnetic Nanoparticles: toward Design of Advanced Electrocatalyst for Full Water Splitting, ACS applied materials & interfaces, 10 *(*37*)*, 31300 – 31311 (2018).

[238] T. Schmitz, U. Wiedwald, C. Dubs, B. Gökce, Ultrasmall Yttrium Iron Garnet Nanoparticles with High Coercivity at Low Temperature Synthesized by Laser Ablation and Fragmentation of Pressed Powders, Chemphyschem a European journal of chemical physics and physical chemistry, 18 *(*9*)*, 1125 – 1132 (2017).

[239] A. Kanitz, J. S. Hoppius, M. Del Mar Sanz, M. Maicas, A. Ostendorf, E. L. Gurevich, Synthesis of Magnetic Nanoparticles by Ultrashort Pulsed Laser Ablation of Iron in Different Liquids, Chemphyschem a European journal of chemical physics and physical chemistry, 18 *(*9*)*, 1155 – 1164 (2017).

[240] S. Barcikowski, T. Baranowski, Y. Durmus, U. Wiedwald, B. Gökce, Solid solution magnetic FeNi nanostrand–polymer composites by connecting-coarsening assembly, J. Mater. Chem. C, 3 *(*41*)*, 10699 – 10704 (2015).

[241] S. Jendrzej, L. Gondecki, J. Debus, H. Moldenhauer, P. Tenberge, S. Barcikowski, B. Gökce, Tribological properties of laser-generated hard ceramic particles in a gear drive contact, Applied Surface Science, 467-468, 811 – 818 (2019).

[242] R. Streubel, M. B. Wilms, C. Doñate-Buendía, A. Weisheit, S. Barcikowski, J. H. Schleifenbaum, B. Gökce, Depositing laser-generated nanoparticles on powders for additive manufacturing of oxide dispersed strengthened alloy parts via laser metal deposition, Jpn. J. Appl. Phys., 57 *(4)*, 40310 (2018).

[243] T. Hupfeld, T. Laumer, T. Stichel, T. Schuffenhauer, J. Heberle, M. Schmidt, S. Barcikowski, B. Gökce, A new approach to coat PA12 powders with laser-generated nanoparticles for selective laser sintering, Procedia CIRP, 74, 244 – 248 (2018).

[244] M. B. Wilms, R. Streubel, F. Frömel, A. Weisheit, J. Tenkamp, F. Walther, S. Barcikowski, J. H. Schleifenbaum, B. Gökce, Laser additive manufacturing of oxide dispersion strengthened steels using laser-generated nanoparticle-metal composite powders, Procedia CIRP, 74, 196 – 200 (2018).

[245] C. Doñate-Buendía, F. Frömel, M. B. Wilms, R. Streubel, J. Tenkamp, T. Hupfeld, M. Nachev, E. Gökce, A. Weisheit, S. Barcikowski, F. Walther, J. H. Schleifenbaum, B. Gökce, Oxide dispersion-strengthened alloys generated by laser metal deposition of laser-generated nanoparticle-metal powder composites, Materials & Design, 154, 360 – 369 (2018).

[246] N. M. Bulgakova, A. V. Bulgakov, I. M. Bourakov, N. A. Bulgakova, Pulsed laser ablation of solids and critical phenomena, Applied Surface Science, 197-198, 96 – 99 (2002).

[247] L. S. Brown, T. W. B. Kibble, Interaction of Intense Laser Beams with Electrons, Phys. Rev., 133 *(*3A*)*, A705-A719 (1964).

[248] J. Furmanski, A. M. Rubenchik, M. D. Shirk, B. C. Stuart, Deterministic processing of alumina with ultrashort laser pulses, Journal of Applied Physics, 102 *(7)*, 73112 (2007).

[249] S. Preuss, A. Demchuk, M. Stuke, Sub-picosecond UV laser ablation of metals, Appl. Phys. A, 61 *(1)*, 33 – 37 (1995).

[250] N. Patra, K. Akash, S. Shiva, R. Gagrani, H. S. P. Rao, V. R. Anirudh, I. A. Palani, V. Singh, Parametric investigations on the influence of nano-second Nd 3+ :YAG laser wavelength and fluence in synthesizing NiTi nano-particles using liquid assisted laser ablation technique, Applied Surface Science, 366, 104 – 111 (2016).

[251] D. Devaux, R. Fabbro, L. Tollier, E. Bartnicki, Generation of shock waves by laser-induced plasma in confined geometry, Journal of Applied Physics, 74 *(*4*)*, 2268 – 2273 (1993).

[252] N. A. Inogamov, V. V. Zhakhovskii, V. A. Khokhlov, Dynamics of Gold Ablation into Water, J. Exp. Theor. Phys., 127 *(1)*, 79 – 106 (2018).

[253] M. Dell'Aglio, R. Gaudiuso, O. de Pascale, A. de Giacomo, Mechanisms and processes of pulsed laser ablation in liquids during nanoparticle production, Applied Surface Science, 348, 4 – 9 (2015).

[254] S. Barcikowski, A. Hahn, A. V. Kabashin, B. N. Chichkov, Properties of nanoparticles generated during femtosecond laser machining in air and water, Appl. Phys. A, 87 *(1)*, 47 – 55 (2007).

[255] M. E. Shaheen, J. E. Gagnon, B. J. Fryer, Femtosecond laser ablation of brass in air and liquid media, Journal of Applied Physics, 113 *(*21*)*, 213106 (2013).

[256] P. A. Danilov, A. A. Ionin, S. I. Kudryashov, A. A. Rudenko, I. N. Saraeva, D. A. Zayarny, Non-monotonic variation of Au nanoparticle yield during

femtosecond/picosecond laser ablation in water, Laser Phys. Lett., 14 *(5)*, 56001 (2017).

[257] I. N. Saraeva, S. I. Kudryashov, A. A. Rudenko, M. I. Zhilnikova, D. S. Ivanov, D. A. Zayarny, A. V. Simakin, A. A. Ionin, M. E. Garcia, Effect of fs/ps laser pulsewidth on ablation of metals and silicon in air and liquids, and on their nanoparticle yields, Applied Surface Science, 470, 1018 – 1034 (2019).

[258] D. D. Evanoff, G. Chumanov, Synthesis and optical properties of silver nanoparticles and arrays, Chemphyschem a European journal of chemical physics and physical chemistry, 6 *(7)*, 1221 – 1231 (2005).

[259] A. Y. Vorobyev, C. Guo, Enhanced absorptance of gold following multipulse femtosecond laser ablation, Phys. Rev. B, 72 *(*19*)*, 1496 (2005).

[260] S. Reich, A. Letzel, B. Gökce, A. Menzel, S. Barcikowski, A. Plech, Incubation effect of pre-irradiation on bubble formation and ablation in laser ablation in liquids, Chemphyschem (2019).

[261] G. M. Hale, M. R. Querry, Optical Constants of Water in the 200-nm to 200-microm Wavelength Region, Appl. Opt., 12 *(*3*)*, 555 – 563 (1973).

[262] P. E. Ciddor, Refractive index of air: new equations for the visible and near infrared, Appl. Opt., 35 *(*9*)*, 1566 – 1573 (1996).

[263] R. R. Letfullin, T. F. George, G. C. Duree, B. M. Bollinger, Ultrashort Laser Pulse Heating of Nanoparticles: Comparison of Theoretical Approaches, Advances in Optical Technologies, 2008 *(*6*)*, 1 – 8 (2008).

[264] D. Du, X. Liu, G. Korn, J. Squier, G. Mourou, Laser-induced breakdown by impact ionization in SiO 2 with pulse widths from 7 ns to 150 fs, Appl. Phys. Lett., 64 *(*23*)*, 3071 – 3073 (1994).

[265] G. W. Yang, Laser ablation in liquids: Applications in the synthesis of nanocrystals, Progress in Materials Science, 52 *(4)*, 648 – 698 (2007).

[266] P. Peyer, L. Berthe, R. Fabbro, A. Sollier, Journal of Physics D: Applied Physics Experimental determination by PVDF and EMV techniques of shock amplitudes induced by 0.6-3 ns laser pulses in a confined regime with water, J Phys D: Appl Phys, 33 *(*5*)*, 498 – 503 (2000).

[267] K. K. Kim, M. Roy, H. Kwon, J. K. Song, S. M. Park, Laser ablation dynamics in liquid phase: The effects of magnetic field and electrolyte, Journal of Applied Physics, 117 *(7)*, 74302 (2015).

[268] X. Liu, M. Atwater, J. Wang, Q. Huo, Extinction coefficient of gold nanoparticles with different sizes and different capping ligands, Colloids and surfaces. B, Biointerfaces, 58 *(*1*)*, 3 – 7 (2007).

[269] S. I. Kudryashov, A. A. Nastulyavichus, A. K. Ivanova, N. A. Smirnov, R. A. Khmelnitskiy, A. A. Rudenko, I. N. Saraeva, E. R. Tolordava, A. Yu. Kharin, I. N.

Zavestovskaya, Y. M. Romanova, D. A. Zayarny, A. A. Ionin, High-throughput laser generation of Si-nanoparticle based surface coatings for antibacterial applications, Applied Surface Science, 470, 825 – 831 (2019).

[270] B. Jaeggi, S. Remund, R. Streubel, B. Goekce, S. Barcikowski, B. Neuenschwander, Laser Micromachining of Metals with Ultra-Short Pulses, JLMN, 12 *(3)* (2017).

[271] C. Wu, M. S. Christensen, J.-M. Savolainen, P. Balling, L. V. Zhigilei, Generation of subsurface voids and a nanocrystalline surface layer in femtosecond laser irradiation of a single-crystal Ag target, Phys. Rev. B, 91 *(3)*, 375 (2015).

[272] R. Sattari, Laser-based Fragmentation of Microparticles for Nanoparticle Generation, JLMN, 3 *(2)*, 100 – 105 (2008).

[273] D. Amans, W. Cai, S. Barcikowski, Status and demand of research to bring laser generation of nanoparticles in liquids to maturity, Applied Surface Science, 488, 445 – 454 (2019).

[274] A. Neumeister, J. Jakobi, C. Rehbock, J. Moysig, S. Barcikowski, Monophasic ligand-free alloy nanoparticle synthesis determinants during pulsed laser ablation of bulk alloy and consolidated microparticles in water, Physical chemistry chemical physics PCCP, 16 *(43)*, 23671 – 23678 (2014).

[275] V. Amendola, I. Fortunati, C. Marega, A. L. Abdelhady, M. I. Saidaminov, O. M. Bakr, High-Purity Hybrid Organolead Halide Perovskite Nanoparticles Obtained by Pulsed-Laser Irradiation in Liquid, Chemphyschem a European journal of chemical physics and physical chemistry, 18 *(9)*, 1047 – 1054 (2017).

[276] M. Rodio, L. Coluccino, E. Romeo, A. Genovese, A. Diaspro, G. Garau, R. Intartaglia, Facile fabrication of bioactive ultra-small protein-hydroxyapatite nanoconjugates via liquid-phase laser ablation and their enhanced osteogenic differentiation activity, Journal of materials chemistry. B, 5 *(2)*, 279 – 288 (2017).

[277] T. Ikehata, Y. Onodera, T. Nunokawa, T. Hirano, S.-i. Ogura, T. Kamachi, O. Odawara, H. Wada, Photodynamic therapy using upconversion nanoparticles prepared by laser ablation in liquid, Applied Surface Science, 348, 54 – 59 (2015).

[278] B. Neuenschwander, B. Jaeggi, M. Schmid, V. Rouffiange, P.-E. Martin, Optimization of the volume ablation rate for metals at different laser pulse-durations from ps to fs, Proc. of SPIE, 8243, 824307 (2012).

[279] A. Tamura, A. Matsumoto, K. Fukami, N. Nishi, T. Sakka, Simultaneous observation of nascent plasma and bubble induced by laser ablation in water with various pulse durations, Journal of Applied Physics, 117 *(17)*, 173304 (2015).

[280] A. Vogel, V. Venugopalan, Mechanisms of pulsed laser ablation of biological tissues, Chemical Reviews, 103 *(2)*, 577 – 644 (2003).

[281] É. Boulais, R. Lachaine, M. Meunier, Plasma mediated off-resonance plasmonic enhanced ultrafast laser-induced nanocavitation, Nano letters, 12 *(9)*, 4763 – 4769 (2012).

[282] V. Kotaidis, A. Plech, Cavitation dynamics on the nanoscale, Appl. Phys. Lett., 87 *(21)*, 213102 (2005).

[283] J. Lombard, T. Biben, S. Merabia, Ballistic heat transport in laser generated nano-bubbles, Nanoscale, 8 *(31)*, 14870 – 14876 (2016).

[284] J. Neumann, R. Brinkmann, Self-limited growth of laser-induced vapor bubbles around single microabsorbers, Appl. Phys. Lett., 93 *(3)*, 33901 (2008).

[285] D. Lapotko, Optical excitation and detection of vapor bubbles around plasmonic nanoparticles, Opt. Express, OE, 17 *(4)*, 2538 – 2556 (2009).

[286] A. Siems, S. A. L. Weber, J. Boneberg, A. Plech, Thermodynamics of nanosecond nanobubble formation at laser-excited metal nanoparticles, New J. Phys., 13 *(4)*, 43018 (2011).

[287] B. Ko, W. Lu, A. V. Sokolov, H. W. H. Lee, M. O. Scully, Z. Zhang, Multi-pulse laser-induced bubble formation and nanoparticle aggregation using MoS2 nanoparticles, Scientific reports, 10 *(1)*, 15753 (2020).

[288] V. Kotaidis, C. Dahmen, G. von Plessen, F. Springer, A. Plech, Excitation of nanoscale vapor bubbles at the surface of gold nanoparticles in water, The Journal of chemical physics, 124 *(18)*, 184702 (2006).

[289] W. Koechner, *Solid-State Laser Engineering*, Springer Series in Optical Sciences, Vol. 1, Springer, New York, NY (2006).

[290] J. M. Liu, Simple technique for measurements of pulsed Gaussian-beam spot sizes, Opt. Lett., 7 *(5)*, 196 – 198 (1982).

[291] Q. X. Wang, K. Manmi, Three dimensional microbubble dynamics near a wall subject to high intensity ultrasound, Physics of Fluids, 26 *(3)*, 32104 (2014).

[292] F. Taccogna, M. Dell'Aglio, M. Rutigliano, G. Valenza, A. de Giacomo, On the growth mechanism of nanoparticles in plasma during pulsed laser ablation in liquids, Plasma Sources Sci. Technol., 26 *(4)*, 45002 (2017).

[293] S. Kohsakowski, F. Seiser, J.-P. Wiederrecht, S. Reichenberger, T. Vinnay, S. Barcikowski, G. Marzun, Effective size separation of laser-generated, surfactant-free nanoparticles by continuous centrifugation, Nanotechnology, 31 *(9)*, 95603 (2019).

[294] J. Stasic, G. Joksic, L. Zivkovic, I. N. Mihailescu, C. Ghica, A. Kuncser, M. Trtica, Focusing geometry-induced size tailoring of silver nanoparticles obtained by laser ablation in water, Laser Phys., 24 *(10)*, 106005 (2014).

[295] K. A. Elsayed, H. Imam, M. A. Ahmed, R. Ramadan, Effect of focusing conditions and laser parameters on the fabrication of gold nanoparticles via laser ablation in liquid, Optics & Laser Technology, 45, 495 – 502 (2013).

[296] M. Maciulevičius, A. Vinčiūnas, M. Brikas, A. Butsen, N. Tarasenka, N. Tarasenko, G. Račiukaitis, Pulsed-laser generation of gold nanoparticles with on-line surface plasmon resonance detection, Appl. Phys. A, 111 *(1)*, 289 – 295 (2013).

[297] S. Reich, P. Schönfeld, P. Wagener, A. Letzel, S. Ibrahimkutty, B. Gökce, S. Barcikowski, A. Menzel, T. Dos Santos Rolo, A. Plech, Pulsed laser ablation in liquids: Impact of the bubble dynamics on particle formation, Journal of colloid and interface science, 489, 106 – 113 (2017).

[298] K. Metwally, S. Mensah, G. Baffou, Fluence Threshold for Photothermal Bubble Generation Using Plasmonic Nanoparticles, J. Phys. Chem. C, 119 *(*51*)*, 28586 – 28596 (2015).

[299] L. Delfour, T. E. Itina, Mechanisms of Ultrashort Laser-Induced Fragmentation of Metal Nanoparticles in Liquids: Numerical Insights, J. Phys. Chem. C, 119 *(*24*)*, 13893 – 13900 (2015).

[300] E.-A. Brujan, K. Nahen, P. Schmidt, A. Vogel, Dynamics of laser-induced cavitation bubbles near an elastic boundary, J. Fluid Mech., 433, 251 – 281 (2001).

[301] D. M. Harris, G. Pucci, V. Prost, J. Quintela Casal, J. W. M. Bush, in *68th Annual Meeting of the APS Division of Fluid Dynamics - Gallery of Fluid Motion*, American Physical Society **2015 - 2015**.

[302] W. K. Lewis, W. G. Whitman, Principles of gas absorption, Ind Eng Chem, 16 *(*12*)*, 1215 – 1220 (1924).

[303] J. Long, M. H. Eliceiri, Z. Vangelatos, Y. Rho, L. Wang, Z. Su, X. Xie, Y. Zhang, C. P. Grigoropoulos, Early dynamics of cavitation bubbles generated during ns laser ablation of submerged targets, Optics express, 28 *(*10*)*, 14300 – 14309 (2020).

[304] T. Hupfeld, S. Salamon, J. Landers, A. Sommereyns, C. Doñate-Buendía, J. Schmidt, H. Wende, M. Schmidt, S. Barcikowski, B. Gökce, 3D printing of magnetic parts by laser powder bed fusion of iron oxide nanoparticle functionalized polyamide powders, J. Mater. Chem. C, 8 *(*35*)*, 12204 – 12217 (2020).

[305] J. Zhang, D. N. Oko, S. Garbarino, R. Imbeault, M. Chaker, A. C. Tavares, D. Guay, D. Ma, Preparation of PtAu Alloy Colloids by Laser Ablation in Solution and Their Characterization, J. Phys. Chem. C, 116 *(*24*)*, 13413 – 13420 (2012).

[306] O. Prymak, J. Jakobi, C. Rehbock, M. Epple, S. Barcikowski, Crystallographic characterization of laser-generated, polymer-stabilized 4 nm silver-gold alloyed nanoparticles, Materials Chemistry and Physics, 207, 442 – 450 (2018).

[307] A. Tymoczko, M. Kamp, C. Rehbock, L. Kienle, E. Cattaruzza, S. Barcikowski, V. Amendola, One-step synthesis of Fe–Au core–shell magnetic-plasmonic nanoparticles driven by interface energy minimization, Nanoscale Horiz., 4 *(*6*)*, 1326 – 1332 (2019).

[308] D. N. Oko, J. Zhang, S. Garbarino, M. Chaker, D. Ma, A. C. Tavares, D. Guay, Formic acid electro-oxidation at PtAu alloyed nanoparticles synthesized by pulsed laser ablation in liquids, Journal of Power Sources, 248, 273 – 282 (2014).

[309] M. Censabella, V. Torrisi, S. Boninelli, C. Bongiorno, M. G. Grimaldi, F. Ruffino, Laser ablation synthesis of mono- and bimetallic Pt and Pd nanoparticles and fabrication of Pt-Pd/Graphene nanocomposites, Applied Surface Science, 475, 494 – 503 (2019).

[310] F. Waag, Y. Li, A. R. Ziefuß, E. Bertin, M. Kamp, V. Duppel, G. Marzun, L. Kienle, S. Barcikowski, B. Gökce, Kinetically-controlled laser-synthesis of colloidal high-entropy alloy nanoparticles, RSC Adv., 9 *(*32*)*, 18547 – 18558 (2019).

[311] S. Grade, J. Eberhard, J. Jakobi, A. Winkel, M. Stiesch, S. Barcikowski, Alloying colloidal silver nanoparticles with gold disproportionally controls antibacterial and toxic effects, Gold Bull, 47 *(*1-2*)*, 83 – 93 (2014).

[312] E. S. Gadelmawla, M. M. Koura, T.M.A. Maksoud, I. M. Elewa, H. H. Soliman, Roughness parameters, Journal of Materials Processing Technology, 123 *(*1*)*, 133 – 145 (2002).

[313] R. Fabbro, C. Max, E. Fabre, Planar laser-driven ablation: Effect of inhibited electron thermal conduction, Phys. Fluids, 28 *(*5*)*, 1463 (1985).

[314] A. Nath, A. Khare, Effect of focusing conditions on laser-induced shock waves at titanium-water interface, Appl. Opt., 50 *(*19*)*, 3275 – 3281 (2011).

[315] A. de Giacomo, M. Dell'Aglio, A. Santagata, R. Gaudiuso, O. de Pascale, P. Wagener, G. C. Messina, G. Compagnini, S. Barcikowski, Cavitation dynamics of laser ablation of bulk and wire-shaped metals in water during nanoparticles production, Physical chemistry chemical physics PCCP, 15 *(*9*)*, 3083 – 3092 (2013).

[316] X. Chen, R.-Q. Xu, J.-P. Chen, Z.-H. Shen, L. Jian, X.-W. Ni, Shock-wave propagation and cavitation bubble oscillation by Nd:YAG laser ablation of a metal in water, Appl. Opt., 43 *(*16*)*, 3251 – 3257 (2004).

[317] L. Martí-López, R. Ocaña, J. A. Porro, M. Morales, J. L. Ocaña, Optical observation of shock waves and cavitation bubbles in high intensity laser-induced shock processes, Appl. Opt., 48 *(*19*)*, 3671 – 3680 (2009).

[318] T. T. P. Nguyen, R. Tanabe, Y. Ito, Laser-induced shock process in under-liquid regime studied by time-resolved photoelasticity imaging technique, Appl. Phys. Lett., 102 *(*12*)*, 124103 (2013).

[319] J. Long, M. H. Eliceiri, Y. Ouyang, Y. Zhang, X. Xie, C. P. Grigoropoulos, Effects of immersion depth on the dynamics of cavitation bubbles generated during ns laser ablation of submerged targets, Optics and Lasers in Engineering, 137, 106334 (2021).

[320] T. T.P. Nguyen, R. Tanabe, Y. Ito, Comparative study of the expansion dynamics of laser-driven plasma and shock wave in in-air and underwater ablation regimes, Optics & Laser Technology, 100, 21 – 26 (2018).

[321] T. T. P. Nguyen, R. Tanabe, Y. Ito, Effects of an absorptive coating on the dynamics of underwater laser-induced shock process, Appl. Phys. A, 116 *(3)*, 1109 – 1117 (2014).

[322] A. Gremminger, J. Pihl, M. Casapu, J.-D. Grunwaldt, T. J. Toops, O. Deutschmann, PGM based catalysts for exhaust-gas after-treatment under typical diesel, gasoline and gas engine conditions with focus on methane and formaldehyde oxidation, Applied Catalysis B: Environmental, 265, 118571 (2020).

[323] D. Kunwar, S. Zhou, A. DeLaRiva, E. J. Peterson, H. Xiong, X. I. Pereira-Hernández, S. C. Purdy, R. ter Veen, H. H. Brongersma, J. T. Miller, H. Hashiguchi, L. Kovarik, S. Lin, H. Guo, Y. Wang, A. K. Datye, Stabilizing High Metal Loadings of Thermally Stable Platinum Single Atoms on an Industrial Catalyst Support, ACS Catal., 9 *(5)*, 3978 – 3990 (2019).

[324] E. Ogel, M. Casapu, D. E. Doronkin, R. Popescu, H. Störmer, C. Mechler, G. Marzun, S. Barcikowski, M. Türk, J.-D. Grunwaldt, Impact of Preparation Method and Hydrothermal Aging on Particle Size Distribution of Pt/γ-Al 2 O 3 and Its Performance in CO and NO Oxidation, J. Phys. Chem. C, 123 *(9)*, 5433 – 5446 (2019).

[325] K. Persson, A. Ersson, S. Colussi, A. Trovarelli, S. G. Järås, Catalytic combustion of methane over bimetallic Pd–Pt catalysts: The influence of support materials, Applied Catalysis B: Environmental, 66 *(*3-4*)*, 175 – 185 (2006).

[326] A. Berkó, J. Szökő, F. Solymosi, Effect of CO on the morphology of Pt nanoparticles supported on TiO2(110)-(1×n), Surface Science, 566-568, 337 – 342 (2004).

[327] H. Xiong, E. Peterson, G. Qi, A. K. Datye, Trapping mobile Pt species by PdO in diesel oxidation catalysts: Smaller is better, Catalysis Today, 272, 80 – 86 (2016).

[328] L. Olsson, E. Fridell, The Influence of Pt Oxide Formation and Pt Dispersion on the Reactions NO2⇔NO+1/2 O2 over Pt/Al2O3 and Pt/BaO/Al2O3, Journal of Catalysis, 210 *(2)*, 340 – 353 (2002).

[329] G. W. Graham, H.-W. Jen, O. Ezekoye, R. J. Kudla, W. Chun, X. Q. Pan, R. W. McCabe, Effect of alloy composition on dispersion stability and catalytic activity for NO oxidation over alumina-supported Pt–Pd catalysts, Catal Lett, 116 *(*1-2*)*, 1 – 8 (2007).

[330] E. Xue, K. Seshan, J. Ross, Roles of supports, Pt loading and Pt dispersion in the oxidation of NO to NO2 and of SO2 to SO3, Applied Catalysis B: Environmental, 11 *(1)*, 65 – 79 (1996).

[331] E. Lira, L. R. Merte, F. Behafarid, L. K. Ono, L. Zhang, B. Roldan Cuenya, Role and Evolution of Nanoparticle Structure and Chemical State during the Oxidation of NO over Size- and Shape-Controlled Pt/γ-Al 2 O 3 Catalysts under Operando Conditions, ACS Catal., 4 *(6)*, 1875 – 1884 (2014).

[332] S. B. Simonsen, I. Chorkendorff, S. Dahl, M. Skoglundh, J. Sehested, S. Helveg, Direct observations of oxygen-induced platinum nanoparticle ripening studied by in situ TEM, Journal of the American Chemical Society, 132 *(*23*)*, 7968 – 7975 (2010).

[333] T. W. Hansen, A. T. Delariva, S. R. Challa, A. K. Datye, Sintering of catalytic nanoparticles: particle migration or Ostwald ripening?, Accounts of chemical research, 46 *(8)*, 1720 – 1730 (2013).

[334] J. H. Pazmiño, J. T. Miller, S. S. Mulla, W. Nicholas Delgass, F. H. Ribeiro, Kinetic studies of the stability of Pt for NO oxidation: Effect of sulfur and long-term aging, Journal of Catalysis, 282 *(1)*, 13 – 24 (2011).

[335] E. Fridell, A. Amberntsson, L. Olsson, A. W. Grant, M. Skoglundh, Platinum Oxidation and Sulphur Deactivation in NO x Storage Catalysts, Topics in Catalysis, 30/31, 143 – 146 (2004).

[336] S. Salomons, R. Hayes, M. Votsmeier, A. Drochner, H. Vogel, S. Malmberg, J. Gieshoff, On the use of mechanistic CO oxidation models with a platinum monolith catalyst, Applied Catalysis B: Environmental, 70 *(*1-4*)*, 305 – 313 (2007).

[337] S. Mulla, N. Chen, L. Cumaranatunge, G. Blau, D. Zemlyanov, W. N. Delgass, W. Epling, F. Ribeiro, Reaction of NO and O2 to NO2 on Pt: Kinetics and catalyst deactivation, Journal of Catalysis, 241 *(2)*, 389 – 399 (2006).

[338] Z. Duan, G. Henkelman, CO Oxidation on the Pd(111) Surface, ACS Catal., 4 *(*10*)*, 3435 – 3443 (2014).

[339] Y. Xu, R. B. Getman, W. A. Shelton, W. F. Schneider, A first-principles investigation of the effect of Pt cluster size on CO and NO oxidation intermediates and energetics, Physical chemistry chemical physics PCCP, 10 *(*39*)*, 6009 – 6018 (2008).

[340] A. Russell, W. S. Epling, Diesel Oxidation Catalysts, Catalysis Reviews, 53 *(4)*, 337 – 423 (2011).

[341] N. Blommaerts, H. Vanrompay, S. Nuti, S. Lenaerts, S. Bals, S. W. Verbruggen, Unraveling Structural Information of Turkevich Synthesized Plasmonic Gold-Silver Bimetallic Nanoparticles, Small (Weinheim an der Bergstrasse, Germany), e1902791 (2019).

[342] Q. Zhang, K. Kusada, D. Wu, N. Ogiwara, T. Yamamoto, T. Toriyama, S. Matsumura, S. Kawaguchi, Y. Kubota, T. Honma, H. Kitagawa, Solid-solution alloy nanoparticles of a combination of immiscible Au and Ru with a large gap of reduction potential and their enhanced oxygen evolution reaction performance, Chemical science, 10 *(*19*)*, 5133 – 5137 (2019).

[343] G. Marzun, A. Levish, V. Mackert, T. Kallio, S. Barcikowski, P. Wagener, Laser synthesis, structure and chemical properties of colloidal nickel-molybdenum nanoparticles for the substitution of noble metals in heterogeneous catalysis, Journal of colloid and interface science, 489, 57 – 67 (2017).

[344] S. Hu, M. Tian, E. L. Ribeiro, G. Duscher, D. Mukherjee, Tandem laser ablation synthesis in solution-galvanic replacement reaction (LASiS-GRR) for the production of

PtCo nanoalloys as oxygen reduction electrocatalysts, Journal of Power Sources, 306, 413 – 423 (2016).

[345] M. Shokouhimehr, Magnetically Separable and Sustainable Nanostructured Catalysts for Heterogeneous Reduction of Nitroaromatics, Catalysts, 5 *(2)*, 534 – 560 (2015).

[346] Y. Feng, Z. Li, H. Liu, C. Dong, J. Wang, S. A. Kulinich, X. Du, Laser-Prepared CuZn Alloy Catalyst for Selective Electrochemical Reduction of CO2 to Ethylene, Langmuir the ACS journal of surfaces and colloids, 34 *(45)*, 13544 – 13549 (2018).

[347] I. Haxhiaj, S. Tigges, D. Firla, X. Zhang, U. Hagemann, T. Kondo, J. Nakamura, G. Marzun, S. Barcikowski, Platinum nanoparticles supported on reduced graphene oxide prepared in situ by a continuous one-step laser process, Applied Surface Science, 469, 811 – 820 (2019).

[348] F. Mafuné, T. Okamoto, M. Ito, Surfactant-free small Ni nanoparticles trapped on silica nanoparticles prepared by pulsed laser ablation in liquid, Chemical Physics Letters, 591, 193 – 196 (2014).

[349] F. Bonaccorso, M. Zerbetto, A. C. Ferrari, V. Amendola, Sorting Nanoparticles by Centrifugal Fields in Clean Media, J. Phys. Chem. C, 117 *(25)*, 13217 – 13229 (2013).

[350] F. Mafuné, J.-y. Kohno, Y. Takeda, T. Kondow, Growth of Gold Clusters into Nanoparticles in a Solution Following Laser-Induced Fragmentation, J. Phys. Chem. B, 106 *(34)*, 8555 – 8561 (2002).

[351] J.-Y. Lin, C. Xi, Z. Li, Y. Feng, D.-Y. Wu, C.-K. Dong, P. Yao, H. Liu, X.-W. Du, Lattice-strained palladium nanoparticles as active catalysts for the oxygen reduction reaction, Chemical communications (Cambridge, England), 55 *(21)*, 3121 – 3123 (2019).

[352] V. Amendola, D. Amans, Y. Ishikawa, N. Koshizaki, S. Scirè, G. Compagnini, S. Reichenberger, S. Barcikowski, Room-Temperature Laser Synthesis in Liquid of Oxide, Metal-Oxide Core-Shells, and Doped Oxide Nanoparticles, Chemistry (Weinheim an der Bergstrasse, Germany), 26 *(42)*, 9206 – 9242 (2020).

[353] G. Marzun, C. Streich, S. Jendrzej, S. Barcikowski, P. Wagener, Adsorption of colloidal platinum nanoparticles to supports: charge transfer and effects of electrostatic and steric interactions, Langmuir the ACS journal of surfaces and colloids, 30 *(40)*, 11928 – 11936 (2014).

[354] Q. Feng, J. V. Moloney, A. C. Newell, E. M. Wright, K. Cook, P. K. Kennedy, D. X. Hammer, B. A. Rockwell, C. R. Thompson, Theory and simulation on the threshold of water breakdown induced by focused ultrashort laser pulses, IEEE J. Quantum Electron., 33 *(2)*, 127 – 137 (1997).

[355] A. Pyatenko, H. Wang, N. Koshizaki, T. Tsuji, Mechanism of pulse laser interaction with colloidal nanoparticles, Laser & Photonics Reviews, 7 *(4)*, 596 – 604 (2013).

[356] A. R. Ziefuß, S. Reich, S. Reichenberger, M. Levantino, A. Plech, In situ structural kinetics of picosecond laser-induced heating and fragmentation of colloidal gold spheres, Physical chemistry chemical physics PCCP, 22 *(9)*, 4993 – 5001 (2020).

[357] M. Casapu, J.-D. Grunwaldt, M. Maciejewski, A. Baiker, S. Eckhoff, U. Gobel, M. Wittrock, The fate of platinum in Pt/Ba/CeO2 and Pt/Ba/Al2O3 catalysts during thermal aging, Journal of Catalysis, 251 *(1)*, 28 – 38 (2007).

[358] K. Du, Ps-Laser and Fs-Laser: Design, Performers and Costs, Aachener Kolloquium für Lasertechnik (2014).

[359] S. Chinnathambi, S. Chen, S. Ganesan, N. Hanagata, Silicon quantum dots for biological applications, Advanced healthcare materials, 3 *(1)*, 10 – 29 (2014).

[360] M. Labusch, A. P.A. Cunha, S. F. Wirtz, S. Reichenberger, E. Cleve, D. Söffker, S. Barcikowski, Acoustic emission control avoids fluence shifts caused by target runaway during laser synthesis of colloids, Applied Surface Science, 479, 887 – 895 (2019).

[361] H. J. Eichler, J. Eichler, *Laser*, Springer Berlin Heidelberg, Berlin, Heidelberg (2015).

[362] A. Naghilou, O. Armbruster, W. Kautek, Femto- and nanosecond pulse laser ablation dependence on irradiation area, Applied Surface Science, 418, 487 – 490 (2017).

[363] A. Baladi, R. Sarraf Mamoory, Investigation of different liquid media and ablation times on pulsed laser ablation synthesis of aluminum nanoparticles, Applied Surface Science, 256 *(24)*, 7559 – 7564 (2010).

[364] A. Schwenke, P. Wagener, S. Nolte, S. Barcikowski, Influence of processing time on nanoparticle generation during picosecond-pulsed fundamental and second harmonic laser ablation of metals in tetrahydrofuran, Appl. Phys. A, 104 *(1)*, 77 – 82 (2011).

[365] C. L. Sajti, S. Petersen, A. Menéndez-Manjón, S. Barcikowski, In-situ bioconjugation in stationary media and in liquid flow by femtosecond laser ablation, Appl. Phys. A, 101 *(2)*, 259 – 264 (2010).

[366] S.K. Friedlander, Particle diffusion in low-speed flows, Journal of colloid and interface science, 23 *(2)*, 157 – 164 (1967).

[367] R. Jordinson, The flat plate boundary layer. Part 1. Numerical integration of the Orr-Sommerfeld equation, J. Fluid Mech., 43 *(4)*, 801 – 811 (1970).

[368] N. Dabir-Moghaddam, Z. Liu, B. Wu, Modeling of the shrinking process of a bubble induced by laser metal ablation in water and experimental verification, Journal of Applied Physics, 121 *(4)*, 44908 (2017).

[369] C. Lechner, M. Koch, W. Lauterborn, R. Mettin, Pressure and tension waves from bubble collapse near a solid boundary: A numerical approach, The Journal of the Acoustical Society of America, 142 *(6)*, 3649 (2017).

[370] P. Koukouvinis, G. Strotos, Q. Zeng, S. R. Gonzalez-Avila, A. Theodorakakos, M. Gavaises, C.-D. Ohl, Parametric Investigations of the Induced Shear Stress by a Laser-

Generated Bubble, Langmuir the ACS journal of surfaces and colloids, 34 *(22)*, 6428 – 6442 (2018).

[371] A. de Bonis, A. Galasso, A. Santagata, R. Teghil, Laser ablation of GaAs in liquid: the role of laser pulse duration, J. Phys. D: Appl. Phys., 49 *(3)*, 35301 (2016).

[372] A. Hamad, L. Li, Z. Liu, A comparison of the characteristics of nanosecond, picosecond and femtosecond lasers generated Ag, TiO2 and Au nanoparticles in deionised water, Appl. Phys. A, 120 *(4)*, 1247 – 1260 (2015).

[373] H. Muto, K. Miyajima, F. Mafuné, Mechanism of Laser-Induced Size Reduction of Gold Nanoparticles As Studied by Single and Double Laser Pulse Excitation, J. Phys. Chem. C, 112 *(15)*, 5810 – 5815 (2008).

[374] A. Takami, H. Kurita, S. Koda, Laser-Induced Size Reduction of Noble Metal Particles, J. Phys. Chem. B, 103 *(8)*, 1226 – 1232 (1999).

[375] C. S. R. Nathala, A. Ajami, A. A. Ionin, S. I. Kudryashov, S. V. Makarov, T. Ganz, A. Assion, W. Husinsky, Experimental study of fs-laser induced sub-100-nm periodic surface structures on titanium, Optics express, 23 *(5)*, 5915 – 5929 (2015).

[376] S. Gräf, F. A. Müller, Polarisation-dependent generation of fs-laser induced periodic surface structures, Applied Surface Science, 331, 150 – 155 (2015).

[377] A. Abou-Saleh, E. T. Karim, C. Maurice, S. Reynaud, F. Pigeon, F. Garrelie, L. V. Zhigilei, J.-P. Colombier, Spallation-induced roughness promoting high spatial frequency nanostructure formation on Cr, Appl. Phys. A, 124 *(4)*, 688 (2018).

[378] A. Y. Vorobyev, C. Guo, Reflection of femtosecond laser light in multipulse ablation of metals, Journal of Applied Physics, 110 *(4)*, 43102 (2011).

[379] R. Lou, G. Zhang, G. Li, X. Li, Q. Liu, G. Cheng, Design and Fabrication of Dual-Scale Broadband Antireflective Structures on Metal Surfaces by Using Nanosecond and Femtosecond Lasers, Micromachines, 11 *(1)* (2019).

[380] David R. Lide, *CRC Handbook of Chemistry and Physics*, 2005th ed., Internet Version 2005, CRC Press (2005).

[381] A. M. Howatson, P. G. Lund, J. D. Todd, *Engineering Tables and Data*, Springer Netherlands, Dordrecht (1972).

[382] Goodfellow, *Platinum (Pt) Material Information*, http://www.goodfellow.com/A/Platinum.html. 03.08.2020.

[383] N. Lasemi, U. Pacher, L. V. Zhigilei, O. Bomatí-Miguel, R. Lahoz, W. Kautek, Pulsed laser ablation and incubation of nickel, iron and tungsten in liquids and air, Applied Surface Science, 433, 772 – 779 (2018).

[384] C. Gaudiuso, G. Giannuzzi, A. Volpe, P. M. Lugarà, I. Choquet, A. Ancona, Incubation during laser ablation with bursts of femtosecond pulses with picosecond delays, Optics express, 26 *(4)*, 3801 – 3813 (2018).

[385] F. Di Niso, C. Gaudiuso, T. Sibillano, F. P. Mezzapesa, A. Ancona, P. M. Lugarà, Role of heat accumulation on the incubation effect in multi-shot laser ablation of stainless steel at high repetition rates, Optics express, 22 *(*10*)*, 12200 – 12210 (2014).

[386] P. Dagtepe, V. Chikan, Quantized Ostwald Ripening of Colloidal Nanoparticles, J. Phys. Chem. C, 114 *(*39*)*, 16263 – 16269 (2010).

[387] X. Dong, X. Ji, H. Wu, L. Zhao, J. Li, W. Yang, Shape Control of Silver Nanoparticles by Stepwise Citrate Reduction, J. Phys. Chem. C, 113 *(*16*)*, 6573 – 6576 (2009).

[388] M. Tiemann, F. Marlow, J. Hartikainen, Ö. Weiss, M. Lindén, Ripening Effects in ZnS Nanoparticle Growth, J. Phys. Chem. C, 112 *(*5*)*, 1463 – 1467 (2008).

[389] Strem Chemicals Inc., *Silver Nanoparticles, Reactant-Free*, https://www.strem.com/uploads/resources/documents/silver_reactant_free_nanoparticles.pdf. 06.08.2020.

[390] nanoComposix, *5 nm Silver Nanospheres, Citrate, BioPure*, https://tools.nanocomposix.com/cdn/coa/Silver/Spheres/BioPure/AG5-SS-BP-CIT-SCM0014.pdf?107%20953. 06.08.2020.

[391] Cytodiagnostics, *Product Data Sheet, Silver Nanoparticles, >99% Reactant Free*, http://portal.cytodocs.com/documents/Product-Sheets/Product-Sheet-Reactant-Free-Silver-Nanoparticles.pdf. 06.08.2020.

[392] BBI solutions, *Life Science Gold Colloid starter pack - 5nm/10nm/20nm/40nm*, https://bbisolutions.com/eu/catalog/product/view/id/272/s/gold-colloid-5nm-10nm-20nm-40nm/category/25/. 06.08.2020.

[393] nanoComposix, *10 nm Citrate BioPure Gold*, https://tools.nanocomposix.com/cdn/coa/Gold/Spheres/BioPure/AU10-BP-CIT-DAG1728.pdf?3602223. 06.08.2020.

[394] Strem Chemicals Inc., *Reactant-Free and Stabilized Gold Nanoparticles*, https://www.strem.com/uploads/resources/documents/cdiag.pdf. 06.08.2020.

[395] Sigma Aldrich, *Product Specification Gold nanoparticles - 10 nm diameter, OD 1, stabilized suspension in citrate buffer*, https://www.sigmaaldrich.com/Graphics/COfAInfo/SigmaSAPQM/SPEC/74/741957/741957-BULK_____ALDRICH__.pdf. 13.02.2021.

[396] nanoComposix, *5 nm Platinum Nanoparticles, Citrate, NanoXact*, https://tools.nanocomposix.com/cdn/coa/Platinum/PT5-NX-CIT-ECP1477.pdf?1231229. 06.08.2020.

[397] Strem Chemicals Inc., *Platinum nanoparticles, pure, (<20nm) in water at 100mg/L (surfactant and reactant-free, stabilized with < 0.01 mmol/l of citrate)*, https://www.strem.com/catalog/v/78-1402/53/items_7440-06-4. 06.08.2020.

[398] *DIN EN ISO 10628-1:2015-04, Schemata für die chemische und petrochemische Industrie_- Teil_1: Spezifikation der Schemata (ISO_10628-1:2014); Deutsche Fassung EN_ISO_10628-1:2015*, Beuth Verlag GmbH, Berlin.

[399] *ISO 3511-1:1977-07, Messen, Steuern, Regeln in der Verfahrenstechnik; Zeichen für die funktionelle DarstellungMessen, Steuern, Regeln in der Verfahrenstechnik; Zeichen für die funktionelle DarstellungMessen, Steuern, Regeln in der Verfahrenstechnik; Zeichen für die funktionelle Darstellung; Teil 1: Grundforderungen*, Beuth Verlag GmbH, Berlin.

[400] BBI solutions, *Molar Concentration of Gold Nanoparticles (Colloid)*, https:// www.bbisolutions.com/eu/technical-support/gold/nanoparticles/molar-concentration-of-gold-nanoparticles-collo. 25.07.2019.

[401] nanoComposix, *Gold Nanoparticles: Spheres*, https://nanocomposix.eu/pages/gold-nanoparticles-spheres. 26.07.2019.

[402] Sigma Aldrich, *Gold Nanoparticles: Properties and Applications*, https:// www.sigmaaldrich.com/technical-documents/articles/materials-science/nanomaterials/gold-nanoparticles.html. 26.07.2019.

[403] Alfa Aesar, *Nanoparticles*, https://www.alfa.com/de/nanoparticles/. 26.07.2019.

[404] stream, *product catalog*, https://www.strem.com/catalog/gl/25/gold. 26.07.2019.

[405] IMRA, *i-colloid nanoparticles*, http://nano.imra.com/products/i-colloids/. 26.07.2019.

[406] Cytodiagnostics, *Laser Ablated Gold Nanoparticles*, http://www.cytodiagnostics.com/store/pc/viewCategories.asp?idCategory=306. 26.07.2019.

[407] Bundesministerium der Finanzen, *AfA-Tabelle für den Wirtschaftszweig "Maschinenbau": Aktenzeichen IV D 2-S 1551-470/01* **2001**.

[408] P. Wagener, J. Jakobi, C. Rehbock, V. S. K. Chakravadhanula, C. Thede, U. Wiedwald, M. Bartsch, L. Kienle, S. Barcikowski, Solvent-surface interactions control the phase structure in laser-generated iron-gold core-shell nanoparticles, Scientific reports, 6, 23352 (2016).

[409] T.-C. Lin, C. Cao, M. Sokoluk, L. Jiang, X. Wang, J. M. Schoenung, E. J. Lavernia, X. Li, Aluminum with dispersed nanoparticles by laser additive manufacturing, Nature communications, 10 *(1)*, 4124 (2019).

[410] J. H. Martin, B. D. Yahata, J. M. Hundley, J. A. Mayer, T. A. Schaedler, T. M. Pollock, 3D printing of high-strength aluminium alloys, Nature, 549 *(*7672*)*, 365 – 369 (2017).

[411] A. Miyazaki, I. Balint, K.-i. Aika, Y. Nakano, Preparation of Ru Nanoparticles Supported on γ-Al2O3 and Its Novel Catalytic Activity for Ammonia Synthesis, Journal of Catalysis, 204 *(2)*, 364 – 371 (2001).

[412] M. Shekhar, J. Wang, W.-S. Lee, W. D. Williams, S. M. Kim, E. A. Stach, J. T. Miller, W. N. Delgass, F. H. Ribeiro, Size and support effects for the water-gas shift catalysis over gold nanoparticles supported on model Al2O3 and TiO2, Journal of the American Chemical Society, 134 *(*10*)*, 4700 – 4708 (2012).

[413] R. Peng, S. Li, X. Sun, Q. Ren, L. Chen, M. Fu, J. Wu, D. Ye, Size effect of Pt nanoparticles on the catalytic oxidation of toluene over Pt/CeO2 catalysts, Applied Catalysis B: Environmental, 220, 462 – 470 (2018).

[414] M. Comotti, W.-C. Li, B. Spliethoff, F. Schüth, Support effect in high activity gold catalysts for CO oxidation, Journal of the American Chemical Society, 128 *(3)*, 917 – 924 (2006).

[415] P. Denton, A. Giroir-Fendler, H. Praliaud, M. Primet, Role of the Nature of the Support (Alumina or Silica), of the Support Porosity, and of the Pt Dispersion in the Selective Reduction of NO by C3H6 under Lean-Burn Conditions, Journal of Catalysis, 189 *(2)*, 410 – 420 (2000).

[416] M. A. Barakat, R. I. Al-Hutailah, E. Qayyum, J. Rashid, J. N. Kuhn, Pt nanoparticles/TiO2 for photocatalytic degradation of phenols in wastewater, Environmental technology, 35 *(*1-4*)*, 137 – 144 (2014).

[417] S. M. Yoo, S. B. Rawal, J. E. Lee, J. Kim, H.-Y. Ryu, D.-W. Park, W. in Lee, Size-dependence of plasmonic Au nanoparticles in photocatalytic behavior of Au/TiO 2 and Au@SiO 2 /TiO 2, Applied Catalysis A: General, 499, 47 – 54 (2015).

[418] W. Dong, S. Reichenberger, S. Chu, P. Weide, H. Ruland, S. Barcikowski, P. Wagener, M. Muhler, The effect of the Au loading on the liquid-phase aerobic oxidation of ethanol over Au/TiO2 catalysts prepared by pulsed laser ablation, Journal of Catalysis, 330, 497 – 506 (2015).

[419] E. Maurer, S. Barcikowski, B. Gökce, Process Chain for the Fabrication of Nanoparticle Polymer Composites by Laser Ablation Synthesis, Chem. Eng. Technol., 40 *(9)*, 1535 – 1543 (2017).

[420] Y. Li, C. Rehbock, M. Nachev, J. Stamm, B. Sures, A. Blaeser, S. Barcikowski, Matrix-specific mechanism of Fe ion release from laser-generated 3D-printable nanoparticle-polymer composites and their protein adsorption properties, Nanotechnology (2020).

[421] A. Blaeser, N. Million, D. F. D. Campos, L. Gamrad, M. Köpf, C. Rehbock, M. Nachev, B. Sures, S. Barcikowski, H. Fischer, Laser-based in situ embedding of metal nanoparticles into bioextruded alginate hydrogel tubes enhances human endothelial cell adhesion, Nano Res., 9 *(*11*)*, 3407 – 3427 (2016).

[422] D.-G. Yu, W.-C. Lin, C.-H. Lin, Y.-H. Yeh, M.-C. Yang, Construction of antithrombogenic polyelectrolyte multilayer on thermoplastic polyurethane via layer-by-layer self-assembly technique, Journal of biomedical materials research. Part B, Applied biomaterials, 83 *(1)*, 105 – 113 (2007).

[423] O. Catanzano, V. D'Esposito, S. Acierno, M. R. Ambrosio, C. de Caro, C. Avagliano, P. Russo, R. Russo, A. Miro, F. Ungaro, A. Calignano, P. Formisano, F. Quaglia, Alginate-hyaluronan composite hydrogels accelerate wound healing process, Carbohydrate polymers, 131, 407 – 414 (2015).

[424] S. L. Fenn, P. N. Charron, R. A. Oldinski, Anticancer Therapeutic Alginate-Based Tissue Sealants for Lung Repair, ACS applied materials & interfaces, 9 *(*28*)*, 23409 – 23419 (2017).

[425] S.-H. Hsu, C.-M. Tang, H.-J. Tseng, Biocompatibility of poly(ether)urethane-gold nanocomposites, Journal of biomedical materials research. Part A, 79 *(4)*, 759 – 770 (2006).

[426] A. GhavamiNejad, A. R. Unnithan, A. Ramachandra Kurup Sasikala, M. Samarikhalaj, R. G. Thomas, Y. Y. Jeong, S. Nasseri, P. Murugesan, D. Wu, C. Hee Park, C. S. Kim, Mussel-Inspired Electrospun Nanofibers Functionalized with Size-Controlled Silver Nanoparticles for Wound Dressing Application, ACS applied materials & interfaces, 7 *(22)*, 12176 – 12183 (2015).

[427] E. N. Sowa-Söhle, A. Schwenke, P. Wagener, A. Weiss, H. Wiegel, C. L. Sajti, A. Haverich, S. Barcikowski, A. Loos, Antimicrobial efficacy, cytotoxicity, and ion release of mixed metal (Ag, Cu, Zn, Mg) nanoparticle polymer composite implant material, BioNanoMaterials, 14 *(*3-4*)* (2013).

[428] S. Grade, J. Eberhard, A. Neumeister, P. Wagener, A. Winkel, M. Stiesch, S. Barcikowski, Serum albumin reduces the antibacterial and cytotoxic effects of hydrogel-embedded colloidal silver nanoparticles, RSC Adv., 2 *(*18*)*, 7190 (2012).

[429] K. Liu, Y. Song, S. Chen, Defective TiO2-supported Cu nanoparticles as efficient and stable electrocatalysts for oxygen reduction in alkaline media, Nanoscale, 7 *(*3*)*, 1224 – 1232 (2015).

[430] H. Wang, Y. Huang, Z. Tan, X. Hu, Fabrication and characterization of copper nanoparticle thin-films and the electrocatalytic behavior, Analytica Chimica Acta, 526 *(1)*, 13 – 17 (2004).

[431] B. Batra, S. Lata, M. Sharma, C. S. Pundir, An acrylamide biosensor based on immobilization of hemoglobin onto multiwalled carbon nanotube/copper nanoparticles/polyaniline hybrid film, Analytical biochemistry, 433 *(2)*, 210 – 217 (2013).

[432] D. Jiang, Q. Liu, K. Wang, J. Qian, X. Dong, Z. Yang, X. Du, B. Qiu, Enhanced non-enzymatic glucose sensing based on copper nanoparticles decorated nitrogen-doped graphene, Biosensors & bioelectronics, 54, 273 – 278 (2014).

[433] G. Marzun, H. Bönnemann, C. Lehmann, B. Spliethoff, C. Weidenthaler, S. Barcikowski, Role of Dissolved and Molecular Oxygen on Cu and PtCu Alloy Particle Structure during Laser Ablation Synthesis in Liquids, Chemphyschem a European journal of chemical physics and physical chemistry, 18 *(*9*)*, 1175 – 1184 (2017).

[434] P. V. Kazakevich, V. V. Voronov, A. V. Simakin, G. A. Shafeev, Production of copper and brass nanoparticles upon laser ablation in liquids, Quantum Electronics, 34 *(*10*)*, 951 – 956 (2004).

[435] P. Liu, H. Wang, X. Li, M. Rui, H. Zeng, Localized surface plasmon resonance of Cu nanoparticles by laser ablation in liquid media, RSC Adv., 5 *(*97*)*, 79738 – 79745 (2015).

[436] G. H. Chan, J. Zhao, E. M. Hicks, G. C. Schatz, R. P. van Duyne, Plasmonic Properties of Copper Nanoparticles Fabricated by Nanosphere Lithography, Nano Lett., 7 *(7)*, 1947 – 1952 (2007).

[437] K. P. Rice, E. J. Walker, M. P. Stoykovich, A. E. Saunders, Solvent-Dependent Surface Plasmon Response and Oxidation of Copper Nanocrystals, J. Phys. Chem. C, 115 *(*5*)*, 1793 – 1799 (2011).

[438] A. Schoonderbeek, V. Schütu, O. Haupt, U. Stute, Laser Processing of Thin Films for Photovoltaic Applications, JLMN, 5 *(3)*, 248 – 255 (2010).

[439] D. Trusheim, M. Schulz-Ruhtenberg, T. Baier, S. Krantz, D. Bauer, J. Das, Investigation of the Influence of Pulse Duration in Laser Processes for Solar Cells, Physics Procedia, 12, 278 – 285 (2011).

[440] Schott AG, Optical Glass - Data Sheets, Schott AG, 2014 .

[441] M. Jakubith, *Grundoperationen und chemische Reaktionstechnik: Eine Einführung in die Technische Chemie*, Wiley-VCH, Weinheim (2005).

[442] Ministerium für Arbeit, Gesundheit und Soziales des Landes Nordrhein-Westfalen, *Tarifregister Nordrhein-Westfalen*, http://www.tarifregister.nrw.de/tarifinformationen/tarifdaten_branchen/index.php. 31.08.2020.

[443] innogy SE, *Preise der Grund- und Zusatzversorgung*, iam.innogy.com. 31.08.2020.

[444] KS Medizintechik, *Aqua-Bidest Reinstwasser*, https://www.ksmedizintechnik.de/produkt/aqua-bidest-reinstwasser/. 31.08.2020.

[445] Merck KGaA, *Trisodium citrate dihydrate*, https://www.sigmaaldrich.com/catalog/product/sial/s1804?lang=de&region=DE. 31.08.2020.

[446] Merck KGaA, *Sodium chloride*, https://www.sigmaaldrich.com/catalog/product/sigald/s9888?lang=de&region=DE. 31.08.2020.

[447] fisher scientific, *Gosselin™ Gerade Behälter*, https://www.fishersci.de/shop/products/straight-containers-4/p-7015036. 31.08.2020.

[448] fisher scientific, *Fisherbrand™ Komfort-Untersuchungshandschuhe aus Nitril*, https://www.fishersci.de/shop/products/fisherbrand-comfort-nitrile-exam-gloves-18/p-3702998. 31.08.2020.

[449] fisher scientific, *Kimberly-Clark™ Kimtech™ Pure W4 Wischtücher 7646 – 5 Packungen mit je 100 weißen Tüchern*, https://www.fishersci.de/shop/products/polypropylene-dry-wiper/11797968#?keyword=t%26uuml%3Bcher. 31.08.2020.

8. Appendix

In the appendix, the first section provides general experimental information such as used devices and chemicals. The supplementary results for some experiments, as well as material data sheets, are presented in the second section. Additionally, the acknowledgments (8.3), curriculum vitae (8.4), contributions (8.5), and declarations (8.6) can be found in this section.

8.1. Methods and materials

In the following general information about the methods, applied lasers, and analytical devices are given. Detailed information about the methods and materials can be found in each section. The general data evaluation for each method is explained in the following.

UV-Vis extinction measurement

A UV-Vis spectrometer is used to obtain information about the quality and concentration of a colloid. Therefore, a 10 mm thick Quartz glass cuvette is used, and the baseline is determined with the respective solvent. Colloids are ultrasonicated for 1 min and diluted before the measurement so that a maximal extinction of 1.5 is not exceeded. The usual measurement range is 190 to 900 nm. For the concentration determination, the extinction at 270 nm, 380 nm, and the integrated extinction between 300 and 600 nm are used for Ag, Au, and Pt, respectively.

ADC measurement

The hydrodynamic particle size is determined with an analytical disc centrifuge rotating with 24000 min^{-1}. The gradient is built with a sucrose solution, and a PVP standard solution is used. Due to the density difference, the lower detection limit of the device is 5, 4, and 4 nm for Ag, Au, and Pt. For the evaluation, both number- and mass-weighted, the area under the curve is normalized to 1. Then, the diameter of the maximum d_{max}, the diameter where 50 and 90 % of the particles are smaller d_{50} and d_{90}, and the mass/number fractions of particles smaller than 10 and 20 nm are determined.

TEM analysis

For TEM analysis, samples are dripped on carbon-coated copper meshed immediately after their preparation and dried. No ligands or stabilizers are added. The images are analyzed automatically with the ImageJ add-on “ParticleSizer”.

Determination of the laser fluence

According to [290], the spot diameter for different laser energies is measured at the same focusing condition. Then, the squared spot diameter is plotted in dependence of the

logarithm of the pulse energy. The laser spot diameter can be derived from the resulting slop and the damage threshold fluence from the x-axis interception. With the laser spot diameter, the laser fluence in the target surface can be calculated according to Eq. S 1. If the focal distance is varied, e.g., in section 0, the spot diameter is determined for each distance.

$$F = \frac{2 \cdot E_P}{\pi \cdot w_0^2} \qquad \text{Eq. S 1}$$

F: fluence [J/cm²]

E_P: pulse energy [J]

w_0: laser spot radius [cm]

For the mean laser fluence in the liquid layer, the laser beam diameter before the lenses is determined by the knife-edge method and measures 4.4 mm. By using geometrical optics and the laser spot diameter, the fluence for each position in the liquid layer can be calculated (Fig. S 1). The mean laser fluences are then calculated by the mean value theorem.

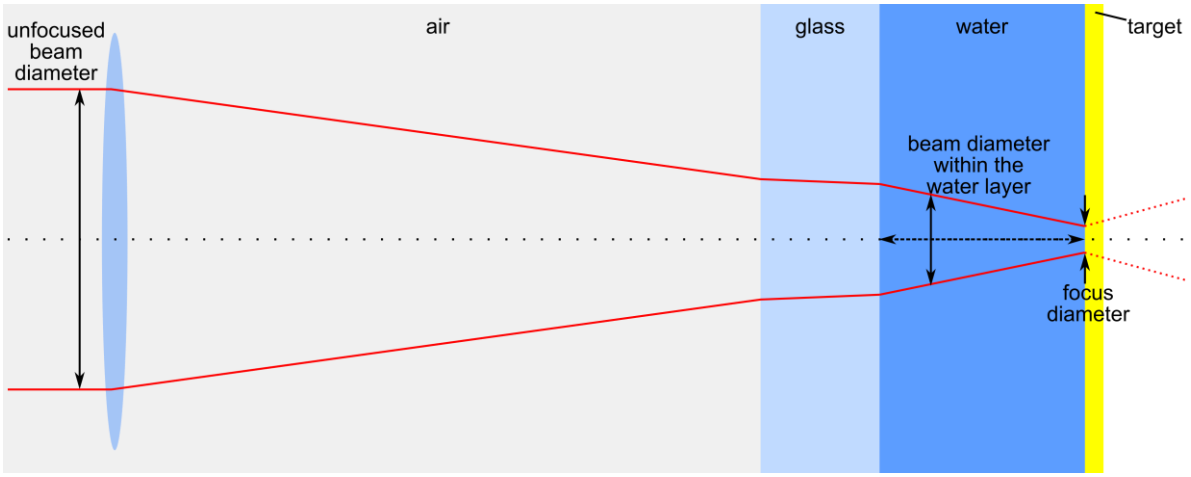

Fig. S 1: Scheme of the beam path for determination of the fluences in the liquid layer of the ablation chamber; the diameter of the unfocused beam and the focus diameter are known so that the beam diameter at each position within the liquid layer (dashed arrow) can be calculated.

Tab. S 1: Lasers and analytical instruments used in the thesis at hand

devices	**information**
ICCD camera	Andor Solis iStar, serial number DH334T-18H-13
xenon flash lamp	Hamamatsu, serial number L4633-01
lasers	Amphos, 500flex, $\lambda_L = 1030\ nm, \tau_P = 3\ ps/5p\ s,\ \bar{P} = 500\ W, f_R = 2 - 10\ MHz$
	CryLaS, eMOPA1064-500, $\lambda_L = 1064\ nm,\ \tau_P = 1\ ns,\ \bar{P} = 500\ mW,\ f_R = 1 - 1000\ Hz$

	CryLaS, DSS1064-Q4, $\lambda_L = 1064\,nm, \tau_P = 1\,ns, \bar{P} = 150\,mW, f_R = 1 - 1000Hz$
	InnoLas, picolo AOT, $\lambda_L = 1064\,nm, \tau_P = 600\,ps,\ E_P = 60\,\mu J$
	InnoLas, Spitlight DPSS-250-100, $\lambda_L = 1064\,nm, \tau_P = 9\,ns,\ E_P = 610\,\mu J$
	Rofin PowerlineE20 $\lambda_L = 1064\,nm, \tau_P = 5\,ns, \bar{P} = 9\,W, f_R = 20 - 15000Hz$
oscilloscope	Teledyne Technologies, WaveAce2034
UV-Vis spectrometer	Thermo Scientific, Evolution 201, 10 mm quarz cuvette
analytical disc centrifuge	CPS instruments, DC2400; used at 24 000 rpm and a laser wavelength of 405 nm
power meter	Coherent, Field Max II-Top
piston pump	Ismatec ISM 321 C
transmission electron microscope	Zeiss, EM 910, 120 kV
zeta potential	PSS Nicomp, 380 ZLS, 635 nm laser
confocal 3D microscope	NanoFocus, µsurf custom
optical microscope	Olympus Deutschland, CX 40, 5x magnification
pH meter	PCE, PCE-PHD 1
scale	PESA Waagen, Precisa 300-9234/H

Tab. S 2: Chemicals used in the experiments

substance	**supplier, information**
Ag plate	Alfa Aesar,99.99 %, thickness of 0.5 mm
Au plate	Allgemeine Gold- und Silberscheideanstalt, 99.99 %, thickness of 0.5 mm
PtPd plate	Allgemeine Gold- und Silberscheideanstalt AG, $Pt_{0.66}Pd_{0.33}$ (molar composition)
Pt plate	Alfa Aesar, 99.99 %, thickness of 0.5 mm
PVP solution	CPS instruments, for analysis, ρ=1.385,$\bar{d}$=237nm, FWHM=23nm
sodium chlorine	VWR International, 99.9 %
sucrose	AppliChem, for analysis, D(+)
tetraethylammonium hydroxide	Alfa Aesar, aqueous solution 35 wt.%
trisodium citrate	AppliChem GmbH, high purity

Tab. S 3: Physical properties used for calculation in this thesis, the values refer to 20 °C

property	symbol	value	unit	reference
refractive index, water at 20 °C, 1064 nm	n_w	1.326	1	[261]
refractive index, optical glass at 1064 nm	n_G	1.5066	1	[440]
refractive index, air at 1064 nm	n_A	1.0003	1	[262]
density, silver	ρ_{Ag}	10.49	g/cm³	[380]
density, gold	ρ_{Au}	19.3	g/cm³	[380]
density, platinum	ρ_{Pt}	21.45	g/cm³	[380]
density, water	ρ_w	1	g/cm³	[380]
molar weight, silver	M_{Ag}	107.87	g/mol	[380]
molar weight, gold	M_{Au}	196.97	g/mol	[380]
molar weight, platinum	M_{Pt}	195.08	g/mol	[380]
dynamic viscosity, water	η_w	0.001	Pa·s	[380]
specific heat capacity, water	c_p	4190	J/(kg·K)	[380]

8.2. Results and discussion

If available, supplementary results, as figures or calculations, for the experiments presented in this thesis are given in the following.

8.2.1. Cavitation bubble investigation at 1 ns pulse duration

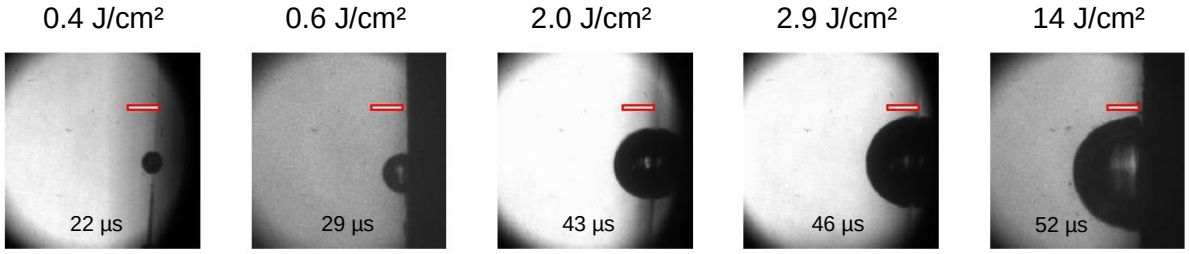

Fig. S 2: Maximal cavitation bubble extensions observed with a 1 ns laser system at the respective laser fluences; the scale bar equals 250 µm. The respective delay time is given in each image.

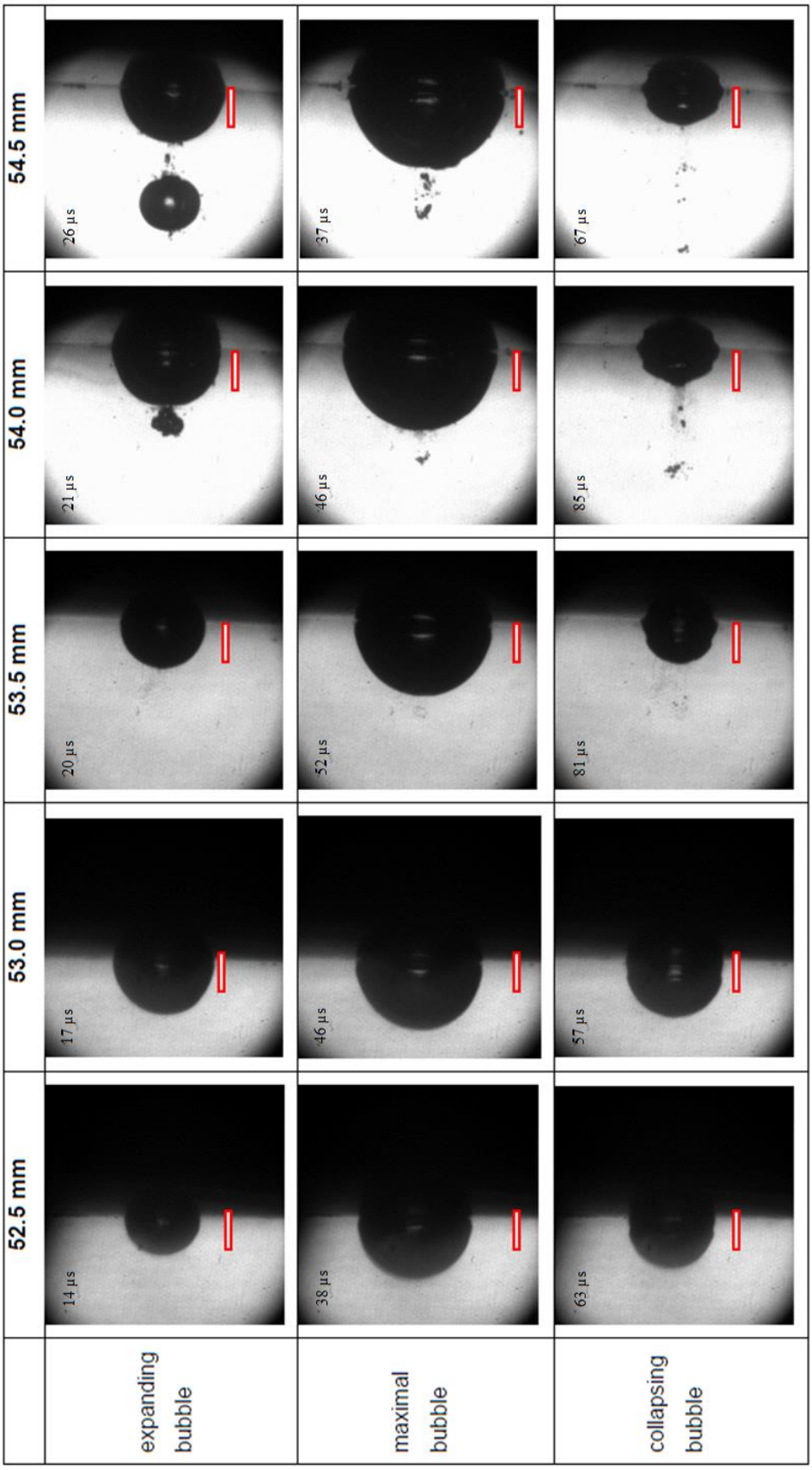

Fig. S 3: Exemplary cavitation bubbles at different distances between the target surface and the focusing lenses, i.e., different focal distances, during the expansion, the maximal extension, and the shrinking phase; the scale bar equals 250 µm. All images are obtained with a fluence of 14 J/cm². The respective delay time is given in each image.

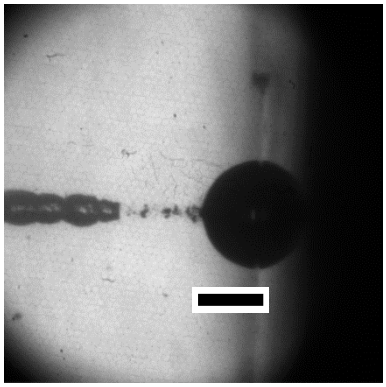

c(Ag) = 91 mg/L
l = 53.5 mm
F = 14 J/cm²

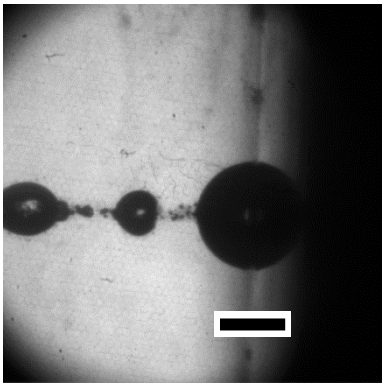

c(Ag) = 91 mg/L
l = 53.5 mm
F = 14 J/cm²

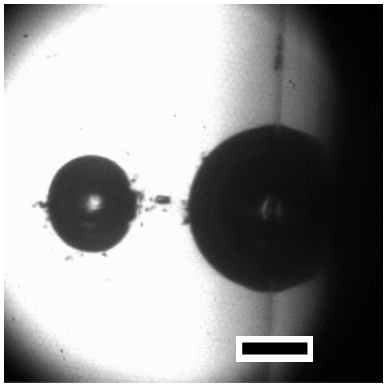

c(Ag) = 0 mg/L
l = 54.5 mm
F = 14 J/cm²

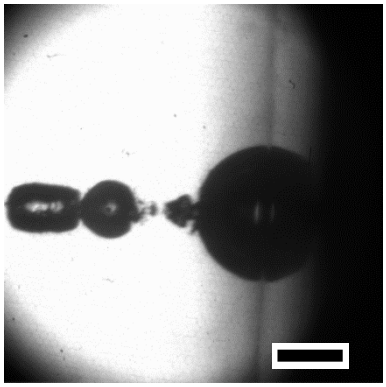

c(Ag) = 5 mg/L
l = 53.5 mm
F = 14 J/cm²

Fig. S 4: Bubble cascade images; the scale bars equal 250 µm. The experimental settings for each image are given below the respective image, where c(Ag) is the concentration of Ag NPs in the liquid, l is the focal distance, and F the fluence.

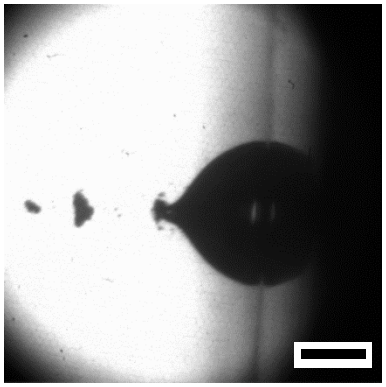

c(Ag) = 5 mg/L
l = 53.5 mm
F = 14 J/cm²

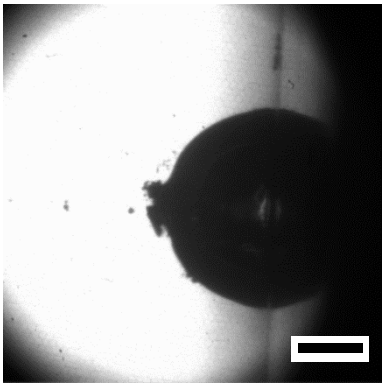

c(Ag) = 0 mg/L
l = 54.5 mm
F = 14 J/cm²

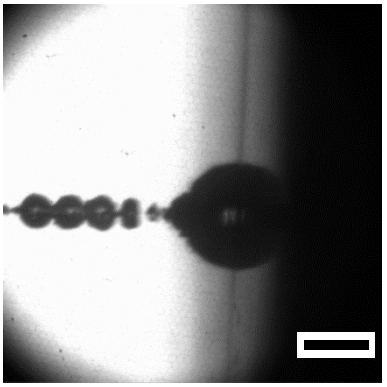

c(Ag) = 2.3 mg/L
l = 53.5 mm
F = 14 J/cm²

Fig. S 5: Cavitation bubble images, where spike- and ripple-like structures instead of hemispheres are observed; the scale bars equal 250 µm. The experimental settings for each image are given below the respective image, where c(Ag) is the concentration of Ag NPs in the liquid, l is the focal distance, and F the fluence.

Calculation of flow parameter

Tab. S 4: Process and material (water) parameters for estimation of the flow condition in the ablation chamber

title	symbol	value	unit
flow velocity	v	20	cm/min
fluid density	ρ	1.0	g/cm³
fluid dynamic viscosity	η	1.0	m(Pa s)
characteristic diameter	d	0.80	cm
hydrodynamic NP radius	r	15	nm

Calculation of the Reynolds number Re results in laminar flow behavior

$$Re = \frac{\rho \cdot d \cdot v}{\eta} = 17$$

Estimation of the diffusion coefficient of the NP D_{NP}

$$D_{NP} = \frac{k_B \cdot T}{6 \cdot \pi \cdot \eta \cdot r} = 1.5 \cdot 10^{-11}\, {m^2}/{s}$$

Estimation of the mass transfer coefficient β for a spherical particle by the empirical equation [441]:

$$Sh = 1.6 \cdot Re^{0.54}$$

$$\beta = 1.6 \cdot \frac{D_{NP}}{2 \cdot r} \cdot \left(\frac{2 \cdot v \cdot r \cdot \rho}{\eta}\right)^{0.54} = 5.4 \cdot 10^{-6}\, {m}/{s}$$

Calculation of the stationary layer thickness δ_c

$$\delta_c = \frac{D_{NP}}{\beta} = 2.7\ \mu m$$

Since the NP distribution in the stationary layer is unknown, only the NP concentration in the completely mixed flow layer can be determined. With the values given in Tab. S 5, a concentration of about 3 µg/L, is calculated. It is assumed that the main part of the NP is trapped in the stationary layer after the cavitation bubble collapse, which means that the local NP concentration in the stationary layer is to an unknown extend higher than 3 µg/L.

Tab. S 5: Process parameters for calculation of the NP concentration in the mixed flow layer

title	value	unit
productivity per pulse	1	ng/pulse
repetition rate	0.5	Hz
flow rate	10	mL/min

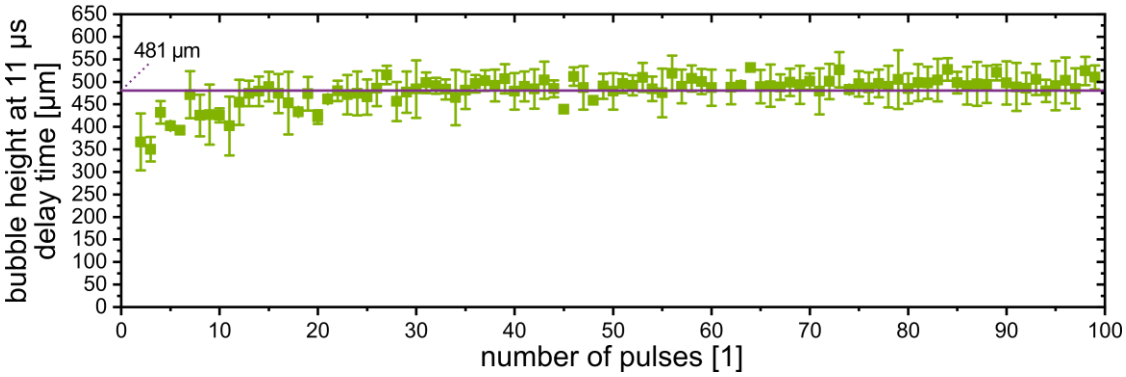

Fig. S 6: Cavitation bubble height at a delay time of 11 µs in dependency on the number of applied number of pulse on the same spot, the purple line presents the fit between 25 and 100 pulses

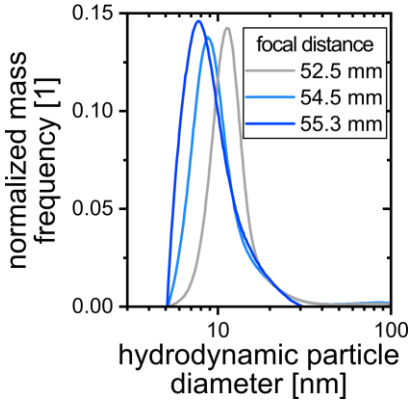

Fig. S 7: Mass-weighted, hydrodynamic size distribution measured by analytical disc centrifugation for Ag NPs at a focal distance of 52.5, 54.5, and 55.3 mm. The data are normalized so that the area under the curve equals 1.

8.2.2. Influence of the process parameters on both the NP productivity and size

Calculation of the laser fluence when varying the distance between the target and focusing lens

The angle of incidence of the laser beam on the target surface was calculated using geometric considerations. The refraction at the phase boundaries was calculated using Snell's law. The parameters used for the calculation via Eq. S 2 and Eq. S 3 are given in Tab. S 6. Note that this calculation results in the nominal laser fluence (the incident fluence that reaches the target immersed in the liquid assuming plain water), whereas exact calculation of the effective fluence (the energy that is deposited in the target) would require to determine the laser attenuation in the colloid volume of the beam path reaching the target (with the attenuation depending on nanoparticle concentration, nanoparticle size distribution and eventually self-focusing effects) as well as the temperature-dependent target reflectivity at the given wavelength.

$$F = \frac{2 \cdot E_P}{\pi \cdot w_0^2} \qquad \text{Eq. S 2}$$

$$I = \frac{2 \cdot P_P}{\pi \cdot w_0^2} \qquad \text{Eq. S 3}$$

F: fluence [J/cm²]

E_P: pulse energy [J]

w_0: 1/e²-beam radius [cm]

I: laser intensity [W/cm²]

P_P: pulse power [W]

Tab. S 6: Laser beam parameters for calculation of the laser beam fluence

parameter	value
spot diameter on the target surface at the focal distance of maximal productivity [70]	69 µm
experimentally determined focal distance between the lens and the target surface at the point of maximal productivity	124.4 mm
width of the ablation chamber window	2.2 mm
refractive index of the ablation chamber window (N-BK7), taken from data sheets provided by SCHOTT North America, Inc.	1.5071
width of the liquid layer over the ablation target	5 mm
refractive index of water [261]	1.3265

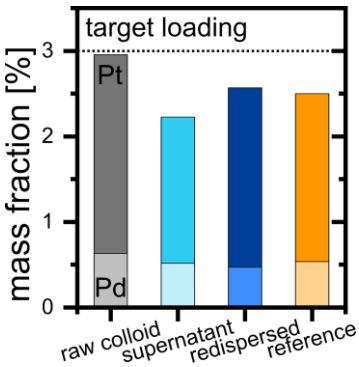

Fig. S 8: ICP-OES measurement of the laser-generated PtPd particles supported on Al_2O_3

Tab. S 7: NP composition of the different PtPd/Al_2O_3 catalysts, obtained by ICP-OES measurements

	Pt	Pd
raw	3.69	1
supernatant	3.30	1
redispersed	4.45	1
reference	3.66	1

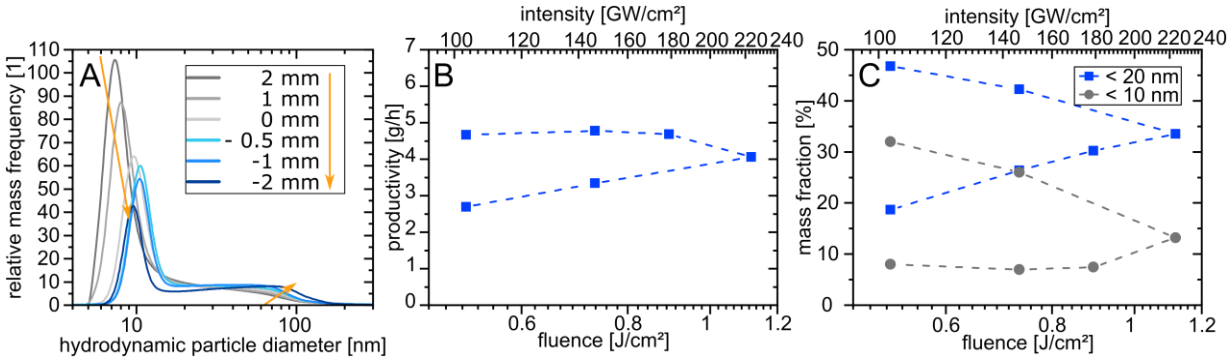

Fig. S 9: Influence of the change in the distance between the focal length and the ablation target position on the nanoparticle size distribution (A), the overall productivity (B), and the relative mass fraction of particle smaller than 20 and 10 nm (C) for a target made of 2:1 alloy of platinum and palladium

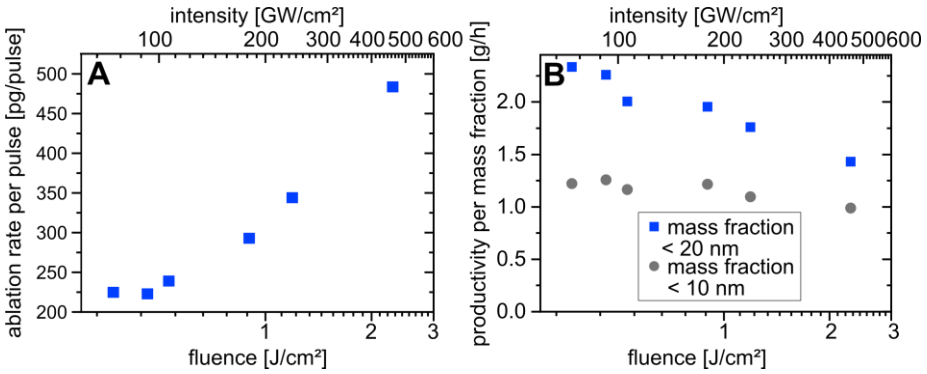

Fig. S 10: (A) Dependency of the pulse-specific productivity on the laser pulse energy and repetition rate, (B) change in the mass productivity of NPs <10 nm and <20 nm as a function of the laser pulse energy

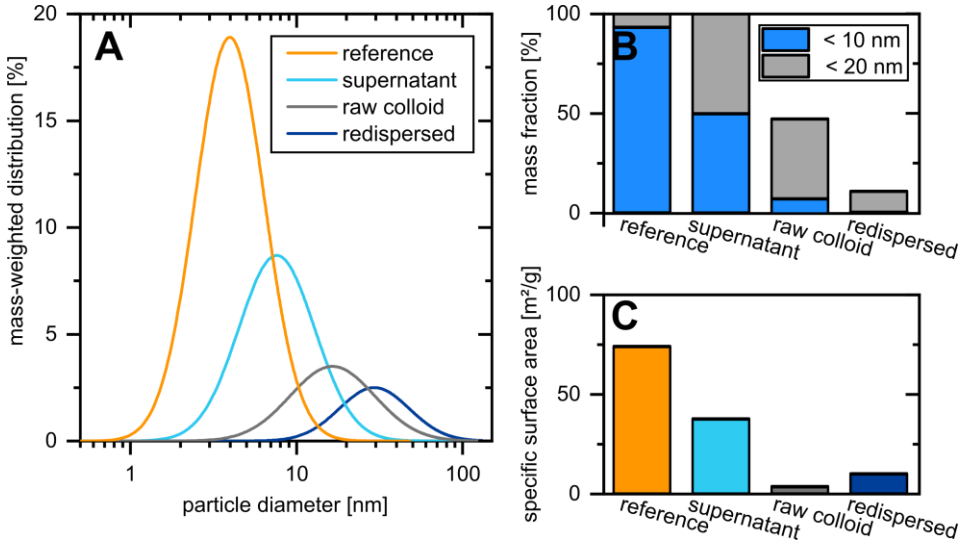

Fig. S 11: Mass-weighted particle size distribution (A) and particle size fractions <10 nm and <20 nm (B) as well as the specific surface area (C) of the $PtPd/Al_2O_3$ catalysts compared in Fig. 29

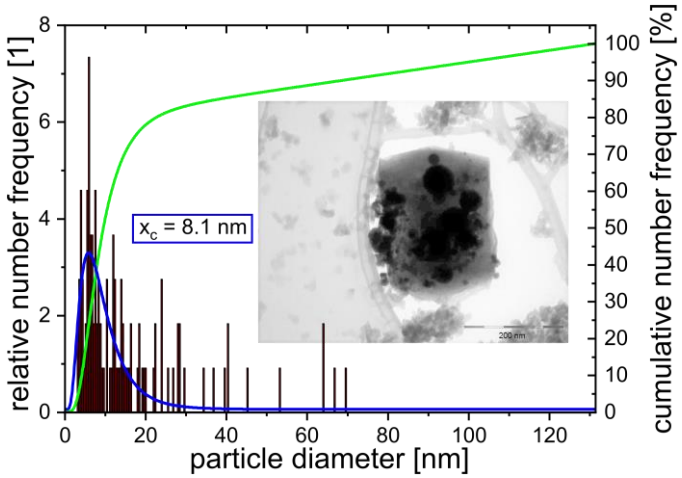

Fig. S 12: TEM histogram of the raw colloid ($PtPd/Al_2O_3$), fitted with a log-normal distribution (blue line), moreover the cumulative number frequency (green line) and an exemplary TEM image are shown

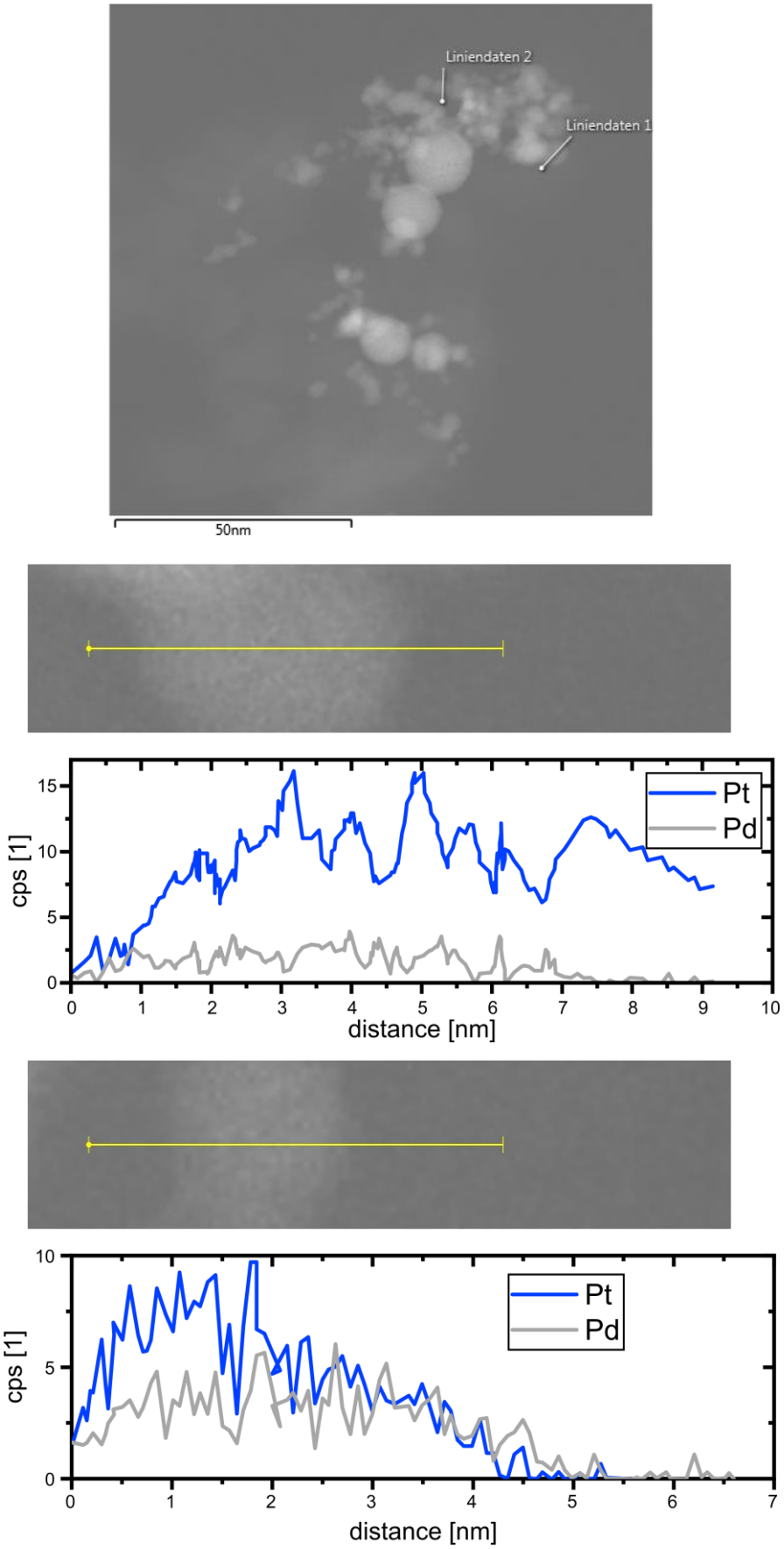

Fig. S 13: TEM picture and EDX line scans of the raw laser-generated colloid validating NP alloy formation

8.2.3. Focal position and target thickness

Selection of a suitable focusing optic

In Tab. S 8, possible lenses and lens combinations for the automated device are listed. Since the investment costs for f-theta lenses are more than 100 times higher than for plano-convex lenses, they are not suitable for the device. The combination of two lenses with a focal distance of 60 mm is neglected in the following consideration due to the Rayleigh length of <0.1 mm. For the 60 mm lens (1xf60) and the combination of two 100 mm lenses (2f100), the maximal image radius (Fig. S 14) and maximal effective Rayleigh length (Fig. S 15) are determined. Due to the stronger beam focusing of the 2f100 combination, higher ablation yields were achieved than the 1f60 system. Consequently, the 2f100 combination is chosen for focusing the laser beam of the automated device.

Tab. S 8: Different possible lenses and lens combination for the automated device, where the CryLaS GmbH did the calculation for the Rayleigh length and the maximal image radius; the gray shaded columns were examined further

lens combination	focal length [mm]	Rayleigh length [mm]	max. image radius [mm]
f-theta lens	100	3.2	35*
f-theta lens	63	1.3	36*
one plano convex lens	60	1.2	5
two plano convex lenses each f = 60 mm	30	0.054	4.5
two plano convex lenses each f = 100 mm	50	0.259	8.5

*: information from Sill optics

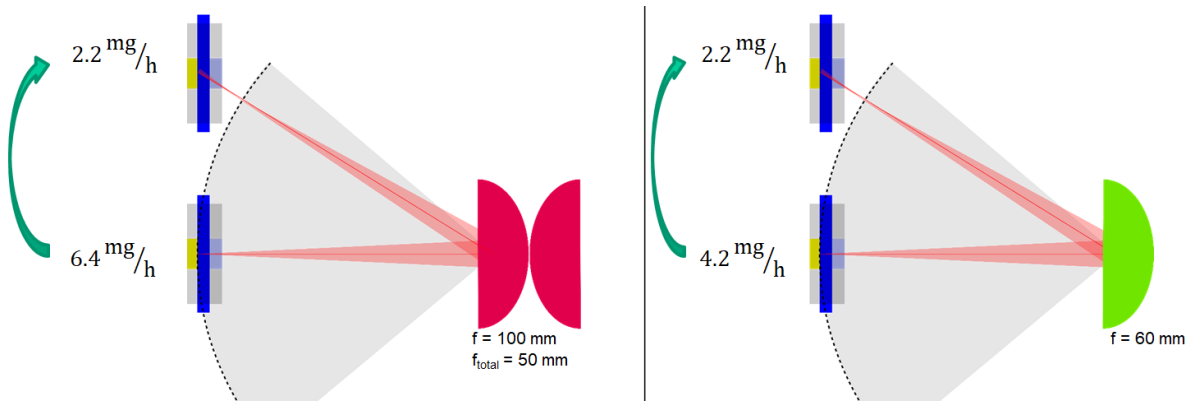

Fig. S 14: Determination of the effective maximal image radius by analyzing the maximal productivity at different incident angles for Au

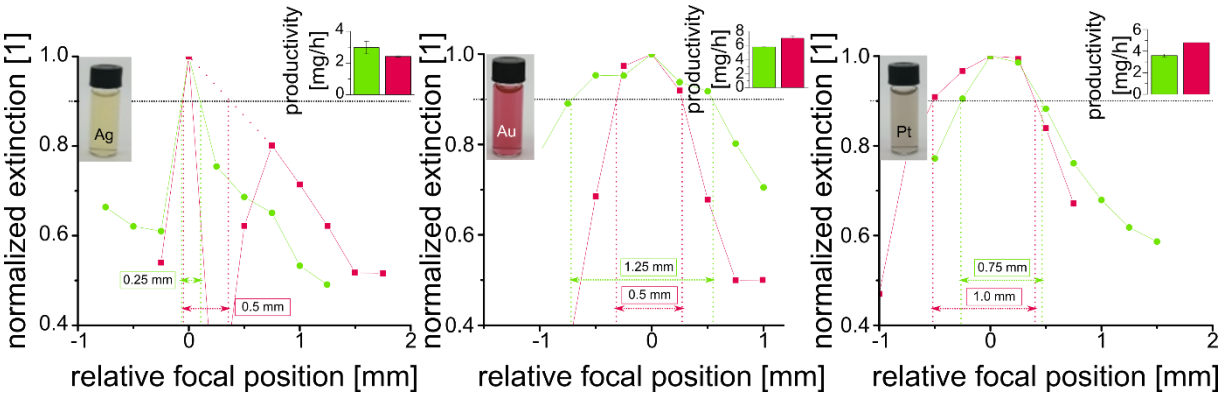

Fig. S 15: Determination of the effective Rayleigh length by analyzing the maximal extinction at different focal distances for Ag, Au, and Pt

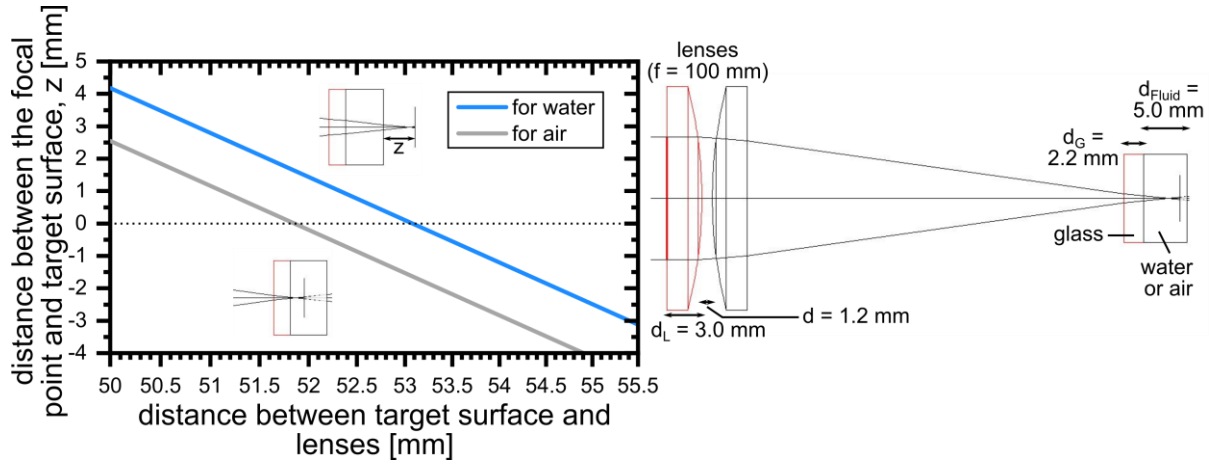

Fig. S 16: Calculation of the beam diameter in air and water with the software WinLens3D Basic in dependence of the relative focal distance. Further physical parameters are given in Tab. S 3.

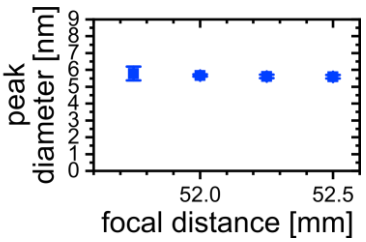

Fig. S 17: Number-weighted peak diameter for Au in dependence of the focal distance

Tab. S 9: Capacities of an ablation capsule assuming complete target ablation

	Silver	Gold	Platinum
metal price* per capsule (target dimensions: 5 x 10 x 0.5 mm) [€]	0.13	22.73	13.50
workdays per capsule [d]	3.9	4.6	3.1
volume of colloid produced per capsule [L]	2.6	4.8	5.4

* the mean value from 29.07.2019 to 29.07.2020 is taken for the calculation

8.2.4. Liquid flow rate

An exemplary calculation of the stationary layer thickness

The process parameters for experiments with the Amphos flex500 [32] and eMOPA1064-500 (Tab. S 10) are used to calculate different dimensionless characteristic numbers, the diffusion coefficient of the NPs, and the concentration boundary layer thickness.

Tab. S 10: Process parameters for calculation of characteristic numbers for the Amphos flex500 and eMOPA1064-500

	Amphos flex500	eMOPA1064-500	unit
flow rate, $\dot{V}$	26000	1	cm³/min
chamber cross section, A	0.9	0.5	cm²
flow velocity, v	28889	2	cm/min
liquid layer height, d	0.5	0.5	cm
chamber length, l	10	10	cm
exemplary particle size, r	15	15	nm

Calculation of the Reynolds number, Re

$$Re_{Amphos} = \frac{\rho \cdot v \cdot d}{\eta} = 23\,900 \qquad \text{Eq. S 4}$$

$$Re_{eMOPA} = \frac{\rho \cdot v \cdot d}{\eta} = 1.7 \qquad \text{Eq. S 5}$$

Calculation of the diffusion coefficient, D

$$D = \frac{k_B \cdot T}{6 \cdot \pi \cdot \eta \cdot r} = 14 \cdot 10^{-12}\,\frac{m^2}{s} \qquad \text{Eq. S 6}$$

Calculation of the Bodenstein number, Bo

$$Bo_{Amphos} = \frac{v \cdot l}{D} = 34 \cdot 10^9 \qquad \text{Eq. S 7}$$

$$Bo_{eMOPA} = \frac{v \cdot l}{D} = 230 \cdot 10^3 \qquad \text{Eq. S 8}$$

Calculation of the mass transfer coefficient, β, assuming adsorption of particles onto solids [441]

$$\beta_{Amphos} = 1.6 \cdot \left(\frac{v \cdot 2 \cdot r \cdot \rho}{\eta}\right)^{0.54} \cdot \frac{D}{2 \cdot r} = 0.26 \cdot 10^{-3}\ \frac{m}{s} \qquad \text{Eq. S 9}$$

$$\beta_{eMOPA} = 1.6 \cdot \left(\frac{v \cdot 2 \cdot r \cdot \rho}{\eta}\right)^{0.54} \cdot \frac{D}{2 \cdot r} = 1.5 \cdot 10^{-6}\ \frac{m}{s} \qquad \text{Eq. S 10}$$

Calculation of the concentration boundary layer thickness, δ

$$\delta_{Amphos} = \frac{D}{\beta} = 54\ nm \qquad \text{Eq. S 11}$$

$$\delta_{eMOPA} = \frac{D}{\beta} = 9.400\ \mu m \qquad \text{Eq. S 12}$$

8.2.5. Ablation time

Tab. S 11: SEM images for Ag, Au, Pt targets showing unirradiated target spot and such target spot which are irradiated with one laser pulse (1 ns, 1064 nm, 15 J/cm²)

	Ag	**Au**	**Pt**
unirradiated	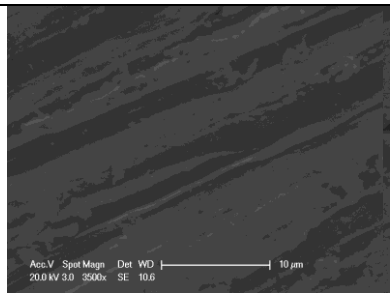	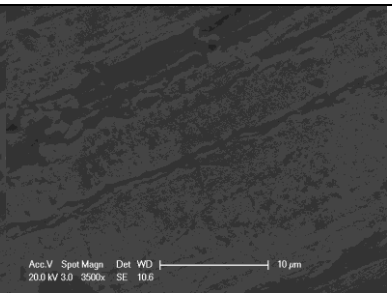	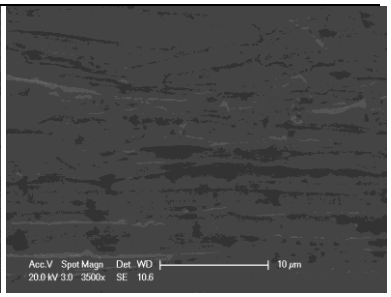
irradiated, after 1st run	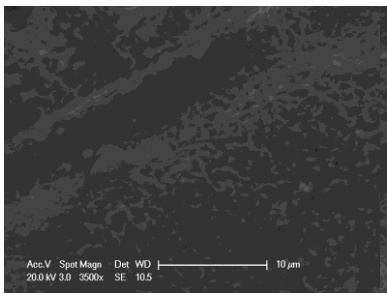	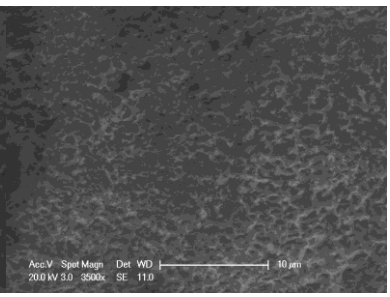	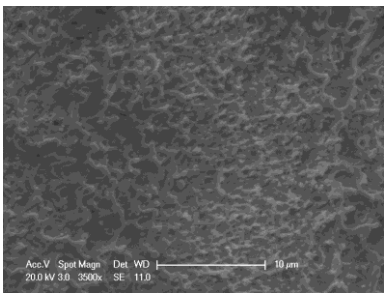

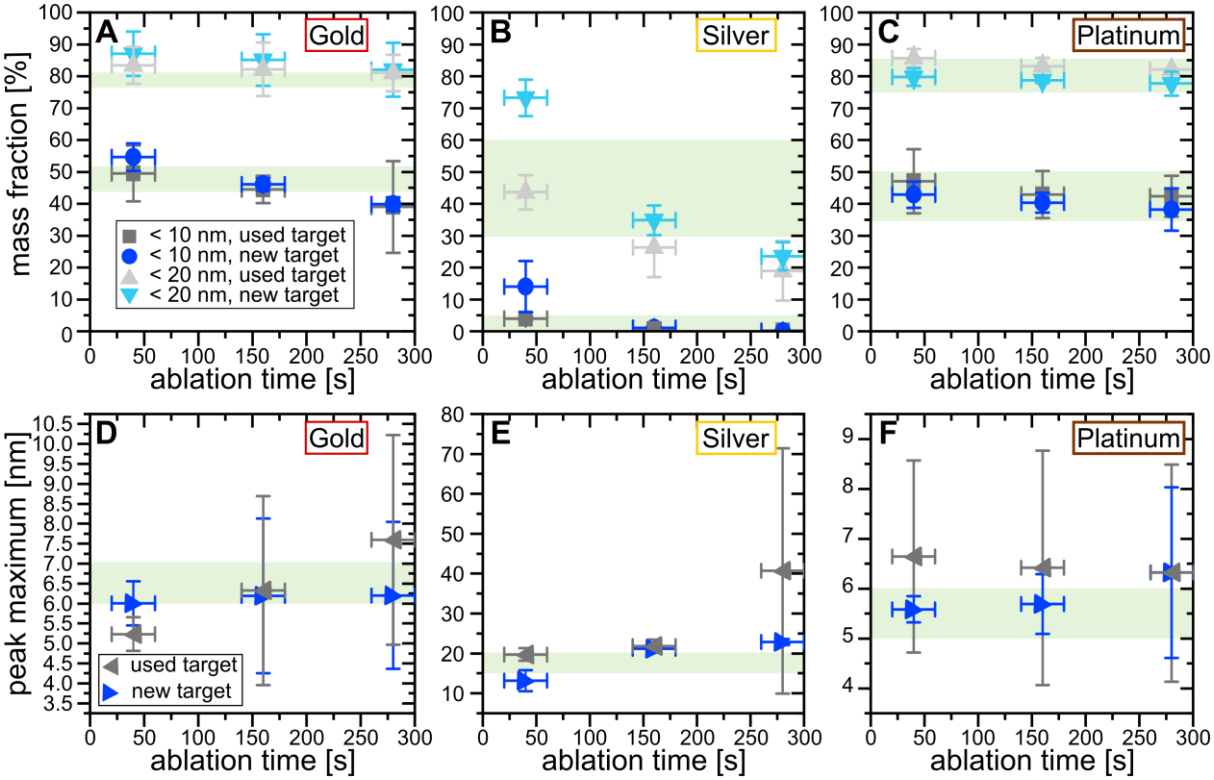

Fig. S 18: Time-dependent change in the mass fraction <10 nm and <20 nm of the Au (A), Ag (B), and Pt (C) and peak maximum for Au (D), Ag (E), and Pt (F); the green shaded area mark the variance due to a change in the focal plane shift as determined in Fig. 32

Calculation of Ag target heating

The calculation needs to consider the heat transfer from the liquid through the stationary layer to the Ag surface and the heat conduction through the Ag target. The temperature at the backside of the Ag target is measured (see Fig. 41), and the heat flux is given by the derivative of the temperature of the time (see Fig. S 19). The temperature at the Ag front side is calculated by Eq. S 13, and the result is given below.

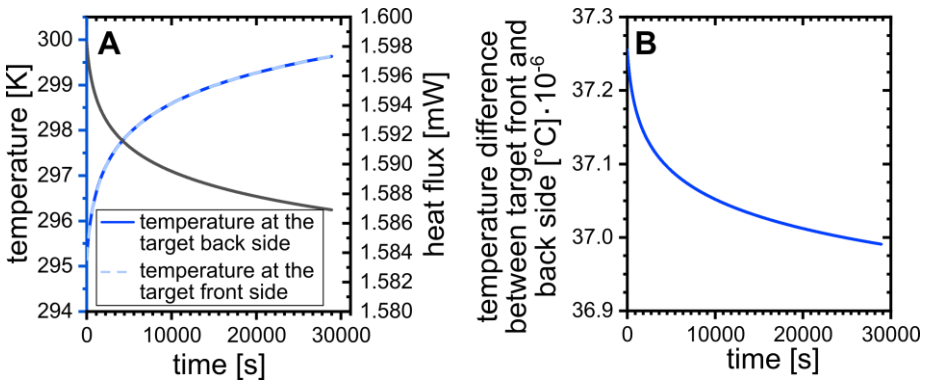

Fig. S 19: Temperature and heat flux through the Ag target over 8 h ablation, calculated with fitted data shown in Fig. 41 and the calculated temperature at the target front phase (A). Moreover, the overall temperature difference between the target front and backside is calculated (B).

$$\dot{Q} = \frac{\lambda \cdot A}{d} \cdot \left(T_{front} - T_{back}\right) \quad \text{Eq. S 13}$$

where:

$\dot{Q}$: heat flux $[W]$, calculated according to $\dot{Q} = \frac{\partial T}{\partial t}$

λ: thermal conductivity of Ag $\left[\frac{W}{m \cdot K}\right]$, $429\ \frac{W}{m \cdot K}$ [380]

A: irradiated target area$[m^2]$, 10 mm x 5 mm

d: target thickness $[m]$, 5 mm

T_{front}: temperature of the target surface in contact with the liquid phase $[K]$, calculated

T_{back}: temperature of the target surface in contact with air $[K]$, measured and fit

For the calculation of the heat transfer, first, the heat transfer coefficient needs to be estimated by the following empiric equation for forced convection:

$$\alpha = 0.021 \cdot \frac{\lambda}{l} \cdot Re^{0.8} \cdot Pr^{0.43} \cdot \Gamma^{-0.05} = 5.6\ \frac{W}{m^2 \cdot K} \quad \text{Eq. S 14}$$

$$Re = \frac{v \cdot d}{\nu} = 1.8 \quad \text{Eq. S 15}$$

$$Pr = \frac{c_p \cdot \eta}{\lambda} = 4.9 \quad \text{Eq. S 16}$$

$$\Gamma = \frac{l}{d} = 2 \quad \text{Eq. S 17}$$

where:

α: coefficient of heat transfer $\left[\frac{W}{m^2 \cdot K}\right]$

λ: thermal conductivity $\left[\frac{W}{m \cdot K}\right]$, $429\ \frac{W}{m \cdot K}$ for Ag and $0.87\ \frac{W}{m \cdot K}$ for water [380]

l: pipe length $[m]$, here the length of the irradiated area, 10 mm

Re: Reynolds number

Pr: Prandtl number

Γ: dimensionless geometry number

v: flow velocity $\left[\frac{m}{s}\right]$, $3.7 \cdot 10^{-4}\,\frac{\mathrm{m}}{\mathrm{s}}$

d: inner tube diameter $[m]$, 5 mm

ν: kinematic viscosity of the liquid (water) $\left[\frac{m^2}{s}\right]$, $1.0 \cdot 10^{-6}\,\frac{\mathrm{m}^2}{\mathrm{s}}$ [380]

c_p: specific heat capacity of water $\left[\frac{J}{g \cdot K}\right]$, $4.2\ \frac{\mathrm{J}}{\mathrm{g \cdot K}}$ [380]

η: dynamic viscosity of water $[Pa \cdot s]$, $1.0\ \mathrm{mPa \cdot s}$ [380]

$$\dot{Q} = \alpha \cdot A \cdot (T_{in} - T_{out}) = 0.5\ mW \qquad \text{Eq. S 18}$$

where:

T_{in}: liquid temperature at the ablation chamber entrance after 8 h ablation $[K]$, 293 K (measured)

T_{out}: liquid temperature at the ablation chamber outlet after 8 h ablation $[K]$, 295 K (measured)

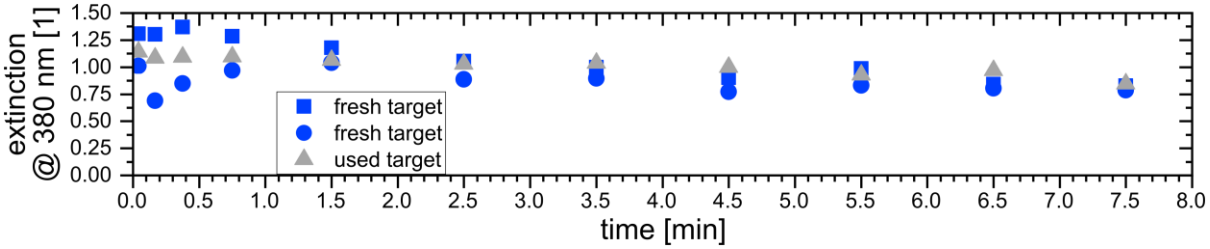

Fig. S 20: Time-dependent extinction of gold during long time ablation of 8 h with two fresh and one previously used target

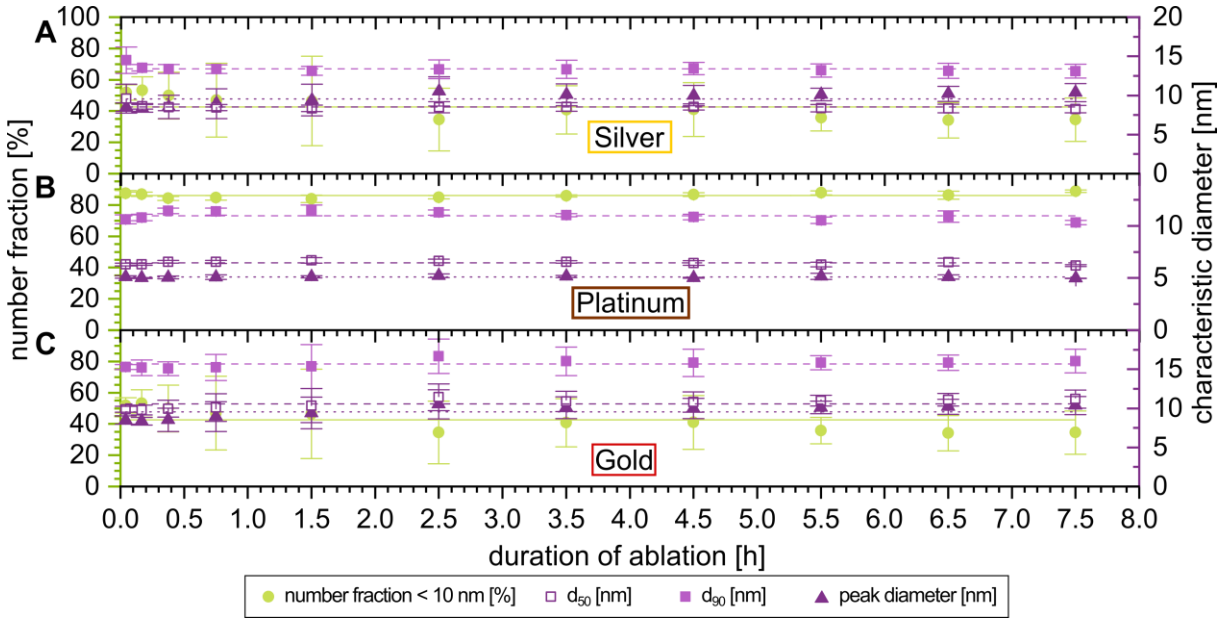

Fig. S 21: Number weighted size variation of silver stabilized with citrate (A), gold (B), and platinum (C) during long time ablation of 8 h, the lines are the result of a constant fit between 1.5 h – 7.5 h

8.2.6. Reproducibility and robustness of the automated laser ablation process

8.2.6.1. Safety data sheet for silver, gold, and platinum colloids

Sicherheitsdatenblatt - Silberkolloid gemäß Verordnung (EG) Nr. 1907/2006

Erstellt am: **03.03.2020**
Überarbeitet am : **22.07.2020**
Gültig ab:
Version: 1.0 **Ersetzt Version:** -

Abschnitt 1: Bezeichnung des Stoffs beziehungsweise des Gemischs und des Unternehmens

1.1 Produktidentifikator

Stoffname / Handelsname: Silbernanopartikel

Index-Nr.:

EG-Nr.: 231-131-3

CAS-Nr.: 7440-22-4

REACH-Registrierungsnr.: Eine Registriernummer für diesen Stoff ist nicht vorhanden, da der Stoff oder seine Verwendung von der Registrierung ausgenommen sind, die jährliche Tonnage keine Registrierung erfordert oder die Registrierung für einen späteren Zeitpunkt vorgesehen ist.

Andere Bezeichnungen: kolloidales Silber, Nanosilber, Silberkolloid

1.2 Relevante identifizierte Verwendungen des Stoffs oder Gemischs und Verwendungen, von denen abgeraten wird

Relevante identifizierte Verwendungen: Laborchemikalien, Herstellung von Stoffen

Verwendungen, von denen abgeraten wird: Nicht für Haushaltsanwendungen, als Nahrungsergänzungsmittel oder Medikament verwenden

1.3 Einzelheiten zum Lieferanten, der das Sicherheitsdatenblatt bereitstellt

Hersteller / Lieferant

Universität Duisburg-Essen

Straße/Postfach

Universitaetsstr. 7

Nat.-Kenn./PLZ/Ort

D-45141 Essen

Kontaktstelle für technische Information

Telefon

+49 (0)201-183-6173

1.4 Notrufnummer

0800 181 7059 (CHEMTREC Deutschland)

+49 696 43508409 (CHEMTREC weltweit)

Erstellt am: **03.03.2020**
Überarbeitet am : **22.07.2020**
Gültig ab:
Version: 1.0 **Ersetzt Version:** -

Abschnitt 2: Mögliche Gefahren

2.1 Einstufung des Stoffs oder Gemischs

Einstufung gemäß der Verordnung (EG) Nr. 1272/2008.

Langfristig (chronisch) gewässergefährdend (Kategorie 1), H411

Den Volltext der in diesem Abschnitt aufgeführten Gefahrenhinweise finden Sie unter Abschnitt 16.

2.2 Kennzeichnungselemente

Kein gefährlicher Stoff oder gefährliches Gemisch gemäß der Verordnung (EG) Nr. 1272/2008.

Piktogramm:

Signalwort: keins

Gefahrenbestimmende Komponenten für die Etikettierung enthält:

Gefahrenhinweise:

H411	Giftig für Wasserorganismen, mit langfristiger Wirkung.

Sicherheitshinweise:

P273	Freisetzung in die Umwelt vermeiden.

Weitere Kennzeichnungselemente

keine

2.3 Sonstige Gefahren

Dieser Stoff/diese Mischung enthält keine Komponenten in Konzentrationen von 0,1 % oder höher, die entweder als persistent, bioakkumulierbar und toxisch (PBT) oder sehr persistent und sehr bioakkumulierbar (vPvB) eingestuft sind.

Abschnitt 3: Zusammensetzung/Angaben zu Bestandteilen

3.1 Stoffe

Bei diesem Produkt handelt es sich um ein Gemisch.

3.2 Gemische

Stoffname: Ag Nanopartikel
EG-Nr.: 231-131-3 CAS-Nr. : 7440-22-4 Index-Nr.: - REACH-Registrierungsnr.: -
Einstufung gemäß Verordnung (EG) Nr. 1272/2008:
Aquatic Acute 1;
Aquatic Chronic 1;
H400, H410
M-Faktor - Aquatic Acute: 100 - Aquatic Chronic: 100

In Übereinstimmung mit den maßgeblichen Rechtsvorschriften müssen keine Komponenten mitgeteilt werden.

Abschnitt 4: Erste-Hilfe-Maßnahmen

4.1 Beschreibung der Erste-Hilfe-Maßnahme

Arzt konsultieren. Dem behandelnden Arzt dieses Sicherheitsdatenblatt vorzeigen.

Nach Einatmen

Bei Einatmen, betroffene Person an die frische Luft bringen. Bei Atemstillstand, künstlich beatmen.

Nach Hautkontakt

Mit Seife und viel Wasser abwaschen.

Nach Augenkontakt

Augen vorsorglich mit Wasser ausspülen.

Nach Verschlucken

Nie einer ohnmächtigen Person etwas durch den Mund einflößen. Mund mit Wasser ausspülen.

4.2 Wichtigste akute und verzögert auftretende Symptome und Wirkungen

Die wichtigsten bekannten Symptome und Wirkungen sind auf dem Kennzeichnungsetikett (siehe Abschnitt 2.2) und/oder in Kapitel 11 beschrieben

4.3 Hinweise auf ärztliche Soforthilfe oder Spezialbehandlung

Keine Daten verfügbar

Abschnitt 5: Maßnahmen zur Brandbekämpfung

5.1 Löschmittel

Geeignet: Wassersprühnebel, alkoholbeständigen Schaum, Trockenlöschmittel oder Kohlendioxid verwenden.

5.2 Besondere vom Stoff oder Gemisch ausgehende Gefahren

Keine giftigen Zersetzungsprodukte bekannt.

Nicht brennbar.

5.3 Hinweise für die Brandbekämpfung

Im Brandfall, wenn nötig, umgebungsluftunabhängiges Atemschutzgerät tragen.

Abschnitt 6: Maßnahmen bei unbeabsichtigter Freisetzung

6.1 Personenbezogene Vorsichtsmaßnahmen, Schutzausrüstungen und in Notfällen anzuwendende Verfahren

Dämpfe/Nebel/Gas nicht einatmen.

Für angemessene Lüftung sorgen.

Persönliche Schutzausrüstung siehe unter Abschnitt 8.

6.2 Umweltschutzmaßnahmen

Weiteres Auslaufen oder Verschütten verhindern, wenn dies ohne Gefahr möglich ist.

Nicht in die Kanalisation gelangen lassen. Ein Eintrag in die Umwelt ist zu vermeiden.

6.3 Methoden und Material für Rückhaltung und Reinigung

Zur Entsorgung in geeignete und verschlossene Behälter geben.

6.4 Verweis auf andere Abschnitte

Entsorgung: siehe Abschnitt 13

Abschnitt 7: Handhabung und Lagerung

7.1 Schutzmaßnahmen zur sicheren Handhabung

Informationen über Schutzmaßnahmen befinden sich im Abschnitt 8.

7.2 Bedingungen zur sicheren Lagerung unter Berücksichtigung von Unverträglichkeiten

Angaben zu den Lagerbedingungen

Behälter dicht verschlossen an einem trockenen, gut belüfteten Ort aufbewahren. Geöffnete Behälter sorgfältig verschließen und aufrecht lagern um jegliches Auslaufen zu verhindern. An einem kühlen Ort aufbewahren. Vor Gebrauch gut schütteln.

Empfohlene Lagerungstemperatur 2 - 8 °C

Lichtempfindlich. In Dunkelheit lagern.

Nicht einfrieren.

Anforderungen an Lagerräume und Behälter

Lagerklasse: 12 Nicht brennbare Flüssigkeiten

7.3 Spezifische Endanwendungen

Außer den in Abschnitt 1.2 genannten Verwendungen sind keine weiteren spezifischen Verwendungen vorgesehen.

Abschnitt 8: Begrenzung und Überwachung der Exposition / Persönliche Schutzausrüstung

8.1 Zu überwachende Parameter

Grenzwerte für die Exposition am Arbeitsplatz und/oder biologische Grenzwerte

Arbeitsplatzgrenzwerte (AGW) Deutschland

Stoffname: Silber ; CAS-Nr. : 7440-22-4

Nicht notwendig.

8.2 Begrenzung und Überwachung der Exposition

Geeignete technische Steuerungseinrichtungen

Allgemein übliche Arbeitshygienemaßnahmen.

Die beim Umgang mit Chemikalien üblichen Vorsichtsmaßnahmen sind zu beachten. Vor den Pausen und bei Arbeitsende Hände waschen.

Individuelle Schutzmaßnahmen - persönliche Schutzausrüstung

Augen- / Gesichtsschutz

Verwenden Sie zum Augenschutz nur Equipment, dass nach behördlichen Standards, wie NIOSH (US) oder EN 166 (EU), getestet und zugelassen wurde.

Hautschutz

Handschuhe

Mit Handschuhen arbeiten. Handschuhe müssen vor Gebrauch untersucht werden. Benutzen Sie eine geeignete Ausziehmethode (ohne die äußere Handschuhoberfläche zu berühren), um Hautkontakt mit diesem Produkt zu vermeiden. Entsorgung der kontaminierten Handschuhe nach Benutzung im Rahmen gesetzlicher Bestimmungen und der guten Laborpraxis. Waschen und Trocknen der Hände.

Die ausgewählten Schutzhandschuhe müssen die Spezifikationen der EG-Richtlinie 2016/425 und die davon abgeleitete Norm EN 374 erfüllen.

Anderer Hautschutz

Undurchlässige Schutzkleidung. Die Art der Schutzausrüstung muss je nach Konzentration und Menge des gefährlichen Stoffes am Arbeitsplatz ausgewählt werden.

Atemschutz

Kein Atemschutz notwendig. Bei störenden Emissionen Atemschutzmaske Typ OV/AG (US) oder ABEK (EU EN 14387) verwenden! Atemschutzgeräte und Komponenten müssen nach entsprechenden staatlichen Standards (beispielsweise NIOSH (US) oder CEN (EU)) zugelassen sein.

Begrenzung und Überwachung der Umweltexposition

Weiteres Auslaufen oder Verschütten verhindern, wenn dies ohne Gefahr möglich ist. Nicht in die Kanalisation gelangen lassen. Ein Eintrag in die Umwelt ist zu vermeiden.

Abschnitt 9: Physikalische und chemische Eigenschaften

9.1 Angaben zu den grundlegenden physikalischen und chemischen Eigenschaften

Aussehen	
- Aggregatzustand:	Flüssig, Suspension
- Farbe :	gelb
Geruch :	Keine Daten verfügbar
Geruchsschwelle :	Keine Daten verfügbar
pH-Wert :	6,0 bis 8,0
Schmelzpunkt/Gefrierpunkt :	0 °C
Siedebeginn und Siedebereich :	100 °C
Flammpunkt :	Nicht anwendbar
Verdampfungsgeschwindigkeit :	Keine Daten verfügbar
Entzündbarkeit (fest, gasförmig) :	Keine Daten verfügbar
obere/untere Entzündbarkeits- oder Explosionsgrenzen :	Keine Daten verfügbar
Dampfdruck :	23 hPa
Dampfdichte :	Keine Daten verfügbar

relative Dichte :	1,0 g/cm³
Löslichkeit(en) :	in Wasser vollständig mischbar
Verteilungskoeffizient: n-Octanol/Wasser :	Keine Daten verfügbar
Selbstentzündungstemperatur :	Keine Daten verfügbar
Zersetzungstemperatur :	Keine Daten verfügbar
Viskosität :	1 mPas
explosive Eigenschaften :	Keine Daten verfügbar
oxidierende Eigenschaften :	Keine Daten verfügbar

9.2 Sonstige Angaben

Keine Daten verfügbar

Abschnitt 10: Stabilität und Reaktivität

10.1 Reaktivität

Keine Daten verfügbar

10.2 Chemische Stabilität

Stabil unter angegebenen Lagerungsbedingungen.

10.3 Möglichkeit gefährlicher Reaktionen

Keine Daten verfügbar

10.4 Zu vermeidende Bedingungen

Temperaturen unterhalb von 2 °C und oberhalb von 30 °C

10.5 Unverträgliche Materialien

Starke Oxidationsmittel
Salze
Säuren

Gefährliche Zersetzungsprodukte

10.6 Weitere Zersetzungsprodukte-Keine Daten verfügbar

Im Brandfall können gefährliche Zersetzungsprodukte entstehen (Kohlenstoffoxide, Natriumoxide).

Im Brandfall: siehe Kapitel 5

Abschnitt 11: Toxikologische Angaben

11.1 Angaben zu toxikologischen Wirkungen

akute Toxizität

Keine Daten verfügbar

Ätz-/Reizwirkung auf die Haut

Keine Daten verfügbar

schwere Augenschädigung/-reizung

Keine Daten verfügbar

Sensibilisierung der Atemwege/Haut

Keine Daten verfügbar

Keimzell-Mutagenität

Keine Daten verfügbar

Karzinogenität

IARC: Kein Bestandteil dieses Produkts, der in einer Konzentration von gleich oder mehr als 0.1% vorhanden ist, wird durch das IARC als voraussichtliches, mögliches oder erwiesenes krebserzeugendes Produkt für den Menschen identifiziert.

Reproduktionstoxizität

Keine Daten verfügbar

spezifische Zielorgan-Toxizität bei einmaliger Exposition

Keine Daten verfügbar

spezifische Zielorgan-Toxizität bei wiederholter Exposition

Keine Daten verfügbar

Aspirationsgefahr

Keine Daten verfügbar

Symptome und Wirkungen (verzögerte und chronische) mit Angaben der Expositionswege auch: Informationen über Toxikokinetik, Stoffwechsel und Verteilung

Keine Daten verfügbar

Kann bei wiederholter oraler Aufnahme Argyrie hervorrufen (eine schiefergraue oder blaue Verfärbung der Haut und des tieferliegenden Gewebes durch die Einlagerung unlöslichen Silberalbuminats).

Abschnitt 12: Umweltbezogene Angaben

12.1 Toxizität

Keine Daten verfügbar

12.2 Persistenz und Abbaubarkeit

Keine Daten verfügbar

12.3 Bioakkumulationspotenzial

Keine Daten verfügbar

12.4 Mobilität im Boden

Keine Daten verfügbar

12.5 Ergebnis der PBT- und vPvB-Beurteilung

Dieser Stoff/diese Mischung enthält keine Komponenten in Konzentrationen von 0,1 % oder höher, die entweder als persistent, bioakkumulierbar und toxisch (PBT) oder sehr persistent und sehr bioakkumulierbar (vPvB) eingestuft sind.

12.6 Andere schädliche Wirkungen

Giftig für Wasserorganismen, mit langfristiger Wirkung.

Abschnitt 13: Hinweise zur Entsorgung

13.1 Verfahren der Abfallbehandlung

Behandlung verunreinigter Verpackungen

Wie ungebrauchtes Produkt entsorgen.

Abfallschlüssel gemäß Abfallverzeichnis-Verordnung (AVV)

06 Abfälle aus anorganisch-chemischen Prozessen (06 03 13*)

Besondere Vorsichtsmaßnahmen

Restmengen und nicht wieder verwertbare Lösungen einem anerkannten Entsorgungsunternehmen zuführen.

Abschnitt 14: Angaben zum Transport

14.1 UN-Nummer

ADR/RID: 3082 IMDG: 3082 IATA: 3082

14.2 Ordnungsgemäße UN-Versandbezeichnung

ADR/RID

ADR/RID: UMWELTGEFÄHRDENDER STOFF, FLÜSSIG, N.A.G. (Silver)

IMDG-Code / ICAO-TI / IATA-DGR

IMDG: ENVIRONMENTALLY HAZARDOUS SUBSTANCE, LIQUID, N.O.S. (Silver)
IATA: Environmentally hazardous substance, liquid, n.o.s. (Silver)

14.3 Transportgefahrenklassen

ADR/RID: 9 IMDG: 9 IATA: 9

14.4 Verpackungsgruppe

ADR/RID: III IMDG: III IATA: III

14.5 Umweltgefahren

Kennzeichen umweltgefährdende Stoffe

ADR/RID / IMDG-Code / ICAO-TI / IATA-DGR: x ja / ☐ nein
Marine Pollutant: ☐ ja / x nein

14.6 Besondere Vorsichtshinweise für den Verwender

EHS-Kennzeichnung erforderlich (ADR 2.2.9.1.10, IMDG Code 2.10.3) für Einzelverpackungen und kombinierte Verpackungen mit Innenverpackung mit Gefahrstoffen > 5L für Flüssigkeiten und > 5 kg für Feststoffe.

14.7 Massengutbeförderung gemäß Anhang II des MARPOL- Übereinkommens und gemäß IBC-Code

Keine Daten verfügbar

Abschnitt 15: Rechtsvorschriften

15.1 Vorschriften zu Sicherheit, Gesundheits- und Umweltschutz/spezifische Rechtsvorschriften für den Stoff oder das Gemisch

Dieses Sicherheitsdatenblatt erfüllt die Anforderungen der Verordnung (EG) Nr. 1907/2006.

REACH - Beschränkungen der Herstellung, des Inverkehrbringens und der Verwendung bestimmter gefährlicher Stoffe, Zubereitungen und Erzeugnisse (Anhang XVII)

15.2 Stoffsicherheitsbeurteilung

Für dieses Produkt wurde keine Stoffsicherheitsbeurteilung durchgeführt.

Abschnitt 16: Sonstige Angaben

Änderungen gegenüber der letzten Version

-

Abkürzungen

TWG:

AGW: Arbeitsplatzgrenzwert

Literaturangaben und Datenquellen

https://echa.europa.eu, 03.03.2020

Methoden gemäß Artikel 9 der Verordnung (EG) Nr. 1272/2008 zur Bewertung der Informationen zum Zwecke der Einstufung verwendet wurden

Wortlaut der Gefahrenhinweise und/oder Sicherheitshinweise auf die in Abschnitt 2 bis 15 Bezug genommen wird

H411 Giftig für Wasserorganismen, mit langfristiger Wirkung.

Schulungen für Arbeitnehmer

Erstellt am:	**03.03.2020**		
Überarbeitet am :	**22.07.2020**		
Gültig ab:			
Version:	1.0	**Ersetzt Version:**	-

Weitere Informationen

Die vorliegenden Informationen sind nach unserem besten Wissen zusammengestellt, sie erheben aber keinen Anspruch auf Vollständigkeit und sollten vom Benutzer nur als Leitfaden verstanden werden. Die Universität Duisburg-Essen schließt jegliche Haftung für Schäden aus, die beim Umgang oder im Kontakt mit diesen Chemikalien auftreten können. Für allgemeine Geschäftsbedingungen und zusätzliche Informationen siehe die Rückseite unserer Rechnungen oder Lieferscheine.

Sicherheitsdatenblatt - Goldkolloid gemäß Verordnung (EG) Nr. 1907/2006

Erstellt am: **03.03.2020**
Überarbeitet am : **22.07.2020**
Gültig ab:
Version: 1.0 **Ersetzt Version:** -

Abschnitt 1: Bezeichnung des Stoffs beziehungsweise des Gemischs und des Unternehmens

1.1 Produktidentifikator

Stoffname / Handelsname: Goldnanopartikel

Index-Nr.:

EG-Nr.: 231-165-9

CAS-Nr.: 7440-57-5

REACH-Registrierungsnr.: Eine Registriernummer für diesen Stoff ist nicht vorhanden, da der Stoff oder seine Verwendung von der Registrierung ausgenommen sind, die jährliche Tonnage keine Registrierung erfordert oder die Registrierung für einen späteren Zeitpunkt vorgesehen ist.

Andere Bezeichnungen: kolloidales Gold, Nanogold, Goldkolloid

1.2 Relevante identifizierte Verwendungen des Stoffs oder Gemischs und Verwendungen, von denen abgeraten wird

Relevante identifizierte Verwendungen: Laborchemikalien, Herstellung von Stoffen

Verwendungen, von denen abgeraten wird: Nicht für Haushaltsanwendungen, als Nahrungsergänzungsmittel oder Medikament verwenden

1.3 Einzelheiten zum Lieferanten, der das Sicherheitsdatenblatt bereitstellt

Hersteller / Lieferant

Universität Duisburg-Essen

Straße/Postfach

Universitaetsstr. 7

Nat.-Kenn./PLZ/Ort

D-45141 Essen

Kontaktstelle für technische Information

Telefon

+49 (0)201-183-6173

1.4 Notrufnummer

0800 181 7059 (CHEMTREC Deutschland)

+49 696 43508409 (CHEMTREC weltweit)

Abschnitt 2: Mögliche Gefahren

2.1 Einstufung des Stoffs oder Gemischs

Kein gefährlicher Stoff oder gefährliches Gemisch gemäß der Verordnung (EG) Nr. 1272/2008.

2.2 Kennzeichnungselemente

Kein gefährlicher Stoff oder gefährliches Gemisch gemäß der Verordnung (EG) Nr. 1272/2008.

2.3 Sonstige Gefahren

keine

Abschnitt 3: Zusammensetzung/Angaben zu Bestandteilen

3.1 Stoffe

Bei diesem Produkt handelt es sich um ein Gemisch.

3.2 Gemische

Stoffname: Au Nanopartikel

EG-Nr.: 231-165-9 CAS-Nr. : 7440-57-5 Index-Nr.: REACH-Registrierungsnr.: -

Einstufung gemäß Verordnung (EG) Nr. 1272/2008: Kein gefährlicher Stoff oder gefährliches Gemisch

In Übereinstimmung mit den maßgeblichen Rechtsvorschriften müssen keine Komponenten mitgeteilt werden.

Abschnitt 4: Erste-Hilfe-Maßnahmen

4.1 Beschreibung der Erste-Hilfe-Maßnahme

Arzt konsultieren. Dem behandelnden Arzt dieses Sicherheitsdatenblatt vorzeigen.

Nach Einatmen

Bei Einatmen, betroffene Person an die frische Luft bringen. Bei Atemstillstand, künstlich beatmen.

Nach Hautkontakt

Mit Seife und viel Wasser abwaschen.

Nach Augenkontakt

Augen vorsorglich mit Wasser ausspülen.

Nach Verschlucken

Nie einer ohnmächtigen Person etwas durch den Mund einflößen. Mund mit Wasser ausspülen.

4.2 Wichtigste akute und verzögert auftretende Symptome und Wirkungen

Die wichtigsten bekannten Symptome und Wirkungen sind auf dem Kennzeichnungsetikett (siehe Abschnitt 2.2) und/oder in Kapitel 11 beschrieben

4.3 Hinweise auf ärztliche Soforthilfe oder Spezialbehandlung

Keine Daten verfügbar

Abschnitt 5: Maßnahmen zur Brandbekämpfung

5.1 Löschmittel

Geeignet: Wassersprühnebel, alkoholbeständigen Schaum, Trockenlöschmittel oder Kohlendioxid verwenden.

5.2 Besondere vom Stoff oder Gemisch ausgehende Gefahren

Keine giftigen Zersetzungsprodukte bekannt.

5.3 Hinweise für die Brandbekämpfung

Im Brandfall, wenn nötig, umgebungsluftunabhängiges Atemschutzgerät tragen.

Abschnitt 6: Maßnahmen bei unbeabsichtigter Freisetzung

6.1 Personenbezogene Vorsichtsmaßnahmen, Schutzausrüstungen und in Notfällen anzuwendende Verfahren

Dämpfe/Nebel/Gas nicht einatmen.
Für angemessene Lüftung sorgen.
Persönliche Schutzausrüstung siehe unter Abschnitt 8.

6.2 Umweltschutzmaßnahmen

Keine besonderen Umweltschutzmaßnahmen erforderlich.

6.3 Methoden und Material für Rückhaltung und Reinigung

Zur Entsorgung in geeignete und verschlossene Behälter geben.

6.4 Verweis auf andere Abschnitte

Entsorgung: siehe Abschnitt 13

Abschnitt 7: Handhabung und Lagerung

7.1 Schutzmaßnahmen zur sicheren Handhabung

Informationen über Schutzmaßnahmen befinden sich im Abschnitt 8.

7.2 Bedingungen zur sicheren Lagerung unter Berücksichtigung von Unverträglichkeiten

Angaben zu den Lagerbedingungen

Behälter dicht verschlossen an einem trockenen, gut belüfteten Ort aufbewahren. Geöffnete Behälter sorgfältig verschließen und aufrecht lagern um jegliches Auslaufen zu verhindern. An einem kühlen Ort aufbewahren. Vor Gebrauch gut schütteln.

Empfohlene Lagerungstemperatur 2 - 8 °C

Nicht einfrieren.

Anforderungen an Lagerräume und Behälter

Lagerklasse: 12 Nicht brennbare Flüssigkeiten

7.3 Spezifische Endanwendungen

Außer den in Abschnitt 1.2 genannten Verwendungen sind keine weiteren spezifischen Verwendungen vorgesehen.

Abschnitt 8: Begrenzung und Überwachung der Exposition / Persönliche Schutzausrüstung

8.1 Zu überwachende Parameter

Grenzwerte für die Exposition am Arbeitsplatz und/oder biologische Grenzwerte

Arbeitsplatzgrenzwerte (AGW) Deutschland

Enthält keine Stoffe mit Arbeitsplatzgrenzwerten.

8.2 Begrenzung und Überwachung der Exposition

Geeignete technische Steuerungseinrichtungen

Allgemein übliche Arbeitshygienemaßnahmen.
Die beim Umgang mit Chemikalien üblichen Vorsichtsmaßnahmen sind zu beachten. Vor den Pausen und bei Arbeitsende Hände waschen.

Individuelle Schutzmaßnahmen - persönliche Schutzausrüstung

Augen- / Gesichtsschutz

Verwenden Sie zum Augenschutz nur Equipment, dass nach behördlichen Standards, wie NIOSH (US) oder EN 166 (EU), getestet und zugelassen wurde.

Hautschutz

Handschuhe

Mit Handschuhen arbeiten. Handschuhe müssen vor Gebrauch untersucht werden. Benutzen Sie eine geeignete Ausziehmethode (ohne die äußere Handschuhoberfläche zu berühren), um Hautkontakt mit diesem Produkt zu vermeiden. Entsorgung der kontaminierten Handschuhe nach Benutzung im Rahmen gesetzlicher Bestimmungen und der guten Laborpraxis. Waschen und Trocknen der Hände.

Die ausgewählten Schutzhandschuhe müssen die Spezifikationen der EG-Richtlinie 2016/425 und die davon abgeleitete Norm EN 374 erfüllen.

Anderer Hautschutz

Undurchlässige Schutzkleidung. Die Art der Schutzausrüstung muss je nach Konzentration und Menge des gefährlichen Stoffes am Arbeitsplatz ausgewählt werden.

Atemschutz

Kein Atemschutz notwendig. Bei störenden Emissionen Atemschutzmaske Typ OV/AG (US) oder ABEK (EU EN 14387) verwenden! Atemschutzgeräte und Komponenten müssen nach entsprechenden staatlichen Standards (beispielsweise NIOSH (US) oder CEN (EU)) zugelassen sein.

Begrenzung und Überwachung der Umweltexposition

Weiteres Auslaufen oder Verschütten verhindern, wenn dies ohne Gefahr möglich ist. Nicht in die Kanalisation gelangen lassen. Ein Eintrag in die Umwelt ist zu vermeiden.

Abschnitt 9: Physikalische und chemische Eigenschaften

9.1 Angaben zu den grundlegenden physikalischen und chemischen Eigenschaften

Aussehen	
- Aggregatzustand:	Suspension
- Farbe :	rot
Geruch :	Keine Daten verfügbar
Geruchsschwelle :	Keine Daten verfügbar

pH-Wert :	6,0 bis 8,0
Schmelzpunkt/Gefrierpunkt :	0 °C
Siedebeginn und Siedebereich :	100 °C
Flammpunkt :	Nicht anwendbar
Verdampfungsgeschwindigkeit :	Keine Daten verfügbar
Entzündbarkeit (fest, gasförmig) :	Keine Daten verfügbar
obere/untere Entzündbarkeits- oder Explosionsgrenzen :	Keine Daten verfügbar
Dampfdruck :	23 hPa
Dampfdichte :	Keine Daten verfügbar
relative Dichte :	1,0 g/cm³
Löslichkeit(en) :	in Wasser vollständig mischbar
Verteilungskoeffizient: n-Octanol/Wasser :	Keine Daten verfügbar
Selbstentzündungstemperatur :	Keine Daten verfügbar
Zersetzungstemperatur :	Keine Daten verfügbar
Viskosität :	1 mPas
explosive Eigenschaften :	Keine Daten verfügbar
oxidierende Eigenschaften :	Keine Daten verfügbar

9.2 Sonstige Angaben

Keine Daten verfügbar

Abschnitt 10: Stabilität und Reaktivität

10.1 Reaktivität

Keine Daten verfügbar

10.2 Chemische Stabilität

Stabil unter angegebenen Lagerungsbedingungen.

10.3 Möglichkeit gefährlicher Reaktionen

Keine Daten verfügbar

10.4 Zu vermeidende Bedingungen

Temperaturen unterhalb von 2 °C und oberhalb von 30 °C

10.5 Unverträgliche Materialien

Salze
Säuren

10.6 Gefährliche Zersetzungsprodukte

Weitere Zersetzungsprodukte-Keine Daten verfügbar
Im Brandfall können gefährliche Zersetzungsprodukte entstehen, Art der Zersetzungsprodukte unbekannt.
Im Brandfall: siehe Kapitel 5

Abschnitt 11: Toxikologische Angaben

11.1 Angaben zu toxikologischen Wirkungen

akute Toxizität
Keine Daten verfügbar
Ätz-/Reizwirkung auf die Haut
Keine Daten verfügbar
schwere Augenschädigung/-reizung
Keine Daten verfügbar
Sensibilisierung der Atemwege/Haut
Keine Daten verfügbar
Keimzell-Mutagenität
Keine Daten verfügbar
Karzinogenität
IARC: Kein Bestandteil dieses Produkts, der in einer Konzentration von gleich oder mehr als 0.1% vorhanden ist, wird durch das IARC als voraussichtliches, mögliches oder erwiesenes krebserzeugendes Produkt für den Menschen identifiziert.
Reproduktionstoxizität
Keine Daten verfügbar
spezifische Zielorgan-Toxizität bei einmaliger Exposition
Keine Daten verfügbar
spezifische Zielorgan-Toxizität bei wiederholter Exposition
Keine Daten verfügbar
Aspirationsgefahr
Keine Daten verfügbar

Symptome und Wirkungen (verzögerte und chronische) mit Angaben der Expositionswege auch: Informationen über Toxikokinetik, Stoffwechsel und Verteilung

Keine Daten verfügbar

Abschnitt 12: Umweltbezogene Angaben

12.1 Toxizität

Keine Daten verfügbar

12.2 Persistenz und Abbaubarkeit

Keine Daten verfügbar

12.3 Bioakkumulationspotenzial

Keine Daten verfügbar

12.4 Mobilität im Boden

Keine Daten verfügbar

12.5 Ergebnis der PBT- und vPvB-Beurteilung

Eine PBT/vPvB Beurteilung ist nicht verfügbar, da eine Stoffsicherheitsbeurteilung nichterforderlich/nicht durchgeführt wurde.

12.6 Andere schädliche Wirkungen

Keine Daten verfügbar

Abschnitt 13: Hinweise zur Entsorgung

13.1 Verfahren der Abfallbehandlung

Behandlung verunreinigter Verpackungen

Wie ungebrauchtes Produkt entsorgen.

Abfallschlüssel gemäß Abfallverzeichnis-Verordnung (AVV)

06 Abfälle aus anorganisch-chemischen Prozessen (06 03 13*)

Besondere Vorsichtsmaßnahmen

Restmengen und nicht wieder verwertbare Lösungen einem anerkannten Entsorgungsunternehmen zuführen.

Abschnitt 14: Angaben zum Transport

14.1 UN-Nummer

ADR/RID: - IMDG: - IATA: -

14.2 Ordnungsgemäße UN-Versandbezeichnung

ADR/RID

kein Gefahrgut

IMDG-Code / ICAO-TI / IATA-DGR

Not dangerous goods

14.3 Transportgefahrenklassen

ADR/RID: - IMDG: - IATA: -

14.4 Verpackungsgruppe

ADR/RID: - IMDG: - IATA: -

14.5 Umweltgefahren

Kennzeichen umweltgefährdende Stoffe

ADR/RID / IMDG-Code / ICAO-TI / IATA-DGR: ☐ ja / x nein

Marine Pollutant: ☐ ja / x nein

14.6 Besondere Vorsichtshinweise für den Verwender

Keine Daten verfügbar

14.7 Massengutbeförderung gemäß Anhang II des MARPOL- Übereinkommens und gemäß IBC-Code

Keine Daten verfügbar

Abschnitt 15: Rechtsvorschriften

15.1 Vorschriften zu Sicherheit, Gesundheits- und Umweltschutz/spezifische Rechtsvorschriften für den Stoff oder das Gemisch

Dieses Sicherheitsdatenblatt erfüllt die Anforderungen der Verordnung (EG) Nr. 1907/2006.

15.2 Stoffsicherheitsbeurteilung

Für dieses Produkt wurde keine Stoffsicherheitsbeurteilung durchgeführt.

Abschnitt 16: Sonstige Angaben

Änderungen gegenüber der letzten Version

-

Abkürzungen

-

Literaturangaben und Datenquellen

https://echa.europa.eu, 03.03.2020

Methoden gemäß Artikel 9 der Verordnung (EG) Nr. 1272/2008 zur Bewertung der Informationen zum Zwecke der Einstufung verwendet wurden

Wortlaut der Gefahrenhinweise und/oder Sicherheitshinweise auf die in Abschnitt 2 bis 15 Bezug genommen wird

Schulungen für Arbeitnehmer

Erstellt am: **03.03.2020**
Überarbeitet am : **22.07.2020**
Gültig ab:
Version: 1.0 **Ersetzt Version:** -

Weitere Informationen

Die vorliegenden Informationen sind nach unserem besten Wissen zusammengestellt, sie erheben aber keinen Anspruch auf Vollständigkeit und sollten vom Benutzer nur als Leitfaden verstanden werden. Die Universität Duisburg-Essen schließt jegliche Haftung für Schäden aus, die beim Umgang oder im Kontakt mit diesen Chemikalien auftreten können. Für allgemeine Geschäftsbedingungen und zusätzliche Informationen siehe die Rückseite unserer Rechnungen oder Lieferscheine.

Sicherheitsdatenblatt - Platinkolloid gemäß Verordnung (EG) Nr. 1907/2006

Erstellt am: **03.03.2020**
Überarbeitet am : **22.07.2020**
Gültig ab:
Version: 1.0 **Ersetzt Version:** -

Abschnitt 1: Bezeichnung des Stoffs beziehungsweise des Gemischs und des Unternehmens

1.1 Produktidentifikator

Stoffname / Handelsname: Platinnanopartikel

Index-Nr.:

EG-Nr.: 231-116-1

CAS-Nr.: 7440-06-4

REACH-Registrierungsnr.: Eine Registriernummer für diesen Stoff ist nicht vorhanden, da der Stoff oder seine Verwendung von der Registrierung ausgenommen sind, die jährliche Tonnage keine Registrierung erfordert oder die Registrierung für einen späteren Zeitpunkt vorgesehen ist.

Andere Bezeichnungen: kolloidales Platin, Nanoplatin, Platinkolloid

1.2 Relevante identifizierte Verwendungen des Stoffs oder Gemischs und Verwendungen, von denen abgeraten wird

Relevante identifizierte Verwendungen: Laborchemikalien, Herstellung von Stoffen

Verwendungen, von denen abgeraten wird: Nicht für Haushaltsanwendungen, als Nahrungsergänzungsmittel oder Medikament verwenden

1.3 Einzelheiten zum Lieferanten, der das Sicherheitsdatenblatt bereitstellt

Hersteller / Lieferant

Universität Duisburg-Essen

Straße/Postfach

Universitaetsstr. 7

Nat.-Kenn./PLZ/Ort

D-45141 Essen

Kontaktstelle für technische Information

Telefon

+49 (0)201-183-6173

1.4 Notrufnummer

0800 181 7059 (CHEMTREC Deutschland)

+49 696 43508409 (CHEMTREC weltweit)

Abschnitt 2: Mögliche Gefahren

2.1 Einstufung des Stoffs oder Gemischs

Kein gefährlicher Stoff oder gefährliches Gemisch gemäß der Verordnung (EG) Nr. 1272/2008.

2.2 Kennzeichnungselemente

Kein gefährlicher Stoff oder gefährliches Gemisch gemäß der Verordnung (EG) Nr. 1272/2008.

2.3 Sonstige Gefahren

keine

Abschnitt 3: Zusammensetzung/Angaben zu Bestandteilen

3.1 Stoffe

Bei diesem Produkt handelt es sich um ein Gemisch.

3.2 Gemische

Stoffname: Pt Nanopartikel

EG-Nr.: 231-116-1 CAS-Nr. : 7440-06-4 Index-Nr.: REACH-Registrierungsnr.: -

Einstufung gemäß Verordnung (EG) Nr. 1272/2008: Kein gefährlicher Stoff oder gefährliches Gemisch

In Übereinstimmung mit den maßgeblichen Rechtsvorschriften müssen keine Komponenten mitgeteilt werden.

Abschnitt 4: Erste-Hilfe-Maßnahmen

4.1 Beschreibung der Erste-Hilfe-Maßnahme

Arzt konsultieren. Dem behandelnden Arzt dieses Sicherheitsdatenblatt vorzeigen.

Nach Einatmen

Bei Einatmen, betroffene Person an die frische Luft bringen. Bei Atemstillstand, künstlich beatmen.

Nach Hautkontakt

Mit Seife und viel Wasser abwaschen.

Nach Augenkontakt

Augen vorsorglich mit Wasser ausspülen.

Nach Verschlucken

Nie einer ohnmächtigen Person etwas durch den Mund einflößen. Mund mit Wasser ausspülen.

4.2 Wichtigste akute und verzögert auftretende Symptome und Wirkungen

Die wichtigsten bekannten Symptome und Wirkungen sind auf dem Kennzeichnungsetikett (siehe Abschnitt 2.2) und/oder in Kapitel 11 beschrieben

4.3 Hinweise auf ärztliche Soforthilfe oder Spezialbehandlung

Keine Daten verfügbar

Abschnitt 5: Maßnahmen zur Brandbekämpfung

5.1 Löschmittel

Geeignet: Wassersprühnebel, alkoholbeständigen Schaum, Trockenlöschmittel oder Kohlendioxid verwenden.

5.2 Besondere vom Stoff oder Gemisch ausgehende Gefahren

Keine giftigen Zersetzungsprodukte bekannt.

5.3 Hinweise für die Brandbekämpfung

Im Brandfall, wenn nötig, umgebungsluftunabhängiges Atemschutzgerät tragen.

Abschnitt 6: Maßnahmen bei unbeabsichtigter Freisetzung

6.1 Personenbezogene Vorsichtsmaßnahmen, Schutzausrüstungen und in Notfällen anzuwendende Verfahren

Dämpfe/Nebel/Gas nicht einatmen.
Für angemessene Lüftung sorgen.
Persönliche Schutzausrüstung siehe unter Abschnitt 8.

6.2 Umweltschutzmaßnahmen

Keine besonderen Umweltschutzmaßnahmen erforderlich.

6.3 Methoden und Material für Rückhaltung und Reinigung

Zur Entsorgung in geeignete und verschlossene Behälter geben.

6.4 Verweis auf andere Abschnitte

Entsorgung: siehe Abschnitt 13

Abschnitt 7: Handhabung und Lagerung

7.1 Schutzmaßnahmen zur sicheren Handhabung

Informationen über Schutzmaßnahmen befinden sich im Abschnitt 8.

7.2 Bedingungen zur sicheren Lagerung unter Berücksichtigung von Unverträglichkeiten

Angaben zu den Lagerbedingungen

Behälter dicht verschlossen an einem trockenen, gut belüfteten Ort aufbewahren. Geöffnete Behälter sorgfältig verschließen und aufrecht lagern um jegliches Auslaufen zu verhindern. An einem kühlen Ort aufbewahren. Vor Gebrauch gut schütteln.

Empfohlene Lagerungstemperatur 2 - 8 °C

Nicht einfrieren.

Anforderungen an Lagerräume und Behälter

Lagerklasse: 12 Nicht brennbare Flüssigkeiten

7.3 Spezifische Endanwendungen

Außer den in Abschnitt 1.2 genannten Verwendungen sind keine weiteren spezifischen Verwendungen vorgesehen.

Abschnitt 8: Begrenzung und Überwachung der Exposition / Persönliche Schutzausrüstung

8.1 Zu überwachende Parameter

Grenzwerte für die Exposition am Arbeitsplatz und/oder biologische Grenzwerte

Arbeitsplatzgrenzwerte (AGW) Deutschland

Enthält keine Stoffe mit Arbeitsplatzgrenzwerten.

8.2 Begrenzung und Überwachung der Exposition

Geeignete technische Steuerungseinrichtungen

Allgemein übliche Arbeitshygienemaßnahmen.
Die beim Umgang mit Chemikalien üblichen Vorsichtsmaßnahmen sind zu beachten. Vor den Pausen und bei Arbeitsende Hände waschen.

Individuelle Schutzmaßnahmen - persönliche Schutzausrüstung

Augen- / Gesichtsschutz

Verwenden Sie zum Augenschutz nur Equipment, dass nach behördlichen Standards, wie NIOSH (US) oder EN 166 (EU), getestet und zugelassen wurde.

Hautschutz

Handschuhe

Mit Handschuhen arbeiten. Handschuhe müssen vor Gebrauch untersucht werden. Benutzen Sie eine geeignete Ausziehmethode (ohne die äußere Handschuhoberfläche zu berühren), um Hautkontakt mit diesem Produkt zu vermeiden. Entsorgung der kontaminierten Handschuhe nach Benutzung im Rahmen gesetzlicher Bestimmungen und der guten Laborpraxis. Waschen und Trocknen der Hände.

Die ausgewählten Schutzhandschuhe müssen die Spezifikationen der EG-Richtlinie 2016/425 und die davon abgeleitete Norm EN 374 erfüllen.

Anderer Hautschutz

Undurchlässige Schutzkleidung. Die Art der Schutzausrüstung muss je nach Konzentration und Menge des gefährlichen Stoffes am Arbeitsplatz ausgewählt werden.

Atemschutz

Kein Atemschutz notwendig. Bei störenden Emissionen Atemschutzmaske Typ OV/AG (US) oder ABEK (EU EN 14387) verwenden! Atemschutzgeräte und Komponenten müssen nach entsprechenden staatlichen Standards (beispielsweise NIOSH (US) oder CEN (EU)) zugelassen sein.

Begrenzung und Überwachung der Umweltexposition

Weiteres Auslaufen oder Verschütten verhindern, wenn dies ohne Gefahr möglich ist. Nicht in die Kanalisation gelangen lassen. Ein Eintrag in die Umwelt ist zu vermeiden.

Abschnitt 9: Physikalische und chemische Eigenschaften

9.1 Angaben zu den grundlegenden physikalischen und chemischen Eigenschaften

Aussehen	
- Aggregatzustand:	Suspension
- Farbe :	bräunlich
Geruch :	Keine Daten verfügbar
Geruchsschwelle :	Keine Daten verfügbar

pH-Wert :	6,0 bis 8,0
Schmelzpunkt/Gefrierpunkt :	0 °C
Siedebeginn und Siedebereich :	100 °C
Flammpunkt :	Nicht anwendbar
Verdampfungsgeschwindigkeit :	Keine Daten verfügbar
Entzündbarkeit (fest, gasförmig) :	Keine Daten verfügbar
obere/untere Entzündbarkeits- oder Explosionsgrenzen :	Keine Daten verfügbar
Dampfdruck :	23 hPa
Dampfdichte :	Keine Daten verfügbar
relative Dichte :	1,0 g/cm³
Löslichkeit(en) :	in Wasser vollständig mischbar
Verteilungskoeffizient: n-Octanol/Wasser :	Keine Daten verfügbar
Selbstentzündungstemperatur :	Keine Daten verfügbar
Zersetzungstemperatur :	Keine Daten verfügbar
Viskosität :	1 mPas
explosive Eigenschaften :	Keine Daten verfügbar
oxidierende Eigenschaften :	Keine Daten verfügbar

9.2 Sonstige Angaben

Keine Daten verfügbar

Abschnitt 10: Stabilität und Reaktivität

10.1 Reaktivität

Keine Daten verfügbar

10.2 Chemische Stabilität

Stabil unter angegebenen Lagerungsbedingungen.

10.3 Möglichkeit gefährlicher Reaktionen

Keine Daten verfügbar

10.4 Zu vermeidende Bedingungen

Temperaturen unterhalb von 2 °C und oberhalb von 30 °C

10.5 Unverträgliche Materialien

Salze

Säuren

10.6 Gefährliche Zersetzungsprodukte

Weitere Zersetzungsprodukte-Keine Daten verfügbar

Im Brandfall können gefährliche Zersetzungsprodukte entstehen, Art der Zersetzungsprodukte unbekannt.

Im Brandfall: siehe Kapitel 5

Abschnitt 11: Toxikologische Angaben

11.1 Angaben zu toxikologischen Wirkungen

akute Toxizität

Keine Daten verfügbar

Ätz-/Reizwirkung auf die Haut

Keine Daten verfügbar

schwere Augenschädigung/-reizung

Keine Daten verfügbar

Sensibilisierung der Atemwege/Haut

Keine Daten verfügbar

Keimzell-Mutagenität

Keine Daten verfügbar

Karzinogenität

IARC: Kein Bestandteil dieses Produkts, der in einer Konzentration von gleich oder mehr als 0.1% vorhanden ist, wird durch das IARC als voraussichtliches, mögliches oder erwiesenes krebserzeugendes Produkt für den Menschen identifiziert.

Reproduktionstoxizität

Keine Daten verfügbar

spezifische Zielorgan-Toxizität bei einmaliger Exposition

Keine Daten verfügbar

spezifische Zielorgan-Toxizität bei wiederholter Exposition

Keine Daten verfügbar

Aspirationsgefahr

Keine Daten verfügbar

Symptome und Wirkungen (verzögerte und chronische) mit Angaben der Expositionswege auch: Informationen über Toxikokinetik, Stoffwechsel und Verteilung

Keine Daten verfügbar

Abschnitt 12: Umweltbezogene Angaben

12.1 Toxizität

Keine Daten verfügbar

12.2 Persistenz und Abbaubarkeit

Keine Daten verfügbar

12.3 Bioakkumulationspotenzial

Keine Daten verfügbar

12.4 Mobilität im Boden

Keine Daten verfügbar

12.5 Ergebnis der PBT- und vPvB-Beurteilung

Eine PBT/vPvB Beurteilung ist nicht verfügbar, da eine Stoffsicherheitsbeurteilung nichterforderlich/nicht durchgeführt wurde.

12.6 Andere schädliche Wirkungen

Keine Daten verfügbar

Abschnitt 13: Hinweise zur Entsorgung

13.1 Verfahren der Abfallbehandlung

Behandlung verunreinigter Verpackungen

Wie ungebrauchtes Produkt entsorgen.

Abfallschlüssel gemäß Abfallverzeichnis-Verordnung (AVV)

06 Abfälle aus anorganisch-chemischen Prozessen (06 03 13*)

Besondere Vorsichtsmaßnahmen

Restmengen und nicht wieder verwertbare Lösungen einem anerkannten Entsorgungsunternehmen zuführen.

Abschnitt 14: Angaben zum Transport

14.1 UN-Nummer

ADR/RID: - IMDG: - IATA: -

14.2 Ordnungsgemäße UN-Versandbezeichnung

ADR/RID

kein Gefahrgut

IMDG-Code / ICAO-TI / IATA-DGR

Not dangerous goods

14.3 Transportgefahrenklassen

ADR/RID: - IMDG: - IATA: -

14.4 Verpackungsgruppe

ADR/RID: - IMDG: - IATA: -

14.5 Umweltgefahren

Kennzeichen umweltgefährdende Stoffe

ADR/RID / IMDG-Code / ICAO-TI / IATA-DGR: ☐ ja / x nein

Marine Pollutant: ☐ ja / x nein

14.6 Besondere Vorsichtshinweise für den Verwender

Keine Daten verfügbar

14.7 Massengutbeförderung gemäß Anhang II des MARPOL- Übereinkommens und gemäß IBC-Code

Keine Daten verfügbar

Abschnitt 15: Rechtsvorschriften

15.1 Vorschriften zu Sicherheit, Gesundheits- und Umweltschutz/spezifische Rechtsvorschriften für den Stoff oder das Gemisch

Dieses Sicherheitsdatenblatt erfüllt die Anforderungen der Verordnung (EG) Nr. 1907/2006.

15.2 Stoffsicherheitsbeurteilung

Für dieses Produkt wurde keine Stoffsicherheitsbeurteilung durchgeführt.

Abschnitt 16: Sonstige Angaben

Änderungen gegenüber der letzten Version

-

Abkürzungen

-

Literaturangaben und Datenquellen

https://echa.europa.eu, 03.03.2020

Methoden gemäß Artikel 9 der Verordnung (EG) Nr. 1272/2008 zur Bewertung der Informationen zum Zwecke der Einstufung verwendet wurden

Wortlaut der Gefahrenhinweise und/oder Sicherheitshinweise auf die in Abschnitt 2 bis 15 Bezug genommen wird

Schulungen für Arbeitnehmer

Erstellt am:	**03.03.2020**		
Überarbeitet am :	**22.07.2020**		
Gültig ab:			
Version:	1.0	**Ersetzt Version:**	-

Weitere Informationen

Die vorliegenden Informationen sind nach unserem besten Wissen zusammengestellt, sie erheben aber keinen Anspruch auf Vollständigkeit und sollten vom Benutzer nur als Leitfaden verstanden werden. Die Universität Duisburg-Essen schließt jegliche Haftung für Schäden aus, die beim Umgang oder im Kontakt mit diesen Chemikalien auftreten können. Für allgemeine Geschäftsbedingungen und zusätzliche Informationen siehe die Rückseite unserer Rechnungen oder Lieferscheine.

8.2.6.2. Material data sheet for silver colloid

	Normal value	Specification after automated synthesis
General information:		
Formula:	Ag	
Formula Weight:	107.87 g/mol	
Nanoparticle purity:	99.99 %	> 99 %
Appearance, color:	colloid, yellow	
Mass concentration:	99 mg/L	55 – 190 mg/L
Particle concentration*:	$9.3 \cdot 10^{15}$ particle/L	$(2 – 17) \cdot 10^{15}$ particle/L
Stability:		
Storage Temperature:	2 - 8 °C	
Shelf life:	6 months	
Solvent:	0.25 mmol/L sodium citrate	
Zeta potential:	-63 mV	< -30 mV
pH value:	8	7 – 9
Size properties:		
Primary peak diameter (TEM):	7 nm	< 10 nm
Hydrodynamic peak diameter (numb, ADC):	7 nm	< 11 nm
Hydrodynamic peak diameter (mass, ADC):	10 nm	< 13 nm
Surface (TEM):	68 m²/g	>60 m²/g
Aspect ratio:	1.3	<1.5
Polydispersity Index (TEM):	0.1	<0.3
Polydispersity Index (ADC):	0.3	< 0.4
Optical properties:		
Absorption Max/SPR-Peak:	400 nm	< 405 nm
Optical density (OD) @SPR:	4	> 2
Molar extinction coefficient @ 270 nm:	13 L/(mol cm)	> 8 L/(mol cm)
Molar extinction coefficient SPR peak:	53 L/(mol cm)	> 39 L/(mol cm)

* calculated by primary particle diameter

Exemplary hydrodynamic size distribution

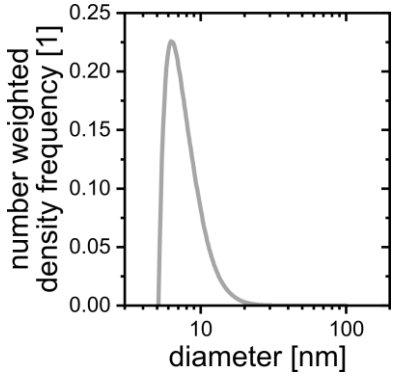

Exemplary TEM image

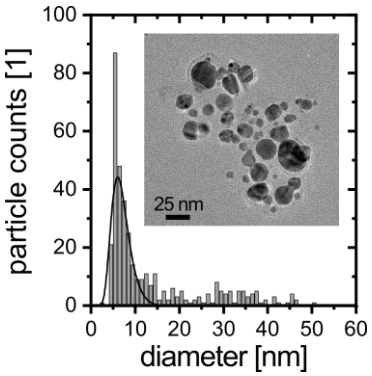

Exemplary UV-Vis spectrum

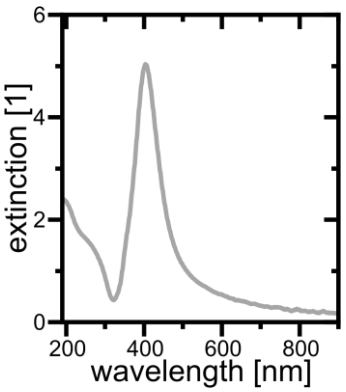

8.2.6.3. Material data sheet for gold colloid

	Normal value	Specification after automated synthesis
General information:		
Formula:	Au	
Formula Weight:	196.97 g/mol	
Nanoparticle purity:	99.99 %	> 99 %
Appearance, color:	colloid, red	
Mass concentration:	93 mg/L	55 – 130 mg/L
Particle concentration*:	$13.8 \cdot 10^{15}$ particle/L	$(12 – 71) \cdot 10^{15}$ particle/L
Colloidal stability:		
Storage Temperature:	2 - 8 °C	
Shelf life:	6 months	
Solvent:	0.1 mmol/L NaCl	
Zeta potential:	-63 mV	< -30 mV
pH value:	6	5 – 7
Size properties:		
Primary peak diameter (TEM):	9 nm	< 12 nm
Hydrodynamic peak diameter (numb, ADC):	9 nm	< 12 nm
Hydrodynamic peak diameter (mass, ADC):	11 nm	< 15 nm
Specific surface (TEM):	40 m²/g	> 30 m²/g
Aspect ratio:	1.3	< 1.4
Polydispersity Index (TEM):	0.12	< 0.2
Polydispersity Index (ADC):	0.3	< 0.4
Optical properties:		
Absorption Max/SPR-Peak:	520 nm	< 525 nm
Optical density (OD):	1.3	> 0.6
Molar extinction coefficient @ 380 nm:	211 L/(mol cm)	> 195 L/(mol cm)
Molar extinction coefficient SPR peak:	282 L/(mol cm)	> 210 L/(mol cm)

* calculated by primary particle diameter

Exemplary hydrodynamic size distribution

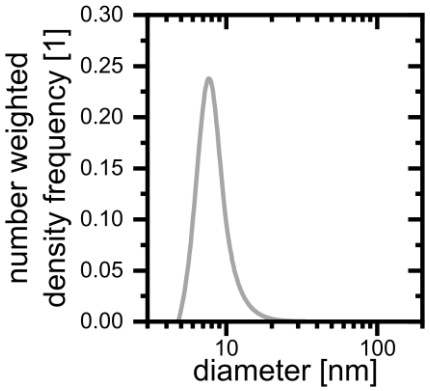

Exemplary TEM image

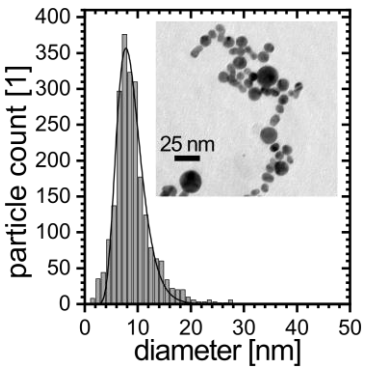

Exemplary UV-Vis spectrum

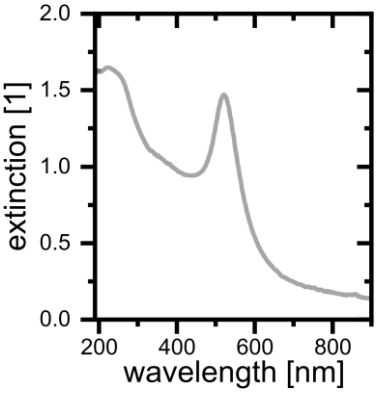

8.2.6.4. Material data sheet for platinum colloid

	Normal value	Specification after automated synthesis
General information:		
Formula:	Pt	
Formula Weight:	195.08 g/mol	
Nanoparticle purity:	99.99 %	> 99 %
Appearance, color:	colloid, brown	
Mass concentration:	96 mg/L	68 – 124 mg/L
Particle concentration*:	$14 \cdot 10^{16}$ particle/L	$(10 – 19) \cdot 10^{16}$ particle/L
Stability:		
Storage Temperature:	2 - 8 °C	
Shelf life:	6 months	
Solvent:	0.1 mmol/L NaCl	
Zeta potential:	-65 mV	< -30 mV
pH value:	6	4 – 7
Size properties:		
Primary peak diameter (TEM):	4 nm	< 4.5 nm
Hydrodynamic peak diameter (numb, ADC):	5 nm	< 7 nm
Hydrodynamic peak diameter (mass, ADC):	7 nm	< 9 nm
Surface (TEM):	70 m²/g	> 65 m²/g
Aspect ratio:	1.4	< 1.5
Polydispersity Index (TEM):	0.2	< 0.3
Polydispersity Index (ADC):	0.1	< 0.2
Optical properties:		
Optical density (OD) @ 300 nm:	0.8	> 0.4
Molar extinction coefficient @ 300 nm:	214 L/(mol cm)	> 195 L/(mol cm)

* calculated by primary particle diameter

Exemplary hydrodynamic size distribution

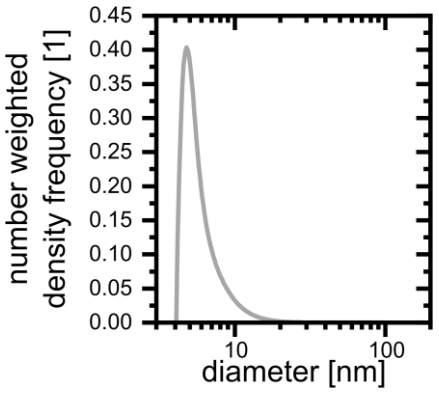

Exemplary TEM image

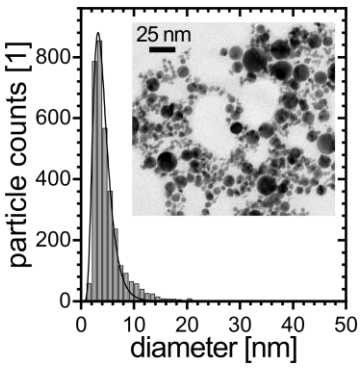

Exemplary UV-Vis spectrum

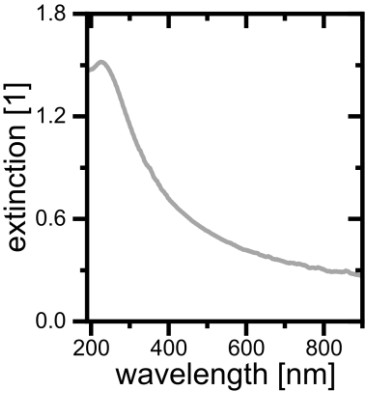

8.2.7. Preliminary hazardous analysis of the automated ablation process

Tab. S 12: Equipment list for the device, with the number corresponding to the items in Fig. 50

No.	Description	Manufacturer	Material	Modell	comment
B-1	2L fluid tank	VWR	HDPE	215-3013	
B-2	2L fluid tank	VWR	HDPE	215-3013	
B-3	2L fluid tank	VWR	HDPE	215-3013	
B-4	collecting vessel	-	-	-	chosen and provided by user
B-5	3D printed ablation chamber with 1 target, 2 optical windows, and valves V-2 and V-3	Shapeways (3D print)	smooth fine detail plastic, PA12		
E-1	raspberry pi	CryLaS GmbH	-	3B	
E-2	control unit for P-1 to P-3	Bartels Mikrotechnik GmbH	-	mp6-QuadKEY	
E-3	laser control unit	CryLaS GmbH	-	eMOPA1064-500	
E-4	circuit board for O-2 and O-3	CryLaS GmbH	-		
O-1	laser	CryLaS GmbH	-	eMOPA1064-500	
O-2	galvanometric mirrow	CryLaS GmbH	N-BK7, -C coated		
O-3	galvanometric mirror	CryLaS GmbH	N-BK7, -C coated		
O-4	focussing lens	Thorlabs	N-BK7, -C coated	LA1251-C	2 lenses with 100 mm focal distance
P-1	piezoelectric double-membrane micro pump	Bartels Mikrotechnik GmbH	PPSU (material in contact with fluid)	mp6-hyb	
P-2	piezoelectric double-membrane micro pump	Bartels Mikrotechnik GmbH	PPSU (material in contact with fluid)	mp6-hyb	

P-3	piezoelectric double-membrane micro pump	Bartels Mikrotechnik GmbH	PPSU (material in contact with fluid)	mp6-hyb	
V-1	4-way hose connection	VWR	POM	ISMCISM536	https://de.vwr.com/store/product/7829830/tubing-connectors
V-2	quick coupling	Industrial Specialties Mfg. & IS MED Specialties	POM	20 ACV-PB2-02, 1/8" hose barb valued plug	20 ACV-SB2-02, 1/8" hose barb valued socket as a counterpart, is fixed in the chamber holding
V-3	outlet nozzle	Shapeways (3D print)	smooth fine detail plastic	CAD file	
V-4	one-way valve	Cole-Parmer	PP	PP-Miniatur-Rückschlagventil, 1/8"-Schlauchverbinder, Membran	
V-5	one-way valve	Cole-Parmer	PP	PP-Miniatur-Rückschlagventil, 1/8"-Schlauchverbinder, Membran	
V-6	one-way valve	Cole-Parmer	PP	PP-Miniatur-Rückschlagventil, 1/8"-Schlauchverbinder, Membran	

Tab. S 13: Preliminary hazard analysis of the device with the equipment numbers based on Fig. 50 and Tab. S 12

No.	mal-function	effect without safety measures	safety measures	extent of damage	probability of occurrence	consequence for the ablation process if malfunction is detected	interaction of the device with the user
B-1 B-2 B-3	fluid tank is empty or is not in place	· air is pumped through the tubes and ablation chamber · no colloid is produced, potential damage at the ablation capsule	· lower liquid level measurement (L-01, L-02, L-03)	high	probable	ablation does not start	comment for the user on display that fluid tank is empty or removed and that the process is started as soon as a full tank is insert
B-1 B-2 B-3	fluid tank is removed during operation	· air is pumped through the tubes and ablation chamber · no colloid is produced, potential damage at the ablation capsule	· lower liquid level measurement (L-01, L-02, L-03)	high	rare	ablation is aborted	comment for the user on display that fluid tank is empty or removed and that the process is continued as soon as a full tank is insert
B-4	is not set in place or is removed	· colloid is not collected and flows into the device interiour · corrosion of the device, electronics next to the device could be damaged	· B-7 collects colloid, message on screen remaind user to put vessel into place, confirmation of user is demanded	medium	occasional	none	reminder for user before the ablation is started to put B-4 into place user confirmation is required
B-4	is full	· device interior gets wet, liquid on table/bench · corrosion of the device, electronics next to the device could be damaged	· B-7 collects excess colloid	low	occasional	none	message for user of minimal required vessel volume
B-4	vessel tips	· device interior gets wet, liquid on table/bench · corrosion of the device · damage of electronics next to the device	· B-7 collects excess colloid, base for safe stand	low	rare	none	none

No.	mal-function	effect without safety measures	safety measures	extent of damage	probability of occurrence	consequence for the ablation process if malfunction is detected	interaction of the device with the user
B-5	ablation chamber window is damaged	· liquid inside the device, corrosion by NaCl in the device · no defined volume flow · scattering of laser radiation	· ablation chamber is position over colloid outlet, so liquid drops down, also liquid is collected in B-6 and detected by M-01 · quality of the colloid is monitored by extinction measurement O-02 · device housing protects the user from scattered irradiation	medium	rare	process is aborted if threshold values for M-01 or O-02 are not within their specifications anymore	error message according to Tab. 12 is shown on the display
B-5	ablation target is damaged/ has holes	· no guaranteed colloid quality · ablation chamber is potentially damaged	· O-01 detects IR irradiation behind the ablation target	low	probable	process is aborted if threshold values for O-01 is not within its specifications anymore	error message according to Tab. 12 is shown on the display
B-5	is removed during operation	· user can be harmed by laser irradiation	· mechanisal interlock blocks irradiation · I-01 detects removal of the ablation capsule	high	occasional	process is aborted if threshold values for I-01 is not within its specifications anymore	message for the user, that the process is aborted since the target capsule has been removed

No.	mal-function	effect without safety measures	safety measures	extent of damage	probability of occurrence	consequence for the ablation process if malfunction is detected	interaction of the device with the user
B-6	is full	· Liquid inside the device, corrosion by NaCl in the device · no guaranteed colloid quality · damage of electronics next to the device	· moisture sensor M-01 detects small amounts of liquid in the tray	medium	occasional	process is aborted if threshold values for M-01 is not within its specifications anymore	error message according to Tab. 12 is shown on the display
B-7	is full	· Liquid inside the device, corrosion by NaCl in the device · no guaranteed colloid quality · damage of electronics next to the device	· upper liquid level measurement L-04	medium	probable	process is aborted if threshold values for L-04 is not within its specifications anymore	message on screen to empty vessel before ablation is started and confirmation of user is demanded
O-1	does not emit irradiation	· no colloid is produced	· O-02 detects no increase in extinction	low	occasional	process is aborted if threshold values for O-01 is not within its specifications anymore	error message according to Tab. 12 is shown on the display
O-2 O-3	do not move	· no/hardy any colloid is produced	· O-01 detects IR irradiation behind the ablation target · O-02 detects no increase in extinction	low	occasional	process is aborted if threshold values for O-01 and O-02 are not within their specifications anymore	error message according to Tab. 12 is shown on the display
P-1 P-2 P-3	do not work	· no fluid is pumped through the tubes and the ablation capsule · no colloid is produced	· O-02 detects no change · L-01/L-02/L-03 changes in the liquid level	high	rare	process is aborted if threshold values for O-02 is not within its specifications anymore	error message according to Tab. 12 is shown on the display

No.	mal-function	effect without safety measures	safety measures	extent of damage	probability of occurrence	consequence for the ablation process if malfunction is detected	interaction of the device with the user
P-1 P-2 P-3 V-4 V-5 V-6	leakage	· Liquid inside the device · corrosion by NaCl in the device · no defined volume flow	· positioned over B-6 · leakage detection with M-01	medium	rare	process is aborted if threshold values for M-01 is not within its specifications anymore	error message according to Tab. 12 is shown on the display

Tab. S 14: Overview of the selected sensors

usage in device	sensor type	description
Vis sensor	Vis emitting diode	“Cree LED C503B-BAS/BAN”, 470 nm, angle of half intensity ± 15°, diameter 5 mm,
Vis sensor	Vis detecting diode	Light Dependent Resistor Module (SE012), Iduino, 25.0 x 15.0 mm
IR sensor	IR emitting diode	„Vishay TSAL 6200“ peak wavelength 940 nm, angle of half intensity ± 17°, diameter 5 mm, GaAlAs
IR sensor	IR detecting diode	“Iduino Flame Sensor Module, SE060”, highest irradiance responsivity from 760 to 1100 nm, detection angle ~60 °, size 30.0 x 15.0 mm
liquid level senor	capacitive sensor	“SparkFun Single Button Capacitive Touch Breakout - AT42QT1011”, maximal panel thickness up to 12 mm glass/ 6 mm plastic
humidity/leakage sensor	conductivity sensor	“Waveshare Liquid Level Sensor Water” dimension 19.0 mm x 63.0 mm
temperatur sensor	temperatur sensor	“Iduino 1485330 Temperatursensor”, -55 °C to +125 °C
target monitoring	IR detecting diode	“Iduino Flame Sensor Module, SE060”, wavelength 760 to 1100 nm, detection angle ~60 °, size 30.0 x 15.0 mm

8.2.8. Selection and adjustment of sensors

For the determination of the run-in period, water is continuously pumped through the setup, and the detector data in dependence of the run time is collected. The data are evaluated in terms of the signal-time correlation, which should approach zero. Since the sensor signal over time is not normally distributed, Spearman’s rank-order correlation is chosen to determine the correlation coefficient. As depicted in Fig. S 22, no significant change in the sensor signal over time is reached after 60 minutes, which concludes that a minimal run-in period of 60 min is required after the diode was switched off.

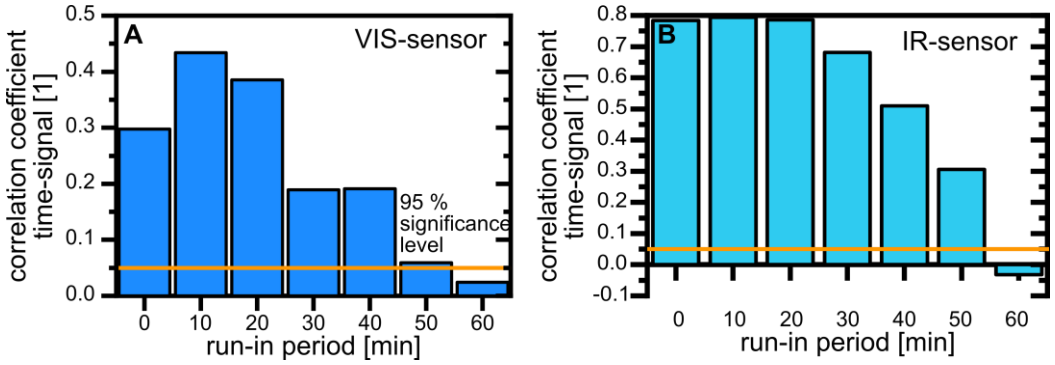

Fig. S 22: Run-in period for the LED used for the concentration measurement O-02 (A) and the IR LED used for the target monitoring (B)

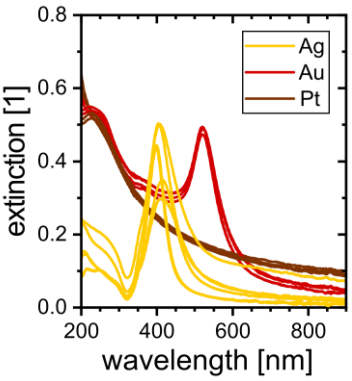

Fig. S 23: Exemplary UV-Vis spectra of Ag, Au, and Pt

8.2.9. Economic feasibility of colloids from automated laser ablation

Tab. S 15: Material costs of the device per piece for calculation of the short- and long-term break-even price, the letters in brackets show the item's category (L: laser, C: case, M: mechanics, F: fluidics, E: electronics, O: optics)

Sum [€/piece]	**19758.35**
Item	**€/piece**
laser, eMOPA (L)	13500.00
scanner (O)	150.00
lenses (O)	68.84
flow chamber (F)	267.84
mounting mechanism for flow chamber (M)	400.00
Touch display (M)	32.10
check valve (F)	17.46
laser controler (OEM) (E)	0.00
assembly plate (M)	2000.00

Item	**€/piece**
controller Scanner (E)	100.00
controler Pumpe (E)	0.00
sensor, concentration (E)	3.29
tubes (F)	10.00
electronical interlock, laser (E)	0.00
sensor, temperature (E)	14.32
sensor, liquid level (E)	6.20
sensor, liquid level (E)	6.20
sensor, liquid level (E)	6.20

cooler (M)	0.00
overall controller (E)	38.65
case fan (M)	0.00
fluid tank (F)	1.50
fluid tank (F)	1.50
fluid tank (F)	1.50
pump (F)	329.00
4-way-valve (F)	1.81
vessel (F)	1.50
vessel (F)	1.50
collection basin (F)	0.00
quick coupling (F)	9.37

sensor, leakage (E)	11.92
sensor, liquid level (E)	6.20
power supply laser (E)	67.38
power supply PC (E)	0.00
controler scanner (E)	0.00
power supply scanner (E)	0.00
sensor, IR (E)	4.07
case for scanner (M)	0.00
case (C)	2600.00
electronic components (e.g., wires, socket) (E)	100.00

Tab. S 16: Variable manufacturing costs for the device

Sum [€/piece]	**603.35**		
Item	**€/year**	**€/piece**	**comment**
Logistic (shipping costs Eckstein)		0	purchase of equipment of 2 devices simultaneous
Logistic (Bartels)		18	can be reduced by purchasing
Logistic (CryLaS)		47.49	package (DHL) + 27 € bulky item + 3 € collection of package
Logistic (Shapeways)		6.27	
Logistic (ColeParmer)	7.62	0.76	Cross connectors are shipped in packaging units of 10 additionally ordering of 10 checking valves;
Logistic (Conrad)		0	shipment value for one device over the limit for free shipment
Logistic (VWR)		10	
Logistic (Projekter)		20.49	package (DHL) + 3 € package collection
Logistic (NordsonMedical)	3.33	0.33	packaging units of 25 pieces; ordering 3x per year to cover demand for capsules (shipping costs are split by annually produced pieces)
package material and shipping costs for the device		500	

Tab. S 17: Fixes costs for the device; personnel costs according to the "Tarifvertrag für den Öffentlichen Dienst"

Sum [€/year]	**147200**
Item	**€/year**
employee costs, founder	80000
employee costs, technician	60000
employee costs, temporal assistant	7200

Tab. S 18: Overhead costs for the device and the capsules

Sum [€/year]	**77000**
Item	**€/year**
rent	30000
travel costs	1000
costs for advertisement	20000
office supplies	20000
insurance	3000
legal assistance	3000

Tab. S 19: Material costs of the capsule per piece for calculation of the short- and long-term break-even price

Sum [€/piece], Ag/Au/Pt	**122.84**	**195.44**	**193.44**
Item		€/piece	
printing costs for the flow chamber		45.00	
optical window		60.00	
IR sensor		4.07	
metall target (0.05x0.5x1 cm³) Ag/Au/Pt	5.00	77.00	75.00
Quickcoupling		9.37	

Tab. S 20: Variable manufacturing costs for the capsule

Sum		**16.6033**	
Item	**€/year**	**€/piece**	**comment**
Logistic (Shapeways)		6.27	
Logistic (Conrad)		0	
package material and shipping costs for the capsule		10	
Logistic (NordsonMedical)	16.67	0.3333	packaging units of 25 pieces; ordering 3x per year to cover demand for capsules (shipping costs are split by annually produces pieces)

Tab. S 21: Fixed and running costs of the automated colloid production considering the production of 100 mL per week, if not marked in the description, the costs are valid independently of the produced colloid material

		costs
fixed costs	**purchase price of the device**	**85 000 €**
running costs	capsule price per piece	215 €/piece
	produced colloid per capsule (75% of material used)	2.0 L/piece
	capsules (Ag)	**568.40 €/year**
	capsule price per piece	360 €/piece
	produced colloid per capsule (75% of material used)	3.6 L/piece
	capsules (Au)	**517.31 €/year**
	capsule price per piece	350 €/piece
	produced colloid per capsule (75% of material used)	4.0 L/piece
	capsules (Pt)	**452.53 €/year**
	hourly wage of one laboratory chemist [442]	20.77 €/h
	time for device handling	0.25 h/100mL
	personnel costs	**270.01 €/year**
	device power consumption	200 W
	power costs [443]	0.29 €/(kWh)
	productivity (Ag)	10 mg/h
	productivity (Au)	13 mg/h
	productivity (Pt)	20 mg/h
	energy costs (Ag)	**3.01 €/year**
	energy costs (Au)	**2.32 €/year**
	energy costs (Pt)	**1.51 €/year**
	water for flushing	2.6 L/year
	stabilizer solution for flushing and synthesis	7.8 L/year
	costs for water and stabilizer solutions (0.1 mmol/L NaCl or 0.25 mmol/L trisodium citrate) [444–446]	10.21 €/year
	costs for, e.g., vessels, gloves [447–449]	43.47 €/year
	expendable materials	**53.68 €/year**
	total (Ag)	**895.10 €/year**
	total (Au)	**843.32 €/year**
	total (Pt)	**777.73 €/year**

Tab. S 22: Overview of the distributor prices for precursor salts and metal foils for the calculation of the ablation capsule price; the lowest price (green) and highest price (orange) are marked for each metal and each synthesis method

distributor	prices for Silver nitrate > 99 % [US$/g($AgNO_3$)] (price for precipitated silver [US$/g])	prices for K_2PtCl_6 >90 % [US$/g($K_2PtCl_6$)] (price for precipitated platinum [US$/g])	prices for H_2PtCl_6 >90 % [US$/g($H_2PtCl_6$)] (price for precipitated platinum [US$/g])	silver 99.99% purity, 0.5 mm thick [US$/g]	platinum 99.99% purity, 0.5 mm thick [US$/g]
Sigma-Aldrich, Germany	2.74 (4.28)	45.94 (114.86)	363.00 (957.00)	27.39 19.69	236.96
Alfa Aesar, Germany	1.42 (2.21)	75.70 (189.24)	52.21 (137.40)	11.76	138.99
Goodfellow	-	-	-	6.31	37.23
Carl Roth	1.82 (2.84)	-	96.9 (257.24)	-	-
mean value	1.99 ± 0.55 (3.11 ± 0.87	126.75 ± 119.50 (331.15 ± 316.74)		16 ± 8	138± 82

Tab. S 23: Costs determined in [65] for the chemical synthesis of Au NPs

laboratory assistant	23.97	€/h
energy	0.20	€/h
investment costs	3 926	€

Tab. S 24: Calculation of the variable costs for the chemical synthesis of colloids with a concentration of 100 mg/L and data from Tab. S 20 and Tab. S 21.

batch size [mg]	produc-tivity [mg/h]	production time [h/batch]	working time [h/batch]	personnel costs [€/batch]	energy costs [€/batch]	Ag variable costs [€/g]	Au variable costs [€/g]	Pt variable costs [€/g]
1	3.5	0.29	0.12	2.80	0.02	2821.99	3085.60	3117.10
3	8.32	0.36	0.15	3.60	0.03	1211.03	1474.63	1506.13
10	16.2	0.62	0.27	6.39	0.05	647.19	910.79	942.29
100	25.4	3.94	1.77	42.35	0.34	429.71	693.31	724.81
500	26.8	18.64	8.43	202.14	1.64	410.37	673.98	705.48
1000	27	37.04	16.77	401.89	3.27	**407.96**	**671.56**	**703.09**

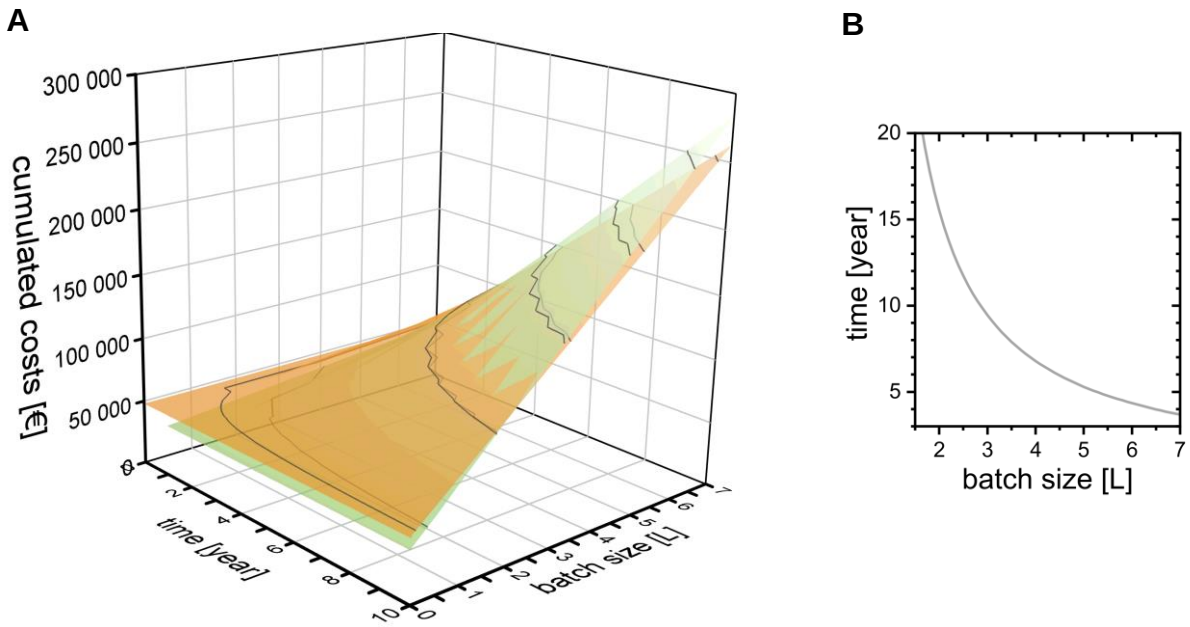

Fig. S 24: The cumulated costs for gold colloids produced with the automated device (orange surface) and chemically (green surface) in dependency of the depreciation time and the required mean weekly batch size (A) is shown. The intersection line between both surfaces represents the amortization time of the automated device, which is a function of the required amount of colloid and is shown in (B).

8.2.10. Downstream production of functional materials with the automated device

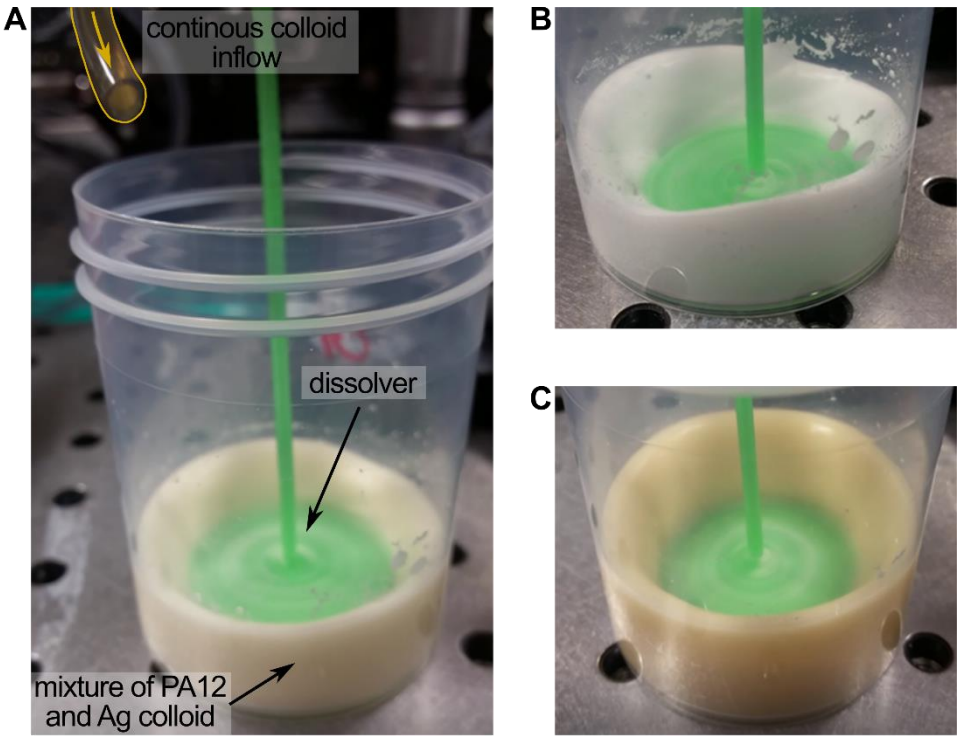

Fig. S 25: Setup for the ablation-coupled downstream supporting of PA12 powder with Ag, where a dissolver is used to distribute the powder in the liquid, which would otherwise float on the liquid surface (A). Before the ablation process is started, PA12 powder is mixed in water to achieve a milky-white dispersion (A). After the ablation process is finished, the dispersion's color has changed to yellow.

8.3. Acknowledgments

Vielen Dank an …

…meinen Doktorvater Prof. Dr.-Ing. Stephan Barcikowski für die Möglichkeit meine Promotion in seinem Arbeitskreis zu absolvieren, für das zahlreiche fachliche Feedback und die konstruktive Kritik. Zudem bedanke ich mich für die Möglichkeit an Konferenzen teilnehmen zu dürfen.

…Prof. Dr. Heinz Huber für die Übernahme des Korreferats und die ausführlichen fachlichen Diskussionen.

…PD Dr. Bilal Gökce für die Aufnahme in seine Forschungsgruppe.

…das Zentrale Innovationsprogramm Mittelstand (ZIM) des Bundesministeriums für Wirtschaft und Energie (BMWi) für die Finanzierung meines Forschungsprojektes.

…meine Projektpartner bei Projekter Industrial Design und der CryLaS GmbH Susanne Boers, Nariman Kazroni, Sébastien Lienhard, Johannes Negendank, Fabian Winter, Dr. Hartmut Zimmermann. Vielen Dank für eure Unterstützung, Kreativität und Faszination für unser Projekt.

…die Technische Chemie I für die Zusammenarbeit und zahlreichen gemeinsamen Unternehmungen. Ein besonderer Dank geht hier an:

- …Florian de Kock für deine Hilfe bei Werkstattarbeiten und dem 3d-Drucken.
- …Jurij Jakobi für die Durchführungen von TEM Messungen.
- …Mark Kalus für den Austausch über die Ablation und Shadowgraphie.
- …René Streubel für die Unterstützung bei technischen Fragestellungen.
- …Nina Stockem für deine Unterstützung bei allen organisatorischen und Verwaltungsangelegenheiten.
- … Florian, Jurij, René und Nina für eure Geduld in alles Beschaffungs- und SAP-Angelegenheiten.
- …Vladislav Shavrov für unermüdliches abarbeiten von Messreihen
- …Tobias Bessel für deinen Fleiß während deines Praktikums und deine Unterstützung bei der Sensorimplementierung

…Rosa van Vlodrop und Andreas Schielke für die gemeinsamen Kaffeerunden, die häufig für die nötige Pause gesorgt und viel Freude in den Arbeitsalltag gebracht haben.

…Jonas Dittrich für deine Geduld und deine Unterstützung insbesondere während der Schreibphase aber auch für die gemeinsamen Erlebnisse und Erfahrungen der letzten Jahre.

8.4. Curriculum Vitae

Der Lebenslauf ist in der Online-Version aus Gründen des Datenschutzes nicht enthalten.

Der Lebenslauf ist in der Online-Version aus Gründen des Datenschutzes nicht enthalten.

8.5. Publication and conference contributions

During this thesis, several peer-reviewed articles and conference contributions are published. The contributions are listed below, starting with peer-reviewed publications and followed by poster presentations.

Peer-reviewed publications:

Dittrich, S., Streubel, R., McDonnell, C., Huber, H.P., Barcikowski, S., Gökce, B. Comparison of the productivity and ablation efficiency of different laser classes for laser ablation of gold in water and air. Appl. Phys. A 125, 432 (2019).

Dittrich, S., Kohsakowski, S., Wittek, B., Hengst, C., Gökce, B., Barcikowski, S., Reichenberger, S. Increasing the Size-Selectivity in Laser-Based g/h Liquid Flow Synthesis of Pt and PtPd Nanoparticles for CO and NO Oxidation in Industrial Automotive Exhaust Gas Treatment Benchmarking, Nanomaterials, 10 (8), 1582 (2020).

Dittrich, S., Barcikowski, S., Gökce, B. Plasma and nanoparticle shielding during pulsed laser ablation in liquids cause ablation efficiency decrease, Opto-Electronic Advances, 4 (1), 20007201 – 20007215 (2021).

Dittrich, S., Spellauge, M., Gökce, B., Huber, H. P., Barcikowski, S. Picosecond resolved pump-probe microscopy revealing the mechanism of high power-specific productivity of sub-ns laser ablation in liquid, to be submitted (2021)

Poster presentations (*: presenting author)

Stephan, S.*, Reichenberger, S., Streubel, R., Barcikowski, S., Gökce, B. Productivity, efficiency and cost effectiveness of different laser systems for the synthesis of ligand-free platinum nanoparticles. In: 8th NRW Nano Conference, Dortmund, Germany (November 2018)

Stephan, S.*, Streubel, R., McDonnell, C., Huber, H.P., Barcikowski, S., Gökce, B. Comparison of laser ablation in water and air with different laser classes regarding productivity and economic feasibility. In: European Materials Research Society Spring Meeting, Nice, France (May 2019)

Dittrich, S.*, Streubel, R., McDonnell, C., Huber, H.P., Barcikowski, S., Gökce, B. Productivity and economic feasibility of laser ablation in water and air with different laser classes In: Annual celebration of the Center for Nanointegration Duisburg-Essen (CENIDE), Duisburg, Germany (November 2019)

Dittrich, S.*, Streubel, R., McDonnell, C., Huber, H.P., Barcikowski, S., Gökce, B. Comparison of nanoparticle synthesis by laser ablation in water and air regarding productivity and economic feasibility. In: CENIDE conference, Bergisch Gladbach, Germany (February 2020)

8.6. Declaration of scientific contributions

Parts of the results presented in this thesis have been published in peer-reviewed papers in cooperation with co-authors, with my own contributions declared as follows:

Chapter 4.1.1

Dittrich, S., Streubel, R., McDonnell, C., Huber, H.P., Barcikowski, S., Gökce, B.
Comparison of the productivity and ablation efficiency of different laser classes for laser ablation of gold in water and air. Appl. Phys. A 125, 432 (2019).
DOI: 10.1007/s00339-019-2704-8

SD performed the ablation experiments with the Rofin Powerline E20 and DSS-1064-Q4 lasers. Ablations with the Amphos flex500 are performed by RS. SD prepared the original draft. HPH, SB, and GB supervised the study and all authors reviewed the final manuscript.

Chapter 4.1.2

Dittrich, S., Barcikowski, S., Gökce, B.
Plasma and nanoparticle shielding during pulsed laser ablation in liquids cause ablation efficiency decrease. Opto-Electronic Advances, 4 (1), 20007201 – 20007215 (2021).
DOI: 10.29026/oea.2021.200072

SD performed all experiments and prepared the original draft. SB and BG supervised the study and all authors reviewed the final manuscript.

Chapter 4.1.3

Dittrich, S., Spellauge, M., C., Huber, H.P., Barcikowski, S., Gökce, B.
Origin of high ablation efficiency of sub-nanosecond laser ablation in liquid revealed by pump-probe microscopy. (to be submitted)

SB, BG, and HPH proposed the original idea and supervised the project. SD and MS fabricated the samples, performed the measurements, and prepared the original manuscript draft. SD and MS contributed equally to this work. All authors reviewed and edited the manuscript.

Chapter 4.2.1

Dittrich, S., Kohsakowski, S., Wittek, B., Hengst, C., Gökce, B., Barcikowski, S., Reichenberger, S.

Increasing the Size-Selectivity in Laser-Based g/h Liquid Flow Synthesis of Pt and PtPd Nanoparticles for CO and NO Oxidation in Industrial Automotive Exhaust Gas Treatment Benchmarking, Nanomaterials, 10 (8), 1582 (2020).

DOI: 10.3390/nano10081582

The experiments were conducted by SK and SR. The data were analyzed by SK, SR, and SD. SD prepared the original draft. BG, SB, and SR supervised the study and all authors reviewed the final manuscript.

Hiermit erkläre ich, dass ich für die vorliegende Arbeit mit dem Titel

„Development of a desktop device for automated laser ablation in liquids“

selbst verfasst und dabei nur die angegebenen Hilfsmittel und Quellen verwendet wurden. Alle inhaltlich oder wörtlich zitierten Stellen sind textlich mit Literaturhinweisen markiert und kenntlich gemacht worden. Außerdem versichere ich, dass ich die Arbeit in dieser oder ähnlicher Form bei keiner anderen Universität eingereicht worden ist und ich noch nie an einem Promotionsverfahren der Universität Duisburg-Essen oder einer anderen Universität teilgenommen habe.

Essen, _____

_____

Sarah Dittrich